# Structural and Functional Imaging of the Human and Small Animal Eyes Using Ultrahigh Speed Fourier Domain Optical Coherence Tomography



by

Woo Jhon Choi

B.S., Electrical and Computer Engineering
B.S., Biomedical Engineering
A.B., Physics
Duke University, 2009

S.M. Electrical Engineering and Computer Science
Massachusetts Institute of Technology, 2011

Submitted to the
DEPARTMENT OF ELECTRICAL ENGINEERING AND COMPUTER SCIENCE
in partial fulfillment of the requirements for the degree of
DOCTOR OF PHILOSOPHY in ELECTRICAL ENGINEERING AND COMPUTER SCIENCE

at the

MASSACHUSETTS INSTITUTE OF TECHNOLOGY

September 2014



Signature of Author: Signature redacted
Department of Electrical Engineering and Computer Science
August 12, 2014

Certified by: Signature redacted
James G. Fujimoto
Professor of Electrical Engineering and Computer Science
Thesis Supervisor

Accepted by: Signature redacted
Leslie A. Kolodziejski
Professor of Electrical Engineering and Computer Science
Chair, Department Committee on Graduate Students

# Structural and Functional Imaging of the Human and Small Animal Eyes Using Ultrahigh Speed Fourier Domain Optical Coherence Tomography

by

Woo Jhon Choi

Submitted to the Department of Electrical Engineering and Computer Science in August 2014 in Partial Fulfillment of the Requirements for the Degree of Doctor of Philosophy in Electrical Engineering and Computer Science

## Abstract

Optical coherence tomography (OCT) is a non-invasive optical imaging technique that allows the three-dimensional structure of biological tissue to be visualized with micrometer resolution. In ophthalmology OCT has the unique advantage that it provides cross-sectional images of the retina and choroid noninvasively and in vivo, which have led OCT to be a clinical standard for the diagnosis of a variety of retinal diseases. Although current commercial Fourier domain OCT systems have high imaging speeds of 20-100kHz A-scan rates, these imaging speeds are not sufficient for more advanced structural and functional imaging techniques. Current state-of-the-art spectral domain and swept source OCT provide ultrahigh imaging speeds of >200kHz A-scan rates. These speeds enable functional imaging of retinal blood flow, OCT angiography of the retinal and choroidal microvasculature, and wide field volumetric structural imaging of the retina and choroid. In this thesis, advances in structural and functional ophthalmic imaging techniques for the human and small animal eyes are investigated using ultrahigh speed Fourier domain OCT. The following topics are discussed: (1) a method for numerically extracting and compensating dispersion mismatch in ultrahigh resolution spectral domain OCT, (2) ultrahigh speed spectral domain imaging in the small animal eye for measuring total retinal blood flow, (3) development of ultrahigh speed phase stable swept source OCT system for human retinal imaging, (4) OCT angiography of the choriocapillaris in the human eye, (5) clinical applications of OCT angiography in retinal diseases, including diabetic retinopathy and age-related macular degeneration, (6) small animal anesthesia protocol for functional hemodynamic imaging, and (7) imaging of neurovascular coupling in small animals using ultrahigh speed OCT.

Thesis Supervisor: James G. Fujimoto

Title: Elihu Thomson Professor of Electrical Engineering and Computer Science

## Acknowledgements

I would like to thank Dr. Bernhard Baumann, currently at the Medical University of Vienna, for being such a wonderful colleague, mentor, and friend in the past four years. Being able to learn something every day and to discuss new ideas and thoughts openly is a rare opportunity that Dr. Baumann provided during my career as a doctoral candidate at MIT.

The completion of this thesis was made possible largely by Eric Moult, a junior graduate student who joined Prof. Fujimoto group only last year. Eric supported me greatly in the past few months both scientifically and mentally. Although we cannot work together here at MIT as long as I would like, I am certain that our friendship will last for many years to come.

All the work that I have accomplished at MIT was possible because of Prof. James Fujimoto, my research advisor. I cannot thank him more for being such a great mentor. The research environment that he offered was more than any graduate student can possibly expect from a research group.

# Table of Contents

# Chapter 1

# Introduction to Optical Coherence Tomography

## 1.1 Introduction

Optical coherence tomography (OCT) is a noncontact and noninvasive optical imaging technique that enables depth-resolved imaging of biological tissue, in vivo, with micrometer resolution[1]. OCT is now widely used in multiple fields of biomedicine, including ophthalmology, cardiology, and endoscopy[2]. A large number of novel applications of OCT and new discoveries using OCT continue to be reported in the literature. To date, the most widely accepted OCT application is retinal imaging. The retina is the only tissue of the central nervous system that is optically accessible noninvasively. Therefore, retinal imaging with OCT is interesting for basic science as well as for clinical medicine. In the field of ophthalmology, OCT has rapidly become a clinical standard for diagnosis and monitoring of retinal diseases.

Current commercial ophthalmic OCT systems provide only structural images of the human retina over a relatively small fundus area because of limited imaging speeds. Ultrahigh imaging speeds enable larger fundus coverage with higher volumetric sampling density, which provides higher image quality. In addition, although it has been long recognized that it is also possible to perform functional hemodynamic imaging, such as blood flow measurement and angiographic imaging of the microvasculature, applications of these methods on the posterior eye have been challenging due to the limited imaging speeds. Since functional hemodynamic imaging requires repeated scanning of the same location for time-resolved measurements, ultrahigh imaging speeds are critical for clinical and preclinical applications of these techniques.

For human retinal imaging, the maximum amount of optical power incident on the cornea is limited due to safety issues. Therefore, the maximum achievable OCT imaging speed is determined by the minimum required detection sensitivity, which is typically ~97dB or higher to achieve reasonable image quality in patients with retinal diseases. The development of Fourier domain detection techniques has dramatically improved the sensitivity of OCT[3, 4], enabling OCT imaging speeds orders of magnitude faster compared to a decade ago. However, recent advances in camera imaging speeds[5] and swept source sweep rates[6] can now result in theoretical maximum achievable sensitivities lower than the desired sensitivities of 97dB or higher. Therefore, it is essential to understand the theory of Fourier domain OCT when designing ultrahigh speed OCT systems in order to optimize data quality.

### 1.2 Theory of Fourier domain OCT

Fourier domain OCT is based on low coherence interferometry using a modified Michelson interferometer. As shown in Figure 1.1, a fiber-based 2 × 2 optical coupler is typically used to avoid the need for aligning bulk optics and to increase stability and flexibility. As will be shown below, OCT requires detecting interference signal at multiple wavenumbers. Depending on whether it is a swept source OCT system or spectral domain OCT system, the detector can be a single photodiode or a spectrometer. For swept source OCT, a rapidly tunable swept light source that emits only a single optical wavenumber at a time is employed, and a single photodiode with a high speed analog-to-digital converter can be used to record the OCT signal. For spectral domain OCT, a broad bandwidth light source that simultaneously emits a broad range of wavenumbers is employed, and a diffraction grating-based spectrometer with a line-scan camera is used. The relative path lengths in the reference arm and sample arm are defined as $z_R$ and $z_S$, respectively. Although the details of implementation are different, the theoretical analyses of

swept source and spectral domain OCT are essentially the same since they are both based on Fourier domain detection.

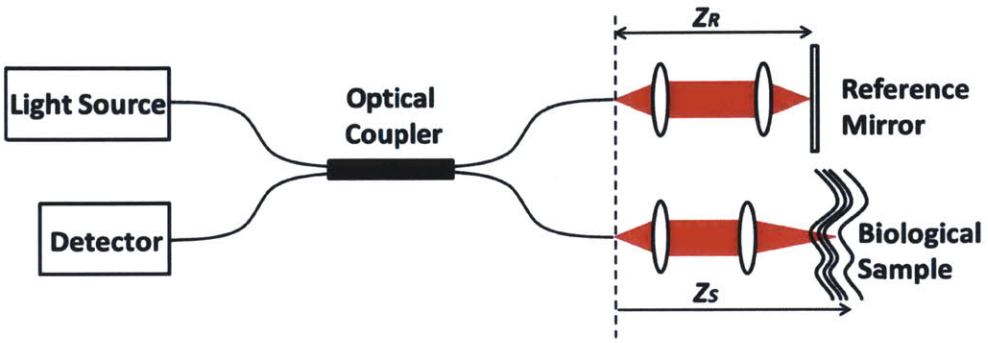


**Figure 1.1.** A schematic of a Fourier domain OCT system. The modified Michelson interferometer splits the light into the reference and sample arms. The interference signal from the reference mirror and sample is detected to generate an OCT scan. The relative path lengths in the reference arm and sample arm are defined as $z_R$ and $z_S$, respectively.

If the coupling ratio of the optical coupler is 50/50 and the electric field from the light source is $2E(k)$, the electric fields at the detector from the reference arm and sample arm as a function of wavenumber $k$ are given by $E_R(k) = E(k) r_R e^{j2kz_R}$ and $E_S(k) = E(k)\sum_n r_{s_n} e^{j2kz_{S_n}}$, where $z_R$, $z_{S_n}$, $r_R$,and $r_S$ are the electric field from the reference arm, electric field from the sample arm, wavenumber, reference arm delay, sample arm delay, reference arm reflectivity, and sample arm reflectivity, respectively. The summation in the expression for the sample arm electric field reflects the fact that the sample arm contains biological tissue with multiple scatterers at different path delays. Since the total electric field at the detector is the sum of the individual electric fields, the intensity at the detector can be expressed as:

$$I(k) = \left|E_R(k) + E_S(k)\right|^2 \simeq \left|E(k)\right|^2 \left[ R_R(k) + 2\,\mathrm{Re}\left\{ r_R^*(k) \sum_n r_{S_n}(k) e^{j2k\Delta z_n} \right\} \right] \tag{1.1}$$

where $R_R(k) \equiv |r_R(k)|^2$ is the power reflectivity of the reference arm mirror. The optical path length difference between the reference arm mirror and the $n^{th}$ scatterer in the sample is defined as $2\Delta z_n \equiv z_R - z_{S_n}$. Note that the interference between the scatters in the sample is negligible and omitted in Equation (1.1) because $|r_S| \ll |r_R|$ in biological tissue.

Since the electrical signal is proportional to the incident optical power on the detector, the detected signal can be expressed as:

$$\begin{aligned} I_D(k) &= \rho(k) I(k) = \rho(k) S(k) \left[ R_R(k) + 2\,\mathrm{Re}\left\{ r_R^*(k) \sum_n r_{S_n}(k) e^{j2k\Delta z_n} \right\} \right] \\ &= \rho(k) S(k) \left[ R_R(k) + 2\sqrt{R_R(k)} \sum_n |r_{S_n}(k)| \cos(2k\Delta z_n + \theta_n(k)) \right] \end{aligned} \tag{1.2}$$

where $S(k) \equiv |E(k)|^2$, $\theta_n(k) \equiv \angle r_{S_n}(k) - \angle r_R(k)$, and $\rho(k)$ is detector responsivity. Note that the second term is the sum of sinusoids oscillating at a frequency $2\Delta z_n$ and with an amplitude $r_{S_n}(k)$. Therefore, by taking the Fourier transform of the detected signal, $I_D(k)$, it is possible to generate the field reflectivity profile of the sample as a function of path length difference $2\Delta z_n$. Assuming $r_{S_n}(k) = r_{S_n}$ and $\theta_n(k) = \theta_n$ for simplicity, the Fourier transform of $I_D(k)$ can be expressed as:

$$\widetilde{I_D}(z) = \mathbb{F}\{I_D(k)\} = \eta(z) + 2\pi \sum_n |r_{S_n}| e^{-j\theta_n} \gamma(z - 2\Delta z_n) + 2\pi \sum_n |r_{S_n}| e^{j\theta_n} \gamma(z + 2\Delta z_n) \tag{1.3}$$

where $\eta(z) \equiv \mathbb{F}\{\rho(k) S(k) R_R(k)\}$ and $\gamma(z) \equiv \mathbb{F}\left\{\rho(k) S(k) \sqrt{R_R(k)}\right\}$. $\eta(z)$ is the DC component and is located near the zero delay position $z = 0$. However, the second term is composed of distinct peaks located at $z = 2\Delta z_n$ with an amplitude $|r_{S_n}| e^{-j\theta_n}$ and a point spread function $\gamma(z)$. Note that $\rho(k) S(k) \sqrt{R_R(k)}$ can be interpreted as the effective bandwidth of the OCT system. The width of the point spread function, or effectively the axial resolution of the OCT system, is inversely proportional to the effective bandwidth of the OCT system. The third term is the same as the second term except that the peaks occur on the other side of the zero delay and the amplitude is

complex conjugated because the interference signal is always real-valued. $e^{-j\theta_n}$ and $e^{j\theta_n}$ rotate the phasor of the signal in the complex plane by $-\theta_n$ and $\theta_n$, respectively. Note that $2\pi\sum_n |r_{S_n}| e^{j\theta_n} \gamma(z \pm 2\Delta z_n)$ provides the depth profile of the sample, called an OCT A-scan. By translating the sample or scanning the OCT beam in the transverse direction using a galvanometer optical scanner, a two- or three-dimensional image can be generated as shown in Figure 1.2.

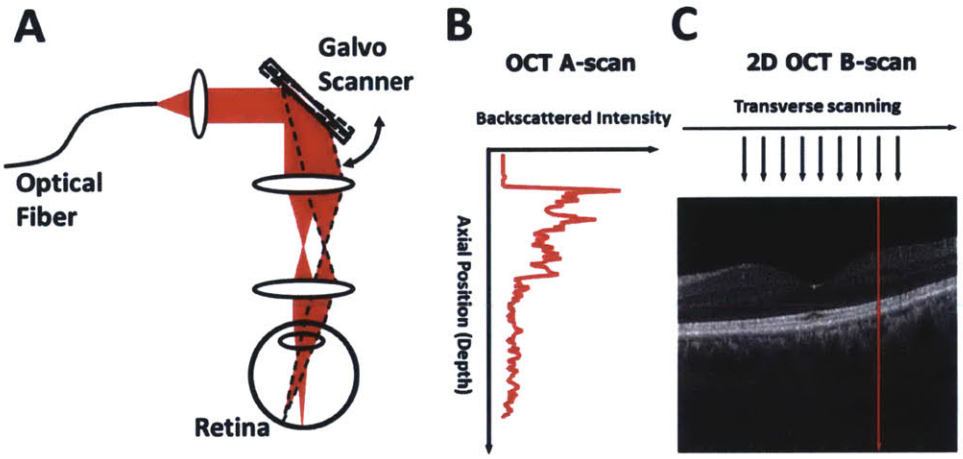


**Figure 1.2.** (A) A schematic of an ophthalmic OCT sample arm for retinal imaging. (B) An OCT A-scan provides a depth profile of the retina. (C) By scanning the OCT beam in the transverse direction while acquiring multiple OCT A-scans sequentially in time, a two-dimensional OCT B-scan can be generated. The back-scattered light intensity is coded in gray-scale with brighter pixels corresponding to higher reflectivity.

### 1.3 Noise and sensitivity

Sensitivity in Fourier domain OCT can be defined as the maximum attenuation of optical power in the sample arm before it becomes impossible to detect the backscattered signal from the sample. Because of noise, the sensitivity of any OCT system is finite. The derivation of the

expression for OCT sensitivity in this section closely follows that provided by Choma et al[4]. For the case when there is a single reflector in the sample arm, one can obtain the following by sampling Equation (1.2) uniformly in wavenumber using an analog-to-digital converter or a spectrometer:

$$I_D[m] = \rho[m]S[m]\left[R_R + 2\sqrt{R_R}|r_S|\cos(2k_m\Delta z + \theta)\right] \tag{1.4}$$

Note that the magnitude of the point spread function is independent of depth and is easily evaluated by assuming that the reflector is at the zero delay position $\Delta z = 0$ since the discrete Fourier transform at $z = 0$ is simply the sum of all samples. Therefore, the magnitude of the peak corresponding to the reflector in the Fourier domain is expressed as:

$$\left|\tilde{I}(z = 2\Delta z)\right| = \sqrt{R_R}|r_S|\sum_{m=0}^{N-1}\rho[m]S[m] \tag{1.5}$$

For simplicity, the sample and reference reflectivities are assumed to be independent of wavenumber. For swept source OCT, $N$ is the total number of samples per A-scan, and for spectral domain OCT, the total number of pixels in the line scan camera of the spectrometer.

By increasing the reference power, it is possible to achieve the shot-noise limit where it dominates all other sources of noise. In this limit, the noise variance at the $m^{\text{th}}$ sample is:

$$\sigma_i^2[m] = 2eI_D[m]B \simeq 2eR_RB\rho[m]S[m] \tag{1.6}$$

where $B$ is the bandwidth and $e$ is the charge of an electron. In spectral domain OCT, the bandwidth is one half the A-scan acquisition rate of the spectrometer, and in swept source OCT, one half the sampling rate of the analog-to-digital converter. Note that $\sqrt{R_R} \gg 2|r_S|$ is assumed in Equation (1.4) for simplicity when evaluating Equation (1.6).

As with the signal, noise in the Fourier domain is most conveniently evaluated at the zero delay position assuming that the noise at different samples are independent. In this case, the variance of noise in the Fourier domain is simply the sum of the variances of noise at all samples:

$$\sigma_z^2[z=0] = 2eR_R B\sum_{m=0}^{N-1}\rho[m]S[m] \tag{1.7}$$

Assuming that shot noise is white, the variance of noise at all depth positions are equal, $\sigma_z^2[z=0] = \sigma_z^2$. Using Equations (1.5) and (1.7), the signal-to-noise ratio can be calculated as:

$$SNR = \frac{\rho|r_S|^2\sum_{m=0}^{N-1}S[m]}{2eB} \tag{1.8}$$

where $\rho$ is assumed to be constant for simplicity.

Therefore, the maximum theoretical sensitivity for swept source OCT can be calculated as[4]:

$$(Sensitivity)_{SSOCT} = 10\log_{10}\left(\frac{\rho NS}{4eB_{SSOCT}}\right) \tag{1.9}$$

where $S \equiv 2S(k)$ is the optical power incident on the sample, according to the original assumption that the total electric field generated by the light source is $2E(k)$, or equivalently, that the power generated by the light source is $4|E(k)|^2 = 4S(k)$. For spectral domain OCT the sensitivity can be expressed as:

$$(Sensitivity)_{SDOCT} = 10\log_{10}\left(\frac{\rho S}{4eB_{SDOCT}}\right) \tag{1.10}$$

Note that the two expressions are equivalent since $B_{SSOCT} \propto NB_{SDOCT}$. For human retinal imaging at 1μm wavelengths, the maximum permissible optical power incident on the cornea is ~1.9mW[7]. For a swept source OCT system using a 50/50 optical coupler and photodiode with a responsivity of 0.9A/W, the theoretical maximum sensitivity can be calculated as ~98.2dB at the OCT A-scan

rate of 400kHz. Every time the OCT A-scan rate is doubled, the sensitivity is reduced by additional 3dB.

### 1.4 Comparing measured sensitivity with theoretical sensitivity

In reality, the noise in the Fourier domain is not real-valued as Equation (1.7) suggests. Since the signal is not real-valued either, it is a common practice to take the absolute magnitude of the OCT A-scan to generate a real-valued image. This operation rectifies the noise, but taking the variance of the noise magnitude is not the same as taking the variance of noise. For low speed imaging, this discrepancy is not an issue since the theoretical maximum sensitivity is used only as a ballpark. However, for ultrahigh speed imaging, the theoretical maximum sensitivity should be used as a benchmark to optimize the sensitivity of an OCT system by comparing it with the measured sensitivity. This is particularly important for ultrahigh speed ophthalmic imaging since the maximum permissible exposure is limited strictly for safety[7].

If the reference arm power is sufficiently high, the shot noise, which generally follows a Poisson distribution, approaches the Gaussian limit. For example, if the power from the reference arm at the detector is ~500μW and the sampling interval 1ns, the average number of photons reaching the detector per sampling interval is ~2.5 million at 1um wavelengths, which is safely in the Gaussian limit of the shot noise. By explicitly writing the expression for the discrete Fourier transform of the sampled interferogram, one obtains:

$$\begin{aligned}\widetilde{I_D}[z] &= \sum_{m=0}^{N-1} I_D[m] e^{-j2\pi mz/N} \\ &= \sum_{m=0}^{N-1} \{ I_D[m]\cos(2\pi mz/N) + jI_D[m]\sin(2\pi mz/N) \}\end{aligned} \tag{1.11}$$

Note that for the purpose of noise analysis, $\widetilde{I_D}[z]$ is a complex Gaussian random variable with the mean of $E\left\{\widetilde{I_D}[z]\right\}=0$ and the variance of $\sigma_z^2$ as defined in Equation (1.7). The variance of the complex random variable $\widetilde{I_D}[z]$ can be written explicitly as:

$$\sigma_z^2 \equiv E\left\{\left|\widetilde{I_D}[z]-E\left\{\widetilde{I_D}[z]\right\}\right|^2\right\}=E\left\{\left|\widetilde{I_D}[z]\right|^2\right\} \tag{1.12}$$

However, a common practice that results in a different value is to take the variance of the noise magnitude. This variance can be expressed as:

$$\begin{aligned}\sigma^2 &= E\left\{\left|\left|\widetilde{I_D}[z]\right|-E\left\{\left|\widetilde{I_D}[z]\right|\right\}\right|^2\right\} \\ &= E\left\{\left|\widetilde{I_D}[z]\right|^2\right\}-E^2\left\{\left|\widetilde{I_D}[z]\right|\right\}\end{aligned} \tag{1.13}$$

Since $\widetilde{I_D}[z]$ is a Gaussian random variable, it can be calculated explicitly using a Gaussian probability density function that:

$$E\left\{\left|\widetilde{I_D}[z]\right|\right\}=\sqrt{\frac{2}{\pi}}\sigma_z \tag{1.14}$$

Using Equations (1.12)-(1.14), the two variances can be related to each other as:

$$\sigma^2=\left(1-\frac{2}{\pi}\right)\sigma_z^2 \simeq 0.36\sigma_z^2 \tag{1.15}$$

Note that the noise variance that should be used for calculating an OCT signal-to-noise ratio with Equations (1.9) or (1.10) is $\sigma_z^2$. In other words, $\sigma^2$ erroneously underestimates the variance by a factor of ~0.36 if used without a correction factor. Note that without the correction factor of 0.36, the resulting sensitivity is overestimated by ~4.4dB. Therefore, there are two ways to calculate the variance of noise in Fourier domain OCT. One is to take the mean of the magnitude squared of the noise according to Equation (1.12), and the other is to take the variance of the noise magnitude and divide the result by ~0.36 according to Equation (1.15).

### 1.5 Phase stability

Phase stability is a key characteristics of Fourier domain OCT when Doppler imaging is performed. As described later in the thesis, Doppler OCT requires a phase stable system because the velocity information of the red blood cells is contained in the phase of the OCT signal, which is typically discarded for conventional structural imaging. The existence of noise in any OCT system implies that the phase stability is limited by the signal-to-noise ratio. The analysis of the phase stability of Fourier domain OCT is provided in multiple references[8-10].

$\widetilde{I_D}(z)$ at a given depth can be decomposed into the signal and noise components. This can be visualized as the sum of a signal phasor and a random noise phasor as shown in Figure 1.3. The noise phasor is random and can have an arbitrary angle with respect to the signal phasor. The variance of the resulting angle $\theta$ characterizes the phase stability.

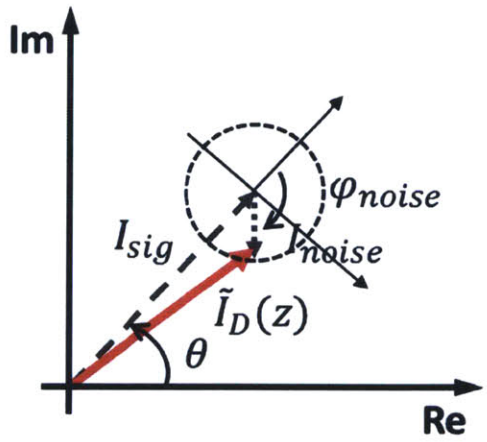


**Figure 1.3.** The phasor representation of the OCT signal and noise. The signal phasor is not random, but the noise phasor is, and it can have an arbitrary angle, $\varphi_{noise}$, with respect to the angle of the signal phasor. The variance of the resulting angle $\theta$ characterizes the phase stability of Fourier domain OCT.

Mathematically, the phase stability can be expressed as:

$$E\left\{\left(\theta - E[\theta]\right)^2\right\} = E\left[\left(\Delta\theta\right)^2\right] \tag{1.16}$$

Assuming $|I_{sig}| >> |I_{noise}|$, the following approximation can be made:

$$E\left[\left(\Delta\theta\right)^2\right] \simeq E\left[\left\{\tan^{-1}\left(\frac{I_{noise}\sin(\varphi_{noise})}{I_{sig}}\right)\right\}^2\right] \simeq E\left[\left(\frac{I_{noise}\sin(\varphi_{noise})}{I_{sig}}\right)^2\right] \tag{1.17}$$

Since $I_{noise}$ and $\sin(\varphi_{noise})$ are statistically independent, Equation (1.17) can be rewritten as:

$$\begin{aligned} E\left[\left(\Delta\theta\right)^2\right] &\simeq \frac{1}{I_{sig}^2} E\left[I_{noise}^2 \sin^2(\varphi_{noise})\right] = \frac{1}{I_{sig}^2} E\left[I_{noise}^2\right] E\left[\sin^2(\varphi_{noise})\right] \\ &= \frac{1}{2}\frac{E\left[I_{noise}^2\right]}{I_{sig}^2} = \frac{1}{2SNR} \end{aligned} \tag{1.18}$$

Note that the phase stability $\delta\theta$ is commonly reported as the standard deviation of the phase difference between consecutive phase measurements, and therefore can be written as[9]:

$$\delta\theta \equiv \sqrt{2E\left[\left(\Delta\theta\right)^2\right]} = SNR^{-\frac{1}{2}} \tag{1.19}$$

### 1.6 Speckle in Fourier domain OCT

Because OCT is a coherent imaging technique, OCT images contain speckle due to constructive and destructive interference. Speckle phenomena are ubiquitous in OCT imaging. For example, when performing Doppler OCT where the phase difference between neighboring A-scans are taken, the effective phase noise in biological tissue, which is different from the phase stability of the system, depends heavily on how well-correlated the speckle patterns are between the neighboring A-scans. In OCT angiography, the speckle decorrelation caused by erythrocyte movements between sequentially acquired B-scans is used to generate motion contrast images. Since almost all OCT applications get affected by speckle directly or indirectly, understanding

the origin of speckle in Fourier domain OCT can be helpful to optimize the image quality and to refine image processing techniques.

Speckle in Fourier domain OCT can be understood in two different ways. One way is to analyze the effect of constructive and destructive interference in the wavenumber domain. In this case, speckle can be understood as an effect similar to the beating in sound waves. The interference signals from particles at slightly different depths can constructively or destructively interfere, resulting in speckle in the OCT depth profile because the observable bandwidth is limited. The other way is to analyze speckle directly in the z-domain or image domain. In this section, the latter will be analyzed in detail.

To understand the effect of speckle, it is helpful to define $k \equiv k_c + \Delta k$ where $k_c$ is the center wavenumber of the OCT system and $\Delta k$ is the deviation from $k_c$. It is also helpful to define $\Delta z_n \equiv \Delta z + \delta z_n$ to analyze the situation where there are multiple scatterers at slightly different depths centered at $z = 2\Delta z$. Rewriting the second term of Equation (1.2) using $k \equiv k_c + \Delta k$ and $\Delta z_n \equiv \Delta z + \delta z_n$, it is possible to obtain:

$$\begin{aligned} I_{D,2}(\Delta k) &= 2\rho(k)S(k)\sqrt{R_R(k)}\sum_n |r_{S_n}| \cos(2k\Delta z_n + \theta_n) \\ &= 2\rho(k)S(k)\sqrt{R_R(k)}\sum_n |r_{S_n}| \cos(2\Delta k\Delta z_n + 2k_c\Delta z + 2k_c\delta z_n + \theta_n) \end{aligned} \tag{1.20}$$

By taking the Fourier transform of Equation (1.20) with respect to $\Delta k$:

$$\widetilde{I_D}(z) = \mathbb{F}\{I_{D,2}(\Delta k)\} = 2\pi e^{jk_c z} \begin{Bmatrix} \sum_n |r_{S_n}| e^{-j(2k_c\Delta z + \theta_n)} e^{-j2k_c\delta z_n} \gamma(z - 2\Delta z - 2\delta z_n) \\ + \sum_n |r_{S_n}| e^{j(2k_c\Delta z + \theta_n)} e^{j2k_c\delta z_n} \gamma(z + 2\Delta z + 2\delta z_n) \end{Bmatrix} \tag{1.21}$$

Evaluating Equation (1.21) at $z = 2\Delta z$ and focusing only on the positive side of the zero delay:

$$\widetilde{I_{D,pos}}(z = 2\Delta z) = 2\pi \left\{ \sum_n |r_{S_n}| \gamma(-2\delta z_n) e^{-j\theta_n} e^{-j2k_c\delta z_n} \right\} \tag{1.22}$$

Equation (1.22) can be understood as the sum of phasors with magnitudes $2\pi|r_{S_n}|\gamma(-2\delta z_n)$ and angles $\theta_n + 2k_c\delta z_n$. As an extreme example, consider a case with two identical scatterers that are quarter wavelength apart. In this case, $\theta_1 = \theta_2$, $|r_{S_1}| = |r_{S_2}|$, and $\delta z_2 - \delta z_1 = \lambda_c/4$. If the axial resolution of the system is much larger than $\lambda_c/4$, which is typically the case for a standard resolution OCT system, $\gamma(-2\delta z_1) \simeq \gamma(-2\delta z_2)$. In this case, the OCT signal $\widetilde{I}_{D,pos}(z = 2\Delta z)$ becomes nearly zero since it is the sum of two phasors with similar magnitudes but opposite orientations. This can be understood as destructive interference. On the contrary, if the two identical particles are half a center wavelength apart, then the two phasors add in phase and result in constructive interference.

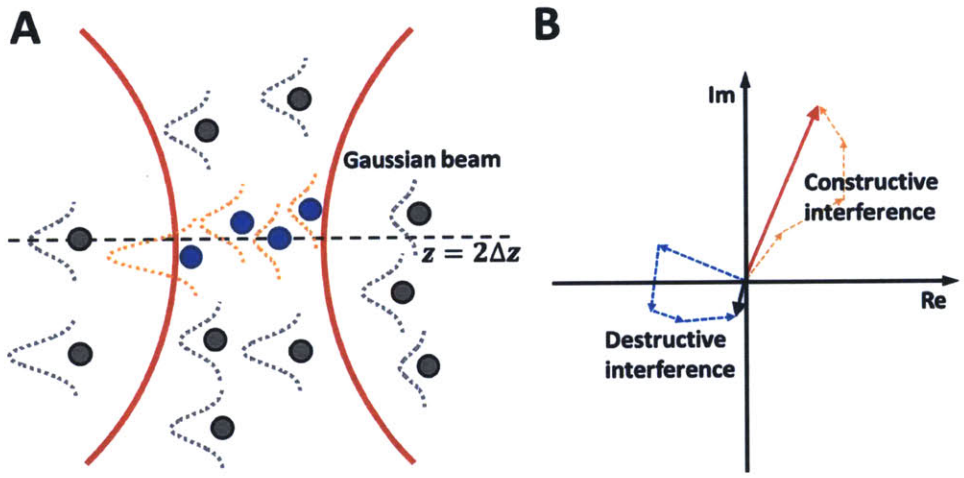


**Figure 1.4.** (A) A schematic showing multiple scatterers in the sample. The dotted Gaussian curves show point spread functions centered at the scatterers. Only the scatterers colored in blue contribute to the OCT signal at depth $z = 2\Delta z$. Other scatterers colored in gray are either outside the Gaussian beam or too far away from $z = 2\Delta z$ axially. (B) Phasors can add constructively (red) or destructively (blue) depending on the exact distribution of the scatterers. The angles of the phasors depend on the axial deviations of

the scatterer positions from $z = 2\Delta z$ and the magnitudes depend on the height of the point spread functions evaluated at $z = 2\Delta z$.

Equation (1.22) can also be used when there are more than two particles that are not necessarily identical to one another. This is pictorially depicted in Figure 1.4 where each scatterer can be represented as a phasor in the complex plane. The dotted Gaussian curves centered at the scatterers show the point spread functions $2\pi|r_{S_n}|\gamma(-2\delta z_n)$. Only the scatterers that have their point spread function tails intercepting the $z = 2\Delta z$ line can contribute to the signal. Only the scatterers colored in blue contribute to the OCT signal at depth $z = 2\Delta z$. Other scatterers colored in gray are either outside the Gaussian beam or too far away from $z = 2\Delta z$ axially. Note that the height of the point spread function at $z = 2\Delta z$ depends on several factors including the transverse scatterer position with respect to the Gaussian beam, $|r_{S_n}|$, axial resolution, and axial deviation of the scatterer position from $z = 2\Delta z$. The height of the point spread function determines phasor the magnitude. The angles of the phasors depend on the axial deviation of the scatterer positions from $z = 2\Delta z$ according to $e^{-j2k_c\delta z_n}$. The resulting phasors can add constructively or destructively depending on the exact distribution of the scatterers.

In biological tissue, the scatterers are randomly distributed, and therefore the sum of the phasors is also random, which results in speckle pattern in OCT image. An example of speckle in an OCT image of the human retina is shown in Figure 1.5. Note that the outer limiting membrane (OLM) indicated by the yellow arrow in 1.5(B) on average is spanned by one constructive speckle in the axial direction unlike the brighter RPE/photoreceptor layers. This implies that the OLM is thinner than the axial resolution of the ultrahigh resolution OCT system, which was ~3μm in tissue. Note that if OCT A-scans consisting an OCT B-scan are highly oversampled in the transverse direction, the change in the distribution of scatterers is minimal between

neighboring A-scans, and the speckle patterns in the neighboring A-scans are highly correlated. This is a necessary condition for Doppler imaging since it requires comparing the phase of neighboring A-scans[11, 12]. On the other hand, if neighboring OCT A-scans are relatively far away from each other, the speckle patterns between them are uncorrelated.

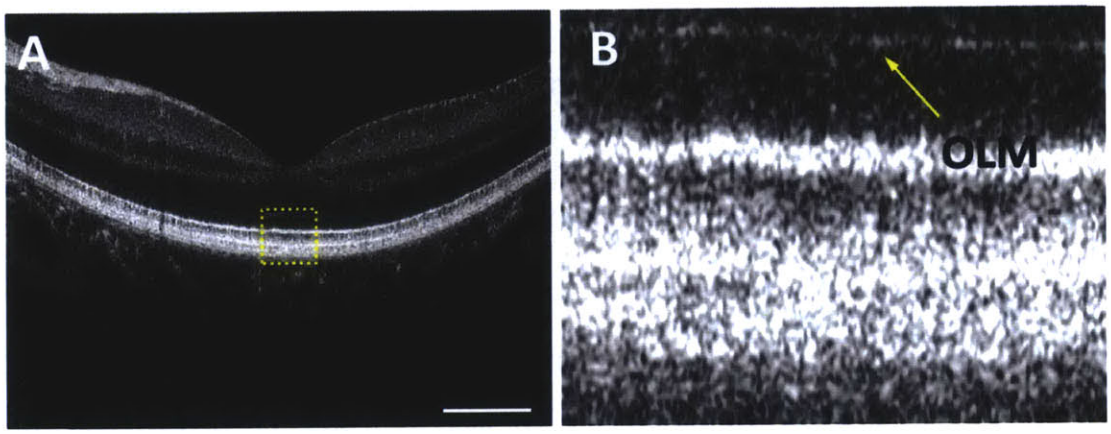


**Figure 1.5.** Speckle pattern in spectral domain ultrahigh resolution OCT image of the human retina. (A) An ultrahigh resolution cross-sectional OCT image of a normal human retina over a 6mm range. (B) A close-up view of the area indicated by the yellow rectangle in (A) clearly shows a speckle pattern due to constructive (bright) and destructive (dark) interference of scatterers in the retina. Note that the outer limiting membrane (OLM) indicated by the yellow arrow in (B) on average is spanned by one constructive speckle in the axial direction unlike the brighter RPE/photoreceptor layers. This implies that the OLM is thinner than the axial resolution of the ultrahigh resolution OCT system, which was ~3μm in tissue. Scale bar: 1mm.

In OCT angiography, A-scans are usually not as highly oversampled as in Doppler OCT. Therefore, the existence of speckle in OCT angiography implies that the galvanometer trajectory used to acquire B-scans need to be highly repeatable. Otherwise, two sequentially acquired B-scans will not be sufficiently correlated to each other, resulting in spurious motion contrast signal

due to scan instability. Note that speckle cannot be suppressed by simply averaging multiple B-scans acquired from the same location because the scatterers in biological tissue other than erythrocytes are usually stationary over a typical image acquisition time.

### 1.7 Scope of thesis

In this thesis, advances in structural and functional ophthalmic imaging techniques for the human and small animal posterior eyes will be investigated using ultrahigh speed Fourier domain OCT with standard or ultrahigh resolution. This thesis has the following aims. Aim 1: Develop next generation ultrahigh speed spectral and swept source OCT systems for integrated structural and functional imaging of the human and small animal eyes. Aim 2: Develop functional imaging techniques for retinal blood flow measurements and capillary visualization, and perform structural and functional ophthalmic imaging in normal humans and small animals. Aim 3: Apply functional imaging techniques to investigate retinal neurovascular coupling in humans and small animals. Aim 4: Deploy a clinical ultrahigh speed OCT prototype to an ophthalmology clinic and perform clinical studies.

The following chapters will discuss various aspects of these aims. Chapter 2 will discuss ultrahigh resolution spectral domain OCT imaging in human subjects. Unlike standard resolution OCT, ultrahigh resolution OCT requires a careful numerical dispersion compensation to optimize the image resolution. Chapter 3 presents small animal Doppler imaging for measuring pulsatile total retinal blood flow using ultrahigh speed spectral domain OCT. It is also demonstrated that a similar technique can be used for human retinal blood flow measurement. Chapter 4 describes the development of an ultrahigh speed phase stable swept source OCT prototype for human retinal imaging. It is demonstrated that this system can be used for measuring pulsatile total retinal blood flow in human subjects. Chapter 5 discusses OCT angiography imaging of the

human choriocapillaris microvasculature using the ultrahigh speed swept source OCT prototype described in Chapter 4. Chapter 6 presents OCT angiography results in patients with age-related macular degeneration. An ultrahigh speed swept source OCT system similar to that described in Chapter 4 was deployed to the New England Eye Center, Tufts Medical Center, to perform clinical studies. Chapter 7 describes OCT angiography in diabetic patients using the same ultrahigh speed swept source OCT system. Chapter 8 discusses anesthesia protocols for measuring retinal blood flow in small animal models using ultrahigh speed spectral domain OCT. Chapter 9 presents measurement of neurovascular coupling induced by visual flicker stimulus in small animal models using ultrahigh speed spectral domain OCT.

## References


1. Huang D, Swanson EA, Lin CP, Schuman JS, Stinson WG, Chang W, Hee MR, Flotte T, Gregory K, Puliafito CA, Fujimoto JG. Optical Coherence Tomography. Science. 1991;254(5035):1178-81. PubMed PMID: 1957169.

2. Drexler W, Fujimoto JG. Optical Coherence Tomography: Technology and Applications Berlin: Springer-Verlag Berlin; 2008.

3. Leitgeb R, Hitzenberger CK, Fercher AF. Performance of Fourier domain vs. time domain optical coherence tomography. Optics Express. 2003;11(8):889-94. PubMed PMID: 19461802.

4. Choma MA, Sarunic MV, Yang CH, Izatt JA. Sensitivity advantage of swept source and Fourier domain optical coherence tomography. Optics Express. 2003;11(18):2183-9. PubMed PMID: 19466106.

5. Potsaid B, Gorczynska I, Srinivasan VJ, Chen YL, Jiang J, Cable A, Fujimoto JG. Ultrahigh speed Spectral/Fourier domain OCT ophthalmic imaging at 70,000 to 312,500 axial scans per second. Optics Express. 2008;16(19):15149-69. PubMed PMID: 18795054; PubMed Central PMCID: PMC2743204.

6. Klein T, Wieser W, Eigenwillig CM, Biedermann BR, Huber R. Megahertz OCT for ultrawide-field retinal imaging with a 1050nm Fourier domain mode-locked laser. Optics Express. 2011;19(4):3044-62. PubMed PMID: ISI:000288860000024.

7. American National Standard for Safe Use of Lasers, ANSI Z136.1. New York: American National Standards Institute; 2007.

8. Yazdanfar S, Yang C, Sarunic MV, Izatt J. Frequency estimation precision in Doppler optical coherence tomography using the Cramer-Rao lower bound. Optics Express. 2005;13(2).

9. Park B, Pierce MC, Cense B, Yun S-H, Mujat M, Tearney G, Bouma B, de Boer J. Real-time fiber-based multi-functional spectral-domain optical coherence tomography at 1.3 μm. Optics Express. 2005;13(11):3931-44. doi: 10.1364/opex.13.003931.

10. Choma MA, Ellerbee AK, Yazdanfar S, Izatt JA. Doppler flow imaging of cytoplasmic streaming using spectral domain phase microscopy. J Biomed Opt. 2006;11(2):-. PubMed PMID: ISI:000237623100033.

11. Chen Z, Milner TE, Srinivas S, Wang X, Malekafzali A, van Gemert MJC, Nelson JS. Noninvasive imaging of in vivo blood flow velocity using optical Doppler tomography. Opt Lett. 1997;22(14):1119-21.

12. Leitgeb RA, Schmetterer L, Drexler W, Fercher AF, Zawadzki RJ, Bajraszewski T. Real-time assessment of retinal blood flow with ultrafast acquisition by color Doppler Fourier domain optical coherence tomography. Optics Express. 2003;11(23):3116-21. PubMed PMID: 19471434.

# Chapter 2

# Extracting and compensating dispersion mismatch in ultrahigh resolution Fourier domain OCT imaging of the retina

## 2.1 Overview

This chapter presents a numerical approach to extract the dispersion mismatch in ultrahigh resolution Fourier domain optical coherence tomography (OCT) imaging of the retina. The method draws upon an analogy with a Shack-Hartmann wavefront sensor. By exploiting mathematical similarities between the expressions for aberration in optical imaging and dispersion mismatch in spectral / Fourier domain OCT, Shack-Hartmann principles can be extended from the two-dimensional paraxial wavevector space to the one-dimensional wavenumber space. For OCT imaging of the retina, different retinal layers, such as the retinal nerve fiber layer, the photoreceptor inner and outer segment junction, or all the retinal layers near the retinal pigment epithelium can be used as point source beacons in the axial direction, analogous to point source beacons used in conventional two-dimensional Shack-Hartman wavefront sensors for aberration characterization. Using this approach and carefully suppressing speckle, the dispersion mismatch in spectral / Fourier domain OCT retinal imaging can be successfully extracted numerically and used for numerical dispersion compensation to generate sharper, ultrahigh-resolution OCT images. Dr. Bernhard Baumann contributed significantly in building the OCT system and performing the theoretical analysis. Mr. Eric A. Swanson and Prof. Fujimoto provided supervision and guidance.

## 2.2 Introduction

After the development and first demonstration of optical coherence tomography (OCT) imaging of the human retina[1, 2], OCT has become a clinical standard in ophthalmic diagnosis and research[3]. Since then, there have been significant efforts in increasing the imaging speed and resolution of OCT. While the axial resolution of standard clinical ophthalmic OCT systems is 5-7 μm, ultrahigh resolution OCT images of the retina with an axial resolution approaching 3 μm or less have been demonstrated using broadband light sources[4-7]. Ultrahigh-resolution imaging is important because it can contribute to better understanding of pathogenesis and enable earlier diagnosis of retinal diseases[8, 9].

For ultrahigh resolution OCT, dispersion mismatch between the sample and reference arms can cause a significant broadening of the axial point spread function[10, 11]. Therefore, to achieve the best possible axial resolution, it is important to compensate for dispersion mismatch accurately. While it is possible to closely match the dispersion of optical components between sample and reference paths and match ocular dispersion by inserting an appropriate length water cell in the OCT reference arm, it is difficult to account for variability in axial eye lengths between different individuals. Therefore, numerical dispersion compensation is typically employed to correct residual dispersion mismatch[6, 7, 12].

Fourier domain OCT is particularly well-suited for numerical dispersion compensation because it provides direct access to the spectral interferogram. However, the exact dispersion mismatch is typically unknown and needs to be found by post processing the OCT data. There are two widely used types of approaches for numerical dispersion compensation in retinal imaging. The first is to use bright specular reflections at the foveal surface[7]. The specular reflection is isolated in depth, shifted to the zero-depth position, and inverse Fourier transformed

to calculate the dispersion mismatch. The limitation of this approach is that it requires a dominant specular reflection which is not always available. The second type of approach is to assume a third order polynomial for the dispersion mismatch and vary the polynomial coefficients to maximize an image sharpness metric[6, 12]. The limitation of this approach is that it assumes a specific polynomial order for the dispersion mismatch and/or the resultant coefficients could be stationary at a local maximum rather than the global maximum. Regardless of these limitations, all of these approaches are widely used, and in principle, should all converge to a single answer. Another recently reported approach, different from the two references above, utilizes the cross-correlation of sub-bandwidth reconstructions[13].

Fourier domain OCT and holography are closely related in that they are both coherent interferometric techniques that utilize both intensity and phase information, although the implementations of the two techniques are considerably different[14]. On the other hand, the Shack-Hartmann wavefront sensor is also related to holography in that it is capable of detecting the sample wavefront. Therefore, there are mathematical similarities between Fourier domain OCT and Shack-Hartmann wavefront sensing which may allow the application of similar analytical tools between the two techniques.

In this chapter, we present a numerical approach to extract the dispersion mismatch in ultrahigh-resolution spectral / Fourier domain OCT retinal imaging using a Shack-Hartmann wavefront sensor analogy. It is demonstrated that by using this approach and carefully suppressing speckle, the dispersion mismatch in spectral / Fourier domain OCT can be successfully extracted numerically, which can then be used for numerical dispersion compensation to generate sharper ultrahigh-resolution OCT images.

## 2.3 Theory and simulation

### *2.3.1 Dispersion mismatch in spectral / Fourier domain OCT*

In OCT, the spectral interferogram detected by the spectrometer as a function of wavenumber can be expressed as[3, 15-17]:

$$I_{\text{int}}(k) = \frac{1}{2}\rho(k)S(k)\sqrt{R_R(k)}\int r_S(\Delta z)\cos\left\{2k\Delta z + \Delta\theta(\Delta z) + \Delta\varphi_{disp}(k)\right\}d\Delta z \qquad (2.1)$$

where $\rho(k)$, $S(k)$, $R_R(k)$, $r_S(\Delta z)$, $\Delta\theta(\Delta z)$, and $\Delta\varphi_{disp}(k)$ are the detector responsivity, optical power spectrum of the light source, power reflectivity of the reference arm, magnitude of the sample field reflectivity, phase of the sample field reflectivity, and dispersion mismatch between the sample and reference arms, respectively. It is important to note that in retinal imaging $\Delta\varphi_{disp}(k)$ is commonly approximated to be depth-independent, and therefore is a common term for signals at all depths.

### *2.3.2 Aberration in optical imaging*

A paraxial plane wave $\exp\{j[k_x x + k_y y + \{k - (k_x^2 + k_y^2)/2k\}z]\}$ that travels through an optical element with small aberration $\exp\{j\phi_{aber}(x, y)\}$ can be expressed as:

$$u(x, y) = \exp\left\{j\left[k_x x + k_y y + \left\{k - \frac{(k_x^2 + k_y^2)}{2k}\right\}z + \phi_{aber}(x, y)\right]\right\} \qquad (2.2)$$

where $k$, $k_x$ and $k_y$ is the wavenumber, $x$ component and $y$ component component of the propagation vector, respectively.

To develop an explicit analogy between aberration in optical imaging and dispersion mismatch in Fourier domain OCT, an arbitrary superposition of aberrated planar wavefronts can be interfered with an ideal reference plane wave as in holography:

$$I(x,y)=\left|e^{jkz}+\int dk_x dk_y r_s(k_x,k_y)\exp\left\{j\left[k_x x+k_y y+\left\{k-\frac{\left(k_x^2+k_y^2\right)}{2k}\right\}z+\phi_{aber}(x,y)\right]\right\}\right|^2 \quad (2.3)$$

where $r_s(k_x,k_y)$ is the weight of superposition for the planar waves. The interference term of Equation (2.3) can be calculated as:

$$I_{\text{int}}(x,y)=\int dk_x dk_y r_s(k_x,k_y)\cos\left\{k_x x+k_y y-\frac{\left(k_x^2+k_y^2\right)}{2k}z+\phi_{aber}(x,y)\right\} \quad (2.4)$$

The mathematical similarities between Equations (2.1) and (2.4) are now apparent where Equation (2.4) is simply a two-dimensional extension of Equation (2.1). This implies dispersion mismatch in spectral / Fourier domain OCT and aberration in optical imaging are mathematically analogous.

*2.3.3 Finding dispersion mismatch using Shack-Hartmann wavefront sensor analogy*

In optical imaging, a Shack-Hartmann wavefront sensor can be used to find the wavefront distortion induced by an aberration term $\phi_{aber}(x,y)$. The Shack-Hartmann typically contains a lenslet array which divides the input wave into multiple subapertures. The local slope of the wavefront at the center of each of the lenslets can be found by the following equations[18]:

$$\partial\phi_{aber}(x,y)/\partial x=\Delta x/f \quad (2.5)$$

$$\partial\phi_{aber}(x,y)/\partial y=\Delta y/f \quad (2.6)$$

where $f$ is the focal length of the lenslets, and $\Delta x$ and $\Delta y$ are the deviations of the focal spots in the $x$ and $y$ directions in relative to the center of the lenslet. These discrete local slopes can be used to reconstruct the input wavefront using integration, characterizing the aberration introduced by the optical element. In imaging the eye using adaptive optics, the optical element is the eye itself, and the aberration of the eye $\phi_{aber}(x,y)$ can be defined as the deviation of the

exiting wavefront after the cornea from an ideal planar wavefront that is assumed to be generated by an ideal optics of the eye with a point source on the retina.

A Shack-Hartmann wavefront sensor can be considered as a local wavefront sampling device. Therefore, utilizing the mathematical analogy developed in the previous sections, it should be possible to perform local phase slope sampling on the spectral / Fourier domain OCT interferogram in order to extract the dispersion mismatch between sample and reference arms. In order to extract dispersion mismatch in spectral / Fourier domain OCT, the lenslet array can be replaced with windowing the interferogram with narrow windows centered at different wavenumbers in the wavenumber space followed by Fourier transformation, which is analogous to the lenslets forming images at the focal plane in a Shack-Hartmann wavefront sensor. In a manner analogous to the way that the lenslets in the Shack-Hartmann wavefront sensor provide local slopes of the incoming wavefront, multiple narrow windows at different center wavenumbers provide local slopes of the phase of the spectral interferogram. Therefore, the dispersion mismatch can be calculated by integrating the phase slope in the wavenumber space in spectral / Fourier domain OCT, just as the wavefront can be calculated by integrating the wavefront slope in the x-y space in Shack-Hartmann wavefront sensing. This analogy is illustrated in Figure 2.1 using an example of parabolic wavefront and phase.

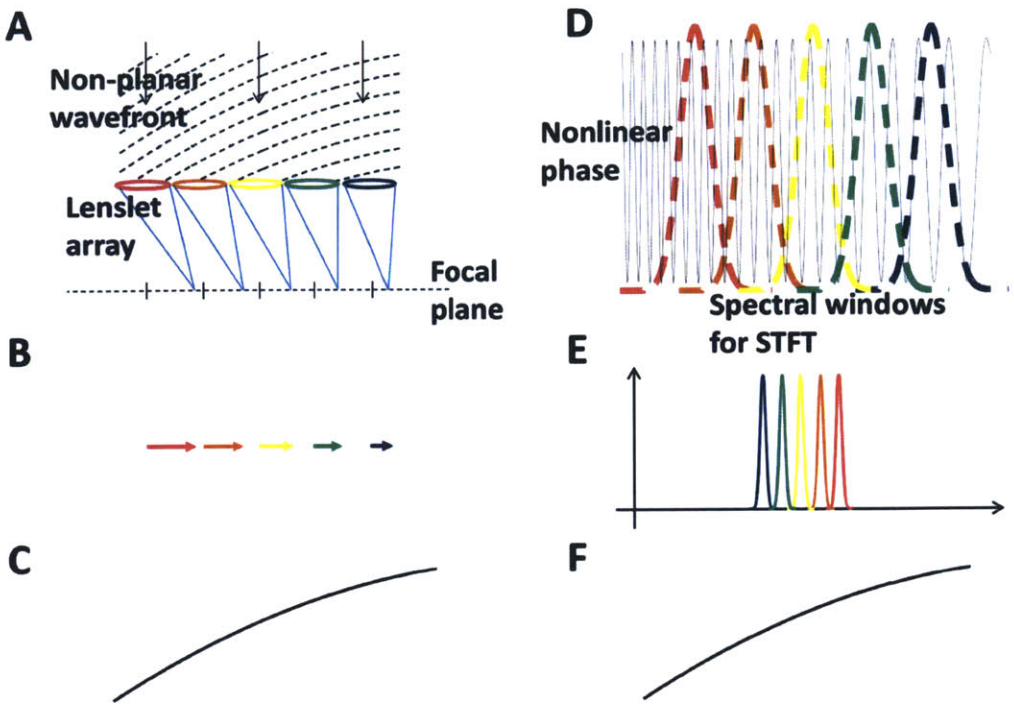


**Figure 2.1.** Finding dispersion mismatch using a Shack-Hartmann wavefront sensor analogy. (A) A lenslet array samples a spatially non-planar parabolic wavefront. (B) The positions of the focused spots on the focal plane are proportional to the local slopes of the wavefront. (C) The wavefront can be reconstructed by integrating the local slope in space. (D) Using multiple spectral windows for STFT, a nonlinear parabolic phase corresponding to a dispersion mismatch can be sampled in wavenumber. (E) The position of the Fourier transform for a given window is proportional to local slope of nonlinear phase. (F) The nonlinear phase can be reconstructed by integrating the local slope in wavenumber. STFT: short-time Fourier transform.

*2.3.4 Simulation*

In order to demonstrate that the dispersion mismatch in spectral / Fourier domain OCT can be found using the analogy described above, a numerical simulation was performed to extract a

known amount of dispersion mismatch introduced between the sample and reference arms. The spectral interferogram from three scatterers at slightly different depths and its Fourier transform are shown in Figures 2.2(A) and (B). When a dispersion mismatch added, the A-scan becomes distorted as shown in Figure. 2.2(C). Figure 2.2(D) shows an example of the effect of short-time Fourier transform using a narrow window centered at a particular wavenumber. The first panel of Figure 2.2(D) shows the effect of windowing on the spectral interferogram. The second panel shows the Fourier transform of the windowed interferogram. Since the window is narrow, it appears as a point or single scatterer, which is analogous to the Shack-Hartmann wavefront sensor, where it is conventionally assumed that the wavefront emerges from a point source. It should also be noted that beyond a certain threshold where it starts to appear as a point scatterer, reducing the window size further does not affect the results significantly. The third panel shows the unwrapped phase of the Hilbert transform of the windowed interferogram shown in the first panel. Note that the location of the peak of the A-scan in the second panel can be defined as the instantaneous slope of this unwrapped phase at the center of the window. This results in a more accurate, sub-pixel location of the peak because of the discrete samples. By sliding the center wavenumber of the window over the entire wavenumber range and integrating the resultant slope in wavenumber, the dispersion mismatch can be extracted as shown in Figure 2.2(E). Note that there is a slight difference between the simulated dispersion mismatch and dispersion mismatch extracted by the algorithm because there is more than one scatterer in the A-scan.

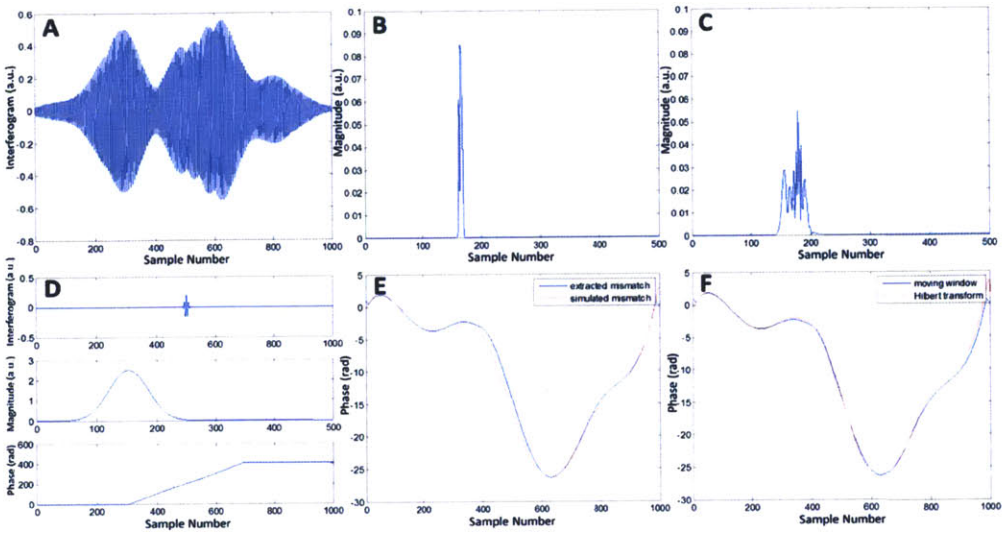


**Figure 2.2.** Simulation for extracting the dispersion mismatch using Shack-Hartmann wavefront sensor analogy. (A) A spectral interferogram with three scatterers and a Gaussian light source. (B) The Fourier transform of (A) without any dispersion mismatch. (C) The Fourier transform of the interferogram with an arbitrary simulated dispersion mismatch introduced. (D) An example of the short-time Fourier transform for a given window location. (E) A comparison of the simulated and extracted dispersion mismatches. (F) A comparison of the extracted dispersion mismatch calculated with short-time Fourier transform with a sweeping window and that calculated with Hilbert transforming the entire spectral interferogram.

This result is expected for a single scatterer, but for multiple scatterers, it is not obvious whether this approach remains valid. However, as will be shown in the next section, by carefully considering the analogy between this approach and the Shack-Hartmann wavefront sensor, it is possible to infer that this approach should still be valid for multiple scatterers when speckles are appropriately managed.

Figure 2.2(F) shows that the entire operation of the sliding window short-time Fourier transform can be simply replaced by Hilbert transformation of the entire interferogram without short-time Fourier transformation. Since the operation described above essentially calculates the integral of the instantaneous slope of the phase, while the Hilbert transform of the entire interferogram calculates the phase, they are equivalent. This fact is highly advantageous computationally because of the high computational cost of short-time Fourier transformation with multiple windows. Therefore, short-time Fourier transformation is used here only for developing the analogy between this approach and the Shack-Hartmann. Note that there is a slight difference between the two curves in Figure 2.2(F) because the instantaneous slope was calculated using a finite window width with a finite wavenumber interval.

*2.3.5 Effect of speckle*

For A-scans with a single scatterer or specular reflections, variations of the approach outlined previously have already been widely used for finding the dispersion mismatch in Fourier domain OCT[7, 19]. However, the validity of this approach for A-scans with multiple scatterers is not obvious without the analogy developed previously.

In Shack-Hartmann wavefront sensing for imaging the eye, it is typically assumed that the wavefront coming from the beacon on the retina is a point source. Although this is true in terms of the resolution of the small lenses in the lenslet array, there are still multiple scatterers that act as the beacon on the retina. Therefore, speckle can be a problem for accurate aberration characterization with a typical Shack-Hartmann wavefront sensor[20]. Similarly, in finding the dispersion mismatch in spectral / Fourier domain OCT using the analogy developed here, speckle can be a severe problem when there are multiple scatterers in a single A-scan. The effect of speckle on the approach described here is shown in Fig. 3. Figure 2.3(A) shows a spectral

interferogram with three scatterers as in Figure 2.2, but with the relative locations shifted to cause severe constructive and destructive interferences. This constructive and destructive interference results in speckle patterns when narrow windows are used for short-time Fourier transform. Note that an analogous problem can occur in Shack-Hartmann wavefront sensors. Figure 2.3(B) shows the dispersion mismatch extracted with the approach described above. Note that an abrupt jump occurs where there is destructive interference. These abrupt jumps can cause a splitting of the OCT point spread function when the dispersion mismatch is used for numerical dispersion compensation.

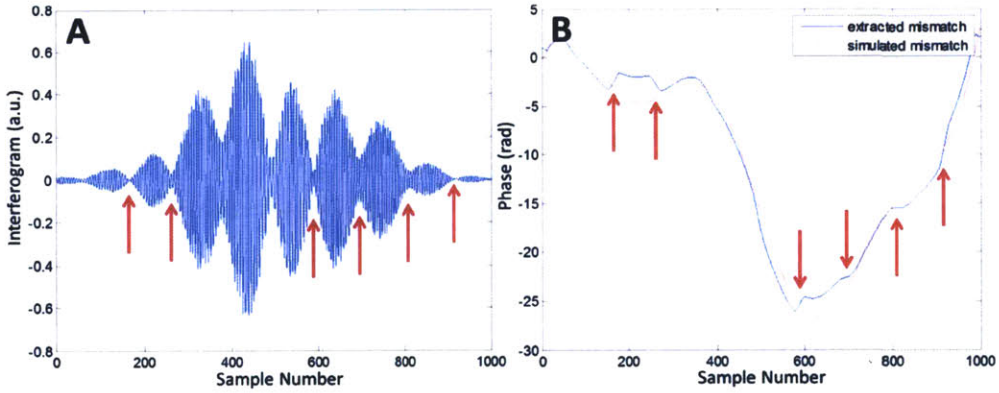


**Figure 2.3.** (A) A spectral interferogram with three scatterers. The wavenumbers where destructive interference occurs are indicated with red arrows. (B) A comparison of the extracted dispersion mismatch and the simulated dispersion mismatch. The red arrows indicate the same wavenumbers as in (A). Note that the abrupt changes in the extracted dispersion mismatch occur at the wavenumbers indicated with the arrows.

One obvious way of suppressing speckle and other noise for the Shack-Hartmann wavefront sensor is to average multiple images assuming small sample movement between acquisitions[21]. In typical OCT imaging, multiple A-scans are acquired while the galvanometer is scanning. Therefore, in order to suppress speckle for extracting the dispersion mismatch in spectral /

Fourier domain OCT, multiple neighboring A-scans with different speckle patterns can be averaged. Note that averaging is not performed on the interferograms, but on the extracted dispersion mismatches from the A-scans. The effect of speckle suppression by averaging the dispersion mismatch will be shown in the results section.

## 2.4 Methodology

### *2.4.1 Ultrahigh-resolution spectral / Fourier domain OCT system*

Two different OCT systems were used in these experiments. A schematic of the OCT systems used is shown in Figure 2.4. For the first system, a commercial broadband superluminescent diode (SLD) light source (Exalos) and a line scan camera (Basler Sprint spL4096-140 km) were used to develop an ultrahigh-resolution spectral domain OCT system at 825 nm with an imaging speed of 70,000 A-scans per second. The full width at half maximum (FWHM) bandwidth of the broadband light source was 161 nm. The spectrometer had a collimating lens with an effective focal length of 76 mm, a 1200 lines/mm transmission holographic grating, and a 160 mm scan lens. The line scan camera had 10 μm square pixels in two rows and was 4096 pixels wide. The camera was read at a 70 kHz line rate using the full 4096 pixels with a 13.1 μs exposure time. The total imaging range was 3.1 mm in tissue with a measured axial resolution of 2.9 μm in tissue after spectral shaping. Using a 70/30 fiber coupler, the power of the OCT beam at the cornea was 750 μW, consistent with American National Standards Institute (ANSI) standards safe exposure limits, and gave a sensitivity of 97 dB. The imaging interface had galvanometer scanners with 5 mm mirrors (Cambridge Technology 6215H), an 80 mm scan lens, and a compound 30 mm effective focal length ocular lens, resulting in a beam diameter of 1.8 mm incident on the cornea. The theoretical retinal spot size calculated with ZEMAX and a standard eye model was ~20 μm.

For the second system, a different broadband SLD (Superlum) centered at 860 nm with a FWHM bandwidth of 137 nm was used in order to increase the imaging speed as well as the system efficiency. For this configuration, the camera was read at a line rate of 91 kHz using the center 3072 pixels with an exposure time of 9.8 μs. An 80/20 fiber coupler used for this configuration to limit the incident power of the OCT beam to 750 μW. Otherwise, the second system was similar to the first. The second system was designed with emphasis on optimizing efficiency and sensitivity, and sensitivity was improved to 98 dB despite the faster imaging speed. The total imaging range remained the same at 3.1 mm in tissue with a measured axial resolution of 3.2 μm in tissue after spectral shaping.

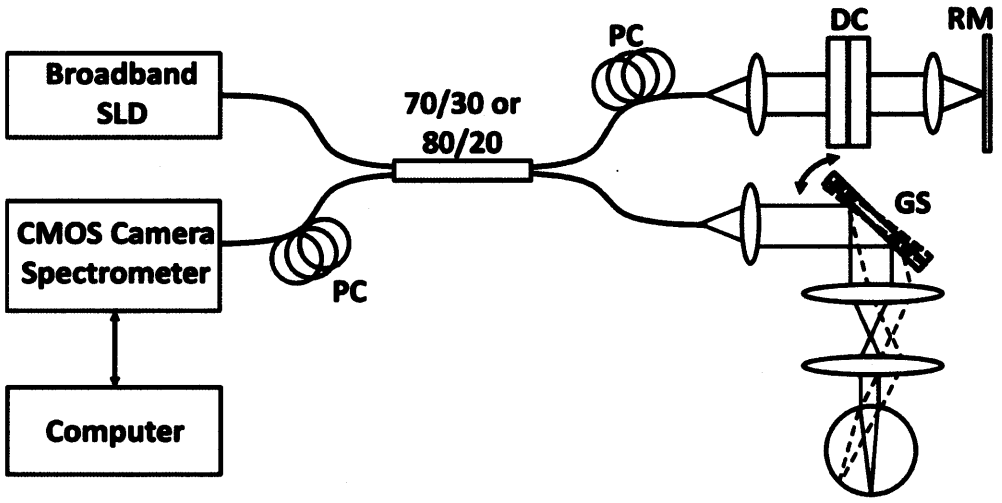


**Figure 2.4.** Schematic of the spectral / Fourier domain ultrahigh-resolution OCT systems. PC: polarization controller, DC: dispersion compensation glass, RM: reference mirror, GS: galvanometer scanner pair, DG: diffraction grating, SLD: superluminescent diode, CMOS: line scan camera. Fiber couplers of 70/30 and 80/20 were used for the first and second systems, respectively.

*2.4.2 System calibration and data processing*

In order to achieve best possible resolution allowed by the spectrometer and light source at all depths, it is critical to decouple the dispersion mismatch from wavelength-to-camera pixel mapping during spectrometer recalibration. For that purpose, the spectrometer was calibrated using an approach similar to that described by Makita et al[19]. Interferometric fringes were recorded by placing a mirror at two different delay positions in the sample arm. The two interferometric fringes were Hilbert transformed to generate phase curves as a function of pixel number. By subtracting the two phase curves, the phase as a function of pixel number, but without dispersion mismatch, was generated. The new sampling positions to linearize the interferometric fringe in wavenumber could be generated by dividing the total phase range by the final number of samples and interpolating the sample positions corresponding to the phase values with uniform intervals. It should be noted that the approach by Makita et al.[19] can also be used for finding the dispersion mismatch in the OCT system. However, unlike our approach discussed here, it is not intended for sample-dependent dispersion mismatch because it requires a calibration mirror.

For all data acquired in this study, the spectrometer output was processed by cubic spline interpolation to linearize the interference signal in wavenumber. The recalibrated interferometric signals were Fourier transformed after numerically compensating for the dispersion mismatch. Zero padding was sometimes performed before Fourier transformation in order to improve layer visualization.

**2.5 Results and discussion**

The approach to extract the dispersion mismatch described above was applied to spectral / Fourier domain OCT images. In OCT images of the retina, there are always multiple scatterers in

a given A-scan, and the effect of speckle should be considered carefully in order to apply this method successfully. The first ultrahigh resolution OCT system was used to acquire the B-scan with 2048 A-scans as shown in Figure 2.5(A). No water cell was used in the reference arm in order to intentionally demonstrate that the approach is capable of extracting a relatively large dispersion mismatch. The method was applied to the A-scans near the center of the fovea. Before implementing the method, the A-scans were zeroed everywhere except at the bright layers near the retinal pigment epithelium (RPE), and inverse Fourier transformed to increase the signal-to-noise ratio of the spectral interferograms and remove signals from undesired layers. The depth range where the A-scan was used is approximately indicated by the yellow dotted lines in Figure 2.5(A). The resulting spectral interferograms were used as the starting point for the approach.

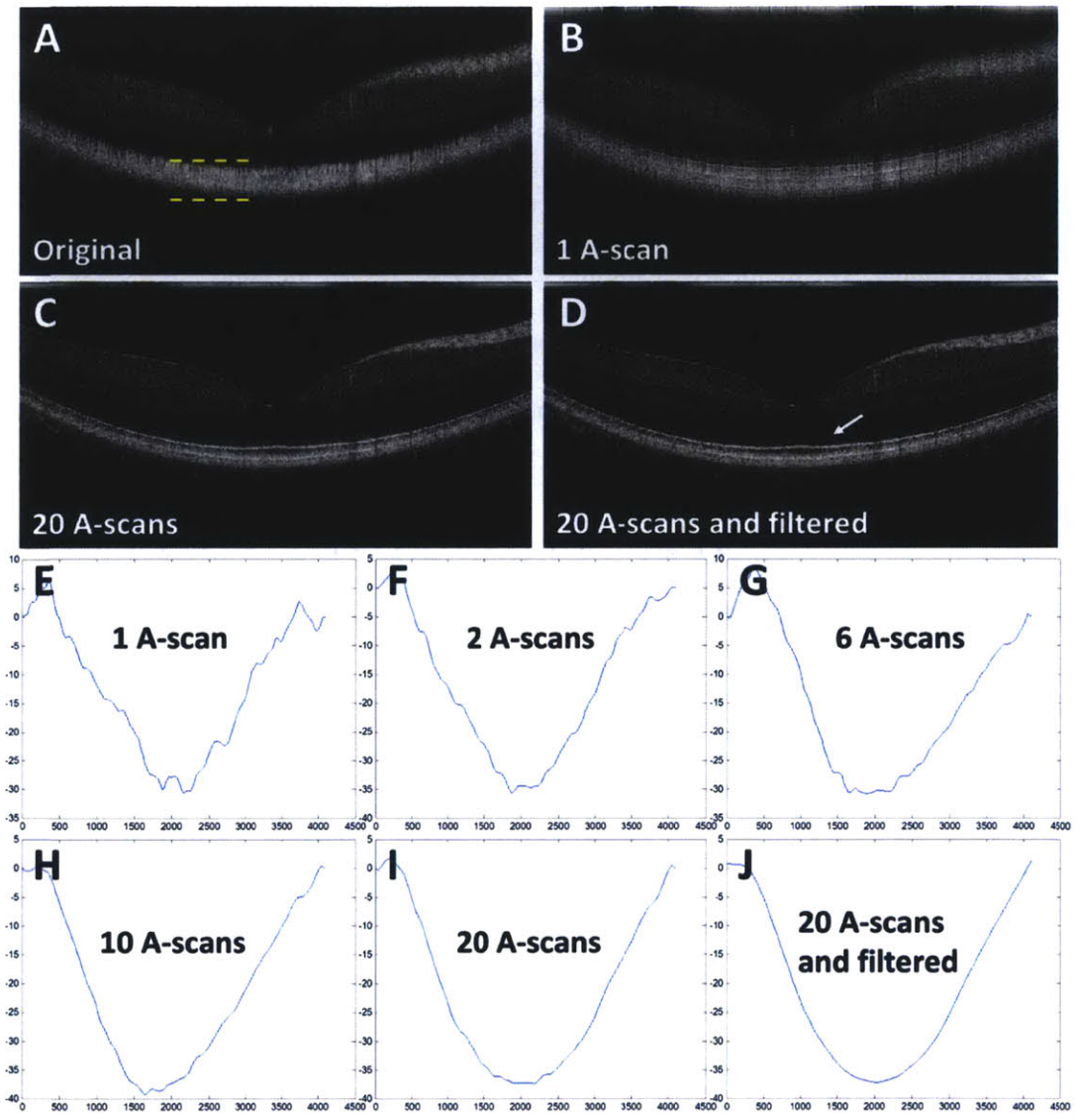


**Figure 2.5.** (A) An original OCT B-scan image of a normal human retina. (B, C, D) OCT B-scans numerically dispersion compensated with the mismatches shown in (E, I, J). The white arrow in (D) indicates the external limiting membrane (ELM). (E-I) Dispersion mismatches extracted from different numbers of A-scans. (J) was obtained by filtering (I) with a Savatzky-Golay filter. For (E-J), the y-axis indicates phase in radian and the x-axis sample number.

Figure 2.5(E) shows the extracted dispersion mismatch from a single A-scan. Note that there are several abrupt jumps in the extracted dispersion mismatch due to noise and speckle, which can be understood in terms of the short-time Fourier transforms described earlier. When this mismatch is used for numerical dispersion compensation, the OCT point spread function splits, as can be seen in Figure 2.5(B). Note that the image became sharper compared to Figure 2.5(A), although image feature appear split multiple times in depth. This is not surprising considering the effect shown earlier in Figure 2.3(B). Figures 2.5(F-I) show the averages of dispersion mismatches extracted from different numbers of A-scans in order to reduce speckle. The extracted dispersion mismatch is averaged according to the number of A-scans indicated. Note that as larger numbers of A-scans are used for averaging, the abrupt jumps in the extracted phase are reduced. Figure 2.5(J) was obtained by filtering Figure 2.5(I) with a Savitzky-Golay filter (polynomial order: 1, window size: 401, number of samples per A-scan: 4096) in order to further suppress the effect of speckle. Figures 2.5(C) and (D) show the numerically dispersion compensated B-scans using the extracted dispersion mismatches shown in Figures 2.5(I) and (J), respectively. Both Figures 2.5(C) and (D) became noticeably sharper than the original image. However, Figure 2.5(D) resulted in a cleaner image as can be seen by examining the area below the external limiting membrane (ELM). It is important to emphasize that the extracted dispersion mismatches are averaged for speckle reduction, while the spectral interferograms are not averaged before extracting the mismatch. It should also be noted that the purpose of averaging is not to increase signal-to-noise ratio, but to reduce the effects of speckle.

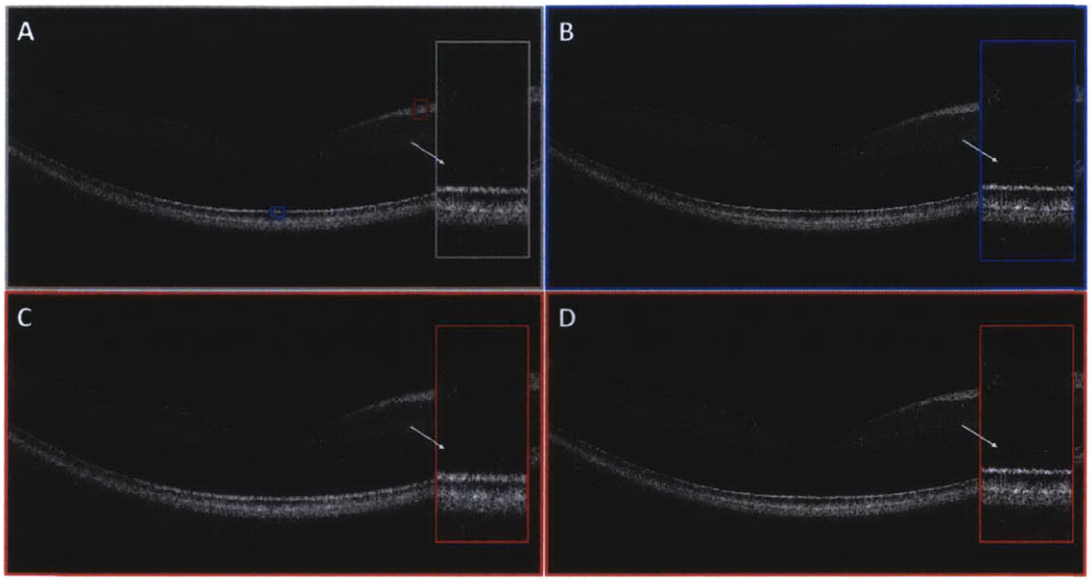


**Figure 2.6.** (A) An original OCT B-scan image of a normal human retina. Dispersion was approximately matched with a water cell in the OCT reference arm. (B) An OCT B-scan numerically dispersion compensated with the dispersion mismatch extracted from a single A-scan near the position indicated by the blue box in (A). Only the IS/OS was used for dispersion mismatch extraction. (C) An OCT B-scan numerically dispersion compensated with the dispersion mismatch extracted from a single A-scan near the position indicated by the red box in (A). The entire NFL was used for dispersion mismatch extraction. (D) The dispersion mismatch was extracted from 20 A-scans near the position indicated by the red box in (A) and averaged and filtered to reduce speckle.

In practice, a water cell is typically used in the reference arm for retinal imaging in order to match dispersion from the vitreous of the eye. Therefore, it is important to test whether this approach can be also used to find a smaller amount of dispersion mismatch. Figure 2.6(A) is an OCT B-scan image of a normal human retina consisting of 2048 A-scans, acquired with the first ultrahigh resolution system, but with a water cell inserted in the reference arm to approximately

match dispersion. Figure 2.6(B) shows a B-scan numerically dispersion compensated with the dispersion mismatch extracted from a single A-scan near the position indicated by the blue box in Figure 2.6(A). Only the inner segment / outer segment junction (IS/OS) was used for extracting the dispersion mismatch. Averaging multiple A-scans did not help in this case because IS/OS acted as a good single scatterer with minimal speckle. Figure 2.6(C) shows a B-scan numerically dispersion compensated with the mismatch extracted from a single A-scan near the position indicated by the red box in Figure 2.6(A). In this case, the entire nerve fiber layer (NFL) was used to extract dispersion mismatch. Because the NFL is thick, there are multiple scatterers in a given A-scan. Therefore, the extracted dispersion mismatch has artifacts due to speckle. Figure 2.6(D) shows a numerically dispersion compensated image with an averaged dispersion mismatch extracted from 20 A-scans near the position indicated by the same red box in Figure 2.6(A). The extracted dispersion mismatch was filtered with a Savatzky-Golay filter (polynomial order: 1, window size: 401, number of samples per A-scan: 3072) before it was used for numerical dispersion compensation. As can be seen, averaging and filtering the extracted phase reduces speckle and achieves more accurate extraction of the dispersion mismatch. This result demonstrates that this approach can be applied to diffuse multiple scatterers as long as the speckle is appropriately managed.

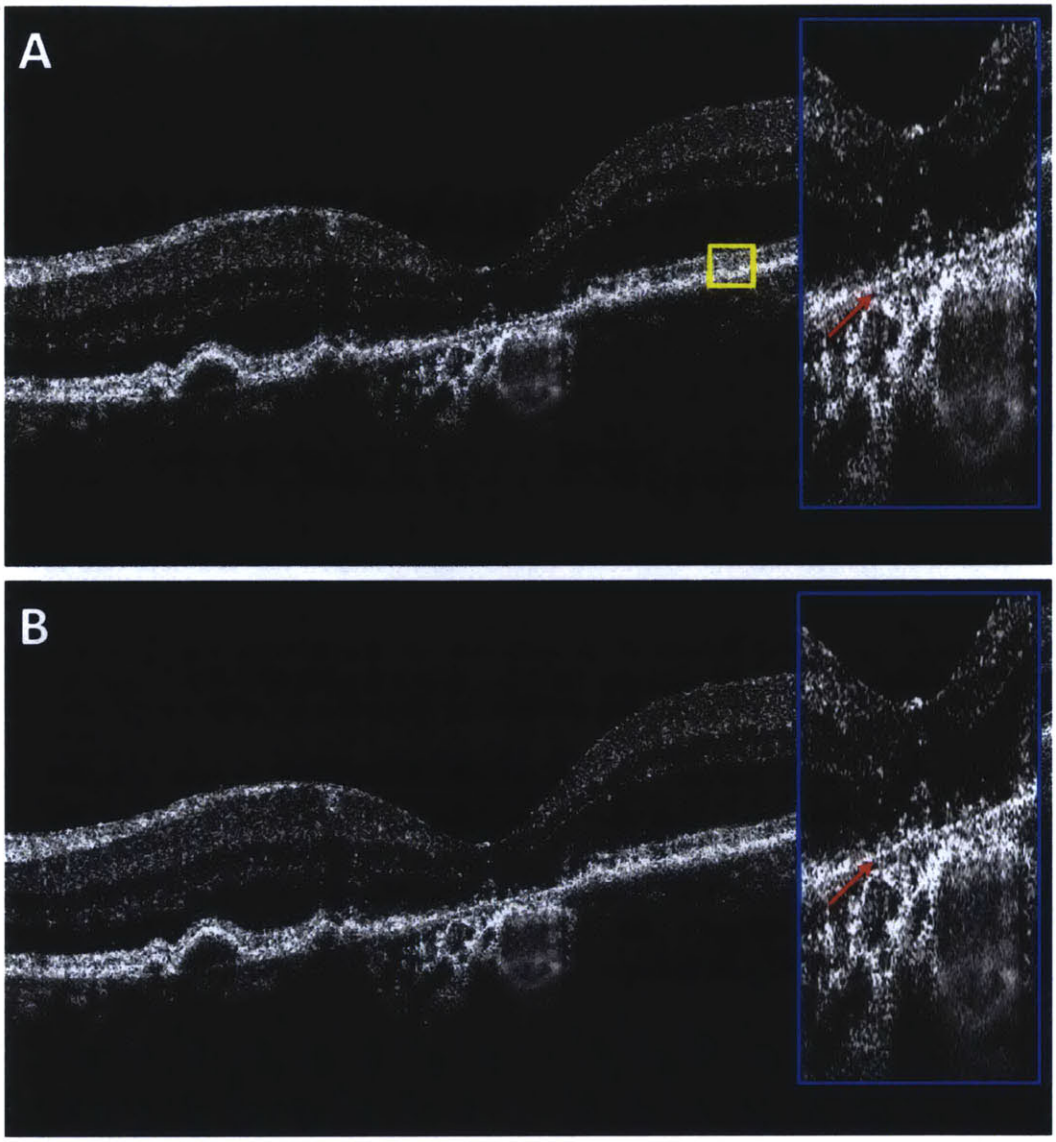


**Figure 2.7.** (A) An original OCT B-scan image of a patient with dry AMD. Dispersion was approximately matcched with a water cell inserted in the OCT reference arm. (B) An OCT B-scan numerically dispersion compensated with the averaged and filtered mismatch extracted from 200 A-scan near the position indicated by the yellow box in (A).

Finally, the approach was applied to images with retinal pathology. Figure 2.7 shows an OCT retinal image acquired from a patient with dry age-related macular degeneration (AMD)

obtained with the second ultrahigh resolution OCT system used at the New England Eye Center. The B-scan image consisted of 16,000 A-scans over 6 mm. A water cell was used in the reference arm for approximate dispersion matching. For this scan pattern, 200 A-scans near the yellow square in Figure 2.7(A) were used to extract the dispersion mismatch. Because of the pathology, it was not possible to separate the IS/OS and the retinal pigment epithelium (RPE), and the entire diffuse bright band near the RPE was used, as indicated by the yellow box. Therefore, a relatively large number of A-scans were required to extract the dispersion mismatch. Another reason that a larger number of A-scans were required is that the scan pattern was very dense and the relative difference between neighboring A-scans was proportionally smaller in terms of speckle. Figure 2.7(B) is a B-scan that is numerically dispersion compensated with the extracted dispersion mismatch averaged over 200 A-scans and filtered with a Savatzky-Golay filter. As can be seen from the zoomed views of Figures 2.7(A) and (B), the image became sharper using numerical dispersion compensation. The effect of dispersion compensation can be seen by examining the thickness of Bruch's membrane near the center of the fovea as indicated by arrows.

There is a very recently published approach that uses the cross-correlation of sub-bandwidth images to characterize and compensate for dispersion as well as sample axial motion artifacts[13]. Although this approach is more closely related to the approach reported here than other approaches mentioned in the introduction in that it uses short-time Fourier transforms, there are still important differences. The approach described in this manuscript does not use cross-correlation of images which can be time consuming especially if it is necessary to achieve sub-pixel accuracy. We also demonstrated that short-time Fourier transforms at multiple wavenumbers can be replaced by single Hilbert transformation, which dramatically reduces

computational time. Finally this chapter demonstrates that speckle in short-time Fourier transforms can pose additional challenges and proposed an approach to reduce its effects and obtain high quality dispersion compensation.

## 2.6 Conclusion

Using a mathematical analogy between the Shack-Hartmann wavefront sensor and Fourier domain OCT, we present an approach to extract the dispersion mismatch between the sample and reference in spectral / Fourier domain OCT. By carefully considering the effect of speckle, which is a common phenomenon occurring in both wavefront sensing and dispersion measurement, the dispersion mismatch was successfully extracted in A-scans with diffuse multiple scatterers as well as a single scatterer. In principle, different approaches for dispersion compensation, including the approach described in this manuscript should converge to a single equivalent solution, which should enable effective compensation of dispersion mismatch. However, the approach described here attempts to extract the dispersion mismatch in a more physically intuitive way, rather than optimizing a metric function. Although this manuscript applies the Shack-Hartmann wavefront sensor analogy to OCT dispersion measurement and compensation, the mathematical analogy also suggests analogs in other applications. For example, it may be possible to extend the approach introduced here to two-dimensions and apply it for characterizing and numerically compensating optical aberration in holography or OCT.

## References


1. Huang D, Swanson EA, Lin CP, Schuman JS, Stinson WG, Chang W, Hee MR, Flotte T, Gregory K, Puliafito CA, Fujimoto JG. Optical Coherence Tomography. Science. 1991;254(5035):1178-81. PubMed PMID: 1957169.

2. Swanson EA, Izatt JA, Hee MR, Huang D, Lin CP, Schuman JS, Puliafito CA, Fujimoto JG. In vivo retinal imaging by optical coherence tomography. Opt Lett. 1993;18(21):1864-6.

3. Drexler W, Fujimoto JG. Optical Coherence Tomography: Technology and Applications Berlin: Springer-Verlag Berlin; 2008.

4. Drexler W, Morgner U, Ghanta RK, Kärtner FX, Schuman JS, Fujimoto JG. Ultrahigh-resolution ophthalmic optical coherence tomography. Nat Med. 2001;7(4):502-7. PubMed PMID: 11283681; PubMed Central PMCID: PMC1950821.

5. Leitgeb RA, Drexler W, Unterhuber A, Hermann B, Bajraszewski T, Le T, Stingl A, Fercher AF. Ultrahigh resolution Fourier domain optical coherence tomography. Optics Express. 2004;12(10):2156-65. PubMed PMID: ISI:000221423800015.

6. Wojtkowski M, Srinivasan VJ, Ko TH, Fujimoto JG, Kowalczyk A, Duker JS. Ultrahigh-resolution, high-speed, Fourier domain optical coherence tomography and methods for dispersion compensation. Optics Express. 2004;12(11):2404-22. PubMed PMID: 19475077.

7. Cense B, Nassif N, Chen TC, Pierce MC, Yun S, Park BH, Bouma B, Tearney G, de Boer JF. Ultrahigh-resolution high-speed retinal imaging using spectral-domain optical coherence tomography. Optics Express. 2004;12:2435-47.

8. Drexler W, Sattmann H, Hermann B, Ko TH, Stur M, Unterhuber A, Scholda C, Findl O, Wirtitsch M, Fujimoto JG, Fercher AF. Enhanced visualization of macular pathology with the use of ultrahigh-resolution optical coherence tomography. Arch Ophthalmol. 2003;121(5):695-706. PubMed PMID: PMID: 12742848; Medline: 22627213 Provider: OCLC.

9. Ko TH, Fujimoto JG, Schuman JS, Paunescu LA, Kowalevicz AM, Hartl I, Drexler W, Wollstein G, Ishikawa H, Duker JS. Comparison of Ultrahigh- and Standard-Resolution Optical Coherence Tomography for Imaging Macular Pathology. Ophthalmology. 2005. PubMed PMID: 16183127.

10. Drexler W, Morgner U, Kartner FX, Pitris C, Boppart SA, Li XD, Ippen EP, Fujimoto JG. In vivo ultrahigh-resolution optical coherence tomography. Opt Lett. 1999;24(17):1221-3.

11. Hitzenberger CK, Baumgartner A, Drexler W, Fercher AF. Dispersion effects in partial coherence interferometry: implications for intraocular ranging. J Biomed Opt. 1999;4(1):144-51.

12. Yasuno Y, Hong YJ, Makita S, Yamanari M, Akiba M, Miura M, Yatagai T. In vivo high-contrast imaging of deep posterior eye by 1-mu m swept source optical coherence tomography and

scattering optical coherence angiography. Optics Express. 2007;15(10):6121-39. PubMed PMID: ISI:000246474300026.

13. Hillmann D, Bonin T, Lührs C, Franke G, Hagen-Eggert M, Koch P, Hüttmann G. Common approach for compensation of axial motion artifacts in swept-source OCT and dispersion in Fourier-domain OCT. Optics Express. 2012;20(6):6761-76. doi: 10.1364/oe.20.006761.

14. Schmitt JM, Xiang SH, Yung KM. Speckle in optical coherence tomography. J Biomed Opt. 1999;4(1):95-105.

15. Wojtkowski M, Leitgeb R, Kowalczyk A, Bajraszewski T, Fercher AF. In vivo human retinal imaging by Fourier domain optical coherence tomography. J Biomed Opt. 2002;7(3):457-63. PubMed PMID: 12175297.

16. Leitgeb R, Hitzenberger CK, Fercher AF. Performance of Fourier domain vs. time domain optical coherence tomography. Optics Express. 2003;11(8):889-94. PubMed PMID: 19461802.

17. Choma MA, Sarunic MV, Yang CH, Izatt JA. Sensitivity advantage of swept source and Fourier domain optical coherence tomography. Optics Express. 2003;11(18):2183-9. PubMed PMID: 19466106.

18. Liang J, Grimm B, Goelz S, Bille JF. Objective measurement of wave aberrations of the human eye with the use of a Hartmann?Shack wave-front sensor. Journal of the Optical Society of America A. 1994;11(7):1949-57. doi: 10.1364/josaa.11.001949.

19. Makita S, Fabritius T, Yasuno Y. Full-range, high-speed, high-resolution 1-mu m spectral-domain optical coherence tomography using BM-scan for volumetric imaging of the human posterior eye. Optics Express. 2008;16(12):8406-20. PubMed PMID: WOS:000256859900009.

20. Hofer H, Artal P, Singer B, Aragon JL, Williams DR. Dynamics of the eye's wave aberration. J Opt Soc Am A. 2001;18(3):497-506. PubMed PMID: WOS:000167156100003.

21. Goodman JW. Speckle Phenomena in Optics: Theory and Applications: ROBERTS & Company PUBL; 2010.

# Chapter 3

# Measurement of pulsatile total blood flow in the human and rat retina using ultrahigh speed spectral / Fourier domain OCT

## 3.1 Overview

This chapter presents an approach to measure pulsatile total retinal arterial blood flow in humans and rats using ultrahigh speed Doppler OCT. The axial blood velocity is measured in an en face plane by raster scanning and the flow is calculated by integrating over the vessel area, without the need to measure the Doppler angle. By measuring flow at the central retinal artery, the scan area can be very small. Combined with ultrahigh speed, this approach enables high volume acquisition rates necessary for pulsatile total flow measurement without modification in the OCT system optics. A spectral domain OCT system at 840nm with an axial scan rate of 244kHz was used for this study. Real-time Doppler C-scan preview is proposed as a guidance tool to enable quick and easy alignment necessary for large scale studies. Data processing for flow calculation can be entirely automatic using this approach because of the simple and robust algorithm. Due to the rapid volume acquisition rate and the fact that the measurement is independent of Doppler angle, this approach is inherently less sensitive to involuntary eye motion. This method should be useful for investigation of small animal models of ocular diseases as well as total blood flow measurements in human patients in the clinic. Dr. Bernhard Baumann contributed significantly in building the OCT system and performing measurements. Jonathan J. Liu developed the initial version of the acquisition software. Dr. Allen C. Clermont, Dr. Edward P. Feener, Dr. Jay S. Duker, and Prof. James G. Fujimoto provided supervision and guidance.

### 3.2 Introduction

Assessing ocular blood flow in vivo is an important research area because many ocular diseases, such as diabetic retinopathy, glaucoma and age-related macular degeneration, are associated with alterations in retinal blood flow. Therefore, the measurement of total retinal blood flow and pulsatility is important for investigating pathophysiology in small animal models of ocular diseases and may also be useful for the diagnosis of these diseases in humans[1-6].

Conventionally, techniques such as color Doppler imaging, scanning laser Doppler flowmetry, retinal vessel analyzer, laser speckle flowgraphy, digital scanning laser ophthalmoscope angiography and laser Doppler velocimetry have been used to characterize hemodynamics in the normal and diseased eyes[2, 5]. However, many of these techniques measure only velocity and not total flow, as in color Doppler imaging and laser Doppler velocimetry, or vessel diameter as in retinal vessel analyzer. One of the main limitations of scanning laser Doppler flowmetry is that it does not provide depth-resolved measurements, thereby making quantitative comparison among different subjects challenging. Other techniques, such as laser speckle flowgraphy or scanning laser ophthalmoscope angiography, also have the limitation that they require intravenous dye injection and/or are difficult to convert into actual flow. Therefore, there has been a considerable demand for new techniques that can reliably assess retinal blood flow *in vivo*[7, 8].

Since structural optical coherence tomography (OCT) imaging has become a clinical standard in many areas of ophthalmic clinical diagnosis and medical research[9], it is desirable to use OCT for functional measurement of total retinal blood flow. Fourier-domain Doppler OCT methods enable direct access to phase and can measure the speed of moving scatterers, such as red blood cells and also enables a dramatic increase in sensitivity and speed compared with time-

domain OCT[8, 10, 11]. However, since Doppler OCT measures only the axial component of velocity that is parallel to the probe beam direction, conventional Doppler techniques require information on blood vessel angles in addition to speed for quantitative assessment of retinal blood flow[7, 12-15]. Another method is to detect Doppler shifts in two different directions using two beams impinging at different angles without explicit extraction of blood vessel angles, but this requires hardware scan modifications and is therefore more difficult to implement with standard commercial OCT patient interfaces[16]. While blood flow has been measured in both humans and small animals using these conventional methods, flow measurement was usually based on an individual arterial or venous branch, rather than the total retina[17].

Total retinal blood flow can be measured using a novel technique which acquires multiple concentric circumpapillary scans with different diameters centered at the optic nerve to intercept all of the retinal vessels while also measuring the vessel angles[7, 15]. However, angle measurement is sensitive to eye motion and errors in detected angle can cause flow measurement error. In order to overcome this limitation, a software approach to register circumpapillary scans, which is used to extract speed information, to motion-corrected two-dimensional raster scan, which is used to extract blood vessel angles, has been developed to reduce measurement variability[18]. It has been recently shown that total retinal flow measurements using circumpapillary scans generated by Fourier-domain Doppler OCT exhibit statistically significant differences between normal and diseased eyes[19].

Recently, an en face Doppler OCT approach which does not require blood vessel angle information, became feasible due to an increase in OCT imaging speed[20, 21]. This en face Doppler technique simplifies total blood flow measurement by using the fact that total flow in a vessel is given by the integral of the product of a differential area and velocity component perpendicular

to the area over the cross-section of the blood vessel. In Doppler OCT, total blood flow can be calculated simply by summing all axial velocity components in an en face plane generated from an OCT raster scan centered at the optic nerve at a given depth location and multiplying the sum with an area calibration factor, which is readily measurable. Our group demonstrated that at a high enough imaging speed, this en face Doppler can be applied to the retina to calculate total retinal blood flow[22]. This method combined with swept source technology has several advantages including negligible fringe washout compared with spectral-domain OCT[23, 24], simple flow calculation without the need for vessel angle information, and compatibility with existing standard OCT patient interface. However, pulsatility still remained a challenge as in all other retinal blood flow measurement techniques, potentially causing up to 50% or higher variation in measured flow values[22, 25].

In this chapter, we present a novel approach to measure total retinal arterial blood flow and pulsatility in rats as well as in humans. As demonstrated previously, the axial blood velocity is measured in an *en face* plane by scanning a raster pattern to avoid the need to measure the Doppler angle and to achieve a simple and robust measurement technique. In addition, total blood flow is measured at or near the central retinal artery in this approach, and therefore, the scan area can be extremely small. Combined with ultrahigh speed Fourier domain OCT, this acquisition scheme enables high repeated volume acquisition rates necessary for pulsatile total blood flow characterization. The total acquisition time required for pulsatile blood flow measurement with this approach is only a few seconds for both humans and small animals because blood flow is continuously recorded in time without gating. Moreover, because of the short acquisition time required per volume, this approach is inherently less sensitive to involuntary patient eye motion, which is highly advantageous for implementation in the clinic.

Due to the simplicity and robustness of data processing algorithm, completely automatic total blood flow calculation was achieved in this study.

## 3.3 Methodology

### *3.3.1 Ultrahigh speed spectral / Fourier domain OCT system*

A sketch of the OCT system used in this experiment is shown in Figure 3.1. A commercially available superluminescent diode (Superlum) and line scan camera (Basler Sprint spL4096-140 km) were used to develop an ultrahigh speed spectral / Fourier domain OCT system at 840nm with an imaging speed of 244,000 A-scans per second. The full width at half maximum (FWHM) bandwidth of the superluminescent diode light source was 55nm. The spectrometer used a collimating lens with an effective focal length of 100mm, a 1200 lines/mm transmission holographic grating and an 80mm scan lens. The line scan camera had 10 μm square pixels in two rows and was 4096 pixels wide. However for this design only 832 pixels were illuminated and the camera was read at a line rate of 244 kHz where the exposure time was 2.8μs, accounting for the reading time. The spectrometer was calibrated by using an approach similar to that described by Makita et al[26]. The output was processed by spline interpolation followed with numerical dispersion compensation and Fourier transformation.

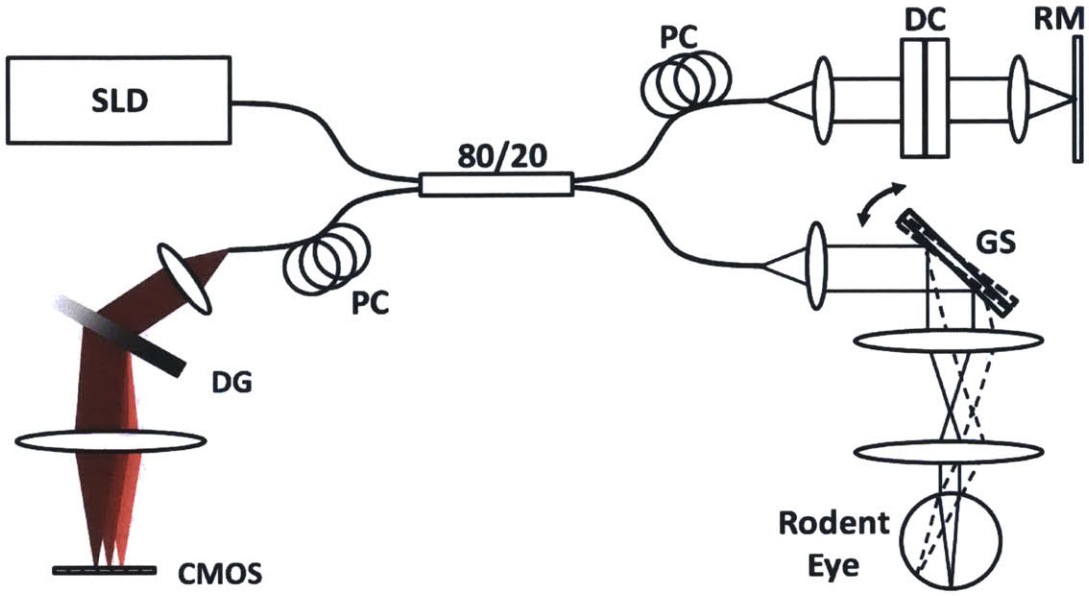


**Figure 3.1.** Schematic of the ultrahigh speed spectral domain OCT system. PC: polarization controller, DC: dispersion compensation glass, RM: reference mirror, GS: galvanometer scanner pair, DG: diffraction grating, SLD: superluminescent diode, CMOS: line scan camera. A similar OCT system with reduced power at the cornea was used for human imaging.

The total imaging range was 1.5mm in tissue with a measured axial resolution of 5.7μm in tissue. The power of the OCT beam at the cornea was 2.5mW for rat imaging, and the system sensitivity was 99dB. A non-contact scanning configuration was used to avoid pressure on the cornea which may change intraocular pressure and retinal blood flow. The scan interface for rat imaging consisted of a pair of galvanometer scanners (Cambridge Technology 6210H, 3mm mirrors), a 50mm scan lens, and an ocular lens with an effective focal length of 12.5mm. The incident beam diameter on the cornea was 0.5mm. A similar system was used for human eye imaging, but the output power at the cornea was reduced to 750μW, consistent with American National Standards Institute (ANSI) standards safe exposure limits, resulting in a sensitivity of

94dB. The human imaging interface consisted of a pair of galvanometer scanners (Cambridge Technology 6215H, 5mm mirrors), a 80mm scan lens, and an ocular lens with an effective focal length of 30mm, resulting in a beam diameter of 1.8mm incident on the cornea. Theoretical spot sizes on the retina calculated with ZEMAX using standard eye models were ~15μm for the small animal interface and ~20μm for the human imaging interface. The phase stability of the spectrometer measured with a common path cover slip interferometer was 1.1mrad (standard deviation of measured phase). The superior phase stability of spectral / Fourier domain OCT enabled robustness necessary for large scale studies without the need for sophisticated trigger fluctuation compensation algorithms as required in swept source OCT. However, the approach proposed here is in principle compatible with any high speed Fourier domain OCT system, including swept source OCT.

*3.3.2 Assessment of Doppler flow velocities*

Doppler flow velocities were calculated using the following equation[8]:

$$v_z = \frac{\lambda_c \Delta\Phi}{4\pi T n} \tag{3.1}$$

where $\lambda_c$ is the light source center wavelength, $\Delta\Phi$ is the phase difference between two consecutive A-scans, $T$ is the time between two A-scans and $n$ is the effective refractive index of the tissue.

Using an acquisition rate of 244,000 A-scans per second, the maximum axial velocity range that could be measured without phase wrapping was ±37.7mm/s in tissue. However, the maximum axial velocity that could be practically unwrapped without ambiguity was ~75.4mm/s in tissue, since only arteries near the central retinal artery were summed in the en face plane for the Doppler OCT flow measurement. No software bulk motion correction was necessary for this

study because the velocity of typical bulk motion of the retina encountered during imaging was negligible compared to the axial velocity of blood near the central retinal artery.

*3.3.3 Total retinal blood flow measurement using en face Doppler OCT*

Total retinal blood flow measurement was based on a method demonstrated by Srinivasan et al. in the small animal brain[20]. This method was later applied by Jenkins et al. for measuring total flow in developmental biology specimens and by Baumann et al. for measuring total flow in the human retina[21, 22]. Flow may be calculated using the following equation:

$$F = \int_S \boldsymbol{v} \cdot d\boldsymbol{A} = \int_S v \cos\theta dA \tag{3.2}$$

where $\boldsymbol{v}$ is the velocity vector of a moving scatterer and $d\boldsymbol{A}$ is the differential area with the vector normal to the surface area. This concept is illustrated in Figure 3.2.

In Doppler OCT, the axial velocity component of a moving scatter can be readily measured without information on the vessel angle. However, using conventional Doppler methods (Figure 3.2(A)), blood vessel angles are needed in addition to the axial velocity in order to calculate flow because the measurement is performed in a cross-sectional plane which is along the direction of the OCT beam. Raster scanning over an en face plane intercepting the blood vessel (Figure 3.2(B)) requires a higher imaging speed because of the larger number of A-scans necessary compared with scanning a cross-sectional plane. On the other hand, the z-component or axial component of the velocity is $v\cos\theta = v_z$ and blood flow in a vessel can also be calculated by simply integrating the axial velocity components in an OCT en face plane that intercepts the vessel (Figure 3.2(B)). Therefore, total retinal blood flow can be measured by scanning an area that intercepts all retinal vessels.

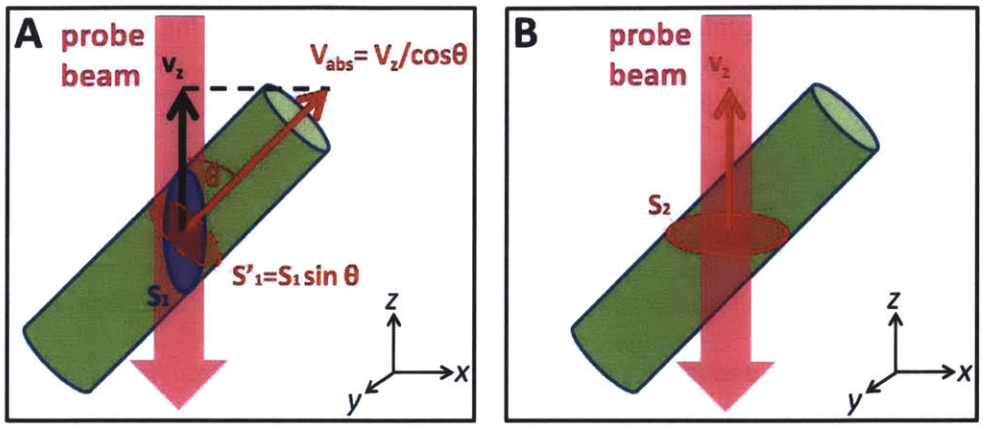


**Figure 3.2.** (A) In conventional Doppler methods, calculation of blood flow involves extraction of the Doppler angle , which is the angle between the probe beam and blood vessel. (B) In en face Doppler, simply integrating the axial velocity components over an en face cross-section that intercepts the vessel provides blood flow.

*3.3.4 Pulsatile total blood flow measurement in the human and rat retina*

One method to intercept all retinal vessels with an en face plane is to scan a large area around the optic nerve head, as in reference[22]. Although this approach measured all retinal vessels, it was not possible to characterize pulsatility in blood flow with this approach because of the limited OCT acquisition speed. Another method to measure pulsatile blood flow with en face Doppler OCT is to use gating to reconstruct pulsatile blood flow as demonstrated by Jenkins et al. in the quail embryo heart tube[21]. However, gating requires additional hardware and software for synchronization as well as a longer total measurement time, which limits its use for large scale studies in humans or rodent models. This paper describes an approach which specifically measures the central retinal artery to rapidly and repeatedly scan a small area, thereby achieving sufficient volume acquisition rate to characterize blood flow pulsatility.

In the rat retina, the central retinal artery is readily accessible by the OCT probe beam, and rapid, repeated scanning of a small area is possible to achieve rapid volume acquisition rate. In the human retina, the central retinal artery cannot always reliably be imaged at 840nm wavelengths due to limited image penetration depth. However, by choosing an en face plane which intercepts all retinal arteries just after they branch from the central retinal artery, the scan area can still be small enough for rapid, repeated volume acquisition necessary for pulsatile blood flow imaging in humans.

By using en face Doppler OCT, knowledge of the angle between the blood vessel and OCT beam, *i.e.* the Doppler angle, is not required, which dramatically simplifies total retinal blood flow measurement. Moreover, because the scanned area is very small and has high sampling density, blood vessel detection and segmentation becomes highly robust and simple, thereby enabling entirely automatic processing algorithms for pulsatile blood flow calculation. Completely automatic processing is especially useful for large scale studies, which are necessary in the investigation of small animal models of ocular diseases as well as in clinical retinal blood flow measurements in human patients with ocular disease. The fact that Doppler angle information is not required also implies that this approach is highly robust to segmentation error which might otherwise lead to large variations in calculated flow from inaccurate Doppler angle measurement.

*3.3.5 Real-time Doppler C-scan preview*

Because of variations in the three-dimensional retinal anatomy in both humans and rats, it is not always obvious which scan area will intercept all the blood vessels necessary to measure total retinal blood flow. One approach is to scan a large area near the optic nerve head as shown in reference[22]. However, a rapid volume acquisition rate is required to characterize pulsatility in

blood flow so it is necessary to limit the scan area in order to achieve rapid scan rates. Because of the vessel geometry and lack of contrast, conventional intensity B-scan previews are not sufficient to reliably locate the central retinal artery or blood vessels of interest. Although OCT intensity fundus projection can sometimes provide a rough location of the central retinal artery, it is still insufficient for defining a small scan area because fundus projection images do not preserve depth-resolved information. This depth-resolved information is critical since blood vessels are not necessarily parallel to the OCT probe beam. An OCT intensity en face cross-section, or C-scan, preserves this depth-resolved information, but the inherent lack of contrast between blood vessels and neighboring tissue limits its practical use for locating blood vessels.

Since reliability and ease of alignment are of key importance for large scale studies involving small animals and humans, we developed a real-time en face Doppler cross-sectional preview, or Doppler C-scan preview. The Doppler C-scan preview can provide an accurate location of the blood vessels of interest as well as preview the quality of the Doppler images that will be acquired.

Because Doppler processing requires oversampling in at least one scan direction and Doppler C-scan preview is useful only if it scans an area larger than the actual area of interest, it requires a large number of A-scans per en face frame. However, it is important to note that the full discrete Fourier transform (DFT) is not required for Doppler C-scan preview because only the phase at a single depth is required from the A-scan. For small animal Doppler imaging, the Doppler C-scan preview consisted of 400 100 A-scans over a 0.5mm×0.5mm area, which resulted in a 12x oversampling in the fast scan direction and 3x oversampling in the slow scan direction. Although the number of A-scans is 100 times larger than that is typically required for an intensity B-scan preview consisting of 400 A-scans, the total number of computations

required for DFT in the preview is even smaller for the Doppler C-scan preview, as long as the number of samples per A-scan is larger than the number of B-scans.

Although fast Fourier transform (FFT) algorithms cannot be used for Doppler C-scan preview because only the Fourier transform at a single depth is computed for a given A-scan, it is still possible to reduce the number of multiplications required by a factor of roughly two by using complex conjugate symmetry ( $e^{-jkn(2\pi/N)} = e^{jk(N-n)(2\pi/N)}$ where $k$ and $n$ are integers) as following[27]:

$$\begin{aligned} X[k] &\equiv \sum_{n=0}^{N-1} x[n] e^{-jkn(2\pi/N)} = \sum_{n=0}^{N-1} x[n]\{\cos(2\pi kn/N) - j\sin(2\pi kn/N)\} \\ &= \sum_{n=0}^{N/2-1} \left[\{x[n]+x[N-n]\}\cos(2\pi kn/N) - j\{x[n]-x[N-n]\}\sin(2\pi kn/N)\right] \end{aligned} \tag{3.3}$$

Without further optimization, a Doppler C-scan preview frame rate of >1fps was achieved, which was fast enough for small animal imaging. Although this frame rate was still useful for human imaging, further optimization in computer hardware and the use of recursive algorithms, such as the Goertzel algorithm[27], should improve the frame rate. These increases in preview speed would be important for imaging patients in the clinic. Figure 3.3 shows a flow chart of how Doppler C-scan preview can be used for alignment and an example of a Doppler C-scan preview image.

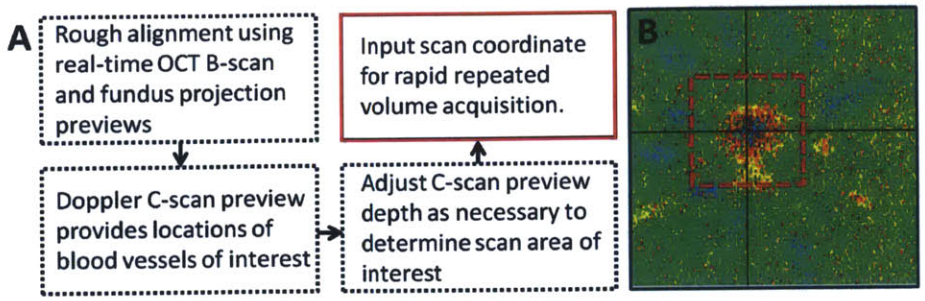


**Figure 3.3.** (A) Flow chart for alignment / acquisition procedure for pulsatile total retinal blood flow imaging. (B) An example of a Doppler C-scan preview image. The red square denotes the scan area of interest, which can be adjusted by moving the crosshair. Velocity wrapping can be observed at the center of the central retinal artery, which can be unwrapped for flow calculation during post-processing.

*3.3.6 Automatic flow calculation*

Flow calculation could be performed entirely automatically for both humans and small animals because of the robustness of the algorithm. The flow chart for the automatic flow calculation scheme is illustrated in Figure 3.4.

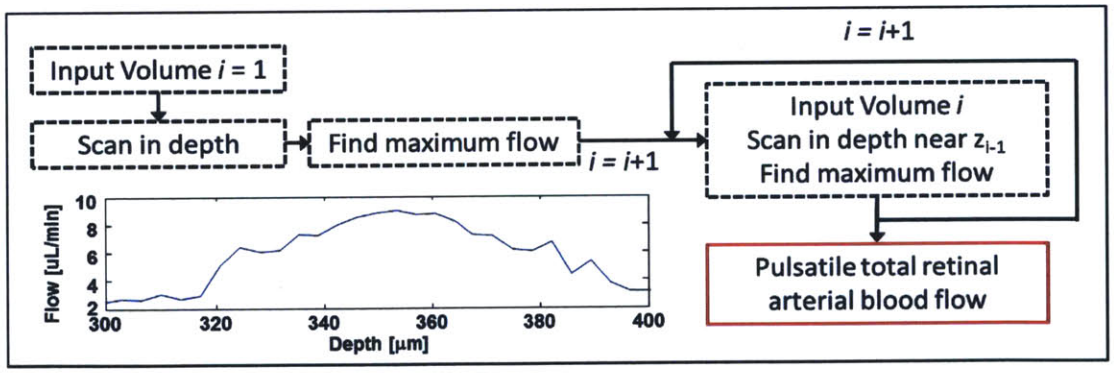


**Figure 3.4.** Flow chart for automatic flow calculation. Because of the robustness of the algorithm, essentially no user input is necessary and entirely automatic processing becomes feasible. The plot which shows flow as a function of depth is generated from a data set acquired from a normal male Sprague Dawley rat.

In situations where the maximum velocity produces one phase wrap, unwrapping can be performed reliably by adding $\pi$ when phase differences cross a negative threshold value. If the velocity is high and produces multiple phase wrapping, unwrapping is more difficult. The first volume from a repeated volumetric data set is used to calculate flow as a function of depth of the en face plane by detecting the central retinal artery by velocity thresholding median-fileterd en face Doppler images. For the rat data sets, because the central retinal artery is accessible with the OCT probe beam, only the largest connected area above a velocity threshold was summed for flow calculation. At shallow depths, an initial rise in flow occurs as multiple retinal arteries enter the field of view. Analyzing progressively deeper depths, eventually the OCT signal is lost due to limited imaging depth and the measured flow decreases. Between these two depth limits, there is a ~30μm depth range in case of the rodent retina, where measurements are free of these two counteracting effects and the measured flow is independent of depth as expected. The flow measured within this depth range corresponds to the true total retinal arterial flow value at the time the volume was acquired. Since repeated volumes are rapidly acquired, for the next volume in the data set it is only necessary to analyze a depth window near the depth where flow was maximal in the previous volume. By iterating this process through the entire data set, a pulsatile total retinal arterial blood flow waveform can be obtained. The length of this depth range where measured flow is constant depends on the scanned area because image penetration depth is usually fixed for a given wavelength. This depth range where constant flow is measured can vary between animals depending on the window size, and must be chosen so that it can intercept all retinal arteries in most animals. Similar effects can also be observed in the human retina where the depth range for measuring constant flow was ~70μm. One major difference between the automatic flow calculation algorithms for the human and rat data comes from the fact that the

central retinal artery cannot always be reliably imaged by the OCT probe beam. Therefore, for the human data, several connected areas above a velocity threshold as well as above a certain area threshold were summed together for flow calculation. Area thresholding was employed in order to exclude small random high velocity regions arising from Doppler noise. It should be noted that shadowing from blood vessels may make Doppler images noisy at deeper depths due to high scattering as in other Doppler OCT methods, and care must be taken in determining the correct depth where flow is calculated.

*3.3.7 Animal protocol*

Animal procedures were performed under an approved protocol by the Committee on Animal Care (CAC) at MIT. For all experiments involving animals, male Sprague Dawley rats weighing 250-500g were used. Immediately before OCT imaging, animals were anesthetized with ketamine/xylazine (ketamine 80mg/kg, xylazine 8mg/kg) or isoflurane (2%) and xylazine (8mg/kg), and dilated with 1% tropicamide. Hypothermia in animals was prevented by using heat pads. The animals were then imaged with the ultrahigh speed OCT system. During imaging, the animals were closely monitored for their heart rate, breathing rate, and oxygen saturation to assess depth of anesthesia and check for signs of distress.

## 3.4 Results and discussion

*3.4.1 Structural and functional blood flow imaging in the rat retina*

Imaging at a rate of 244,000 A-scans per second, a volumetric data set of 700×700 A-scans over 1.5mm×1.5mm can be acquired in only 2.4 seconds. Figure 3.5(A) shows an example of a cross-sectional image from the volumetric data set. Properly anesthetized rats have very stable eyes with minimal eye movement. Therefore, at this speed, 10 neighboring B-scans spanning a lateral distance of only ~20μm can be averaged without requiring registration and have negligible

motion artifacts. This enables high quality structural imaging with suppressed speckle as well as Doppler imaging with a single system.

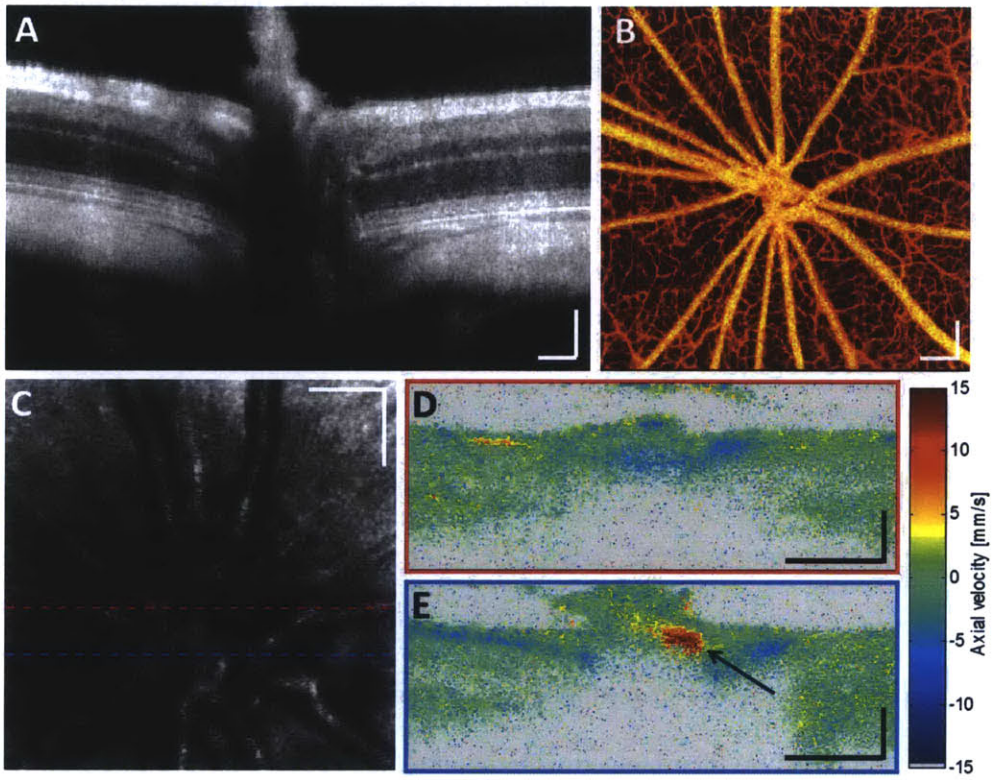


**Figure 3.5.** (A) An OCT cross-sectional image acquired at 244,000 A-scans per second centered at the optic nerve head (ONH). An average of 10 neighboring B- scans from a volumetric data of 700×700 A-scans over 1.5mm×1.5mm is shown. (B) Visualization of the capillary network. (C) An OCT fundus projection view over an area of 0.5mm×0.5mm at ONH. (D) A Doppler B-scan image showing the vasculature located at the red dotted line in the fundus projection view. (E) A Doppler B-scan image showing the vasculature located at the blue dotted line in the fundus projection view. The blue arrow indicates the central retinal artery cross-section. Scale bar: 100μm in all images.

The availability of high-quality volumetric imaging and functional blood flow imaging with a single system makes OCT a powerful tool for studies of disease progression in small animal models. For example, high speed volumetric imaging can enable visualization of capillary network as shown in Figure 3.5(B). This image was generated from a densely scanned volumetric data set using a method similar to speckle correlation mapping approach demonstrated in[28]. Volumetric structural imaging with minimum motion artifact is also useful for accurate measurements of thickness maps. Therefore, combined with pulsatile total retinal blood flow imaging, high speed OCT is capable of both functional and structural imaging and promises to be a powerful tool for investigation of small animal models of retinal diseases.

Figure 3.5(C) shows an OCT fundus view over a 0.5mm×0.5mm area. Figures 3.5(D) and (E) show Doppler B-scan images of the vasculature located at the red and blue dotted lines, respectively, in the fundus projection view. As shown by the blue arrow in Figure 3.5(E), the central retinal artery for this eye is approximately located near the center of the optic nerve. However, the location of an appropriate cross-section for central retinal artery does not necessarily coincide with the center of the optic nerve head in many eyes. Moreover, in many cases, it is not straightforward to define where the center of the optic nerve head is, which necessitates real-time Doppler C-scan preview for pulsatile total retinal blood flow imaging as described previously.

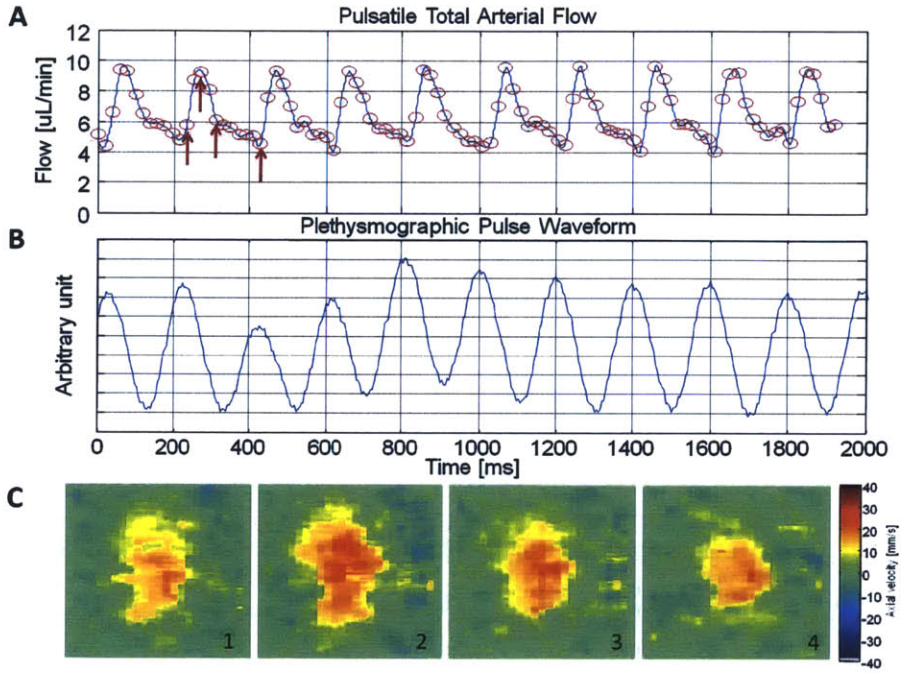


**Figure 3.6.** (A) Pulsatile total retinal arterial blood flow measured at the central retinal artery of a Sprague Dawley rat anesthetized with isoflurane/xylazine. (B) Simultaneously acquired plethysmographic pulse waveform from a pulse oximeter. (C) En face Doppler images at time points indicated by the red arrows in (A). The arrows from left to right in (A) correspond to Doppler images 1 to 4 in (C). 200μm×200μm.

Total Doppler flow measurements in the small animal eye are challenging because the rapid heartbeat requires high speed volumetric imaging. By scanning a smaller area of 200μm×200μm centered at the central retinal artery repeatedly, a volume acquisition rate of up to 140Hz was achieved. At 244kHz axial scan rates, increasing the volume acquisition rate requires smaller Doppler oversampling, which eventually results in loss of phase correlation. In principle, this limit could be overcome with higher imaging speed. For small animal imaging at an A-scan rate of 244kHz, a volume acquisition rate of ~55Hz (150×25 A-scans in each volume with a fast axis scan duty cycle of 85%) provided the most stable pulsatile total blood flow waveform without

compromising the number of volume samples per cardiac cycle. Figures 3.6(A) and (B) show the pulsatile total blood flow measured in the central artery of a Sprague Dawley rat anesthetized with isoflurane/xylazine at a volume acquisition rate of 55Hz and a simultaneously acquired plethysmographic pulse waveform from a pulse oximeter. The heart rate was ~300 beats per minute. Figure 3.6(C) shows en face Doppler images at 4 different time points indicated by the arrows in Figure 3.6(A). Pulsatile changes in axial velocity can be clearly seen. However, parabolic flow profile is not clearly observed because the en face cross-section chosen by the automatic processing software for the calculation of total blood flow was located where the central retinal artery branched into multiple retinal arteries. The black vessel boundaries, determined by the automatic processing software, in Figure 3.6(C) look slightly different from each other because of the vessel segmentation algorithm. With improved automatic blood flow computation software, variations in the segmentation of the vessel cross sections should be reduced. Waveforms in Figures 3.6(A) and (B) do not coincide perfectly in phase due to imperfect synchronization between the two acquisition channels and/or phase delay between the paw measured by the pulse oximeter and the retina.

The flow characteristics of the pulsatile total retinal blood flow shown in Figure 3.6 are summarized in Table 3.1, where the coefficients of variation are indicated in parentheses. The systolic, diastolic and mean flow values were calculated from the 9 pulse cycles shown in Figure 3.6(A). Pulsatility (PI) and resistivity (RI) indices were defined as:

$$PI = (F_{sys} - F_{dias}) / F_{mean} \tag{3.4}$$

$$RI = (F_{sys} - F_{dias}) / F_{sys} \tag{3.5}$$

where $F_{sys}$ is total systolic flow, $F_{dias}$ is total diastolic flow, and $F_{mean}$ is mean total flow. Note that the PI and RI indices used here are different from similar indices conventionally defined in

terms of velocities. The coefficients of variation for all flow characteristics were less than 10%, and it was only 2% for mean flow, demonstrating excellent short-term stability of the measurement technique.

**Table 3.1.** Pulsatile total blood flow characteristics in a normal rat.

| Systolic flow [μl/min] | Diastolic flow [μl/min] | Mean flow [μl/min] | Pulsatility index | Resistivity index |
|---|---|---|---|---|
| 9.42±0.2 (0.02) | 4.44±0.3 (0.06) | 6.40±0.1 (0.02) | 0.78±0.06 (0.08) | 0.53±0.03 (0.06) |

It is important to point out that shadowing of the blood vessels by other ocular structures in front of the vessels can occur and may result in an underestimate in the measured blood flow. However, if present, this shadowing can usually be significantly reduced by carefully tilting the retina to avoid the ocular structures that cast shadows. This alignment can be performed in real-time with the Doppler C-scan preview.

*3.4.2 Effect of anesthesia on retinal blood flow*

Total retinal blood flow is dependent on anesthesia. Figure 3.7 shows an example of pulsatile total retinal blood flow of a Sprague Dawley rat anesthetized with ketamine/xylazine. As seen from Figures 3.6 and 3.7, the mean total retinal flow value is higher by a factor of ~2 for the rat anesthetized with isoflurane/xylazine compared to that with ketamine/xylazine. This is not surprising since isoflurane is a known vasodilator when used at a high concentration. Although the rats imaged in Figures 3.6 and 3.7 are different animals, similar differences in blood flow were consistently measured in other rats. This indicates that a careful choice of anesthesia is required for total retinal blood flow measurement in small animals, depending on the study objectives.

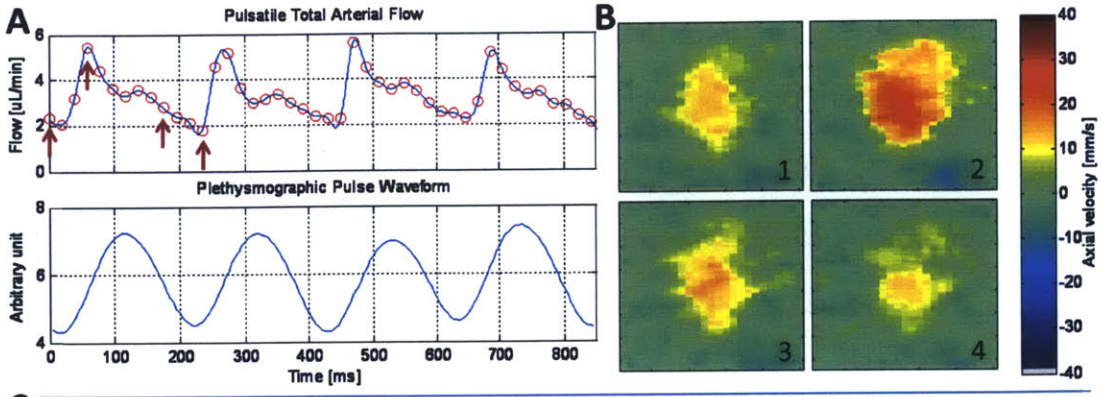


C

| Systolic Flow [µl/min] | Diastolic Flow [µl/min] | Mean Flow [µl/min] | PI | RI |
|---|---|---|---|---|
| 5.35±0.2 (0.04) | 2.08±0.2 (0.10) | 3.28±0.1 (0.04) | 0.99±0.07 (0.07) | 0.61±0.08 (0.08) |

**Figure 3.7.** (A) Pulsatile total flow measured at the central artery of a Sprague Dawley rat anesthetized with ketamine/xylazine and simultaneous acquisition of plethysmographic pulse waveform from a pulse oximeter. (B) En face Doppler images at time points indicated by the red arrows in (A). The arrows from left to right in (A) correspond to Doppler images 1 to 4 in (B). 150µm×150µm. (C) Systolic, diastolic and mean total flow values. PI: pulsatility index, RI: resistance index. Numbers in parentheses are coefficients of variation.

### *3.4.3 Pulsatile total retinal blood flow measurement in humans*

Pulsatile retinal blood flow imaging was also performed in the human retina to demonstrate that the technique can be extended to human retinal imaging. In many cases, the human central retinal artery is located too deep in the optic nerve head for OCT to image. Therefore, it was necessary to scan a relatively larger area of 0.8mm×0.8mm in order to intercept all retinal arteries necessary and measure total retinal blood flow. The Doppler C-scan preview was again a useful tool for locating the blood vessels. However, since the scan area was larger for human imaging, it was less important to determine the exact location of the blood vessels. To maintain a

high enough oversampling factor for Doppler processing, a 400×50 A-scan pattern was used. Although this scan pattern contains significantly larger number of A-scans per *en face* frame, which makes the frame rate slower than in small animal imaging, the human heart rate is also significantly lower and the resultant number of samples per cardiac cycle is roughly the same. For this experiment, at 244kHz axial scan rate, a scan pattern of 400×50 A-scans provided an *en face* frame rate of ~10Hz. This frame rate corresponds to ~10 sampling points per cardiac cycle assuming a resting heart rate of 60 beats per minute. A total data acquisition time of ~2 seconds will capture at least one continuous cardiac cycle in most subjects. Aside from the differences mentioned above, *en face* Doppler OCT successfully measured pulsatile total blood flow in the human retina as well as in the rodent retina.

Figure 3.8 shows OCT images of the optic nerve head of a normal subject. The yellow square in the wide-field en face projection image in Figure 3.8(A) indicates the size and approximate location of the scanned area used for repeated volumetric data acquisition for pulsatile total arterial blood flow measurements. Although a 0.8mm×0.8mm area was chosen in this study with the spectral OCT system, increased imaging speeds provided by future camera and swept source technologies will enable the scanned area to be increased without sacrificing volume acquisition rate, which will facilitate alignment in patients as well as in normal subjects. Figures 3.8(B) and (C) demonstrate the quality of structural images that can be obtained with the high speed spectral domain OCT system used in this study.

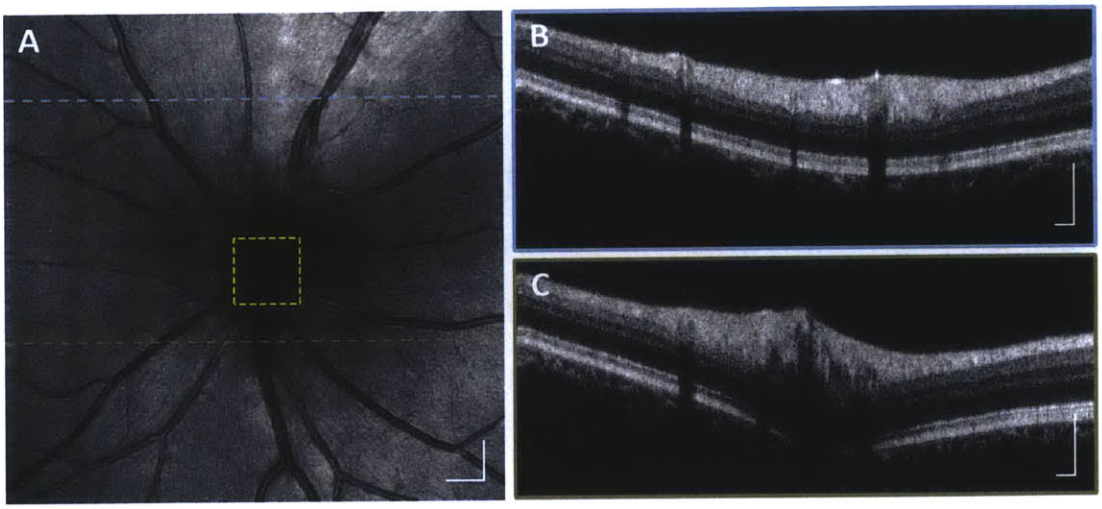


**Figure 3.8.** (A) An intensity en face projection image of the human optic nerve head of a normal subject. The yellow square indicates the size and approximate location of the area of scanning used for repeated volumetric acquisition for pulsatile total blood flow measurements. 600×600 A-scans over 6mm×6mm acquired within 1.7 seconds. Scale bar: 500μm. (B, C) Intensity B-scan images extracted from the locations indicated by the blue and tan dotted lines in (A). Averages of 4 neighboring B-scans displayed in logarithmic scale. Scale bar: 250μm.

Figure 3.9 and Table 2 summarizes pulsatile total arterial blood flow measurements in the same normal subject. Figures 3.9(A) and (B) show examples of an intensity B-scan and corresponding Doppler B-scan from one of the volumetric data sets used for pulsatile blood flow measurement. Figure 3.9(C) shows the pulsatile total arterial blood flow measured in the subject. The heart rate measured by a pulse oximeter was 57 beats per minute. Over the cardiac cycle centered in Figure 3.9(C), the mean total arterial blood flow was 43.2μl/min. The resistivity and pulsatility indices were calculated as 0.48 and 0.69, respectively. The resistivity and pulsatility indices of the subject may appear lower than similarly defined indices based on velocity

measurements due to the low pass filtering effect of the technique, which arises from the limited volume sampling rate of ~10Hz and Doppler velocity noise suppression effects, which result from summing multiple pixels to calculate total flow. Therefore, care is required in interpreting pulsatility and resistivity indices when comparing values measured by different devices. Figure 3.9(D) shows an example of an OCT intensity fundus projection of a volumetric data set. Figure 3.9(E) shows *en face* Doppler images at time points indicated by the red arrows in Figure 3.9(C). The black boundaries around the blood vessel are found by the automatic blood flow computation software. The vessel cross-sections in Figure 3.9(E) look slightly different from each other because slightly different depth locations were chosen by the software for flow measurement. Variations in the segmentation of the vessel cross sections could result in differences in flow measurement. However with improved automatic blood flow computation software, the boundaries should become smoother and more reproducible. Regardless of these effects, pulsatile variation of flow speed can be clearly seen. It may appear that in Figure 3.9(C), the pulsatile total flow trace is not as consistent as in Figure 3.6(A) due to the limited number of cardiac cycles displayed in Figure 3.9(C). However, the actual relative variations between cardiac cycles for the two cases are not significantly different. These variations probably arise from the limited sampling rate.

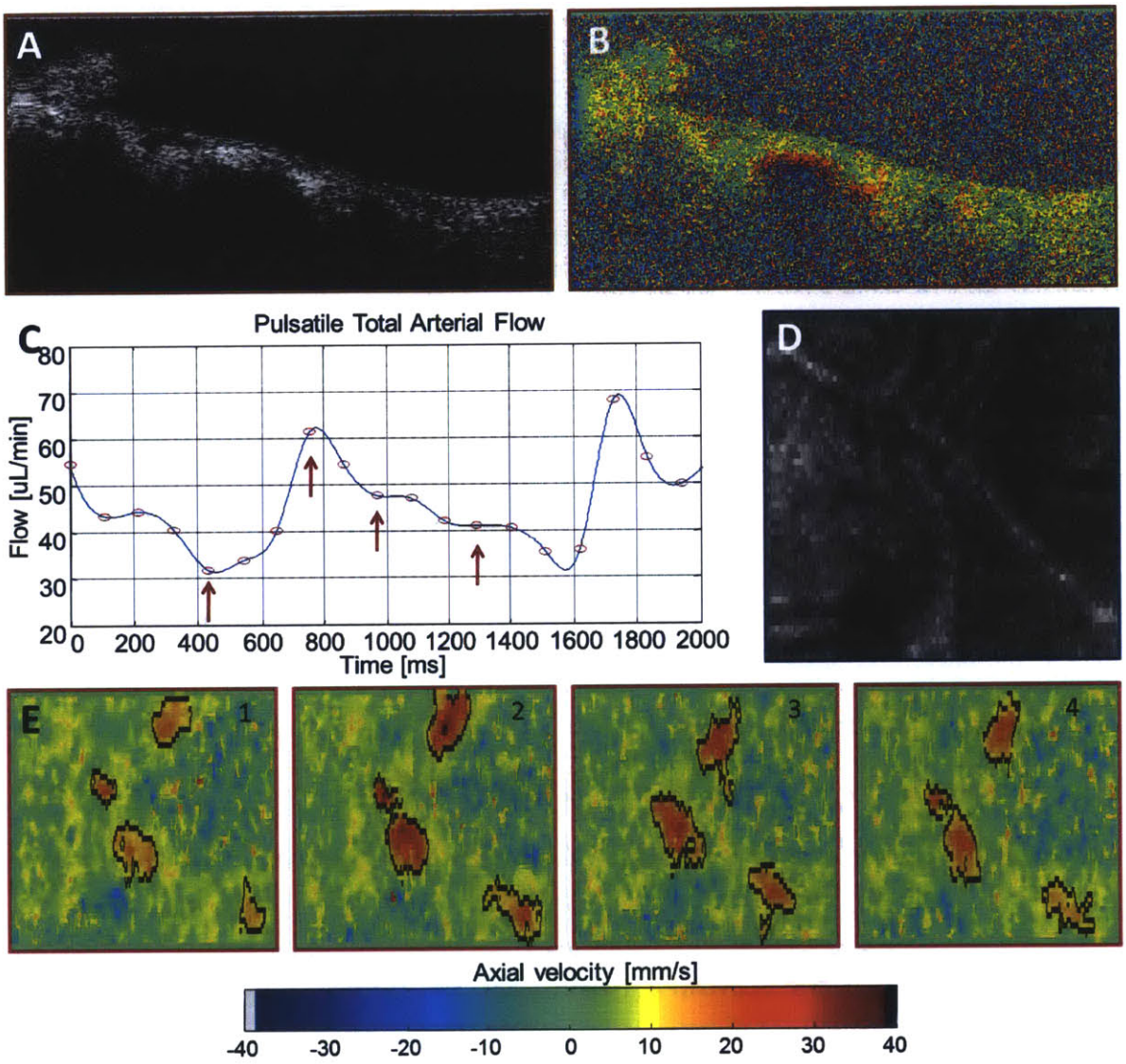


**Figure 3.9.** (A) An intensity B-scan image of the human retina of a normal subject. (B) A Doppler B-scan image corresponding to (A) showing the vasculature. (C) Pulsatile total retinal arterial blood flow measured at near the center of the optic nerve head. (D) An example of intensity fundus projection of a volumetric scan. (E) En face Doppler images at time points indicated by red the arrows in (C). The arrows from left to right in (C) correspond to Doppler images 1 to 4 in (E). 800μm×800μm.

**Table 3.2.** Pulsatile total blood flow characteristics in a normal human subject.

| Systolic flow [μl/min] | Diastolic flow [μl/min] | Mean flow [μl/min] | Pulsatility index | Resistivity index |
|---|---|---|---|---|
| 61.5 | 31.7 | 43.2 | 0.69 | 0.48 |

Another advantage of the technique presented in this paper is that it is inherently less sensitive to involuntary eye motion compared with other Doppler measurements. This is particularly attractive for human retinal imaging. Although a total acquisition time on the order of a few seconds is required for imaging over at least one cardiac cycle, each volumetric data set takes less than 0.1 second to acquire, which makes each volume virtually motion artifact free. In principle, involuntary eye motion in the axial direction does not affect the flow measurement, as long as the movement speed is negligible compared to the axial speed of blood flow and the retina remains within the OCT imaging range. Involuntary eye motion in the lateral direction does not affect the flow measurement either, as long as all the blood vessels are intercepted by the scan area. This scan area can be increased using future OCT instruments with higher imaging speed. This point is important because this approach scales significantly better with OCT imaging speed, compared to conventional approaches used for total blood flow measurement, which may not benefit from increased imaging speeds.

### 3.5 Conclusion

These results demonstrate the ability of en face Doppler OCT to characterize the pulsatile total arterial blood flow in small animals as well as humans. The advantages of en face Doppler include: (1) no hardware modification in OCT hardware is required, so that both structural and functional blood flow imaging can be performed with a single device, (2) knowledge of Doppler angle is not required for flow calculation, resulting in improved accuracy and robustness, (3)

high speed enables detection of velocities of up to 75mm/s and rapid volume acquisition rates necessary to characterize pulsatility, (4) alignment can be easy and simple due to real-time Doppler C-scan preview, (5) measurements can be entirely automatic without requiring user input, and (6) repeated rapid volume acquisition is inherently less sensitive to involuntary eye motion. This method promises to be useful for investigation of small animal models of ocular diseases and can be extended to clinical pulsatile total retinal blood flow measurement in patients.

## References


1. Flammer J, Orgul S, Costa VP, Orzalesi N, Krieglstein GK, Serra LM, Renard JP, Stefansson E. The impact of ocular blood flow in glaucoma. Prog Retin Eye Res. 2002;21(4):359-93. doi: 10.1016/s1350-9462(02)00008-3. PubMed PMID: 12150988.

2. Weinreb RN, Harris A. Consensus Series - 6: ocular blood flow in glaucoma. Amsterdam, The Netherlands: Kugler Publications; 2009. xvi, 159 page p.

3. Harris A, Chung HS, Ciulla TA, Kagemann L. Progress in measurement of ocular blood flow and relevance to our understanding of glaucoma and age-related macular degeneration. Prog Retin Eye Res. 1999;18(5):669-87. PubMed PMID: WOS:000081300300003.

4. Friedman E. A hemodynamic model of the pathogenesis of age-related macular degeneration. Am J Ophthalmol. 1997;124(5):677-82. PubMed PMID: WOS:A1997YD86800008.

5. Schmetterer L, Wolzt M. Ocular blood flow and associated functional deviations in diabetic retinopathy. Diabetologia. 1999;42(4):387-405. doi: 10.1007/s001250051171. PubMed PMID: WOS:000079427100001.

6. Patel V, Rassam S, Newsom R, Wiek J, Kohner E. Retinal Blood-Flow in Diabetic-Retinopathy. Br Med J. 1992;305(6855):678-83. PubMed PMID: 1393111 PubMed Central PMCID: PMC1882919.

7. Wang YM, Bower BA, Izatt JA, Tan O, Huang D. In vivo total retinal blood flow measurement by Fourier domain Doppler optical coherence tomography. J Biomed Opt. 2007;12(4). doi: Artn 041215 Doi 10.1117/1.2772871. PubMed PMID: 17867804.

8. Leitgeb RA, Schmetterer L, Drexler W, Fercher AF, Zawadzki RJ, Bajraszewski T. Real-time assessment of retinal blood flow with ultrafast acquisition by color Doppler Fourier domain optical coherence tomography. Optics Express. 2003;11(23):3116-21. PubMed PMID: 19471434.

9. Drexler W, Fujimoto JG. Optical Coherence Tomography: Technology and Applications Berlin: Springer-Verlag Berlin; 2008.

10. White BR, Pierce MC, Nassif N, Cense B, Park BH, Tearney GJ, Bouma BE, Chen TC, de Boer JF. In vivo dynamic human retinal blood flow imaging using ultra-high-speed spectral domain optical Doppler tomography. Optics Express. 2003;11(25):3490-7. PubMed PMID: 19471483.

11. Leitgeb RA, Schmetterer L, Hitzenberger CK, Fercher AF, Berisha F, Wojtkowski M, Bajraszewski T. Real-time measurement of in vitro flow by Fourier-domain color Doppler optical coherence tomography. Opt Lett. 2004;29(2):171-3. doi: Doi 10.1364/Ol.29.000171. PubMed PMID: ISI:000187880100011.

12. Wehbe H, Ruggeri M, Jiao S, Gregori G, Puliafito CA, Zhao W. Automatic retinal blood flow calculation using spectral domain optical coherence tomography. Optics Express. 2007;15(23):15193-206. PubMed PMID: ISI:000251223600029.

13. Makita S, Fabritius T, Yasuno Y. Quantitative retinal-blood flow measurement with three-dimensional vessel geometry determination using ultrahigh-resolution Doppler optical coherence angiography. Opt Lett. 2008;33(8):836-8. PubMed PMID: WOS:000255769100026.

14. Tao YK, Kennedy KM, Izatt JA. Velocity-resolved 3D retinal microvessel imaging using single-pass flow imaging spectral domain optical coherence tomography. Optics Express. 2009;17(5):4177-88. PubMed PMID: WOS:000264090900117.

15. Wang Y, Lu A, Gil-Flamer J, Tan O, Izatt JA, Huang D. Measurement of total blood flow in the normal human retina using Doppler Fourier-domain optical coherence tomography. Brit J Ophthalmol. 2009;93(5):634-7. doi: 10.1136/bjo.2008.150276. PubMed PMID: WOS:000265530100017.

16. Werkmeister RM, Dragostinoff N, Pircher M, Gotzinger E, Hitzenberger CK, Leitgeb RA, Schmetterer L. Bidirectional Doppler Fourier-domain optical coherence tomography for measurement of absolute flow velocities in human retinal vessels. Opt Lett. 2008;33(24):2967-9. PubMed PMID: WOS:000262609000029.

17. Zhi Z, Cepurna W, Johnson E, Shen T, Morrison J, Wang RK. Volumetric and quantitative imaging of retinal blood flow in rats with optical microangiography. Biomedical Optics Express. 2011;2(3):12. PubMed PMID: 21412463; PubMed Central PMCID: PMC3047363.

18. Singh ASG, Kolbitsch C, Schmoll T, Leitgeb RA. Stable absolute flow estimation with Doppler OCT based on virtual circumpapillary scans. Biomedical optics express. 2010;1(4):1047-59. PubMed PMID: ISI:000208209300001.

19. Wang YM, Fawzi AA, Varma R, Sadun AA, Zhang XB, Tan O, Izatt JA, Huang D. Pilot Study of Optical Coherence Tomography Measurement of Retinal Blood Flow in Retinal and Optic Nerve Diseases. Investigative Ophthalmology & Visual Science. 2011;52(2):840-5. doi: Doi 10.1167/Iovs.10-5985. PubMed PMID: 21051715; PubMed Central PMCID: PMC3053109.

20. Srinivasan VJ, Sakadzic S, Gorczynska I, Ruvinskaya S, Wu WC, Fujimoto JG, Boas DA. Quantitative cerebral blood flow with Optical Coherence Tomography. Optics Express. 2010;18(3):2477-94. PubMed PMID: 20174075; PubMed Central PMCID: PMC2837842.

21. Jenkins MW, Peterson L, Gu S, Gargesha M, Wilson DL, Watanabe M, Rollins AM. Measuring hemodynamics in the developing heart tube with four-dimensional gated Doppler optical coherence tomography. J Biomed Opt. 2010;15(6). doi: Artn 066022
Doi 10.1117/1.3509382. PubMed PMID: ISI:000287171100054.

22. Baumann B, Potsaid B, Kraus MF, Liu JJ, Huang D, Hornegger J, Cable AE, Duker JS, Fujimoto JG. Total retinal blood flow measurement with ultrahigh speed swept source/Fourier domain OCT. Biomed Opt Express. 2011;2(6):1539-52. PubMed PMID: 21698017; PubMed Central PMCID: PMC3114222.

23. Hendargo HC, McNabb RP, Dhalla A-H, Shepherd N, Izatt JA. Doppler velocity detection limitations in spectrometer-based versus swept-source optical coherence tomography. Biomedical optics express. 2011;2(8):2175-88. PubMed PMID: MEDLINE:21833356.

24. Vakoc BJ, Yun SH, de Boer JF, Tearney GJ, Bouma BE. Phase-resolved optical frequency domain imaging. Optics Express. 2005;13(14):5483-93. PubMed PMID: ISI:000230519100035.

25. Rao B, Yu LF, Chiang HK, Zacharias LC, Kurtz RM, Kuppermann BD, Chen ZP. Imaging pulsatile retinal blood flow in human eye. J Biomed Opt. 2008;13(4). doi: Artn 040505 Doi 10.1117/1.2967986. PubMed PMID: ISI:000259901000004.

26. Makita S, Fabritius T, Yasuno Y. Full-range, high-speed, high-resolution 1-mu m spectral-domain optical coherence tomography using BM-scan for volumetric imaging of the human posterior eye. Optics Express. 2008;16(12):8406-20. PubMed PMID: WOS:000256859900009.

27. Oppenheim AV, Schafer RW. Discrete-time signal processing: Prentice Hall; 2010.

28. Enfield J, Jonathan E, Leahy M. In vivo imaging of the microcirculation of the volar forearm using correlation mapping optical coherence tomography (cmOCT). Biomedical optics express. 2011;2(5):1184-93. doi: 10.1364/boe.2.001184.

# Chapter 4

# Phase-sensitive swept source OCT imaging of the human retina with a VCSEL light source

## 4.1 Overview

In Chapter 3, pulsatile total retinal blood flow measurement in a human subject was demonstrated. However, due to the limitation in OCT imaging range and relatively low detection efficiency, spectral domain OCT is not ideal for performing high speed Doppler OCT measurements of total retinal blood flow in human subjects. Despite the challenges in achieving high phase stability, Doppler swept source / Fourier domain OCT has advantages of less fringe washout and faster imaging speeds compared to spectral / Fourier domain detection. This chapter demonstrates swept source OCT with a vertical cavity surface emitting laser (VCSEL) light source at 400kHz sweep rate for phase-sensitive Doppler OCT imaging, measuring pulsatile total retinal blood flow with high sensitivity and phase stability. A robust, simple, and computationally efficient phase stabilization approach for phase-sensitive swept source imaging is also presented. Dr. Benjamin Potsaid was instrumental in developing the optically clocked swept source OCT system using a VCSEL light source. Dr. Vijaysekhar Jayaraman developed the VCSEL swept light source technology used in this study. Dr. Bernhard Baumann contributed significantly in developing the method to phase stabilize the swept source OCT system. Dr. Ireneusz Grulkowski and Jonathan J. Liu developed the initial version of the OCT system together with Dr. Benjamin Potsaid. Chen D. Lu contributed in developing the OCT system.

Alex E. Cable, Dr. David Huang, Dr. Jay S. Duker, and Dr. James G. Fujimoto provided supervision and guidance.

## 4.2 Introduction

Optical coherence tomography (OCT) is gaining increased acceptance as a tool for functional imaging of retinal blood flow using Doppler and phase variance techniques. In Fourier domain OCT, the axial velocity components of moving particles, such as red blood cells, can be extracted from spectral interference phase information[1]. However, phase-sensitive OCT imaging requires high phase stability in the system. For spectral / Fourier domain OCT, phase stability sufficient for Doppler imaging can be easily achieved using a mechanically stable spectrometer and reference arm. However, swept source / Fourier domain OCT suffers from sampling and A-scan trigger jitter, which makes phase-sensitive measurement more challenging. Several different approaches have been proposed to perform phase-sensitive Doppler imaging with swept source OCT. Vakoc et al. and Baumann et al. used an external phase reference to numerically subtract the phase ramp artifact induced by A-scan trigger and sampling fluctuations[2, 3]. However, this approach requires careful adjustment of the reference signal level to avoid autocorrelation noise, while at the same time the phase reference should dominate the signal from the sample. It is also possible to digitize Mach-Zehnder traces simultaneously with OCT interferometric fringes to stabilize the phase, but this requires two A/D channels and increased processing[4].

Despite the challenges in achieving high phase stability, swept source OCT Doppler imaging has many advantages. Swept source OCT is less prone to fringe washout effects than spectral domain OCT[5]. In addition, the ultrahigh speeds provided by Fourier domain detection can enable a simpler and more robust algorithm for total retinal blood flow measurements using en face flow measurement methods[3, 6]. Previous studies with spectral domain OCT showed that retinal

blood flow pulsatility can be resolved by repeatedly scanning the central retinal artery at a high volume acquisition rate, reducing measurement variability[7]. It is difficult to achieve acquisition speeds greater than 300kHz for human retinal imaging using spectral domain OCT[8]. Swept source OCT uses high quantum efficiency photodiodes, avoids spectrometer losses and enables dual balanced detection to increase dynamic range and cancel excess noise. Therefore, if light source relative intensity noise is not excessive, it can achieve higher imaging speeds at equal signal-to-noise ratio than spectral domain OCT.

In this chapter, we demonstrate swept source OCT with a vertical cavity surface emitting laser (VCSEL) light source at a sweep rate of 400kHz for performing phase-sensitive Doppler imaging and measuring pulsatile total retinal blood flow with high system sensitivity and phase stability. A robust, simple, and computationally efficient approach for phase stabilization necessary for phase-sensitive swept source imaging is also presented.

### 4.3 Methodology

The human study protocol was approved by the institutional review board at MIT. Measurements were performed with an ultrahigh speed, swept source OCT system using a VCSEL swept light source[9, 10] centered at 1080nm with an A-scan rate of 400kHz as shown in Figure 4.1(A). The total imaging range was 1.72mm with an axial resolution of 14.8μm in tissue after numerical Kaiser-window spectral shaping. Because of the limited sampling rate of the A/D card (Innovative Integration, X5-400M) used in this experiment, in order to achieve a sufficient imaging range for human retinal imaging, the laser sweep range had to be limited to ~50nm, which in turn limited the axial resolution. However, the maximum sweep range of the VCSEL was >90nm. The VCSEL was swept at 400kHz repetition rate, close to the resonant frequency of the MEMS scanner in the VCSEL, and data was acquired with a unidirectional frequency sweep,

resulting in a 400kHz A-scan rate with a duty cycle of ~50%. The backward sweep of the VCSEL was suppressed by synchronously modulating the semiconductor optical amplifier. The OCT beam power at the cornea was 1.9mW and the system sensitivity measured with a calibrated neutral density filter in the patient interface was 97.1dB (ratio of peak to standard deviation of noise). At 400kHz A-scan rate, the axial velocity range measurable with Doppler OCT without phase wrapping was ±80.0mm/s in tissue, which is sufficient for measuring the velocity of blood in the central retinal arteries. The 3dB sensitivity roll-off range was 1.26mm in tissue, which was limited by the 200MHz bandwidth balanced detector (Thorlabs, PDB460C) and 400MHz A/D card rather than the coherence length of the VCSEL light source. VCSELs have very long coherence lengths and OCT imaging depths of 5 cm were recently reported[10].

In order to achieve high phase stability Doppler OCT imaging, the A/D card was externally clocked using a Mach-Zehnder interferometer (MZI) as shown in Figures 4.1(A) and (B). Because the VCSEL has a long coherence length, the MZI could be set to twice the OCT imaging range and achieve Nyquist sampling without the need to electronically frequency double the optical clock signal. The A/D card was slightly overclocked with a maximum optical clock frequency at ~500MHz. Optical clocking can significantly reduce wavenumber calibration errors compared to fixed rate internal clocking. The A-scan trigger signals were generated by the arbitrary waveform generator that actuated the MEMS VCSEL.

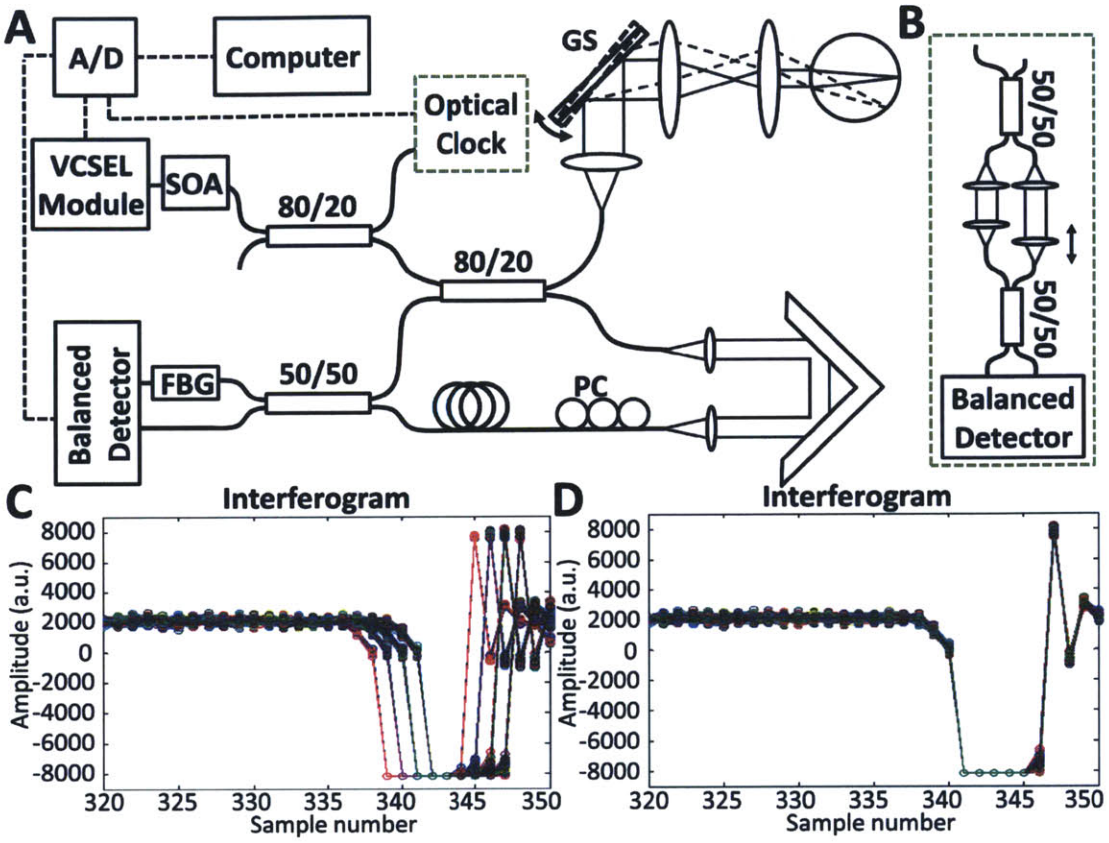


**Figure 4.1.** (A) A schematic of swept source OCT system. (B) A Mach-Zehnder interferometer is used for optical clocking. SOA: semiconductor optical amplifier, PC: polarization controller, FBG: fiber Bragg grating. (C, D) Fiber Bragg grating traces in the OCT interferogram before and after numerical trigger jitter correction.

A-scan trigger fluctuations were numerically compensated using a fixed wavenumber reference signal from a fiber Bragg grating (FBG, OE Land, $\lambda_0$=1057.6nm, Reflectivity=99.9%, $\Delta\lambda$=0.376nm) in transmission mode in one of the balanced detection arms, as shown in Figure 4.1(A). It is important to match the optical path lengths in the arms in order to avoid a relative time delay between the two channels of the balanced detector. Because the FBG transmits all wavelengths except its design wavelengths, which are reflected, it can create a wavenumber

reference signal in the balanced detection output. An insertion loss of less than 10% was measured for the FBG and the loss is expected to be even lower if the fibers were spliced rather than connected using an FC/APC connector. The trigger fluctuation in the OCT interferograms can be numerically compensated during post-processing by shifting the individual interferogram by an integer number of samples as shown in Figures 4.1(C) and (D). This is possible because both the optical clock and the FBG signal are generated at fixed wavenumbers, and therefore any A-line trigger fluctuation can only result in an integer number sample shift. This operation is computationally efficient because the number of samples to be shifted can be determined simply by using a threshold on a small number of samples around the FBG signal as shown in Figures 4.1(C) and (D).

It is important to choose the correct FBG in order to avoid ambiguity of the FBG signal position caused by the overlapping OCT interferometric signal. The FBG FWHM bandwidth should be chosen narrow enough so the slope of the rising (or falling) edge is as fast as possible relative to the A/D sampling frequency, while at the same time the bandwidth should be wide enough so the grating signal can be reliably sampled. This can be realized by choosing an FBG reflectivity of up to ~99%, and allowing the balanced detector circuit to transiently saturate, which does not interfere with the OCT signal if the FBG signal is at the end of the frequency sweep. The system phase stability, defined as the standard deviation of the phase differences between sequential A-scans, measured from a mirror in the patient interface at a signal-to-noise ratio of 53dB 57.5dB (ratio of peak to mean noise) and a depth of 0.3mm was 1.5mrad, which approaches the theoretical limit[11]. The effect of numerical trigger fluctuation compensation on OCT intensity and Doppler images can be seen in Figures 4.2(A-D). This allows the suppression of fixed-pattern noise after background subtraction and removes Doppler line artifacts caused by

phase errors from trigger fluctuations, as demonstrated previously using different approaches[3, 4]. The standard deviation of the phase differences in retinal tissue near the optic nerve head calculated from a B-scan with 3000 A-scans over 3mm range, was 0.32 radians. Figure 4.2(E) shows a typical B-scan with 500 A-scans over a 12mm range on the retina with phase stabilization.

It should be noted that it is possible to use signals from an external fiber Bragg grating to directly trigger the A/D card[12]. However, this method does not always solve the trigger fluctuation problem completely, due to trigger jitter which occurs in many commercial A/D cards. In a different experiment, we observed relative sample shifts between two interferometric signals simultaneously acquired by the two channels of a single A/D card clocked and triggered by a single light source, which is problematic for applications such as polarization-sensitive OCT. However, the approach used here can solve both of these synchronization problems.

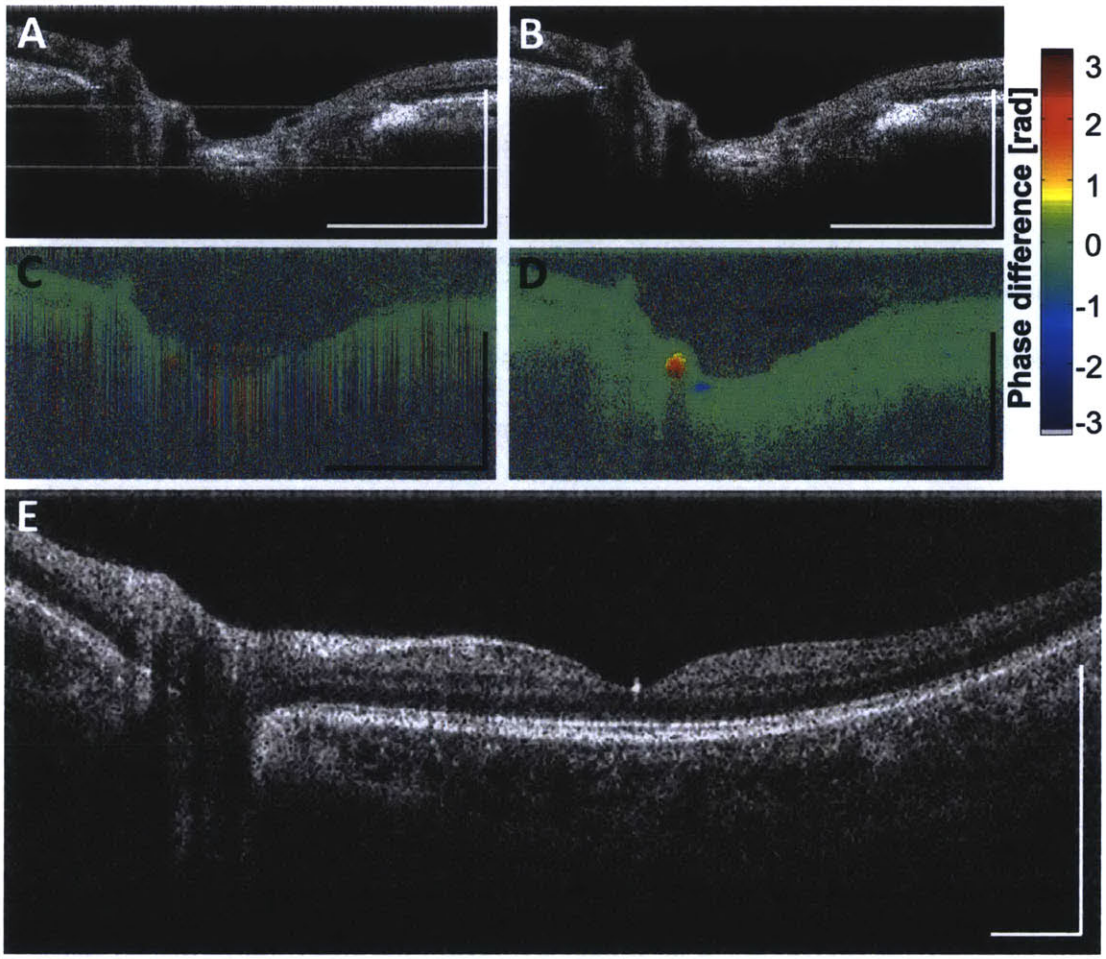


**Figure 4.2.** (A, B) OCT images of optic nerve head before and after the numerical trigger jitter correction. 3000 A-scans over 3mm. (C, D) OCT Doppler images of the optic nerve head before and after the numerical trigger jitter correction. 3000 A-scans over 3mm. (E) A typical OCT B-scan consisting of 500 A-scans over 12mm. All scale bars: 1mm.

### 4.4 Results and discussion

Using the phase-stabilized swept source / Fourier domain OCT system described above, it is possible to perform en face Doppler blood flow measurement in the human retina[3, 6, 7]. The ultrahigh speed enabled a 1.5mm×1.5mm scan area for repeated volume acquisition with 60 B-scans consisting of 750 A-scans each. The estimated spot size on the retina was 20μm and the

2um A-scan spacing had sufficient oversampling necessary for Doppler processing. The 1.5mm×1.5mm scan area is almost 4 times larger than that used in previous measurements performed with a slower 244kHz spectral OCT system[7], without sacrificing volume acquisition rate. The large scan area makes measurements more robust to involuntary transverse eye motion. The 750×60 A-scans per volume were acquired at a volume acquisition rate of 7.6Hz with a galvanometer scanner duty cycle of 85%. An example of time-resolved pulsatile total arterial blood flow measured from a healthy normal subject is shown in Figure 4.3(A). Total retinal arterial blood flow waveforms repeatable over multiple cardiac cycles can be clearly observed. Although the total acquisition time of 6 seconds was chosen for this measurement, it is possible to reduce the acquisition time to ~2 seconds, which is consistent with times used clinically and is sufficient to capture at least one complete cardiac cycle. Figure 4.3(B) shows an en face projection image of one OCT volume used for the measurement. Figures 4.3(C-F) show en face Doppler images at different time points as indicated by the black arrows in Figure 4.3(A). Pulsatile changes in the velocity profile can be clearly seen in the en face planes. The mean total retinal arterial blood flow calculated over the first five cardiac cycles was ~46.5μl/min. Total blood flow measurements could be performed automatically due to the simplicity and robustness of the algorithm.

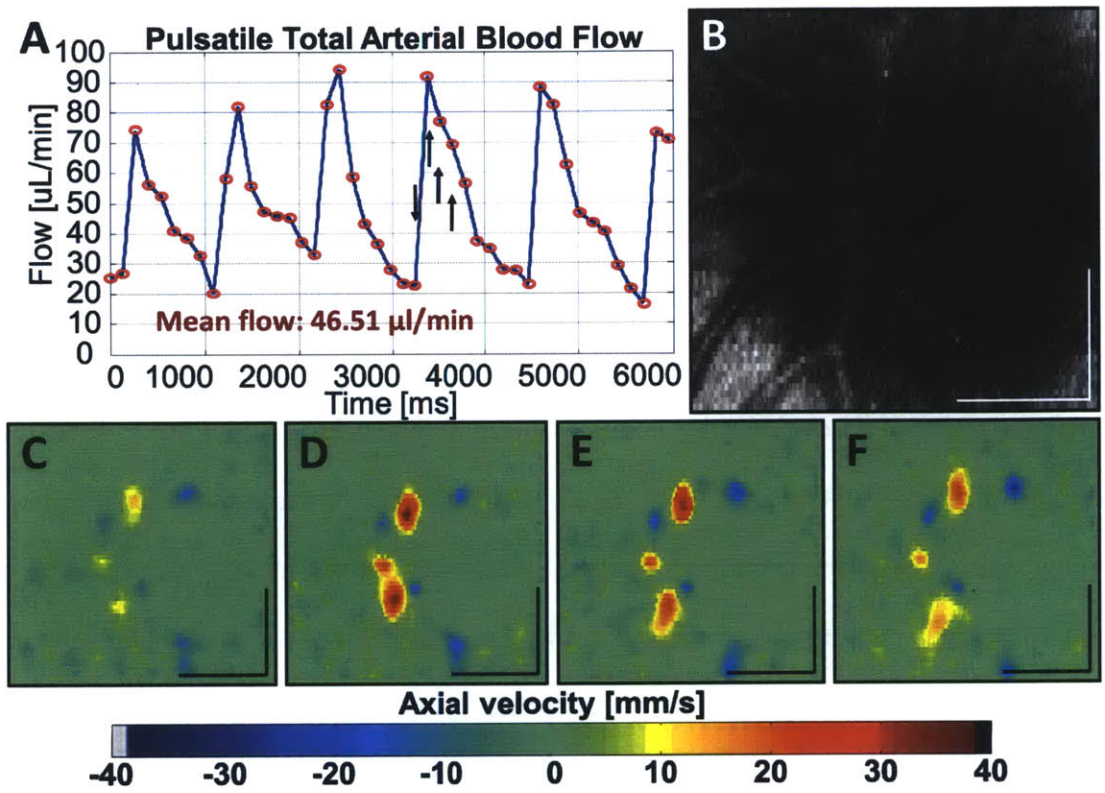


**Figure 4.3.** (A) Time-resolved pulsatile total arterial blood flow. (B) An en face intensity projection image. 1.5mm × 1.5mm. (C-F) En face Doppler images at different time points indicated by the black arrows in (A). 1.5mm × 1.5mm. All scale bars: 500µm.

### 4.5 Conclusion

These results demonstrate the potential of ultrahigh-speed swept source / Fourier domain OCT using a VCSEL light source for phase-sensitive imaging applications, such as Doppler imaging of the human retina for blood flow measurements.

## References


1. Leitgeb RA, Schmetterer L, Drexler W, Fercher AF, Zawadzki RJ, Bajraszewski T. Real-time assessment of retinal blood flow with ultrafast acquisition by color Doppler Fourier domain optical coherence tomography. Optics Express. 2003;11(23):3116-21. PubMed PMID: 19471434.

2. Vakoc BJ, Yun SH, de Boer JF, Tearney GJ, Bouma BE. Phase-resolved optical frequency domain imaging. Optics Express. 2005;13(14):5483-93. PubMed PMID: ISI:000230519100035.

3. Baumann B, Potsaid B, Kraus MF, Liu JJ, Huang D, Hornegger J, Cable AE, Duker JS, Fujimoto JG. Total retinal blood flow measurement with ultrahigh speed swept source/Fourier domain OCT. Biomed Opt Express. 2011;2(6):1539-52. PubMed PMID: 21698017; PubMed Central PMCID: PMC3114222.

4. Braaf B, Vermeer KA, Sicam VADP, van Zeeburg E, van Meurs JC, de Boer JF. Phase-stabilized optical frequency domain imaging at 1-mu m for the measurement of blood flow in the human choroid. Optics Express. 2011;19(21):20886-903. PubMed PMID: ISI:000296065700111.

5. Yun SH, Tearney GJ, de Boer JF, Bouma BE. Motion artifacts in optical coherence tomography with frequency-domain ranging. Optics Express. 2004;12(13):2977-98. PubMed PMID: ISI:000222321200023.

6. Srinivasan VJ, Sakadzic S, Gorczynska I, Ruvinskaya S, Wu WC, Fujimoto JG, Boas DA. Quantitative cerebral blood flow with Optical Coherence Tomography. Optics Express. 2010;18(3):2477-94. PubMed PMID: 20174075; PubMed Central PMCID: PMC2837842.

7. Choi W, Baumann B, Liu JJ, Clermont AC, Feener EP, Duker JS, Fujimoto JG. Measurement of pulsatile total blood flow in the human and rat retina with ultrahigh speed spectral/Fourier domain OCT. Biomedical Optics Express. 2012;3(5):1047-61. PubMed PMID: 22567595; PubMed Central PMCID: PMC3342181.

8. Potsaid B, Gorczynska I, Srinivasan VJ, Chen YL, Jiang J, Cable A, Fujimoto JG. Ultrahigh speed Spectral/Fourier domain OCT ophthalmic imaging at 70,000 to 312,500 axial scans per second. Optics Express. 2008;16(19):15149-69. PubMed PMID: 18795054; PubMed Central PMCID: PMC2743204.

9. Jayaraman V, Cole GD, Robertson M, Uddin A, Cable A. High-sweep-rate 1310 nm MEMS-VCSEL with 150 nm continuous tuning range. Electron Lett. 2012;48(14):867-9. doi: 10.1049/el.2012.1552.

10. Grulkowski I, Liu JJ, Potsaid B, Jayaraman V, Lu CD, Jiang J, Cable AE, Duker JS, Fujimoto JG. Retinal, anterior segment and full eye imaging using ultrahigh speed swept source OCT with vertical-

cavity surface emitting lasers. Biomedical optics express. 2012;3(11):2733-51. PubMed PMID: 23162712; PubMed Central PMCID: PMC3493240.

11. Park B, Pierce MC, Cense B, Yun S-H, Mujat M, Tearney G, Bouma B, de Boer J. Real-time fiber-based multi-functional spectral-domain optical coherence tomography at 1.3 μm. Optics Express. 2005;13(11):3931-44. doi: 10.1364/opex.13.003931.

12. Hendargo HC, McNabb RP, Dhalla A-H, Shepherd N, Izatt JA. Doppler velocity detection limitations in spectrometer-based versus swept-source optical coherence tomography. Biomedical optics express. 2011;2(8):2175-88. PubMed PMID: MEDLINE:21833356.

# Chapter 5

# Choriocapillaris and choroidal microvasculature imaging with ultrahigh speed OCT angiography

## 5.1 Overview

This chapter demonstrates in vivo choriocapillaris and choroidal microvasculature imaging in normal human subjects using optical coherence tomography (OCT). An ultrahigh speed swept source OCT prototype at 1060nm wavelengths with a 400kHz A-scan rate is developed for three-dimensional ultrahigh speed imaging of the posterior eye. OCT angiography is used to image three-dimensional vascular structure without the need for exogenous fluorophores by detecting erythrocyte motion contrast between OCT intensity cross-sectional images acquired rapidly and repeatedly from the same location on the retina. En face OCT angiograms of the choriocapillaris and choroidal vasculature are visualized by acquiring cross-sectional OCT angiograms volumetrically via raster scanning and segmenting the three-dimensional angiographic data at multiple depths below the retinal pigment epithelium (RPE). Fine microvasculature of the choriocapillaris, as well as tightly packed networks of feeding arterioles and draining venules, can be visualized at different en face depths. Panoramic ultra-wide field stitched OCT angiograms of the choriocapillaris spanning ~32mm on the retina show distinct vascular structures at different fundus locations. Isolated smaller fields at the central fovea and ~6mm nasal to the fovea at the depths of the choriocapillaris and Sattler's layer show vasculature structures consistent with established architectural morphology from histological and electron micrograph corrosion casting studies. Choriocapillaris imaging was performed in eight healthy

volunteers with OCT angiograms successfully acquired from all subjects. These results demonstrate the feasibility of ultrahigh speed OCT for in vivo dye-free choriocapillaris and choroidal vasculature imaging, in addition to conventional structural imaging. Kathrin J. Mohler contributed significantly in image acquisition and data analysis for this study. Dr. Benjamin Potsaid, Chen D. Lu, Jonathan J. Liu contributed in developing the ultrahigh speed OCT system. Dr. Vijaysekhar Jayaraman developed the vertical cavity surface emitting laser (VCSEL) light source used for this study. Alex E. Cable, Dr. Jay S. Duker, Dr. Robert Huber, and Prof. James G. Fujimoto provided supervision and guidance.

## 5.2 Introduction

While retinal vasculature supplies oxygen and nutrients to the inner retinal layers, choroidal vasculature is responsible for nourishing the outer retinal layers. Choroidal circulation, the largest source of the blood supply to the posterior eye, is also responsible for transporting metabolic waste from the retinal pigment epithelium (RPE), and hence it plays a key role in normal retinal function[1]. Choroidal circulation is known to be associated with retinal diseases such as age-related macular degeneration (AMD) and diabetic retinopathy (DR)[2, 3], which are major causes of vision loss or impairment. Therefore, visualization of the microvasculature and blood flow in the choriocapillaris, the capillary layer of the choroid, is of great interest.

Imaging the choriocapillaris in vivo is challenging because of highly pigmented choroidal melanocytes and its location below the RPE. Furthermore, unlike retinal blood vessels, capillaries in the choriocapillaris are fenestrated[4], which makes high resolution choriocapillaris imaging with fluorescein and indocyanine green (ICG) angiography more challenging due to dye leakage. As a result, most studies of the choriocapillaris have been limited to postmortem histology or indirect observations such as dye perfusion pattern or time measurement.

Multiple histological studies have investigated the interrelation between photoreceptors, RPE, Bruch's membrane, and choriocapillaris in AMD. By analyzing donor eyes with geographic atrophy (GA), Sarks et al. found that RPE loss is associated with atrophy of the choriocapillaris and choroid [5]. A smaller study by McLeod et al. suggested a linear relationship between the loss of RPE and choriocapillaris in non-exudative AMD patients with GA[6]. A later study by Mullins et al. reported that choriocapillaris density decreases in association with sub-RPE deposit formation[7]. These and other histological studies suggest that choriocapillaris atrophy is associated with RPE atrophy. Although alterations in the choriocapillaris are expected to be secondary to changes in the RPE in non-exudative AMD according to histological studies[5, 8], it is still possible that one of the earliest changes detectable in the retina in vivo could be alterations in choriocapillaris circulation and/or structure. Furthermore, a number of studies report that the location of drusen formation is associated with the underlying choriocapillaris and choroidal vessel structure, thus suggesting that drusen are more likely to form where choroidal perfusion is insufficient[2, 9-11]. In addition, in exudative AMD, changes in the choriocapillaris may occur before changes in the RPE, and could be the primary cause of sub-retinal neovascularization[6]. A number of histological and electron micrograph corrosion casting studies also show choriocapillaris degeneration associated with diabetes[3, 12-15]. Therefore, the ability to image choriocapillaris and larger choroidal vessels in vivo may be useful for the better understanding of pathophysiology, early diagnosis, treatment response monitoring, and pharmaceutical development.

Optical coherence tomography (OCT) can provide depth-resolved information on the posterior eye and is gaining acceptance as a tool for in vivo choroidal imaging. However, the majority of studies on the choroid using OCT have focused on choroidal thickness measurements

or imaging larger choroidal vessels, and to date, only a few studies have demonstrated choriocapillaris imaging consistent with histological and electron micrograph corrosion casts findings, in terms of capillary density. Using OCT phase information, Kurokawa et al. demonstrated choriocapillaris imaging in normal subjects with adaptive optics OCT near the fovea over a very limited field of view, due to limited imaging speed and constraints imposed by adaptive optics[16]. Using OCT phase variance and hardware eye tracking with a second scanning laser ophthalmoscope channel in an OCT system, Braaf et al. demonstrated OCT choriocapillaris angiography of the central fovea from a single normal subject, although the acquisition time per volume was relatively long compared to clinical standards, and multiple volumes were used for averaging[17]. In general, choriocapillaris imaging in vivo using OCT is a relatively unexplored area, and it requires extensive further investigation to relate it to known histological findings in normal and pathological eyes.

In the present study, we investigate in vivo choriocapillaris imaging using ultrahigh speed, speckle variance (decorrelation) OCT angiography. We image different fundus locations and depths to compare results with known histological and electron micrograph corrosion casting studies. OCT angiography enables the investigation of choriocapillaris vascular structure in vivo. Combined with conventional depth-resolved structural imaging capabilities of OCT, OCT angiography promises to be a powerful tool to visualize and investigate the outer retinal layers and choriocapillaris comprehensively in retinal diseases.

## 5.3 Materials and Methods

### *5.3.1 Study Population*

The human study protocol was approved by the Committee on the Use of Humans as Experimental Subjects at the Massachusetts Institute of Technology (MIT) and was in

accordance with the Declaration of Helsinki. Written informed consent forms were obtained from all subjects after explaining the study. Eight normal volunteers (mean age 33.0 ± 11.1 years, range 24 to 54 years) without any known history of retinal diseases participated in the study. All imaging was performed at MIT.

*5.3.2 Ultrahigh Speed Swept Source OCT System*

The ultrahigh speed swept source OCT (SSOCT) prototype used in this experiment is similar to one recently developed by our group[18]. Therefore, only key characteristics or differences in the system are described here. The prototype SSOCT instrument uses a vertical cavity surface emitting laser (VCSEL) swept light source, which generates 400,000 unidirectional wavelength sweeps per second, resulting in an ultrahigh speed OCT A-scan rate of 400kHz. The wavelength tuning range was ~80nm centered at ~1060nm, which provides a 9.6μm full width at half maximum (FWHM) axial resolution in tissue. OCT signals are acquired with an analog-to-digital acquisition card (Alazar Technologies, ATS9360), which is externally clocked at uniform wavenumber intervals using a Mach-Zehnder interferometer output. The maximum clock frequency generated by the interferometer is set at 1.2GHz, resulting in a total imaging range of ~2.44mm in tissue, which is sufficient for posterior eye imaging. The incident optical power at the cornea is ~1.85mW and the system sensitivity measured with a calibrated neutral density filter is ~98.2dB. The measured 3dB sensitivity roll-off (~70% in linear scale) range is >2mm. Low sensitivity roll-off combined with deeper light penetration at 1060nm wavelength, when compared to standard 850nm, is important for deep choroidal imaging. Although OCT phase information was not used in this study, the system was still phase-stabilized by using a fiber Bragg grating to remove undesired fixed pattern noise[18]. The incident beam size on the cornea was ~1mm FWHM, thus yielding an estimated ~10μm FWHM spot size on the retina,

corresponding to a ~24μm Airy disk diameter. However, diffraction from aberrations in the eye is expected to yield a larger spot size.

*5.3.3 Data Acquisition*

Ultrahigh speed SSOCT imaging was performed in one eye of each subject. Imaging was performed with room lights off, without pupil dilation. Two different fundus locations were imaged in all subjects, the central fovea and ~6mm temporal to the fovea. An internal fixation target could be used for imaging these two fundus locations. For one subject, multiple fundus locations spanning ±16mm from the central fovea was imaged to obtain a panoramic montage visualization of the choriocapillaris layer. The internal fixation target could not be used for fundus locations outside of ±6.5mm from the central fovea. In those cases, a small light emitting diode (LED) was used as an external fixation target. For each fundus location, two different retinal field sizes were imaged, 1.5mm×1.5mm and 3mm×3mm. For both field sizes, 4 B-scans were acquired from the same position repeatedly, from 400 B-scan positions in order to generate blood flow contrast, thereby resulting in a total of 1600 B-scans per data set. Each B-scan consisted of 800 A-scans. The time interval between sequential B-scans was ~2.4milliseconds. The total acquisition time was ~3.8seconds per volumetric data set. The 1.5mm field size provides higher sampling density, and thus better image quality, while the 3mm field provides larger coverage on the retina.

*5.3.4 Swept Source OCT Data Processing*

Each OCT signal acquisition consisted of 928 samples, which yielded 464 pixels per A-scan in the axial direction after Fourier transformation. The sample spacing was ~5μm per pixel in depth, which was ~2× smaller than the axial resolution of the system.

*5.3.5 Choriocapillaris OCT Angiography*

OCT angiograms that display contrast from blood flow were generated by calculating cross-sectional images of the speckle decorrelation between the 4 B-scans repeatedly acquired from the same position with a 2.4millisecond time interval. If the imaged tissue is locally stationary (in the axial and transverse directions), all 4 B-scans will be locally identical. However blood vessels will have erythrocyte motion. Because the 4 B-scans are acquired at slightly different times, this motion generates a locally fluctuating back-scattered intensity within the blood vessels in the B-scans. This fluctuation in back-scattered intensity is calculated by comparing the 4 B-scans on a pixel-by-pixel basis (Figure 5.1A). We did not correct for bulk-motion due to involuntary patient eye motion, assuming that the erythrocyte travel speeds are much faster than the patient bulk motion. However, it is possible to correct for the effects of axial bulk motion and to suppress spurious decorrelations from transverse motion, if necessary. By performing this operation for all transverse positions, a volumetric OCT angiographic data set can be obtained from the volumetric intensity data set. In this study, we used OCT intensity information to calculate motion contrast. Similar techniques for generating motion contrast images based on OCT intensity and/or phase information have been described by several research groups[19-27].

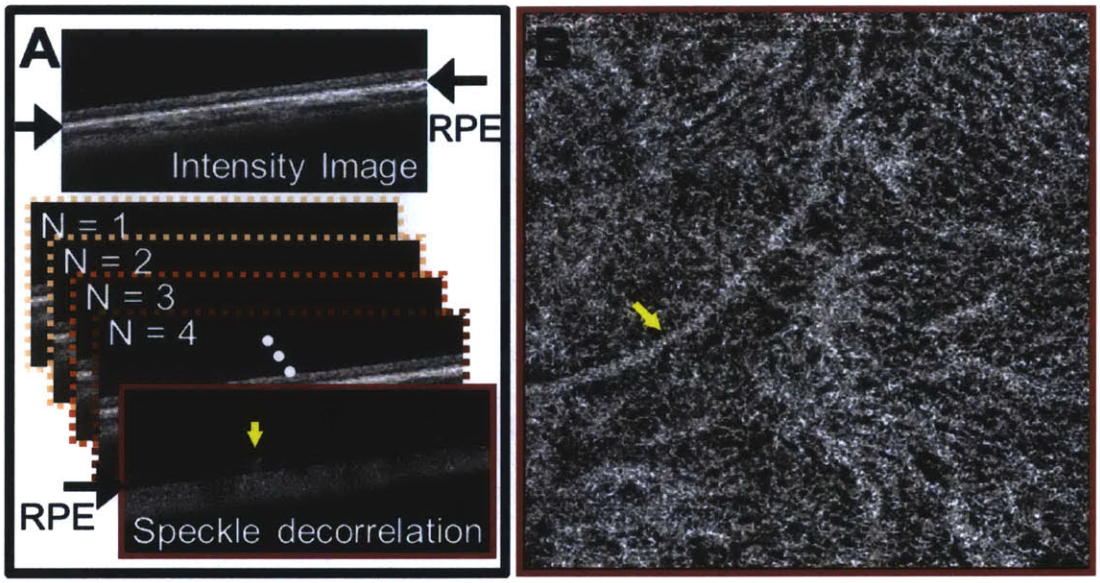


**Figure 5.1.** Generating OCT angiography data from OCT intensity data. (A) Multiple OCT intensity B-scans are acquired from the same location on the retina and compared with each other pixel-by-pixel to detect motion contrast. The resultant OCT cross-sectional angiogram is segmented with respect to the RPE using one of the corresponding intensity images. (B) By performing the steps in (A) volumetrically and displaying the OCT angiography data in an en face plane below the RPE, the choriocapillaris microvasculature can be visualized. Yellow arrows indicate shadowing artifact from thick retinal vessels.

Because the choriocapillaris layer is extremely thin, it is necessary to visualize the three-dimensional angiographic data set in an en face plane in order to resolve choriocapillaris features. The RPE was segmented by using the OCT intensity cross-sectional images in the volumetric data set. Because the angiographic and intensity volumes are from the same data set and are co-registered, the same RPE location can be used to segment the angiographic volume. En face

OCT angiograms of the choriocapillaris at different depths, with respect to the RPE, were generated from the OCT angiographic volume (Figure 5.1B).

### 5.4 Results and Discussion

Figures 5.2A and 5.2B show a panoramic ultra-wide field of view (~32mm) OCT intensity projection image and an OCT angiogram of the choriocapillaris generated by stitching multiple smaller 3mm×3mm fields acquired from a healthy normal subject. The OCT en face angiograms were extracted from a depth immediately below the RPE. Previous histological and electron micrograph corrosion casting studies show that the capillary density and pattern in the choriocapillaris changes depending on the fundus location, with a densely packed honeycomb structure at the central fovea, and a more lobular and less dense structure towards the equator and periphery[13, 28-30]. The wide field in vivo choriocapillaris angiogram in Figure 5.2B demonstrates a spatial variation of the microvasculature consistent with these ex vivo postmortem studies. Figures 5.2C-E are close-up views of OCT angiograms taken from the different regions shown in Figure 5.2B that are used to visualize structural details better.

As seen in the cross-sectional speckle decorrelation angiogram in Figure 5.1A and in the choriocapillaris en face angiogram in Figure 5.1B, large retinal vessels (marked with yellow arrows) tend to cast shadow-like artifacts in the axial direction. Since blood is highly scattering, large retinal blood vessels result in lower signal level below the vessels and more rapidly fluctuating speckle pattern below them, which cause the shadow-like artifacts in the angiographic data. Therefore, it is important to remember that large retinal vessels can produce shadow artifacts in choriocapillaris angiograms and are not part of choroidal vasculature.

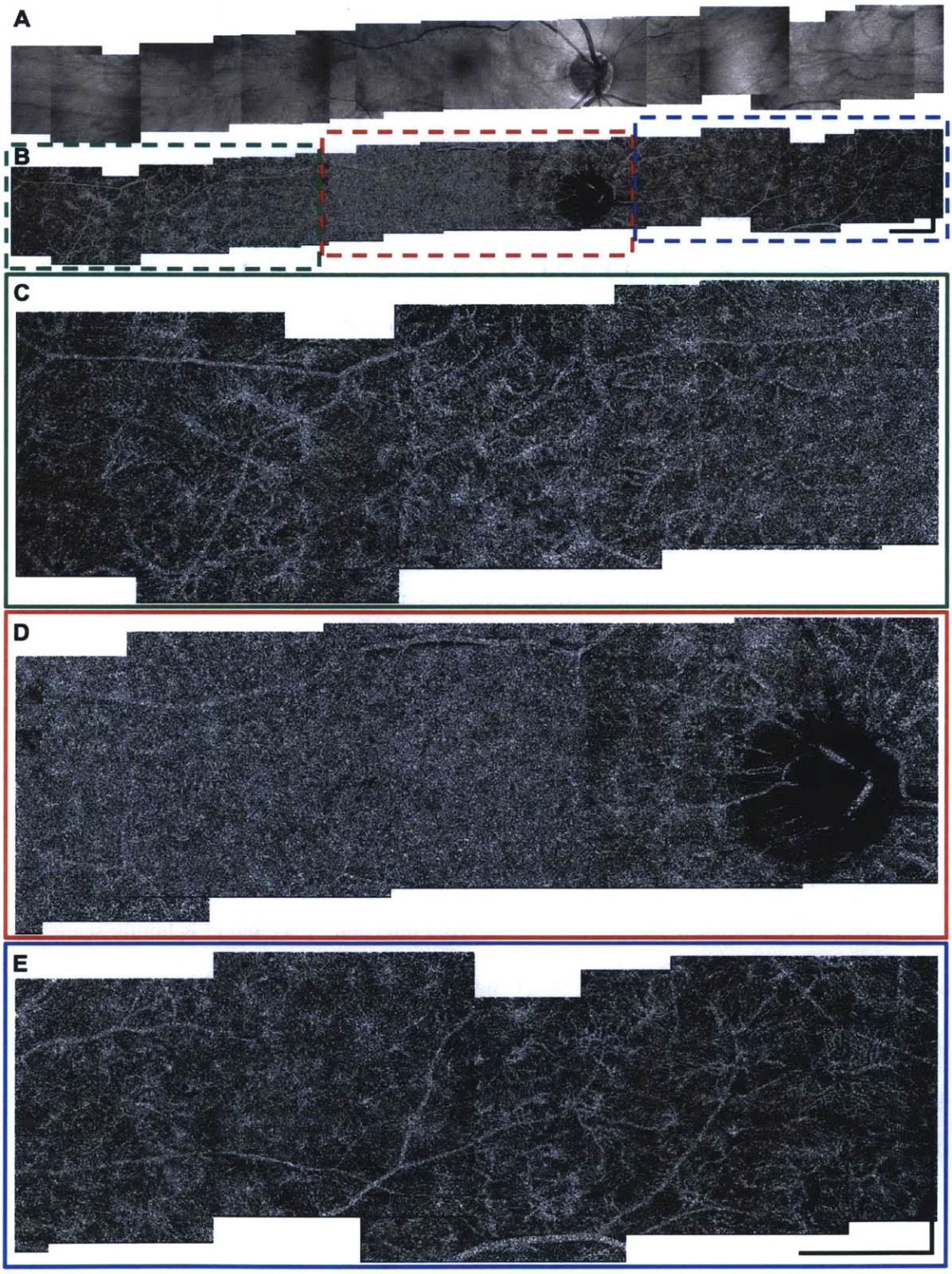
A
B
C
D
E

**Figure 5.2.** Panoramic wide field of view OCT angiogram of the choriocapillaris spanning ~32mm on the retina. (A) Stitched OCT intensity en face projection images. (B) Stitched OCT angiograms of the choriocapillaris. Different microvasculature patterns and densities can be observed at different fundus locations. (C-E) Close-up views of the OCT angiograms of the choriocapillaris in (B) for better visualization. Scale bars: 1.5mm.

Because the choriocapillaris has fine features in the en face plane, high A-scan sampling density and high speed are essential to visualize the microvasculature clearly. The current scan pattern of 800(horizontal)×400(vertical)×4(repeats) A-scans over 3mm×3mm corresponds to a 7.5μm sample spacing in the vertical direction and 3.25μm in the horizontal direction. Since the FWHM spot size on the retina is ~10μm, this corresponds to a moderate oversampling of ~1.33× in the vertical direction and ~2.66× in the horizontal direction, relative to the estimated spot size on the retina. The A-scan rate of the current prototype is 400kHz. Slower speeds would result in lower image quality due to undersampling or would require trading off the field of view and acquisition time. This emphasizes the importance of imaging speed for en face imaging in general, and in particular motion contrast imaging, since it requires scanning the same location repeatedly.

Figures 5.3A-C show 1.5mm×1.5mm en face choriocapillaris angiograms at three different fundus locations from the same normal subject in Figure 5.2. The smaller field size provides better image quality due to higher sampling density. The differences in capillary density and pattern between different fundus locations are clearly visualized. At the central fovea, the capillaries have a honeycomb structure with tightly packed vessel density (Figure 5.3A). At ~6mm temporal to the central fovea, a more lobular and less dense capillary structure can be identified (Figure 5.3B). At ~12mm nasal to the central fovea, the capillary structure becomes

even less dense and with larger lobules (Figure 5.3C). Figures 5.3D-F are en face angiograms extracted from the same volumetric data sets but at ~25-30μm below the choriocapillaris, where feeding arterioles and draining venules in the Sattler's layer are clearly visualized. As in the choriocapillaris, the density of feeding and draining vessels tend to decrease and the vessel diameter increase at fundus locations away from the central fovea. Figures 5.3J and 5.3K, adapted from Olver et al.[29], show electron micrograph corrosion casts of the human choriocapillaris at the posterior pole and equator, respectively, which are displayed in the same scale as in the OCT angiograms for comparison. There is an excellent correspondence of structural features between the OCT angiograms in Figures 5.3A and 5.3C and the electron micrograph corrosion casts in Figures 5.3J and 5.3K, thus suggesting that OCT angiography enables in vivo visualization of the choriocapillaris.

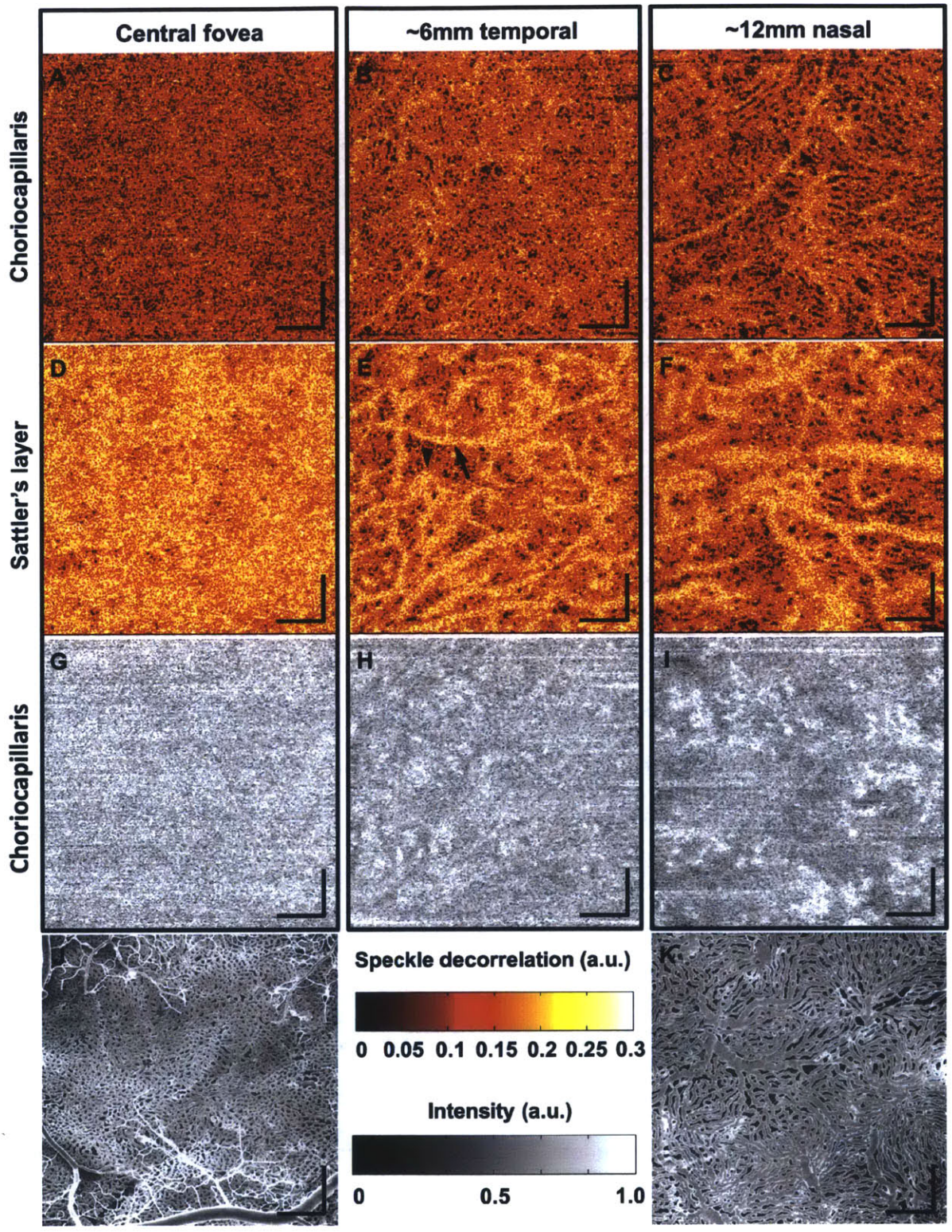
Central fovea
~6mm temporal
~12mm nasal
Choriocapillaris
Sattler's layer
Choriocapillaris
A
B
C
D
E
F
G
H
I
J
K
Speckle decorrelation (a.u.)
0 0.05 0.1 0.15 0.2 0.25 0.3
Intensity (a.u.)
0 0.5 1.0

**Figure 5.3.** 1.5mm×1.5mm en face OCT angiograms at three different fundus locations. (A,D,G) OCT angiogram of the choriocapillaris, OCT angiogram of the Sattler's layer, and en face OCT intensity image (slice) corresponding to the choriocapillaris layer, respectively, at the central fovea. (B,E,H) OCT angiogram of the choriocapillaris, OCT angiogram of the Sattler's layer, and en face OCT intensity image (slice) corresponding to the choriocapillaris layer, respectively, at ~6mm temporal to the central fovea. The arrowhead indicates venules and arrow arteriole in (E). (C,F,I) OCT angiogram of the choriocapillaris, OCT angiogram of the Sattler's layer, and en face OCT intensity image (slice) corresponding to the choriocapillaris layer, respectively, at ~12mm nasal to the central fovea. (J,K) Electron micrographs of corrosion casts reproduced from Olver et al. with permission. Scale bars: 250μm.

Figure 5.3 shows false color images with varying degrees of speckle decorrelation. Although Figure 5.2 can also be displayed in false color, we chose to display only Figure 5.3 in false color to illustrate that it is particularly useful for identifying feeding arterioles and draining venules. Since speckle decorrelation imaging is based on motion contrast, the degree of speckle decorrelation increases if the erythrocyte speed is faster. Therefore, the feeding and draining vessels tend to have higher speckle decorrelation than capillaries, as seen in Figure 5.3. It is less clear how to differentiate feeding arterioles from draining venules when using only OCT angiography. However, previous morphology studies show that venules are centrally located and arterioles are located at the periphery of lobules[13, 28]. Using this information, some venules and arterioles can be identified from the lobular structure of the choriocapillaris, as shown in Figure 5.3E.

Figures 5.3G-I also show en face intensity images corresponding to the en face angiograms in Figures 5.3A-C. Because OCT intensity and angiography volumes are from the same data set, they are co-registered, and it is possible to extract en face angiograms and intensity images from precisely the same depth. As can be seen, the en face intensity images do not exhibit the choriocapillaris pattern seen in the OCT angiograms, which suggests that the intensity image alone cannot easily visualize the vessel lumen and stroma in the choriocapillaris. Intensity images have speckle noise that makes visualization of fine features difficult. However, OCT angiograms can visualize microvasculature in the choriocapillaris by displaying motion contrast from the fluctuation in intensity versus time. This points out that motion-contrast OCT angiography, whether it is using intensity or phase fluctuation information, is necessary to visualize the choriocapillaris structure. However, it should be noted that larger choroidal vessels below the choriocapillaris layer can still be visualized with en face OCT intensity images because their larger size and high flow rates generate contrast from light scattering and fringe washout effects. This is a different type of contrast mechanism from OCT angiography using speckle decorrelation.

Several previous studies have investigated the choriocapillaris using en face OCT intensity images. Motaghiannezam et al. visualize the choriocapillaris and larger choroidal vessels in the Sattler's and Haller's layers in three normal subjects using SSOCT at the 57kHz A-scan rate[31]. Sohrab et al. also studied the choriocapillaris and larger choroidal vessel patterns with commercial SDOCT in patients with early AMD or reticular pseudo-drusen[32]. It should be noted that, while the methods and results in these studies could be clinically useful, OCT angiograms can be more sensitive than en face OCT intensity images for visualizing the choriocapillaris vascular structure. However, it should also be emphasized that the intensity images at greater

depths showing larger choroidal vessels probably still reflect the vasculature, since they can be visualized with both OCT intensity and motion contrast angiography imaging.

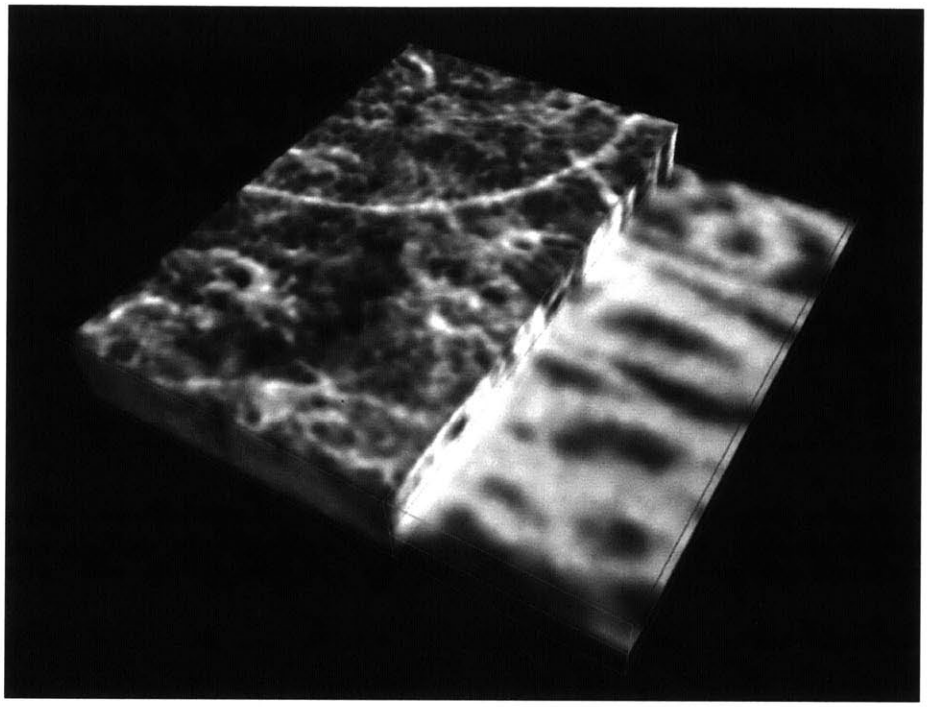

**Figure 5.4.** Three-dimensional rendering of a volumetric angiography data set covering a 1.5mm×1.5mm field on the retina. The locations where feeding arterioles and draining venules branch out to the choriocapillaris can be visualized more easily in three-dimensional rendering. One side of the rendering shows only depths below the choriocapillaris to emphasize the depth-resolving capability of OCT angiography.

Figure 5.4 is a three-dimensional rendering of volumetric OCT angiographic data acquired from a 1.5mm×1.5mm field of view at ~12mm nasal to the central fovea in order to emphasize that OCT angiography is indeed depth-resolved. One side of the volumetric angiogram rendering shows only structures below the choriocapillaris, while the other side shows the choriocapillaris and deeper structures. The rendering below the choriocapillaris layer shows the large feeding and draining vessels, while the rendering at the choriocapillaris layer shows the fine

microvasculature in the choriocapillaris. The locations where the larger choroidal vessels in the Sattler's layer branch out to the choriocapillaris can also be identified in the rendering.

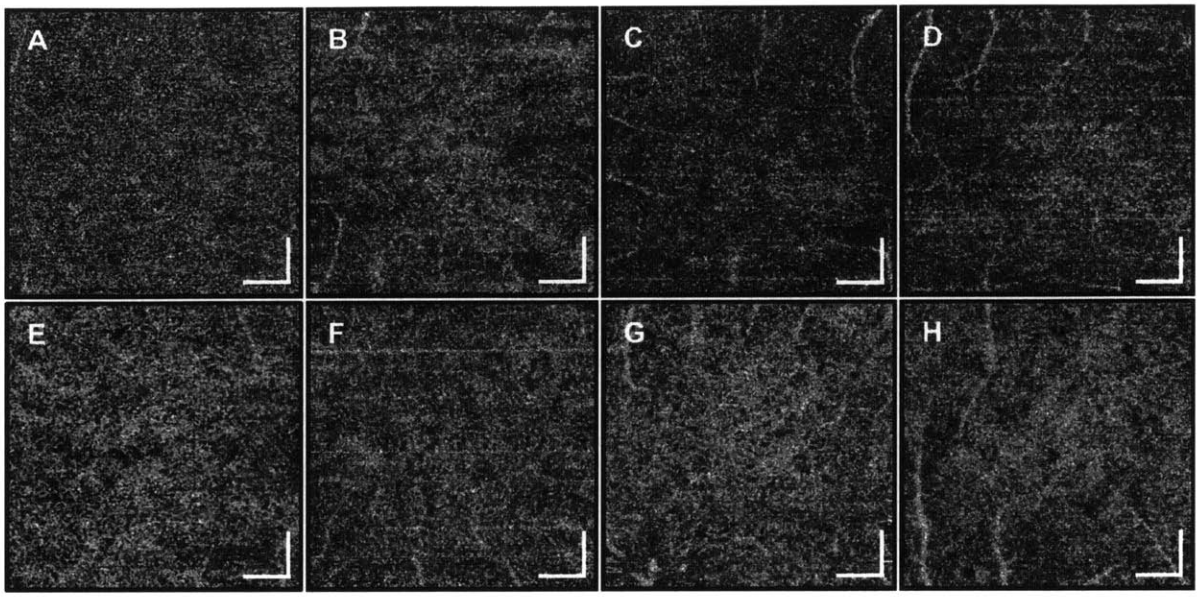


**Figure 5.5.** 1.5mm×1.5mm en face OCT angiograms at the central fovea for eight normal subjects. The choriocapillaris can be visualized in all subjects. Some variation between individuals can be noticed. The angiogram in (A) is the same image as in Figure 3(A) but in grayscale. Scale bars: 250μm.

Figures 5.5 and 5.6 are OCT angiograms of the choriocapillaris from the eight normal subjects at the central fovea and at ~6mm temporal to the fovea. Both 3mm×3mm and 1.5mm×1.5mm field sizes were scanned, but only 1.5mm×1.5mm images are shown for better visualization. In some of the angiograms, sporadic, bright horizontal line artifacts can be seen, resulting from occasional rapid saccadic eye motion. Although there is some variation in the choriocapillaris pattern between individuals, the observed vascular structure agrees well with known architectural morphology, and OCT angiography appears to work in all eight subjects imaged. The observed variations in choriocapillaris structure in the OCT angiograms are likely

caused by actual variation in structure between individuals and not the measurement artifacts. This emphasizes that care should be taken when comparing the choriocapillaris structure between different subjects.

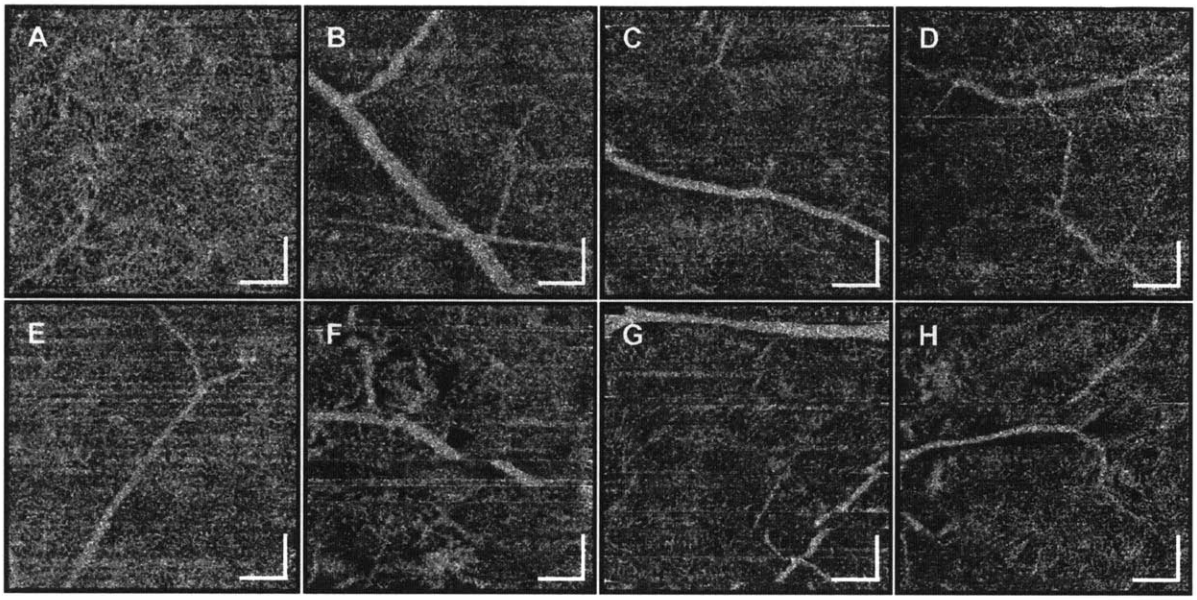


**Figure 5.6.** 1.5mm×1.5mm en face OCT angiograms at ~6mm temporal to the fovea for eight normal subjects. The choriocapillaris can be visualized in all subjects. Some variation between individuals can be noticed. The angiogram in (A) is the same image as in Figure 3(B) but in grayscale. The order of the subjects is the same as in Figure 5. Scale bars: 250μm.

No subject had severe astigmatism (no subject had more than 2.5D of refractive astigmatism), and it appears that mild to moderate levels of astigmatism do not severely affect the angiogram image quality. It should be noted, however, that severe astigmatism would likely reduce the transverse resolution and signal in OCT angiography. This problem could potentially be corrected by using corrective cylindrical lenses in the patient interface or by using adaptive optics. For imaging patients with poor fixation, hardware eye tracking or software motion

correction may be necessary. Furthermore, in AMD patients with irregular RPE contours, a more sophisticated segmentation algorithm would be required to segment the choriocapillaris boundary accurately. It is also possible to make the spot size on the retina smaller by increasing the OCT beam diameter at the cornea, which may improve the transverse resolution of the en face OCT angiogram, but ocular aberrations will limit the effective resolution unless adaptive optics is used.

The major difference between this technique and fluorescein or ICG angiography is that OCT angiography is based on motion contrast. This has several advantages for clinical applications. Since OCT angiography does not require exogenous contrast agents, imaging measurements can be safely and frequently repeated. OCT angiography also images three-dimensional vascular structure and can image fine vascular structure in the choriocapillaris below the RPE. In addition, if the capillary erythrocyte speeds are too slow, OCT angiography would show lower speckle decorrelation values, which can be identified in the en face and cross-sectional OCT angiograms. This is an interesting property, since it suggests that OCT angiography may detect abnormalities in local perfusion before structural abnormalities such as vessel atrophy occur, which could be useful for early diagnosis. Unlike fluorescein or ICG angiography, OCT angiography does not detect dye leakage, which is beneficial for imaging the fenestrated choriocapillaris, but is limited in applications where alterations in vascular permeability are markers of disease.

The ultrahigh speed SSOCT prototype at the long 1060nm wavelength has advantages over commercial spectral domain OCT (SDOCT) systems at 850nm for choroidal imaging. Because of the normal curvature of the retina, OCT imaging away from the macula tends to result in a severe tilt of the retina. This in turn implies that it is difficult to avoid signal loss at all transverse locations, even with enhanced depth imaging (EDI)[33]. Compared with SDOCT, SSOCT has low

sensitivity roll off with range and, combined with the deeper light penetration into tissue at longer wavelengths, it enables choroidal imaging with high signal-to-noise ratio (SNR) at all ranges. Good quality images can be achieved even with a severe retinal tilt (See the intensity image in Figure 5.1A as an example). Due to higher blood flow speed in the choroid than in the retina, SDOCT suffers from fringe washout artifacts that result in a significantly lower signal in blood vessels with fast blood flow speed. These artifacts are virtually absent in SSOCT[34]. Ultrahigh speed imaging with state-of-the-art SSOCT technology enables larger area coverage on the retina for a given total image acquisition time.

Because repeated B-scans are required for OCT angiography, the imaging area is smaller than en face intensity imaging at a given imaging speed. Next-generation commercial OCT systems are expected to have imaging speeds between 70kHz and 100kHz A-scan rates. At a 100kHz A-scan rate, it should be possible to image 1.5mm×1.5mm fields with 400(horizontal)×200(vertical)×4(repeats) A-scans per volume, while maintaining the same transverse sampling density and total acquisition time as in this study, which imaged a 3mm×3mm field at 400kHz with 800(horizontal)×400(vertical)×4(repeats) A-scans per volume. It should be also possible to extend the field size up to 2mm by critical sampling, instead of oversampling by 1.33× as seen in the present study. Field sizes between 1.5mm×1.5mm and 2mm×2mm are relatively small, but it could still enable clinical studies with next-generation commercial OCT systems if the desired scan position is known. In general, further advances in OCT technology and imaging speed are expected to provide progressively larger retinal coverage in the future.

The current study was limited in that only relatively younger normal subjects were imaged. Normal subjects have better ocular stability and reduced ocular opacities when compared with

typical retinal patients. Since only younger subjects were imaged, normal changes in the choriocapillaris associated with aging were not investigated. Further engineering is required to develop an ultrahigh speed SSOCT prototype for use in the ophthalmology clinic. Clinical imaging studies on patients with retinal disease as well as age-matched normal subjects are required in order to assess the ultimate clinical utility of OCT angiography of the choriocapillaris.

### 5.5 Conclusions

The study demonstrated in vivo OCT angiography of the choriocapillaris in healthy volunteers by using long wavelength, ultrahigh speed SSOCT. Fine vascular structure could be imaged using motion contrast, without the need for exogenous contrast agents. OCT angiograms at different depths and fundus locations were consistent with known architectural morphology from early histological and electron micrograph corrosion casting findings. More extensive clinical imaging studies on patients with retinal disease and age-matched normal subjects are required in order to assess the ultimate utility of OCT angiographic imaging of the choriocapillaris. However, OCT and OCT angiography have the advantage in that they enable integrated imaging of both retinal and choroidal structure and vasculature. Since alterations in choriocapillaris structure are implicated in many retinal diseases, OCT angiography promises to enable cross-sectional as well as longitudinal studies in patients for a better understanding of pathogenesis, early diagnosis of diseases, treatment response monitoring, and improved efficiency of pharmaceutical development.

## References


1. Schmetterer L, Kiel J, SpringerLink (Online service). Ocular Blood Flow. Berlin, Heidelberg: Springer Berlin Heidelberg; 2012. Available from: http://dx.doi.org/10.1007/978-3-540-69469-4.

2. Lutty G, Grunwald J, Majji AB, Uyama M, Yoneya S. Changes in choriocapillaris and retinal pigment epithelium in age-related macular degeneration. Mol Vis. 1999;5:35.

3. Cao J, McLeod S, Merges CA, Lutty GA. Choriocapillaris degeneration and related pathologic changes in human diabetic eyes. Arch Ophthalmol. 1998;116(5):589-97. Epub 1998/05/22. PubMed PMID: 9596494.

4. von Sallmann L. The structure of the eye. Arch Ophthalmol. 1961;66(6):920-1. doi: 10.1001/archopht.1961.00960010922023.

5. Sarks JP, Sarks SH, Killingsworth MC. Evolution of Geographic Atrophy of the Retinal-Pigment Epithelium. Eye. 1988;2:552-77. PubMed PMID: 2476333.

6. McLeod DS, Grebe R, Bhutto I, Merges C, Baba T, Lutty GA. Relationship between RPE and Choriocapillaris in Age-Related Macular Degeneration. Investigative Ophthalmology & Visual Science. 2009;50(10):4982-91. doi: Doi 10.1167/Iovs.09-3639. PubMed PMID: 19357355.

7. Mullins RE, Johnson MN, Faidley EA, Skeie JM, Huang JA. Choriocapillaris Vascular Dropout Related to Density of Drusen in Human Eyes with Early Age-Related Macular Degeneration. Investigative Ophthalmology & Visual Science. 2011;52(3):1606-12. doi: Doi 10.1167/Iovs.10-6476. PubMed PMID: 21398287; PubMed Central PMCID: PMC3101687.

8. Bhutto I, Lutty G. Understanding age-related macular degeneration (AMD): Relationships between the photoreceptor/retinal pigment epithelium/Bruch's membrane/choriocapillaris complex. Mol Aspects Med. 2012;33(4):295-317. doi: DOI 10.1016/j.mam.2012.04.005. PubMed PMID: 22542780; PubMed Central PMCID: PMC3392421.

9. Friedman E STKT. Senile choroidal vascular patterns and drusen. Arch Ophthalmol. 1963;69(2):220-30. doi: 10.1001/archopht.1963.00960040226014.

10. Sarks SH, Arnold JJ, Killingsworth MC, Sarks JP. Early drusen formation in the normal and aging eye and their relation to age related maculopathy: a clinicopathological study. Brit J Ophthalmol. 1999;83(3):358-68. doi: 10.1136/bjo.83.3.358.

11. Lengyel I, Tufail A, Hosaini HA, Luthert P, Bird AC, Jeffery G. Association of Drusen Deposition with Choroidal Intercapillary Pillars in the Aging Human Eye. Investigative Ophthalmology & Visual Science. 2004;45(9):2886-92. doi: 10.1167/iovs.03-1083.

12. Fryczkowski AW, Hodes BL, Walker J. Diabetic choroidal and iris vasculature scanning electron microscopy findings. Int Ophthalmol. 1989;13(4):269-79. Epub 1989/07/01. PubMed PMID: 2482264.

13. McLeod DS, Lutty GA. High-resolution histologic analysis of the human choroidal vasculature. Invest Ophthalmol Vis Sci. 1994;35(11):3799-811. Epub 1994/10/01. PubMed PMID: 7928177.

14. Lutty GA, Cao J, McLeod DS. Relationship of polymorphonuclear leukocytes to capillary dropout in the human diabetic choroid. Am J Pathol. 1997;151(3):707-14. Epub 1997/09/01. PubMed PMID: 9284819; PubMed Central PMCID: PMC1857840.

15. Gerl VB, Bohl J, Pitz S, Stoffelns B, Pfeiffer N, Bhakdi S. Extensive deposits of complement C3d and C5b-9 in the choriocapillaris of eyes of patients with diabetic retinopathy. Invest Ophthalmol Vis Sci. 2002;43(4):1104-8. Epub 2002/03/30. PubMed PMID: 11923252.

16. Kurokawa K, Sasaki K, Makita S, Hong Y-J, Yasuno Y. Three-dimensional retinal and choroidal capillary imaging by power Doppler optical coherence angiography with adaptive optics. Optics Express. 2012;20(20):22796-812. doi: 10.1364/oe.20.022796.

17. Braaf B, Vienola KV, Sheehy CK, Yang Q, Vermeer KA, Tiruveedhula P, Arathorn DW, Roorda A, de Boer JF. Real-time eye motion correction in phase-resolved OCT angiography with tracking SLO. Biomed Opt Express. 2013;4(1):51-65. Epub 2013/01/11. doi: 10.1364/BOE.4.000051 177976 [pii]. PubMed PMID: 23304647; PubMed Central PMCID: PMC3539196.

18. Choi W, Potsaid B, Jayaraman V, Baumann B, Grulkowski I, Liu JJ, Lu CD, Cable AE, Huang D, Duker JS, Fujimoto JG. Phase-sensitive swept-source optical coherence tomography imaging of the human retina with a vertical cavity surface-emitting laser light source. Opt Lett. 2013;38(3):338-40. PubMed PMID: 23381430; PubMed Central PMCID: PMC3721635.

19. Makita S, Hong Y, Yamanari M, Yatagai T, Yasuno Y. Optical coherence angiography. Optics Express. 2006;14(17):7821-40. doi: Doi 10.1364/Oe.14.007821. PubMed PMID: 19529151.

20. Fingler J, Schwartz D, Yang CH, Fraser SE. Mobility and transverse flow visualization using phase variance contrast with spectral domain optical coherence tomography. Optics Express. 2007;15(20):12636-53. doi: Doi 10.1364/Oe.15.012636. PubMed PMID: 19550532.

21. Tao YK, Davis AM, Izatt JA. Single-pass volumetric bidirectional blood flow imaging spectral domain optical coherence tomography using a modified Hilbert transform. Optics Express. 2008;16(16):12350-61. doi: Doi 10.1364/Oe.16.012350. PubMed PMID: 18679512.

22. An L, Wang RKK. In vivo volumetric imaging of vascular perfusion within human retina and choroids with optical micro-angiography. Optics Express. 2008;16(15):11438-52. PubMed PMID: 18648464.

23. Mariampillai A, Standish BA, Moriyama EH, Khurana M, Munce NR, Leung MKK, Jiang J, Cable A, Wilson BC, Vitkin IA, Yang VXD. Speckle variance detection of microvasculature using swept-source optical coherence tomography. Opt Lett. 2008;33(13):1530-2. doi: Doi 10.1364/Ol.33.001530. PubMed PMID: 18594688.

24. Vakoc BJ, Lanning RM, Tyrrell JA, Padera TP, Bartlett LA, Stylianopoulos T, Munn LL, Tearney GJ, Fukumura D, Jain RK, Bouma BE. Three-dimensional microscopy of the tumor microenvironment in vivo using optical frequency domain imaging. Nat Med. 2009;15(10):1219-U151. doi: Doi 10.1038/Nm.1971. PubMed PMID: 19749772; PubMed Central PMCID: PMC2759417.

25. Yu LF, Chen ZP. Doppler variance imaging for three-dimensional retina and choroid angiography. J Biomed Opt. 2010;15(1). doi: Artn 016029
Doi 10.1117/1.3302806. PubMed PMID: 20210473; PubMed Central PMCID: PMC2839803.

26. Enfield J, Jonathan E, Leahy M. In vivo imaging of the microcirculation of the volar forearm using correlation mapping optical coherence tomography (cmOCT). Biomedical optics express. 2011;2(5):1184-93. doi: 10.1364/boe.2.001184.

27. Blatter C, Klein T, Grajciar B, Schmoll T, Wieser W, Andre R, Huber R, Leitgeb RA. Ultrahigh-speed non-invasive widefield angiography. J Biomed Opt. 2012;17(7). doi: Artn 070505
Doi 10.1117/1.Jbo.17.7.070505. PubMed PMID: 22894461.

28. Yoneya S, Tso MM. ANgioarchitecture of the human choroid. Arch Ophthalmol. 1987;105(5):681-7. doi: 10.1001/archopht.1987.01060050099046.

29. Olver JM. Functional anatomy of the choroidal circulation: Methyl methacrylate casting of human choroid. Eye. 1990;4(2):262-72.

30. Zhang HR. Scanning electron-microscopic study of corrosion casts on retinal and choroidal angioarchitecture in man and animals. Prog Retin Eye Res. 1994;13(1):243-70. doi: http://dx.doi.org/10.1016/1350-9462(94)90012-4.

31. Motaghiannezam R, Schwartz DM, Fraser SE. In Vivo Human Choroidal Vascular Pattern Visualization Using High-Speed Swept-Source Optical Coherence Tomography at 1060 nm. Investigative Ophthalmology & Visual Science. 2012;53(4):2337-48. doi: 10.1167/iovs.11-7823.

32. Sohrab M, Wu K, Fawzi AA. A Pilot Study of Morphometric Analysis of Choroidal Vasculature In Vivo, Using En Face Optical Coherence Tomography. Plos One. 2012;7(11). doi: ARTN e48631
DOI 10.1371/journal.pone.0048631. PubMed PMID: 23189132; PubMed Central PMCID: PMC3506620.

33. Spaide RF, Koizumi H, Pozonni MC. Enhanced depth imaging spectral-domain optical coherence tomography. Am J Ophthalmol. 2008;146(4):496-500. doi: 10.1016/j.ajo.2008.05.032. PubMed PMID: WOS:000259742200004.

34. Yun SH, Tearney GJ, de Boer JF, Bouma BE. Motion artifacts in optical coherence tomography with frequency-domain ranging. Optics Express. 2004;12(13):2977-98. PubMed PMID: ISI:000222321200023.

# Chapter 6

# Ultrahigh Speed OCT Angiography in Age-Related Macular Degeneration Using Swept Source Optical Coherence Tomography

## 6.1 Overview

There was a major collaborative effort in deploying a vertical cavity surface emitting laser (VCSEL) swept source optical coherence tomography (OCT) system to the New England Eye Center to perform clinical studies. ByunKun Lee, Chen D. Lu, Martin F. Kraus, Jonathan J. Liu, Dr. Benjamin Potsaid, Dr. Zhao Wang, Dr. Vijaysekhar Jayaraman, Alex E. Cable, and Prof. James Fujimoto contributed to the development of the clinical prototype, which was deployed in November, 2013. The purpose of this chapter is to assess the potential of ultrahigh speed swept source OCT angiography in visualizing and investigating microvascular changes in patients with age-related macular degeneration (AMD) using the OCT system deployed to the clinic. 69 eyes of 35 normal volunteers and 65 eyes of 41 patients with AMD were imaged. Dye-free OCT angiograms of the retinal and choriocapillaris microvasculature were obtained in normal volunteers and patients with geographic atrophy (GA), exudative AMD, and early and intermediate dry AMD. Imaging was performed with an ultrahigh speed swept source OCT (SSOCT) prototype at 1μm wavelengths with an A-scan rate of 400kHz. Multiple volumetric OCT scans were acquired with repeated B-scan protocols (500 A-scans × 500 cross-sections × 5 repeated B-scans per cross-section over 6mm × 6mm and 3mm ×3mm). OCT angiography was performed by calculating the speckle decorrelation between B-scans acquired from the same location. The resulting volumetric OCT angiograms were segmented to generate en face

angiograms at multiple depths. Choriocapillaris circulation was almost completely impaired in all 11 eyes with GA in the region of atrophy. 4 out of 5 eyes with GA showing foveal sparing had noticeable choriocapillaris circulation in the region of foveal sparing. In 9 out of 11 eyes with GA, marked reductions in choriocapillaris circulation were observed even beyond the margins of GA. In 16 out of 19 eyes with exudative AMD, the choroidal neovascular membrane (CNVM) could be clearly visualized above the Bruch's membrane. CNVMs were always surrounded by the region with severely impaired choriocapillaris circulation. In dry AMD patients without GA, varying degrees of reduction in choriocapillaris circulation were observed. Impaired choriocapillaris circulation was not always associated with drusen locations. However, impaired choriocapillaris circulation was correlated with RPE/photoreceptor integrity. The results in this chapter clearly demonstrates that the ability of ultrahigh speed OCT angiography to noninvasively visualize retinal and choriocapillaris microvascular abnormalities promises to be an important tool for better understanding of pathogenesis, disease progression assessment, and early diagnosis in AMD. Dr. Nadia K. Waheed contributed significantly to clinical data analysis and recruitment of the subjects. Eric Moult contributed significantly to OCT image processing, OCT data analysis, and OCT data management. Dr. Mehreen Adhi imaged all the patients and recruited normal volunteers for the study. ByungKun Lee contributed to developing and managing the clinical ultrahigh speed swept source OCT system. Dr. Vijaysekhar Jayaraman developed the VCSEL light source used in the OCT system. Dr. Philip J. Rosenfeld, Dr. Jay S. Duker, and Prof. James G. Fujimoto provided supervision and guidance.

## 6.2 Introduction

Age-related macular degeneration (AMD) is a leading cause of vision loss or impairment in developed countries. Although the current clinical practice for monitoring AMD depends mostly

on structural information, choroidal blood circulation is believed to be altered in AMD. The choroid is a highly vascular tissue that is responsible for nourishing the outer retinal layers. Multiple histological studies have investigated the choriocapillaris, the capillary layer of the choroid, in dry AMD[1-4]. In geographic atrophy (GA), loss of the retinal pigment epithelium (RPE) is associated with atrophy of the choriocapillaris and choroid[1, 2]. A study in 2011 found that choriocapillaris density decreases with sub-RPE deposit formation[3]. Exudative AMD results from abnormal vessel growth originating from the choroid into the Bruch's membrane, causing fibrovascular scar formation and retinal detachment due to leakage of fluid. The standard therapy for exudative AMD is intravitreal injection of anti-vascular endothelial growth factors (anti-VEGF)[5-10]. Although the abnormal vessels, called choroidal neovascular membranes (CNVM), are inherently vascular in nature, treatment response monitoring is generally performed using optical coherence tomography (OCT) structural images[11-14].

Despite the vascular abnormalities associated with AMD, the majority of current clinical routines are based on monitoring structural alterations using fundus photography and/or OCT instead of directly visualizing vascular abnormalities, a fact which may be partly attributed to a lack of medical technology capable of noninvasively visualizing the retinal and choroidal microvasculature. OCT angiography is a relatively new OCT imaging technique that generates microvascular angiograms in vivo without the injection of exogenous dyes[15-23]. Unlike dye-based angiography methods, such as FA or indocyanine green angiography (ICGA), OCT angiography uses inter-scan motion to generate contrast. Motion contrast imaging requires rapidly and repeatedly acquiring multiple B-scans from the same location, which necessitates high OCT imaging speeds compared to standard structural imaging. By tracking changes in the OCT intensity and/or phase signal induced by erythrocyte motion in the B-scan, depth-resolved three-

dimensional angiograms can be generated. As OCT is already a clinical standard, OCT angiography is well positioned to be widely useful for therapeutic response monitoring and pharmaceutical development as well as monitoring for disease progression.

OCT angiography is advantageous in that it enables independent visualization of the choriocapillaris and retinal microvasculature. Dye-based angiography techniques such as FA and ICGA usually fail to image the choriocapillaris because of the pigmented choroidal melanocytes and retinal pigment epithelium (RPE). Moreover, vessel fenestration in the choriocapillaris[24] causes dye leakage, obscuring small features of the choriocapillaris in the FA/ICGA images. OCT angiography, however, is based on motion contrast, and therefore avoids this problem. Combined with deeper light tissue penetration at 1um wavelengths compared to standard 800nm wavelengths, OCT angiography can visualize the three-dimensional microvasculature of the choriocapillaris as well as the retina. Since both structural and microvascular information are acquired using the same volumetric OCT data set, the two types of information are necessarily co-registered, making volumetric OCT angiographic imaging a powerful tool for comprehensive assessment of retinal diseases. However, because the retina and choriocapillaris microvasculature lies predominantly along the en face planes, OCT angiography requires dense volumetric scanning of the retina in order to visualize the vasculature in en face planes. OCT angiography of the choriocapillaris has been demonstrated only recently because the small features in the choriocapillaris necessitate a very high sampling density, and therefore, even higher OCT imaging speeds for given retinal coverage[25-28].

Due to the requirement of high imaging speeds, there has been a large gap between technological development and clinical application of OCT angiography. Only recently, OCT angiography was applied in small numbers of patients with AMD. A 2013 study by Kim et al.

demonstrated OCT angiography in 1 normal subject and 1 AMD patient with GA[27]. In 2014, Schwartz et al. reported imaging results from 1 normal subject, 1 dry AMD, 1 exudative AMD, and 1 NPDR patient[29]. In 2014, Jia et al. demonstrated OCT angiography in the retina of 5 normal subjects and 5 exudative AMD patients[30]. Most of the studies above were performed on very small numbers of patients with small OCT fields of view only, and clinical implications of the results were difficult to interpret. All of these studies above were performed at OCT A-scan rates of ~100kHz or less, making clinical practice of the technology challenging due to limited the field sizes and image quality.

The purpose of this study is to assess the potential of OCT angiography using ultrahigh speed SSOCT as well as to use OCT angiography to visualize the microvascular changes in the retina and choriocapillaris in patients with AMD. As the OCT imaging speed increases, OCT angiography is expected to generate higher quality images with larger retinal coverage. The recent development of OCT swept light sources enabled a dramatic improvement in ophthalmic OCT imaging speeds. Our group recently demonstrated ophthalmic SSOCT using a vertical cavity surface emitting laser (VCSEL) swept light source[31], and later developed a phase stable ultrahigh speed SSOCT prototype with an A-scan rate of 400kHz and high phase stability[32], suitable for OCT angiography imaging. This instrument is ~5-10 times faster than standard commercial ophthalmic OCT systems. Two different field sizes were used in this study. The 3mm × 3mm field size is used to obtain superior angiogram image quality. The 6mm × 6mm field size is used to enable large volumetric retinal coverage. These complementary field sizes are used to visualize retinal and choriocapillaris abnormalities in patients with AMD.

## 6.3 Methods

35 normal volunteers and 41 AMD patients (7 patients had GA, 15 patients exudative AMD, and 26 patients had dry AMD without GA in at least one eye) were imaged for this study. The study was approved by the Institutional Review Boards at the Massachusetts Institute of Technology (MIT) and the New England Eye Center (NEEC). All participants including healthy normal volunteers and patients were imaged in the ophthalmology clinic at NEEC, and signed written informed consent was obtained from all subjects before OCT angiography imaging. The research adhered to the Declaration of Helsinki and the Health Insurance Portability and Accountability Act. The AMD patients were classified using on the Age-Related Eye Disease Study (AREDS)[33]. In selected patients, FA and fundus autofluorescence (FAF) was performed in addition to OCT imaging to correlate the image with the OCT angiogram.

OCT angiography was performed with an ultrahigh speed SSOCT research prototype developed at MIT and deployed to NEEC in November, 2013. A similar OCT system was described previously in detail[32], and therefore only key characteristics are summarized here. The prototype system used a VCSEL swept light source with an A-scan rate of 400kHz. The light source was centered at 1μm wavelengths, allowing deeper light penetration into pigmented tissue, such as RPE and choroid, when compared to current commercial standard wavelengths at ~850nm. The full-width at half-maximum (FWHM) axial and transverse resolutions were ~8-9μm and ~10μm (~24μm diffraction-limited Airy disk diameter), respectively, in tissue. OCT signals were sampled with an analog-to-digital acquisition card (Alazar Technologies, ATS9360), externally clocked at a maximum frequency of ~1.1GHz using the signal generated by an external Mach-Zehnder interferometer. The resulting imaging range was ~2.1mm in tissue. The OCT system was phase stabilized using a fiber Bragg grating to suppress undesired fixed pattern

noise in OCT intensity and angiography images, yielding a phase stability of ~1.5mrad at a signal-to-noise ratio of 57dB. The optical power incident on the cornea was ~1.8mW, and the measured system sensitivity was ~98dB.

Two different field sizes were used for OCT angiography in this study: 6mm × 6mm and 3mm × 3mm. For all field sizes, 2500 B-scans were acquired from 500 uniformly sampled locations, which provided 5 repeated B-scans per location for motion contrast imaging. Each B-scan consisted of 500 A-scans, and therefore the total number of A-scans per OCT volume was 500 × 500 × 5 A-scans. With the OCT A-scan rate of 400kHz and a galvanometer duty cycle of 80-85%, the total image acquisition time was ~3.9 seconds per volume. For the 6mm × 6mm field size, the volumetric scan pattern of 500 × 500 × 5 A-scans correspond to an isotropic sampling of the retina at a 12μm interval in the transverse direction, which provides an oversampling of ~2× compared to the ~24μm Airy disk diameter of the OCT beam on the retina. Smaller field sizes yield proportionally denser transverse oversampling, providing higher OCT angiogram quality. The time interval between sequential B-scans is ~1.5ms, and the line dwell time is ~7.5ms (~1.5ms × 5) per line, for all field sizes.

OCT angiography was performed by comparing sequential intensity B-scans (1↔2, 2↔3, 3↔4, and 4↔5) acquired from the same location. The four resulting motion contrast images from a given location were averaged to enhance angiogram image quality. For stationary tissue, the OCT intensity images acquired from the same location should look identical to one another. However, at the locations of blood vessels including capillaries, erythrocyte movements result in local fluctuations in the intensity images. By tracking the locations where the OCT signal fluctuates in time, it is possible to generate a cross-sectional motion contrast image. This operation is performed at all B-scan locations in order to obtain a three-dimensional volumetric

OCT angiogram. For selected cases, every other B-scan was compared (1↔3, 2↔4, 3↔5) to increase the time interval for comparison by 2x, thereby achieving a time interval of ~3ms instead of ~1.5ms without sacrificing the transverse sampling density on the retina. As in the sequential comparison case, the three resulting motion contrast images from a given location were averaged to enhance angiogram image quality. All B-scans were motion-corrected before comparison, using a previously described algorithm[34]. It should be noted that large retinal and choroidal vessels often cast angiographic shadow below the vessels because blood is highly scattering and causes more rapidly fluctuating speckle pattern below.

The three dimensional volumetric angiogram contains both the retinal and choroidal vasculature at different depths. To visualize the choriocapillaris and retinal microvasculature separately, the Bruch's membrane and internal limiting membrane (ILM) were segmented semi-automatically using intensity B-scans in the volumetric data set. Because the intensity B-scans are necessarily co-registered to the cross-sectional OCT angiograms, the segmented Bruch's membrane and ILM locations can be applied directly to the volumetric OCT angiogram. To generate en face retinal OCT angiograms, all depths between the ILM and the Bruch's membrane were projected using maximum projection. Choriocapillaris OCT angiograms were generated by choosing a single en face plane below the RPE. To visualize CNVM in exudative AMD patients, multiple en face planes right above the Bruch's membrane were projected in depth, depending on the exact depth and thickness of the CNVM.

## 6.4 Results

### *6.4.1 Healthy Normal Volunteers*

Normal volunteers recruited for the study were 39.7 ± 13.8 years old (range 19 to 70 years, 69 eyes from 35 subjects). Among the 69 eyes imaged, 33 eyes were from subjects older than 40

years and 7 from older than 60 years. Figure 6.1 shows representative retinal and choriocapillaris angiogram from a 49 year old normal volunteer. All images were centered roughly at the fovea. The image quality for the 3mm × 3mm field size is better than the 6mm × 6mm field size due to the higher sampling density. The 6mm × 6mm field size provides larger retinal coverage while the 3mm × 3mm field size enables the visualization of detailed microvasculature with higher angiogram quality. The eye shown in Figure 6.1 was one of the few with the sparsest choriocapillaris density among the 69 normal eyes. Most of the other eyes had markedly denser choriocapillaris as shown in Figure 6.2. Figure 6.2 shows representative choriocapillaris angiograms from different age groups over 3mm × 3mm and 6mm × 6mm field sizes. In this study, capillary density was not explicitly quantified but inspected qualitatively. Although a slight variation in the choriocapillaris density could be observed, the choriocapillaris of normal subjects was generally dense and homogeneous in the macula. Isolated inter-capillary spots in the choriocapillaris with well-defined boundaries and diameters smaller than ~100μm were not considered abnormal in this study since they were commonly observed in normal subjects as shown in Figure 6.2. These inter-capillary spots appear dark in the OCT angiogram display used in this manuscript where brighter pixels correspond to higher blood flow. Although the number of subjects older than 60 was limited, obvious age dependency in choriocapillaris density was not observed in normal eyes. However, there was a tendency that the choroidal thickness was thinner for eyes with more frequent appearances of dark spots in the choriocapillaris, although this was not explicitly quantified in the current study.

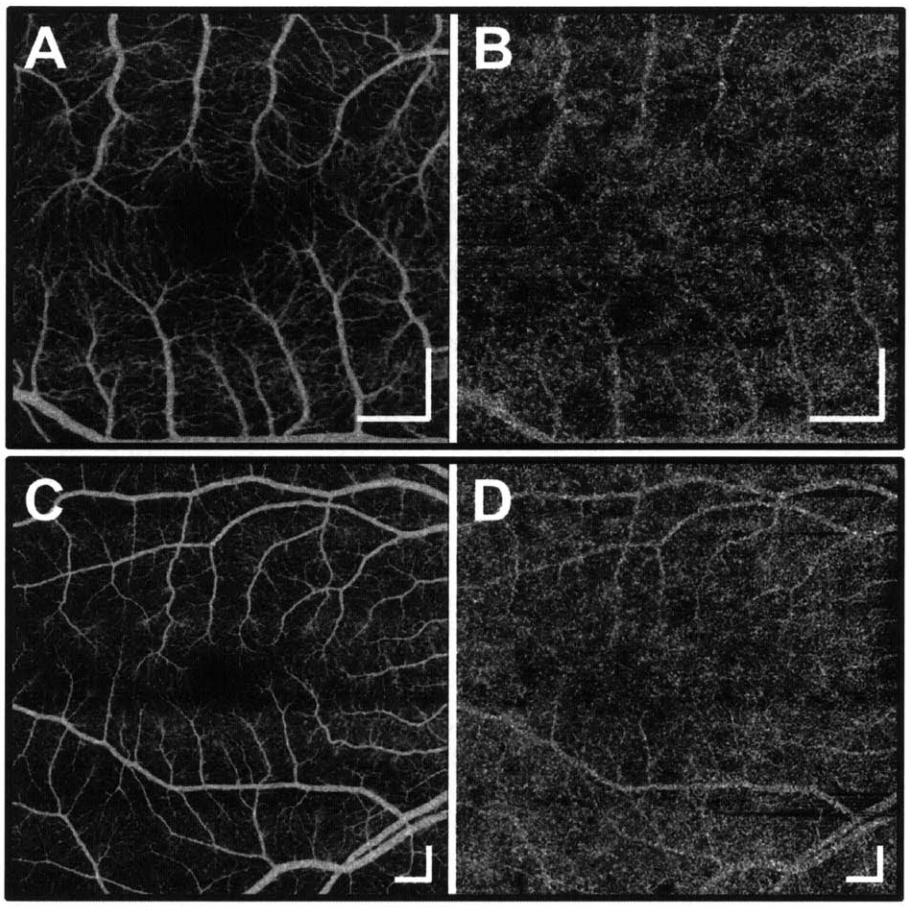


**Figure 6.1.** OCT retinal and choriocapillaris angiograms from a 49 year old normal volunteer. (A) OCT retinal angiogram over a 3mm × 3mm area centered at the fovea. (B) OCT choriocapillaris angiogram over the same 3mm × 3mm extracted from the same volumetric scan as used in (A). Note that the thick retinal arterioles and venules cast angiographic shadow in the choriocapillaris angiogram. (C) OCT retinal angiogram over a 6mm × 6mm area from the same eye as in (A). (D) OCT choriocapillaris angiogram over the same 6mm × 6mm area, extracted from the same volumetric scan as used in (C). This was one of the few eyes with the sparsest choriocapillaris density among the 69 normal eyes. Most of the eyes had significantly denser choriocapillaris. Scale bars: 500μm.

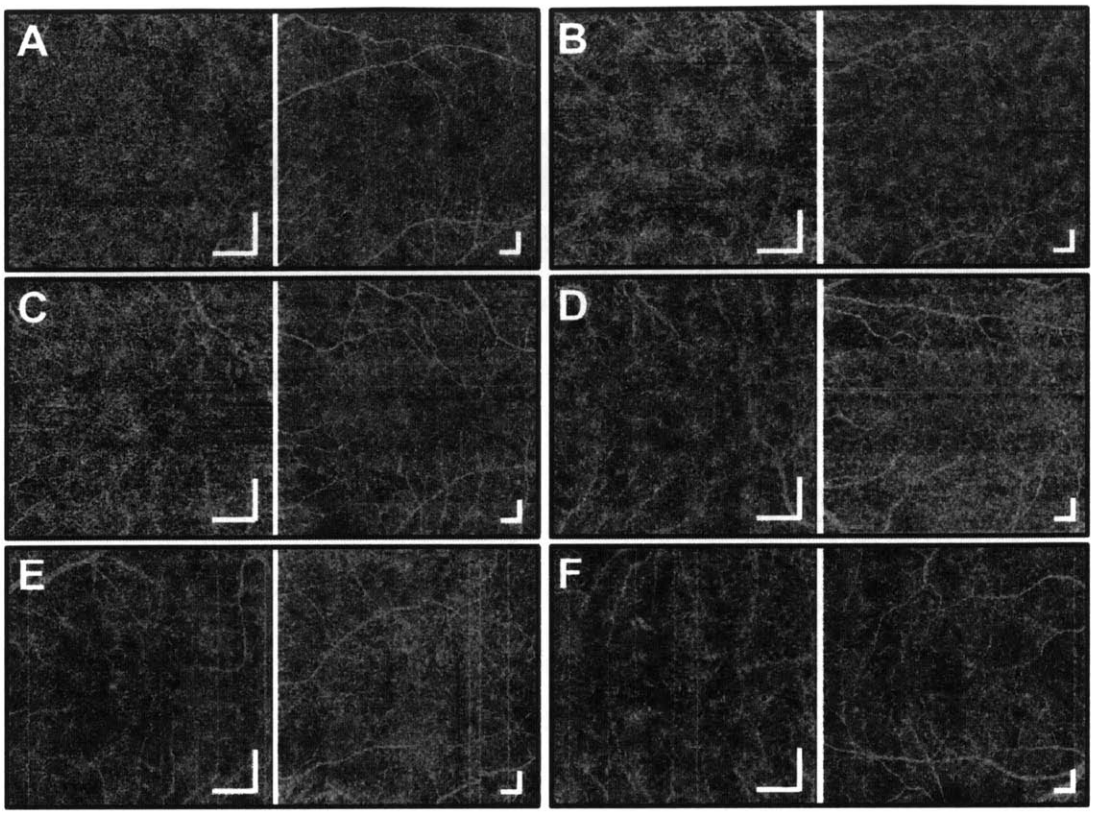


**Figure 6.2.** OCT angiograms of the choriocapillaris from (A) 35, (B) 53, (C) 58, (D) 68, (E) 65, and (F) 70 year old normal volunteers. The angiograms on the left are over 3mm × 3mm and on the right 6mm × 6mm, both centered at the fovea. Choriocapillaris circulation is generally dense and homogeneous over the field of view in normal eyes. Note that thick retinal arterioles and venules cast angiographic shadows on the choriocapillaris angiograms. Vertical or horizontal lines, depending on the orientation of the OCT fast scan axis, are artifacts due to eye motion. Scale bars: 500μm.

*6.4.2 Dry AMD with GA*

11 eyes from 7 dry AMD patients with GA (75.9 ± 6.1 years old, range 65 to 82 years) were imaged with ultrahigh speed OCT angiography. Figure 6.3 shows FAF and OCT data of a 75 year old dry AMD patient with GA centered at the fovea. The intensity en face projection image

in Figure 6.3B clearly delineates the region of GA, which agrees well with the FAF in Figure 3A. Figures 6.3C and 6.3D show the corresponding retinal and choriocapillaris angiograms processed from the same volumetric data set. Note that Figures 6.3B-D are generated from a single OCT volumetric scan, and therefore are necessarily co-registered to one another. The margin of the GA identified from Figure 6.3B is shown in Figure 6.3D as the white dotted boundary for comparison. In general, the choriocapillaris circulation is nearly completely compromised in the region of GA with only large choroidal vessels remaining. However, it can be noticed that there is foveal sparing that appears as a dark island at the central fovea in Figure 6.3B, and that there is corresponding choriocapillaris circulation in the corresponding area as shown in Figure 6.3D. Due to the foveal sparing, the patient had a visual acuity of 20/20. Foveal sparing was observed in 5 of the 11 eyes. 4 of these 5 eyes had some noticeable choriocapillaris circulation in the region of foveal sparing. The retinal microvasculature in Figure 6.3C does not show marked abnormality compared with healthy normal subjects.

Another noteworthy feature is that choriocapillaris circulation is significantly reduced even outside the region of GA, a feature manifested as more frequent appearances of sparser and darker regions in the choriocapillaris angiogram. Figure 6.4 shows three representative cross-sections indicated by white dotted lines in Figure 6.3D, only one of which going through the region of GA. Cross-sectional angiograms need to be interpreted carefully below the RPE because the choriocapillaris as well as large retinal and choroidal vessels often cast angiographic shadow below the vessels. However, by noting that the choriocapillaris is located immediately underneath the Bruch's membrane, the existence of choriocapillaris circulation can be identified unambiguously in cross-sectional angiograms as well in most cases. Although only the cross-

section in Figure 6.4B shows a complete atrophy of the RPE and photoreceptors, choriocapillaris circulation reduction can be identified in all three cross-sections.

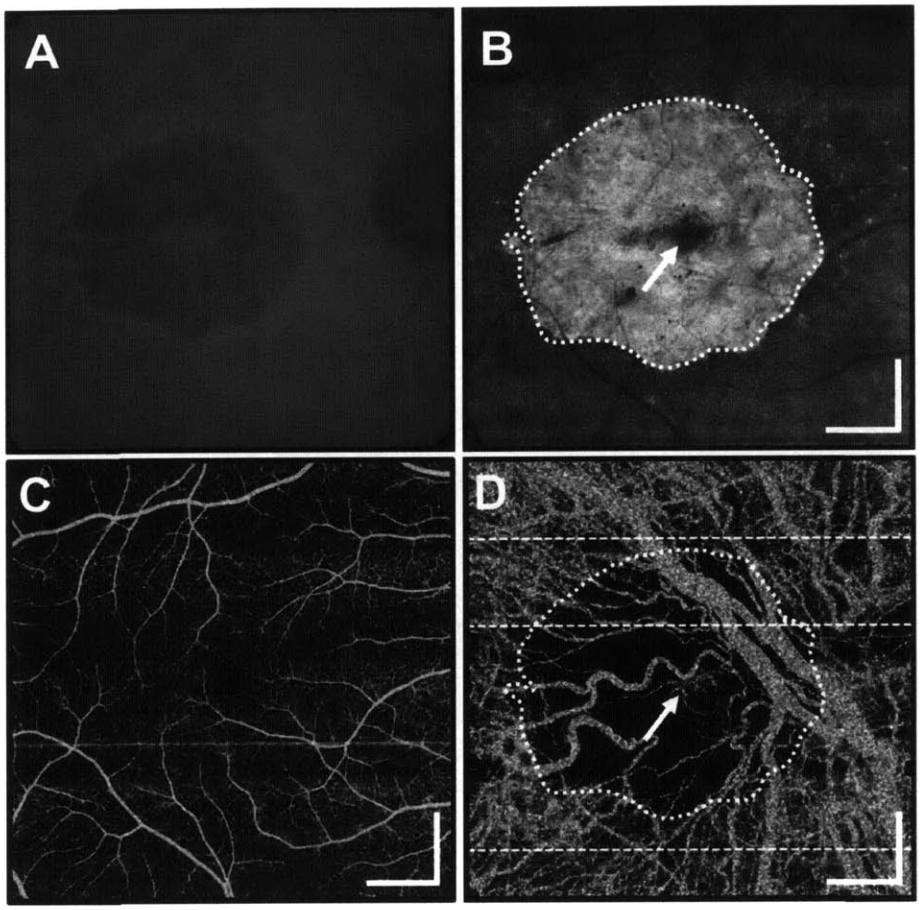


**Figure 6.3.** FAF and OCT images from a 75 year old GA patient with a visual acuity of 20/20. (A) FAF was acquired from a commercial system (Topcon). (B) OCT en face intensity projection image shows the area of GA clearly. The GA margin is delineated with a white dotted contour. The dark region at the fovea indicated by the white arrow corresponds to foveal sparing. (C) OCT angiogram of the retinal microvasculature. The retinal capillary network does not look too abnormal compared to that of normal volunteers. (D) OCT angiogram of the choriocapillaris. Choriocapillaris circulation is almost completely impaired in the region of GA delineated by the white dotted contour.

The area of foveal sparing has residual choriocapillaris circulation as indicated by the white arrow. Note that choriocapillaris circulation is severely compromised even outside the GA margin. The OCT images (B-D) are acquired from a 6mm × 6mm area centered at the fovea. All scale bars: 1mm.

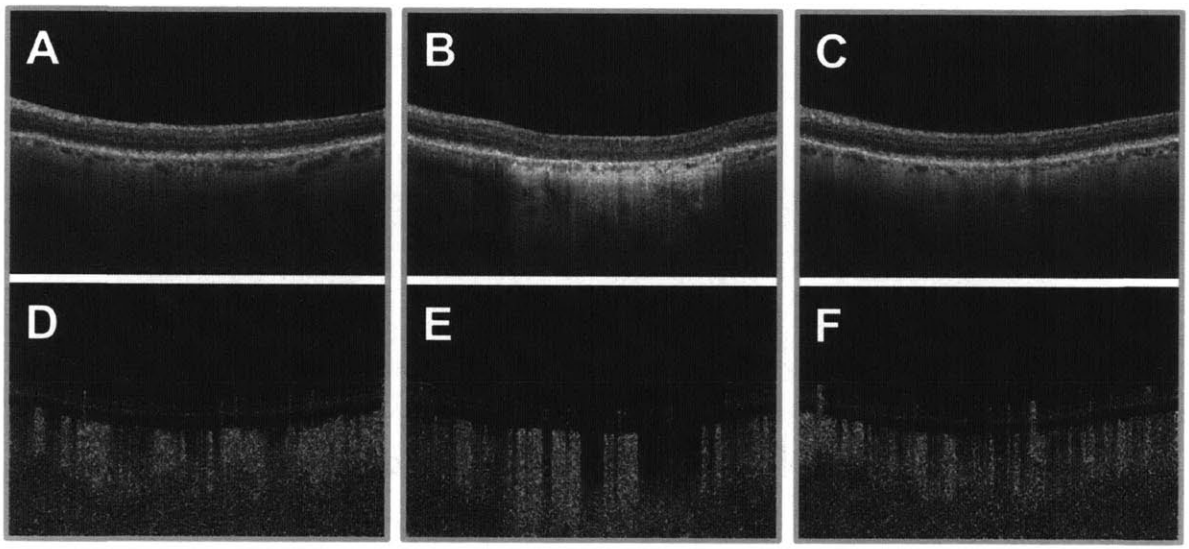


**Figure 6.4.** OCT intensity images and corresponding cross-sectional angiograms. Cross-sectional image pairs (A, D), (B, E), and (C, F) extracted from the three dashed white lines (top, middle, and bottom, respectively) shown in Figure 3D. Only the cross-sectional image pair (B, E) goes through the region of GA, as clearly shown in the intensity image. The choriocapillaris circulation is nearly completely compromised in the region of GA, except for the angiographic shadows due to large choroidal vessels. Although the cross-sectional image pairs (A, D) and (C, F) do not go through the GA, choriocapillaris circulation is noticeably impaired as clearly shown in (D) and (F). Transverse dimensions: 6mm.

There was also a general tendency that RPE/photoreceptor layer integrity was worse when the choriocapillaris circulation underneath was reduced. As shown in Figure 6.4, the region RPE/photoreceptor layer appears more diffuse in the intensity image is loosely correlated with more severely reduced choriocapillaris circulation. The association between impaired choriocapillaris circulation and compromised RPE/photoreceptor integrity was observed in all 11 eyes. Although compromised RPE/photoreceptor layer integrity usually entailed reduced choriocapillaris circulation, the opposite was often not true. It should be noted that impaired choriocapillaris circulation would not necessarily imply a complete degeneration of the choriocapillaris layer because OCT angiography is based on motion contrast, which is described further in the Discussion. Additional representative examples are shown in Figure 6.5 with the GA regions identified from co-registered structural intensity en face projection images delineated as white dotted boundaries. Markedly impaired choriocapillaris circulation extending beyond the margin of GA was found in 9 out of 11 AMD eyes with GA. However, it should be noted that in the 2 eyes that this was not observed, the RPE/photoreceptor layer outside the region of GA appeared nearly perfectly normal and the transition between the normal and GA regions was very abrupt. Both of these eyes were from a single patient. An example is shown in Figures 6.5(D), (H), (I), and (J). On the contrary, the other 9 eyes often exhibited compromised RPE/photoreceptor integrity well outside the region of GA.

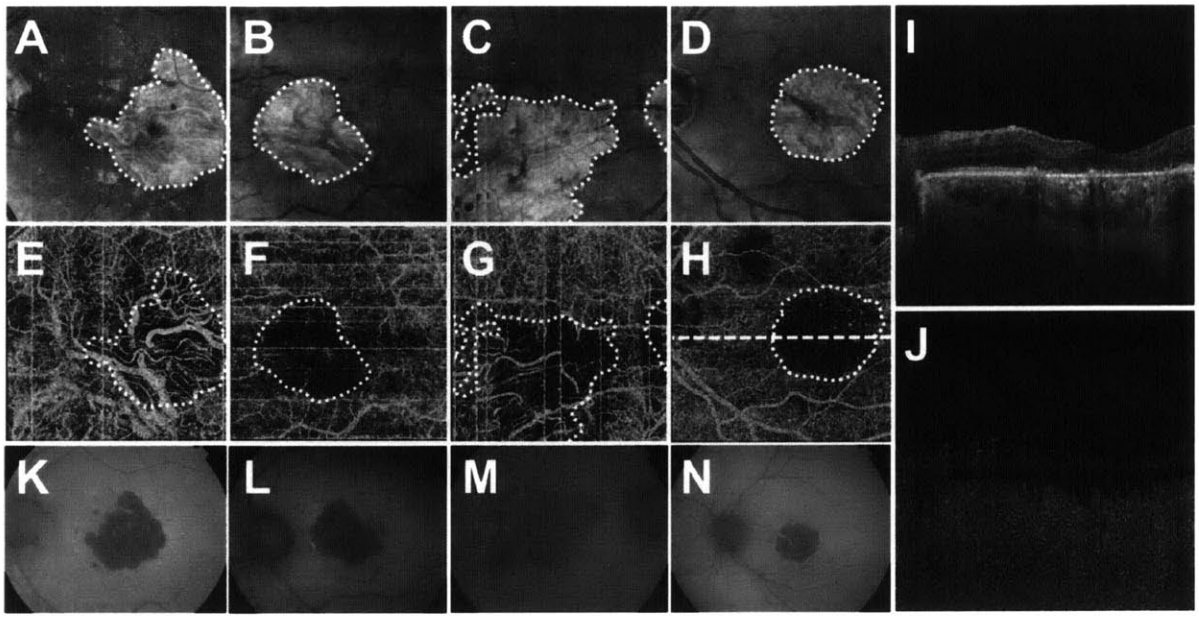


**Figure 6.5.** OCT en face intensity projections (A-D) and corresponding OCT choriocapillaris angiograms (E-H). The GA regions are delineated by white dotted contours. For the cases (A, E), (B, F), and (C, G), choriocapillaris circulation is noticeably impaired in areas outside the GA margin. For (H), choriocapillaris circulation immediately outside the region of GA appears relatively normal. (I, J) OCT intensity and angiographic cross-section pair extracted from the white dashed line in (H). Note that in (I) the RPE/photoreceptor integrity immediately outside the GA region appears nearly normal, and the corresponding choriocapillaris circulation in (J) appears normal immediately outside the GA region as well. (K-N) FAF images from the eyes shown in (A-D). 6mm × 6mm field of view for (A-H).

*6.4.3 Exudative AMD*

19 eyes from 15 exudative AMD patients were imaged (79.7 ± 8.3 years old, range 61 to 92 years). Figure 6 shows an OCT intensity projection, en face OCT angiogram at the level of CNVM, OCT retinal angiogram, OCT choriocapillaris angiogram, and retinal thickness map

from an 87 year old exudative AMD patient all extracted from a single volumetric scan. FA and ICGA acquired from the same patient are also shown for comparison. While FA and ICGA in Figures 6.6E and 6.6F show an area of diffuse dye leakage, OCT angiography shows a detailed CNVM vasculature as shown in Figure 6.6B. Note that FA and ICGA highlight different portions of the CNVM. The retinal angiogram in Figure 6.6C does not look too abnormal. On the contrary, as can be seen in Figure 6.6D, the choriocapillaris circulation is severely compromised particularly in the region where subretinal fluid is formed, as shown in the retinal thickness map in Figure 6.6G. Note that the CNVM casts angiographic shadows, similarly to thick retinal vessels, and therefore the region directly underneath the CNVM vasculature appears to have spurious circulation at the level of choriocapillaris. However, it is possible to visualize clearly that the CNVM area is surrounded by the area of impaired choriocapillaris circulation. The OCT intensity and angiographic cross-sectional images in Figures 6.6H and I extracted from the white dashed lines in Figures 6.6A and B clearly show that the abnormal CNVM vasculature is located above the Bruch's membrane.

Additional OCT angiograms from five exudative AMD cases are shown in Figure 6.7. Note that all CNVMs look different from each other. Out of 19 eyes with exudative AMD, CNVM was clearly visualized with OCT angiography in 16 eyes. Among the 3 eyes that OCT angiography failed to visualize CNVM, one was due to severe subretinal hemorrhage that attenuated OCT signal completely. The other two eyes were confirmed to have inactive CNVM due to anti-VEGF treatment. Considering that CNVM did not actually exist in these two eyes, OCT angiography yielded a high success rate of 94% for visualization of CNVM. In two of the eyes, CNVM was diagnosed after OCT angiography was performed. Choriocapillaris circulation abnormalities were not always correlated with retinal detachment due to subretinal fluid

formation. Retinal angiograms were excluded from the analysis because the retina was severely damaged due to subretinal fluid formation in many eyes with exudative AMD. In all 16 eyes that CNVM was visible with OCT angiography, CNVM was originating from regions with severely compromised choriocapillaris circulation, consistent with a previous OCT angiography finding in 5 exudative AMD eyes with CNVM[30].

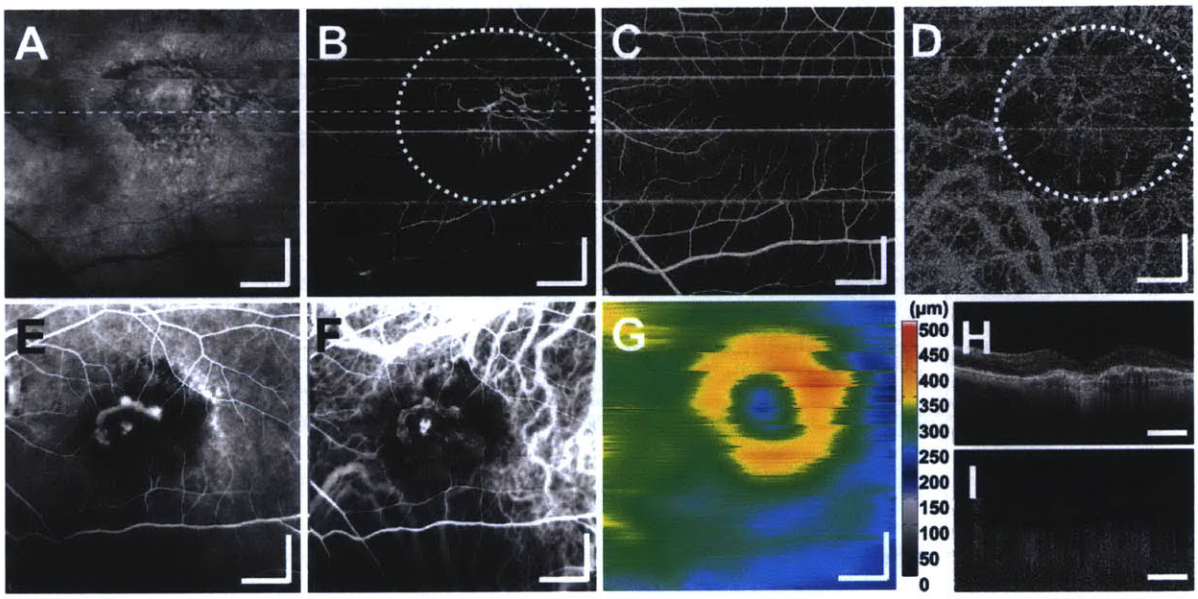


**Figure 6.6.** OCT, FA, and ICGA from an 87 year old exudative AMD patient. (A) OCT intensity projection, (B) en face OCT angiogram at the level of CNVM, (C) OCT retinal angiogram, (D) OCT choriocapillaris angiogram, (E) FA, (F) ICGA, and (G) OCT retinal thickness map. All OCT images are generated from a single volumetric scan. (H) and (I) are OCT intensity and angiographic cross-sections are extracted from the white dashed lines in (A) and (B). All OCT images are from a 6mm × 6mm area. All scale bars: 1mm.

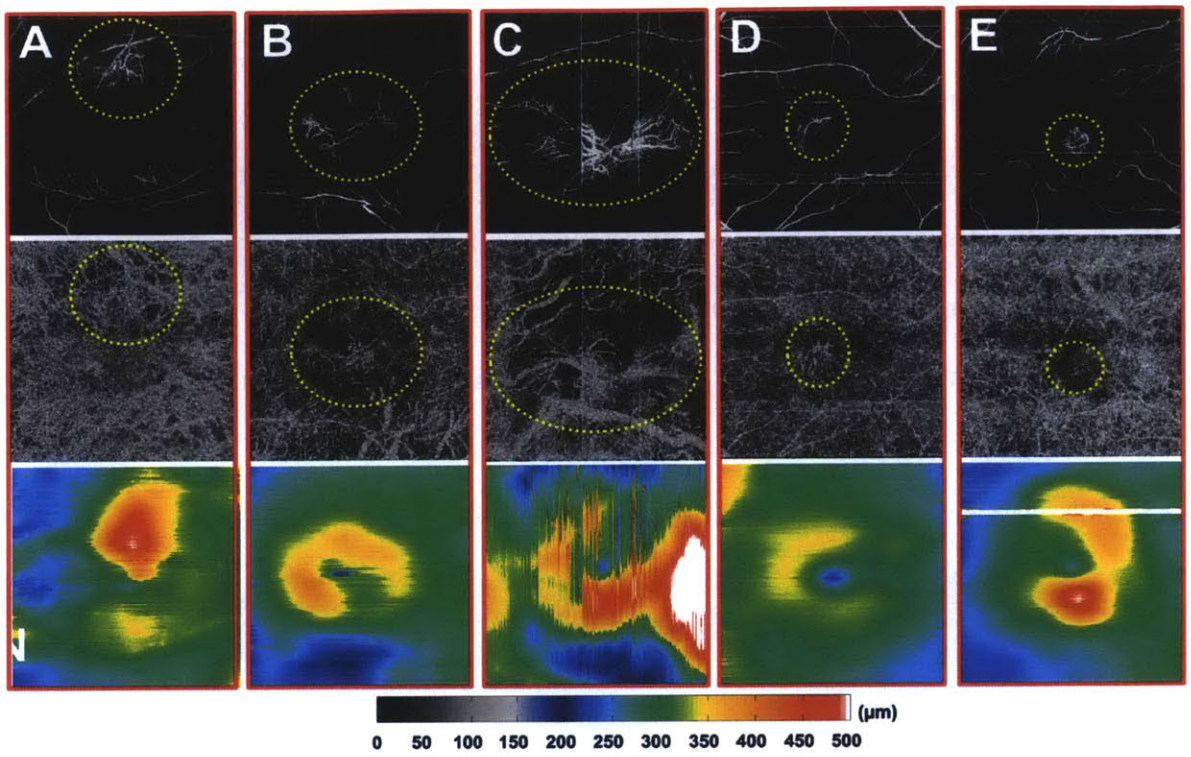


**Figure 6.7.** OCT angiograms of CNVM, OCT angiograms of choriocapillaris, and OCT retinal thickness maps from five exudative AMD patients. In general, CNVMs are surrounded by regions of impaired choriocapillaris circulation, which was observed for CNVM sizes from smaller than 500μm to larger than 5mm in the longest dimensions. Because of angiographic shadowing due to the CNVM vasculature, impaired choriocapillaris circulation underneath the CNVM appears as a halo of reduced choriocapillaris circulation in the choriocapillaris angiograms. All images acquired from 6mm × 6mm areas.

In addition, we also observed that in general the CNVM was surrounded by the area of severely impaired choriocapillaris circulation in 14 eyes out of the 16 eyes (Figure 6.7). This was true for CNVMs of longest dimensions from less than 500μm to greater than 5mm. This observation was possible because of the wide field size of 6mm × 6mm enabled by ultrahigh

speed OCT angiography. It should be noted that the CNVM casts angiographic shadow on choriocapillaris angiograms, and therefore, it is sometimes difficult to visualize impaired choriocapillaris circulation directly underneath the CNVM. However, it can be observed that the CNVM shadow results in a halo of impaired choriocapillaris circulation around the location of CNVM in the choriocapillaris angiograms. This was carefully confirmed in OCT intensity and angiographic B-scans manually as well. In the 2 eyes where CNVM was not proportional to the size of impaired choriocapillaris circulation, CNVM originated from the margin of GA or peripapillary atrophy and grew away from the atrophic region.

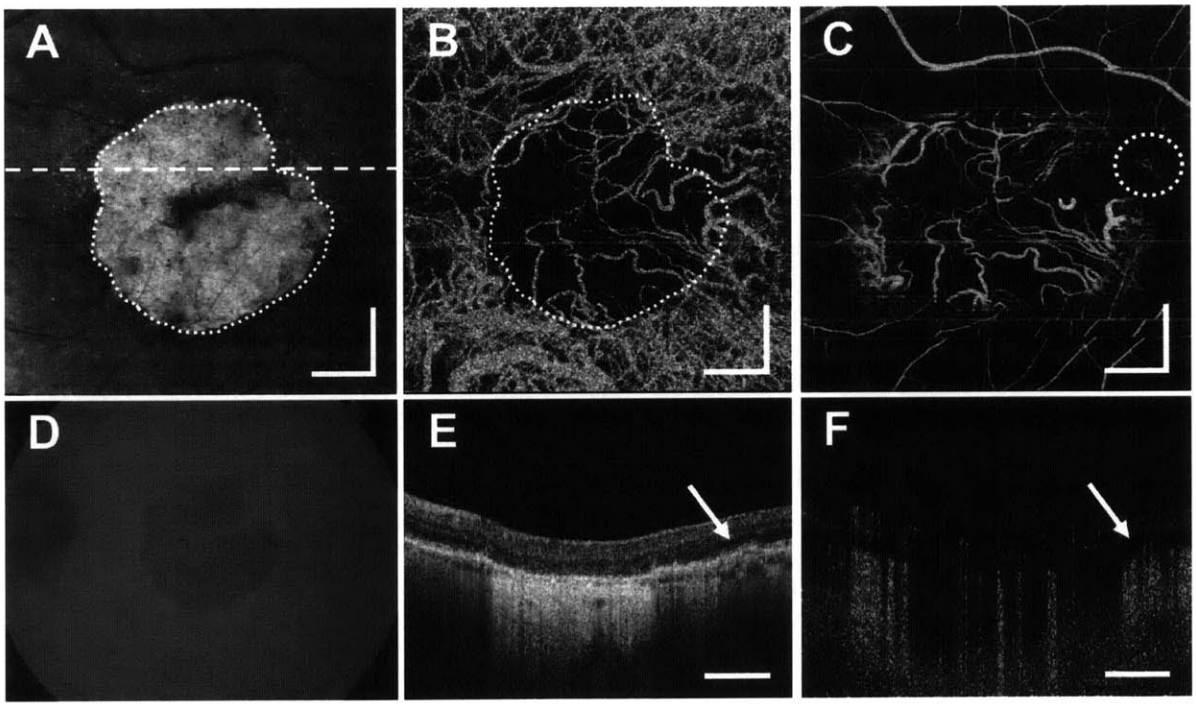


**Figure 6.8.** An example of CNV located next to GA from a 75 year old AMD patient. (A) OCT intensity projection shows the area of geographic atrophy clearly, as indicated by the white dotted contour. (B) OCT choriocapillaris angiogram. The GA area is delineated by a white dotted contour. (C) OCT angiography at the level above Bruch's membrane. The vasculature near the GA margin is from the normal choroid vasculature and appears

in (C) due to segmentation error in the region of GA. (D) FAF shows the region of GA. (E) and (F) show intensity and angiographic cross-sections extracted from the white dashed line in (A). The eye was originally diagnosed to have dry AMD with GA. However, OCT angiography could detect abnormal vasculature above the Bruch's membrane as indicated by white dotted circle in (C). The cross-sections (E) and (F) clearly show that the abnormal vasculature is located above the Bruch's membrane as indicated by the white arrows, but the intensity cross-section does not show significant subretinal fluid. All scale bars: 1mm.

The 17 eyes with active CNVM described above were clinically confirmed to have CNVM. However, it is interesting to note that even among the 11 dry AMD eyes with GA, the authors were able to detect neovascularization above the Bruch's membrane in 2 of the eyes using OCT angiography only without a priori knowledge (these two eyes were not counted as part of the 19 exudative AMD eyes because CNVM was not clinically confirmed using alternative techniques). Neither of the two eyes had significant subretinal fluid formation in OCT or hemorrhage in fundus photographs on the day of examination, and hence FA was never performed. Although it was not explicitly confirmed that these eyes had CNVM using FA, OCT angiography clearly showed abnormal vasculature above the Bruch's membrane in both en face and cross-sectional planes. An example is shown in Figure 6.8. Note that the OCT intensity image does not show significant subretinal fluid. However, the cross-sectional angiogram clearly shows abnormal vasculature above the Bruch's membrane. The CNVM is located close to the region of GA, and as observed in other CNVM examples in this study, is originating from a region with severely impaired choriocapillaris circulation, which in this particular case, extends from the area of GA.

*6.4.4 Early and Intermediate Dry AMD*

35 eyes from 26 early or intermediate dry AMD patients (77.5 ± 9.0 years old, range 59 to 92 years) were imaged. Figure 6.9 shows a fundus photo and OCT data from a 64 year old early dry AMD patient. The OCT angiogram of the retinal microvasculature in Figure 6.9D looks normal. However, the choriocapillaris exhibited a marked reduction and inhomogeneity in vascular density as shown in Figure 6.9G. Note that unlike in normal choriocapillaris, small feeder and draining choroidal vessels are visible in the angiogram because of the reduction in choriocapillaris circulation. It was not immediately clear whether the choriocapillaris abnormalities have direct association with retinal structural abnormalities above when visualized in en face planes as shown in Figures 6.9C and 6.9G. Figures 6.9E and 6.9F show OCT intensity and angiography cross-sections extracted from the dotted lines in Figure 6.9C. As shown in Figures 6.9E and 6.9F, it was possible to identify choriocapillaris abnormalities underneath some drusen as indicated by the yellow arrows. However, drusen locations were also often not correlated with choriocapillaris abnormalities as indicated by the red arrow. Very often, the outer retinal layers directly above focal reductions in choriocapillaris circulation did not appear worse than the neighboring regions.

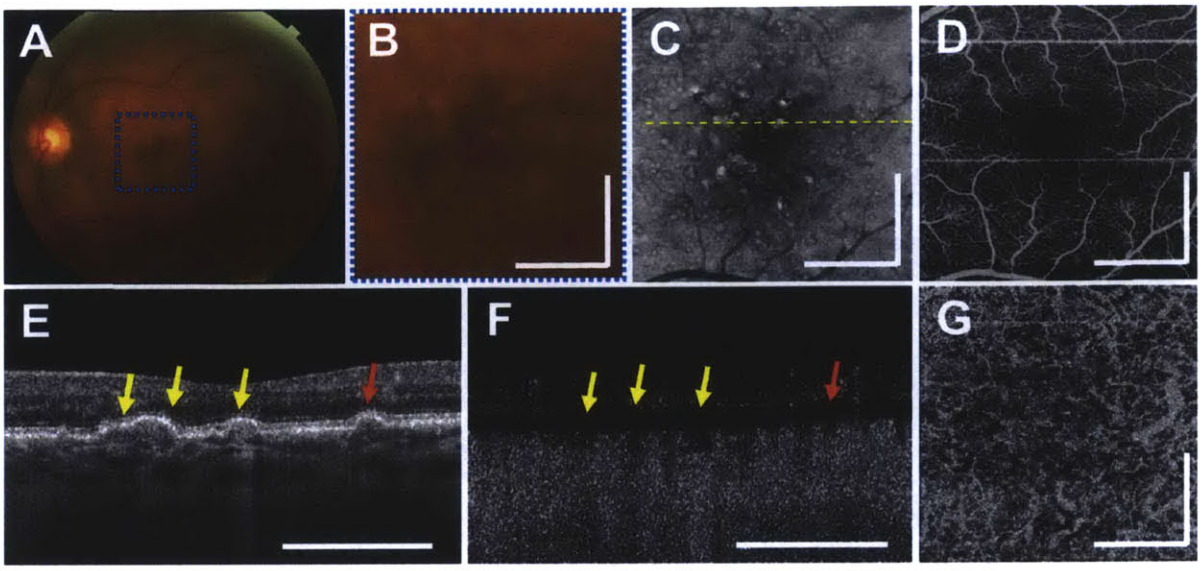


**Figure 6.9:** (A, B) Fundus photo and (C-G) OCT data from a 64 year old dry AMD patient. Fundus photo in (B) is a close up image over a 3mm × 3mm area indicated by blue dotted square in (A). OCT retinal angiogram in (D) looks normal. Abnormalities in (C) the OCT intensity projection and (G) the OCT choriocapillaris angiogram are not clearly associated spatially with one another. (E) OCT intensity cross-section and (F) angiographic cross-section extracted from the yellow dashed line in (C). Some drusen have focal reduction in choriocapillaris circulation underneath as indicated by yellow arrows in (E) and (F). However, drusen with normal choriocapillaris circulation underneath are also visible as indicated a red arrow. The OCT images acquired are from a 3mm × 3mm area. All scale bars: 1mm.

Compromised choriocapillaris circulation was commonly observed in early and intermediate dry AMD without GA as well as in advanced AMD with GA and/or CNV. In some cases, choriocapillaris abnormalities were localized to small areas with the longest dimension of ~1mm while in other cases abnormalities could be observed diffusely spread throughout the entire field

of view. In one eye, there was a large isolated well-defined area of impaired choriocapillaris circulation with the longest dimension ~1mm, with the choriocapillaris elsewhere in the field of view relatively normal. In this particular eye, there were drusen above the choriocapillaris abnormality. The degree of choriocapillaris circulation reduction varied widely between AMD subjects.

There was a general trend that more severe choriocapillaris circulation impairment, diffusely over the field of view, being associated with reduced overall RPE/photoreceptor integrity. In order to assess the relationship between choriocapillaris circulation and RPE/photoreceptor integrity, the choriocapillaris and the RPE/photoreceptor layer integrity were graded according to three categories: normal / mildly impaired, moderately impaired, and severely impaired. For the current analysis, only the average integrity over the 3mm × 3mm field of view was used to grade both the RPE/photoreceptor complex and choriocapillaris. Therefore, small isolated focal abnormalities were ignored if they occupied less than ~10% of the entire field of view.

For choriocapillaris, the abnormal features were defined as regions with at least one of the following: (1) inhomogeneous angiographic signal in the angiogram, (2) patches of reduced circulation with diffuse boundaries, (3) spots of non-perfusion with well-defined boundaries and with maximum dimension greater than ~200μm, (4) spots of reduced perfusion of any size, in between feeder/draining choroidal vessels, (5) any choroidal vessels larger than the choriocapillaris, such as feeder/draining vessels or larger choroidal vessels. Because it was occasionally observed in normal eyes in all age groups, all inter-capillary spots with well-defined boundaries and with maximum dimension less than ~150μm was considered normal. The three categories were defined as the following:

(A) Severely impaired: if the abnormal areas corresponding to non-perfusion, which appears completely black in the angiogram color map used in this manuscript (ignoring the normal inter-capillary spots that also appears black) and the area of visible larger choroidal vessels constitute more than 50% of the total area.

(B) Moderately impaired: if the sum of all abnormal areas satisfying the conditions (1-5), which are not necessarily completely black as is required to be severely impaired, constitute ~ 50% or more of the total area.

(C) Normal / mildly impaired otherwise

Using the grading criteria above, Figure 9G is considered moderately impaired because patches of reduced choriocapillaris circulation between feeder/draining vessels are clearly visible and they constitute more than 50% of the total area.

The RPE/photoreceptor layer was graded according to the following criteria.

(A) Normal / mildly impaired: the IS/OS ellipsoid and RPE look sharp and well-defined. The IS/OS signal comparable to the RPE signal.

(B) Moderately impaired: (1) the IS/OS signal somewhat lower than RPE signal and/or (2) the RPE appears noticeably diffuse and thickened.

(C) Severely impaired: the IS/OS severely disrupted. IS/OS signal is significantly lower than RPE signal. IS/OS band appears so irregular, diffuse, and faint that the entire RPE/photoreceptor band frequently appear as a single diffuse hyper-reflective band.

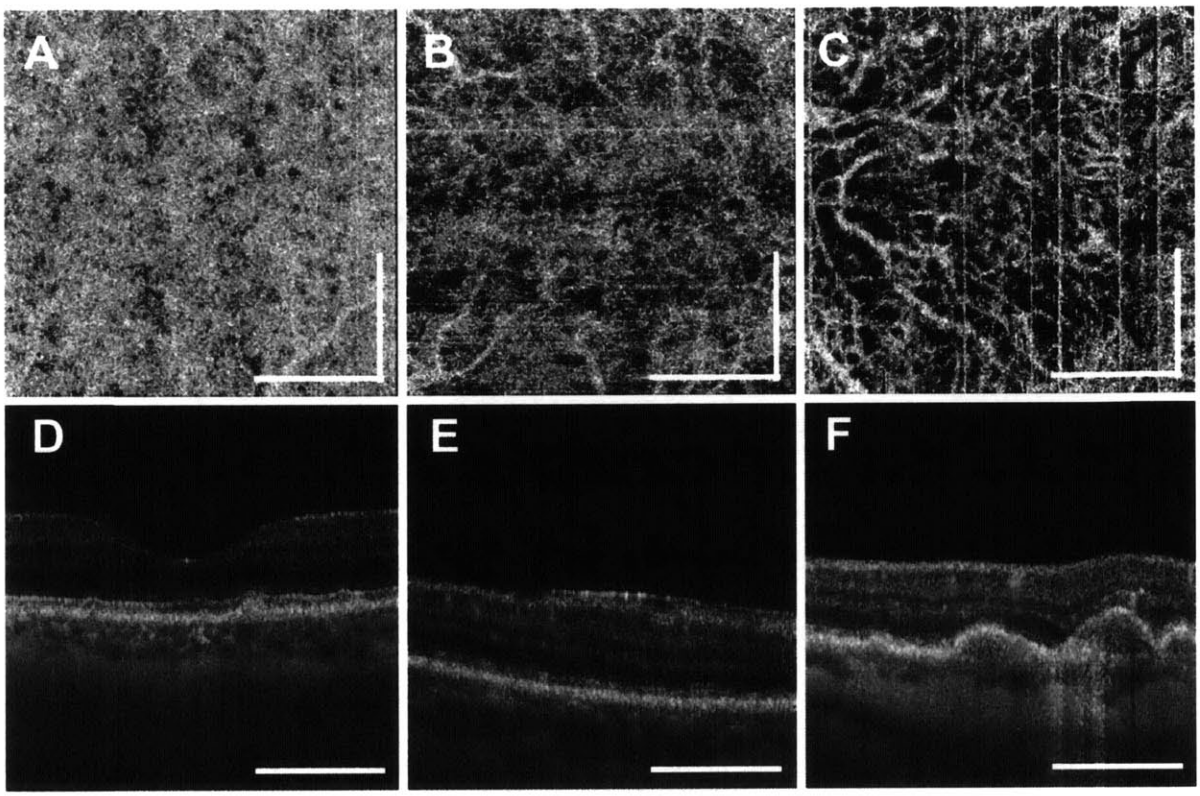


**Figure 6.10.** Choriocapillaris and RPE/photoreceptor showing varying degrees of integrity in dry AMD patients. (A-C) Normal / mildly impaired, moderately impaired, and severely impaired choriocapillaris circulation, respectively. Note that in (A), small isolated inter-capillary spots are not considered abnormal because they can also be found in young normal volunteers. On the contrary, the angiogram in (B) shows patches of inhomogeneous angiographic signal with diffuse boundaries throughout the field of view, which means the circulation is diffusely reduced. (D-F) Normal / mildly impaired, moderately impaired, and severely impaired RPE/photoreceptor layer, respectively. All scale bars: 1mm.

Figures 6.10A-C shows choriocapillaris angiograms from three representative dry AMD cases exhibiting varying degrees of compromised choriocapillaris circulation. Figures 6.10D-F

show the RPE/photoreceptor layers with varying degrees of integrity. Because RPE/photoreceptor integrity varied over the field of view, all 500 cross-sections per volume were used to evaluate the average integrity over the 3mm × 3mm field of view. Three graders independently graded the 35 randomized RPE and 35 randomized choriocapillaris data sets separately, and Spearman's rank correlation coefficient was calculated using the median grades. There was a statistically significant moderate correlation between choriocapillaris circulation and RPE/photoreceptor integrity ($r = 0.57$, $p < 0.001$). Figure 6.10G shows a bar plot of RPE/photoreceptor integrity as a function of choriocapillaris circulation.

### 6.5 Discussion

The fact that OCT angiography generates motion contrast offers several advantages over conventional dye-based angiography techniques. Because OCT angiography does not require the injection of exogenous dyes, it is completely noninvasive. Moreover, since OCT angiography can be performed at any time, unlike dye-based angiography which has a limited time window for imaging, OCT angiography greatly facilitates longitudinal studies as well as the investigation of transient functional response. Noninvasive longitudinal monitoring of nonexudative AMD patients may be useful for disease progression studies and treatment response monitoring. Visualizing different layers of vasculature in depth is challenging with dye-based OCT angiography because it generates two dimensional images. Furthermore, because the choriocapillaris is fenestrated, visualizing the choriocapillaris microvasculature with dye-based angiography is challenging due to dye leakage as well as signal scattering and attenuation from the RPE.

OCT angiograms of the choriocapillaris must be interpreted carefully because of the variation between normal subjects as shown in Figure 6.1. Therefore, in this study the choriocapillaris was

considered abnormal only if there was a significant reduction in choriocapillaris circulation compared to typical normal subjects or a marked inhomogeneity in the microvascular density over the field of view. Small isolated inter-capillary spots (longest dimension <150μm) showing no angiographic signal with well-defined boundaries were not necessarily considered abnormal because these were occasionally observed in healthy normal volunteers as well. However, this study is limited by the lack of older normal subjects which would be a more appropriate control group for AMD patients. In this study, varying degrees of choriocapillaris circulation abnormalities were frequently detected in AMD patients at all stages of the disease, including GA, CNV, and dry AMD.

Impaired choriocapillaris circulation in AMD patients outside the region of GA is surprising because previous histological findings suggest that choriocapillaris degeneration is secondary to RPE loss[2, 4]. Although the results in this study show that the choriocapillaris circulation in the region of GA is nearly completely reduced or there is choriocapillaris atrophy, many of the eyes with GA exhibited impaired choriocapillaris circulation even outside the margin of GA. This is not inconsistent with previous histological findings because OCT angiography and post mortem analyses measure fundamentally different characteristics of the choriocapillaris and choriocapillaris atrophy in histology versus impaired choriocapillaris circulation in OCT angiography should not be simply interpreted interchangeably.

When interpreting OCT angiography data, it is important to distinguish between complete atrophy versus reduced/impaired circulation. Because OCT angiography is based on motion contrast, care must be taken to differentiate very slow erythrocyte speeds in capillaries, or equivalently, impaired circulation at the capillary level, versus complete vascular degeneration and atrophy. In this study, we propose a method to distinguish these two conditions by using

different the time intervals for measuring motion contrast. By comparing every other B-scan (1↔3, 2↔4, 3↔5) instead of sequential B-scans (1↔2, 2↔3, 3↔4, and 4↔5) for motion contrast generation, it is possible to increase the comparison time interval by a factor of two. It should be emphasized that this measurement does not require the acquisition of separate OCT scans. Since the amount of motion contrast increases with increasing time interval, OCT angiography can be made more sensitive to slower erythrocyte movements by using this processing technique. The limitation of using longer time intervals is that faster erythrocyte movements now saturate motion contrast, and therefore, OCT angiography loses its ability to differentiate faster erythrocyte speeds. This essentially dictates that OCT angiography has a fixed dynamic range for erythrocyte speeds, and the dynamic range can be shifted down to a slower velocity range by increasing the time interval for comparison. In addition, increasing the time interval increases sensitivity to parasitic eye movements, which increases the noise level in OCT angiograms.

Figure 6.11 shows the effect of increasing OCT angiography flow sensitivity in a dry AMD patient with GA. The region of GA is delineated with a white dotted boundary. Note that outside the GA margin, the OCT angiography signal becomes denser in Figure 6.11C in the region that appears to have impaired circulation in Figure 6.11B. The region of GA still lacks circulation even with the increased time interval and increased flow sensitivity. This result suggests that in the region of GA, there is effectively no choriocapillaris perfusion, implying that it is highly likely that the choriocapillaris has atrophied. However, outside the GA margin, the choriocapillaris is still perfused, although circulation may be significantly reduced compared to normal eyes. Therefore the impaired choriocapillaris circulation visualized with OCT angiography outside the region of GA does not necessarily contradict previous histological

findings in GA. In general, impaired choriocapillaris circulation in OCT angiography does not imply complete atrophy. Figure 6.11 clearly demonstrates the ability of ultrahigh speed OCT angiography to assess local perfusion at the capillary level. Imaging speed is a key parameter which governs the sensitivity of OCT angiography because B-scans must be repeated with a short time interval in order to differentiate flow impairment. With slower OCT systems with longer time intervals for OCT angiography motion contrast generation, both slow and fast erythrocyte speeds appear saturated in the OCT angiogram. However, by controlling the time interval used to measure motion contrast, ultrahigh speed OCT angiography can distinguish impaired circulation in the retinal capillaries and choriocapillaris versus complete vascular degeneration. This capability promises to be important for elucidated disease pathogenesis as well as better monitoring disease progression and treatment response.

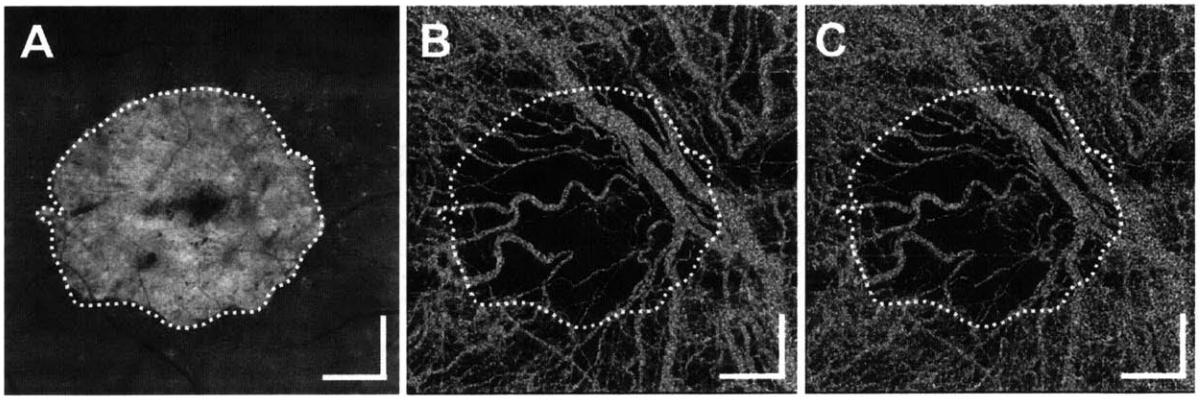


**Figure 6.11.** Effect of performing OCT angiography on sequential B-scans and every other B-scan on the GA patient shown in Figure 3. (A) The OCT intensity projection image is used to identify the margin of GA. The OCT angiogram of the choriocapillaris using every other B-scan shown in (B) in comparison to that using sequential B-scans shown in (A) demonstrates that lower OCT angiography signal outside the margin of GA is not due to a complete choriocapillaris atrophy, but due to reduced choriocapillaris

circulation. Note that in (B) the residual choriocapillaris circulation under the area of foveal sparing also gets more emphasized.

One limitation of the current study is that the number of normal eyes was small and mean age was younger compared to the AMD patients. In the future, a more comprehensive cohort of age-matched normal volunteers will be recruited. This is important in order to differentiate normal aging processes versus disease progression in AMD. However, even among dry AMD patients, a significant variation in choriocapillaris circulation impairment was observed, which was moderately correlated with the RPE/photoreceptor integrity. Considering that normal eyes should not have moderately or severely impaired RPE/photoreceptor layers, it is likely that choriocapillaris circulation impairment is involved in the pathogenesis of dry AMD. Choriocapillaris circulation impairment was not observed in the 6 eyes from normal volunteers older than 60 years old in this study. However further investigation is required to determine whether an older cohort of normal volunteers may show reduction in choriocapillaris circulation. It should also be emphasized that the causal relationship between the RPE/photoreceptor and choriocapillaris impairment cannot be determined from the current study.

One of key advantages of ultrahigh speeds for OCT angiography is that it enables higher image quality and larger retinal coverage. Because OCT angiography requires a repeated B-scan protocol, the field size is more limited compared to conventional OCT structural volumetric imaging. Small imaging fields are harder to use clinically and require cumbersome mosaicking in order to achieve retinal coverage. In this study, 6mm × 6mm field sizes could be achieved with high image quality in patients by using an SSOCT prototype with an A-scan rate of 400kHz. Instruments operating at A-scan rates of 100kHz would be limited to 3mm × 3mm field sizes if comparable image quality was desired. As shown in the Results section, many retinal pathologies,

such as GA and CNVM, require field sizes larger than 3mm × 3mm to image the region of interest, even when it is centered at the field of view. Moreover, vascular lesions do not necessarily occur at the center of the macula. Although it is possible to aim the image acquisition during imaging by adjusting the patient's fixation, this is not clinically practical. Centering the image acquisition on a specific retinal pathology is not only time consuming, but may be impossible if the locations of the lesions are not immediately apparent from structural images or fundus photographs. The data presented in this manuscript was acquired using a standardized imaging protocol which images the macula. Although current commercial OCT systems cannot provide retinal coverage as large as demonstrated in this manuscript, this problem will eventually be solved as the imaging speeds of future commercial OCT increase.

Unlike dye-based angiography, OCT angiography does not visualize show leakage. Although this could be a limitation for the investigation of retinal pathologies involving alterations in vascular permeability, it also has advantages. For example, leakage of CNVM in exudative AMD is used to confirm the existence of CNVM, however leakage can produce hyper fluorescence which impairs visibility and visualization is limited to a two dimensional image without depth resolution. OCT angiography, however, directly visualizes abnormal vasculature in three dimensions, and may be more sensitive for monitoring treatment response. In addition, as shown in Figure 6.6, ICGA and FA highlight different components of CNVM vasculature, potentially due to the difference in molecular sizes, while OCT angiography shows both of them simultaneously. In our study, OCT angiography could visualize CNVM in most exudative AMD patients with active CNVM. The only case OCT angiography failed to visualize CNVM was when there was significant subretinal hemorrhage that attenuated the OCT signal. However, even in this case, subretinal fluid was visible as a marker in OCT structural images.

## 6.6 Conclusion

One of the most interesting clinical findings in the study is that choriocapillaris circulation abnormalities were observed at all stages of AMD including dry AMD with and without GA and CNV. In eyes with GA, choriocapillaris circulation was severely impaired even outside the margin of GA. It would be clinically and scientifically interesting to investigate if the GA progression rate is correlated with choriocapillaris circulation near the GA margin. In exudative AMD, most CNVMs were surrounded by regions of impaired choriocapillaris circulation for all sizes from smaller than 1mm to larger than 5mm in their longest dimensions. Although more comprehensive studies are required to assess the effects of anti-VEGF treatments performed on patients prior to OCT imaging, findings from this small scale study suggest that CNVMs formed in regions to compensate for reduced perfusion from the choroid. In fact, in two of the eyes with GA, where choriocapillaris circulation was severely impaired outside the GA margin, abnormal vasculature above the Bruch's membrane was detected by OCT angiography without a priori knowledge from ophthalmoscopic exam. In these two eyes, the CNVMs did not develop subretinal fluid, which was the reason the CNVMs were not clinically recognized, and the CNVMs may have acted as a blood supply to the outer retina in the nearby region. If this hypothesis is correct, then the decision to perform anti-VEGF treatments on these eyes should be approached with caution. In early and intermediate dry AMD, impaired choriocapillaris circulation was commonly observed, in this finding was moderately correlated with RPE/photoreceptor integrity. Although more comprehensive studies involving a larger number of age-matched normal volunteers is required to differentiate the effects of normal aging and AMD progression on choriocapillaris circulation, the current study suggests that impaired choriocapillaris circulation is involved in the pathogenesis of AMD. The vascular abnormalities

visualized with OCT angiography at early as well as late stages of AMD suggest that OCT angiography may be useful for monitoring disease progression as well as treatment response. The ability to more sensitively assess treatment response over shorter study durations is especially important for pharmaceutical development.

## References


1. Sarks JP, Sarks SH, Killingsworth MC. Evolution of Geographic Atrophy of the Retinal-Pigment Epithelium. Eye. 1988;2:552-77. PubMed PMID: 2476333.

2. McLeod DS, Grebe R, Bhutto I, Merges C, Baba T, Lutty GA. Relationship between RPE and Choriocapillaris in Age-Related Macular Degeneration. Investigative Ophthalmology & Visual Science. 2009;50(10):4982-91. doi: Doi 10.1167/Iovs.09-3639. PubMed PMID: 19357355.

3. Mullins RE, Johnson MN, Faidley EA, Skeie JM, Huang JA. Choriocapillaris Vascular Dropout Related to Density of Drusen in Human Eyes with Early Age-Related Macular Degeneration. Investigative Ophthalmology & Visual Science. 2011;52(3):1606-12. doi: Doi 10.1167/Iovs.10-6476. PubMed PMID: 21398287; PubMed Central PMCID: PMC3101687.

4. Bhutto I, Lutty G. Understanding age-related macular degeneration (AMD): Relationships between the photoreceptor/retinal pigment epithelium/Bruch's membrane/choriocapillaris complex. Mol Aspects Med. 2012;33(4):295-317. doi: DOI 10.1016/j.mam.2012.04.005. PubMed PMID: 22542780; PubMed Central PMCID: PMC3392421.

5. Gragoudas ES, Adamis AP, Cunningham ET, Feinsod M, Guyer DR, Neova VISO. Pegaptanib for neovascular age-related macular degeneration. New England Journal of Medicine. 2004;351(27):2805-16. doi: Doi 10.1056/Nejmoa042760. PubMed PMID: ISI:000226004300005.

6. Brown DM, Kaiser PK, Michels M, Soubrane G, Heier JS, Kim RY, Sy JP, Schneider S, Grp AS. Ranibizumab versus verteporfin for neovascular age-related macular degeneration. New England Journal of Medicine. 2006;355(14):1432-44. PubMed PMID: WOS:000240976200005.

7. Rosenfeld PJ, Brown DM, Heier JS, Boyer DS, Kaiser PK, Chung CY, Kim RY, Grp MS. Ranibizumab for neovascular age-related macular degeneration. New England Journal of Medicine. 2006;355(14):1419-31. PubMed PMID: WOS:000240976200004.

8. Schmidt-Erfurth UM, Pruente C. Management of neovascular age-related macular degeneration. Prog Retin Eye Res. 2007;26(4):437-51. doi: 10.1016/j.preteyeres.2007.03.002. PubMed PMID: WOS:000247453300005.

9. Bressler NM. Antiangiogenic Approaches to Age-Related Macular Degeneration Today. Ophthalmology. 2009;116(10):S15-S23. doi: DOI 10.1016/j.ophtha.2009.06.048. PubMed PMID: ISI:000270794700003.

10. Martin DF, Maguire MG, Fine SL, Ying GS, Jaffe GJ, Grunwald JE, Toth C, Redford M, Ferris FL, 3rd. Ranibizumab and bevacizumab for treatment of neovascular age-related macular degeneration: two-year results. Ophthalmology. 2012;119(7):1388-98. Epub 2012/05/05. doi: 10.1016/j.ophtha.2012.03.053

S0161-6420(12)00321-1 [pii]. PubMed PMID: 22555112; PubMed Central PMCID: PMC3389193.

11. Rosenfeld PJ, Moshfeghi AA, Puliafito CA. Optical coherence tomography findings after an intravitreal injection of bevacizumab (Avastin (R)) for neovascular age-related macular degeneration. Ophthal Surg Las Im. 2005;36(4):331-5. PubMed PMID: WOS:000232140900012.

12. Kaiser PK, Blodi BA, Shapiro H, Acharya NR, Grp MS. Angiographic and optical coherence tomographic results of the MARINA study of ranibizumab in neovascular age-related macular degeneration. Ophthalmology. 2007;114:1868-75. doi: 10.1016/j.ophtha.2007.04.030. PubMed PMID: WOS:000249772500011.

13. Fung AE, Lalwani GA, Rosenfeld PJ, Dubovy SR, Michels S, Feuer WJ, Puliafito CA, Davis JL, Flynn HW, Esquiabro M. An optical coherence tomography-guided, variable dosing regimen with intravitreal ranibizumab (lucentis) for neovascular age-related macular degeneration. Am J Ophthalmol. 2007;143(4):566-83. PubMed PMID: ISI:000245537800003.

14. Lalwani GA, Rosenfeld PJ, Fung AE, Dubovy SR, Michels S, Feuer W, Davis JL, Flynn HW, Jr., Esquiabro M. A variable-dosing regimen with intravitreal ranibizumab for neovascular age-related macular degeneration: year 2 of the PrONTO Study. Am J Ophthalmol. 2009;148(1):43-58 e1. PubMed PMID: 19376495.

15. Makita S, Hong Y, Yamanari M, Yatagai T, Yasuno Y. Optical coherence angiography. Optics Express. 2006;14(17):7821-40. doi: Doi 10.1364/Oe.14.007821. PubMed PMID: 19529151.

16. Fingler J, Schwartz D, Yang CH, Fraser SE. Mobility and transverse flow visualization using phase variance contrast with spectral domain optical coherence tomography. Optics Express. 2007;15(20):12636-53. doi: Doi 10.1364/Oe.15.012636. PubMed PMID: 19550532.

17. Tao YK, Davis AM, Izatt JA. Single-pass volumetric bidirectional blood flow imaging spectral domain optical coherence tomography using a modified Hilbert transform. Optics Express. 2008;16(16):12350-61. doi: Doi 10.1364/Oe.16.012350. PubMed PMID: 18679512.

18. An L, Wang RKK. In vivo volumetric imaging of vascular perfusion within human retina and choroids with optical micro-angiography. Optics Express. 2008;16(15):11438-52. PubMed PMID: 18648464.

19. Mariampillai A, Standish BA, Moriyama EH, Khurana M, Munce NR, Leung MKK, Jiang J, Cable A, Wilson BC, Vitkin IA, Yang VXD. Speckle variance detection of microvasculature using swept-source optical coherence tomography. Opt Lett. 2008;33(13):1530-2. doi: Doi 10.1364/Ol.33.001530. PubMed PMID: 18594688.

20. Vakoc BJ, Lanning RM, Tyrrell JA, Padera TP, Bartlett LA, Stylianopoulos T, Munn LL, Tearney GJ, Fukumura D, Jain RK, Bouma BE. Three-dimensional microscopy of the tumor

microenvironment in vivo using optical frequency domain imaging. Nat Med. 2009;15(10):1219-U151. doi: Doi 10.1038/Nm.1971. PubMed PMID: 19749772; PubMed Central PMCID: PMC2759417.

21. Yu LF, Chen ZP. Doppler variance imaging for three-dimensional retina and choroid angiography. J Biomed Opt. 2010;15(1). doi: Artn 016029
Doi 10.1117/1.3302806. PubMed PMID: 20210473; PubMed Central PMCID: PMC2839803.

22. Jonathan E, Enfield J, Leahy MJ. Correlation mapping: rapid method for retrieving microcirculation morphology from optical coherence tomography intensity images. Dynamics and Fluctuations in Biomedical Photonics Viii. 2011;7898. doi: Artn 78980m
Doi 10.1117/12.879812. PubMed PMID: ISI:000292039000013.

23. Blatter C, Klein T, Grajciar B, Schmoll T, Wieser W, Andre R, Huber R, Leitgeb RA. Ultrahigh-speed non-invasive widefield angiography. J Biomed Opt. 2012;17(7). doi: Artn 070505
Doi 10.1117/1.Jbo.17.7.070505. PubMed PMID: 22894461.

24. von Sallmann L. The structure of the eye. Arch Ophthalmol. 1961;66(6):920-1. doi: 10.1001/archopht.1961.00960010922023.

25. Kurokawa K, Sasaki K, Makita S, Hong Y-J, Yasuno Y. Three-dimensional retinal and choroidal capillary imaging by power Doppler optical coherence angiography with adaptive optics. Optics Express. 2012;20(20):22796-812. doi: 10.1364/oe.20.022796.

26. Braaf B, Vienola KV, Sheehy CK, Yang Q, Vermeer KA, Tiruveedhula P, Arathorn DW, Roorda A, de Boer JF. Real-time eye motion correction in phase-resolved OCT angiography with tracking SLO. Biomed Opt Express. 2013;4(1):51-65. Epub 2013/01/11. doi: 10.1364/BOE.4.000051
177976 [pii]. PubMed PMID: 23304647; PubMed Central PMCID: PMC3539196.

27. Kim DY, Fingler J, Zawadzki RJ, Park SS, Morse LS, Schwartz DM, Fraser SE, Werner JS. Optical imaging of the chorioretinal vasculature in the living human eye. Proc Natl Acad Sci U S A. 2013;110(35):14354-9. Epub 2013/08/07. doi: 10.1073/pnas.1307315110. PubMed PMID: 23918361; PubMed Central PMCID: PMC3761584.

28. Choi W, Mohler KJ, Potsaid B, Lu CD, Liu JJ, Jayaraman V, Cable AE, Duker JS, Huber R, Fujimoto JG. Choriocapillaris and Choroidal Microvasculature Imaging with Ultrahigh Speed OCT Angiography. Plos One. 2013;8(12):e81499. Epub 2013/12/19. doi: 10.1371/journal.pone.0081499
PONE-D-13-33807 [pii]. PubMed PMID: 24349078; PubMed Central PMCID: PMC3859478.

29. Schwartz DM, Fingler J, Kim DY, Zawadzki RJ, Morse LS, Park SS, Fraser SE, Werner JS. Phase-variance optical coherence tomography: a technique for noninvasive angiography. Ophthalmology. 2014;121(1):180-7. Epub 2013/10/26. doi: 10.1016/j.ophtha.2013.09.002
S0161-6420(13)00807-5 [pii]. PubMed PMID: 24156929.

30. Jia Y, Bailey ST, Wilson DJ, Tan O, Klein ML, Flaxel CJ, Potsaid B, Liu JJ, Lu CD, Kraus MF, Fujimoto JG, Huang D. Quantitative Optical Coherence Tomography Angiography of Choroidal Neovascularization in Age-related Macular Degeneration. Ophthalmology. (0). doi: http://dx.doi.org/10.1016/j.ophtha.2014.01.034.

31. Grulkowski I, Liu JJ, Potsaid B, Jayaraman V, Lu CD, Jiang J, Cable AE, Duker JS, Fujimoto JG. Retinal, anterior segment and full eye imaging using ultrahigh speed swept source OCT with vertical-cavity surface emitting lasers. Biomedical optics express. 2012;3(11):2733-51. PubMed PMID: 23162712; PubMed Central PMCID: PMC3493240.

32. Choi W, Potsaid B, Jayaraman V, Baumann B, Grulkowski I, Liu JJ, Lu CD, Cable AE, Huang D, Duker JS, Fujimoto JG. Phase-sensitive swept-source optical coherence tomography imaging of the human retina with a vertical cavity surface-emitting laser light source. Opt Lett. 2013;38(3):338-40. PubMed PMID: 23381430; PubMed Central PMCID: PMC3721635.

33. Kassoff A, Kieval S, Mehu M, Buehler J, Eglow M, Kaufman F, Margherio RR, Cox MS, Garretson B, Hassan T, Ruby A, Trese MT, Werner JC, Williams GA, Regan V, Manatrey P, Cumming K, Zajechowski M, Falk R, Streasick P, Szydlowski L, Dreyer RF, Ma C, Beardsley C, Crider H, Capone A, Aaberg TM, Martin D, Saperstein D, Sternberg P, Curtis L, Stribling B, Gilman J, Myles B, Swords R, Orth DH, Flood TP, Civantos J, deBustros S, Packo KH, MacLeod C, Morrison C, Bryant DA, Doherty D, Sandoval S, Seddon JM, Pinnolis MK, Jones-Devonish DA, Crouse VD, Snow KK, Evans C, Davis N, Callahan C, Walsh D, Dubois J, Burton I, Ferris FL, Chew EY, Csaky K, McCarthy SA, Dabas KH, Goodman L, Kim YJ, Lopez P, Mercer R, Ayres LM, LaRean T, Randall A, Chicca M, Ciatto PF, Kuehl E, Kivitz I, Koutsandreas D, Friberg TR, Eller A, Gorin MB, Alexander J, Mack B, Bressler SB, Bressler NM, Cassel G, Goldberg M, Haller JA, Ratner L, Schachat AP, Sherman SH, Sunness JS, Schenning S, Sackett C, Cain D, Emmert D, George T, Wheeler S, Elman MJ, Ballinger R, Betancourt A, Glasser D, Lammlein J, Seff R, Shuman M, Starr J, Carrigan A, Ringrose C, Mathews T, Sotirakos P, Cain T, Chandra SR, Myers FL, Nork TM, Stevens T, Blodi B, Gottlieb J, Perkins T, Blatz M, Walker W, Harrison B, Knutson G, Krolnik D, Somers G, Davis MD, Klein BEK, Klein R, Hubbard L, Magli YL, Brickbauer J, Ansay S, Armstrong J, Neider M, Wabers H, Baliker J, Kastorff L, Laher K, Badal D, Geithman PL, Miner KD, King WN, Osterly KR, Dohm KL, Onofrey JA, Esser B, Hurtenback C, Fisher MR, Robinson NL, Reimers J, Miller D, Bowman B, Gunter E, Sowell A, Lindblad AS, Ederer F, Milton RC, Gensler G, Anand R, Entler G, Stine E, Berlin SH, Scholl PR, Mengers SA, Ferris FL, Chew EY, Sperduto R, Kurinij N, Grp A-REDSR. The Age-Related Eye Disease Study (AREDS): Design implications AREDS report no. 1. Control Clin Trials. 1999;20(6):573-600. PubMed PMID: 10588299; PubMed Central PMCID: PMC1473211.

34. Guizar-Sicairos M, Thurman ST, Fienup JR. Efficient subpixel image registration algorithms. Opt Lett. 2008;33(2):156-8. doi: 10.1364/ol.33.000156.

# Chapter 7

# Ultrahigh Speed OCT Angiography in Diabetic Eyes Using Swept Source Optical Coherence Tomography

## 7.1 Overview

The purpose of this chapter is to investigate the potential of ultrahigh speed optical coherence tomography (OCT) angiography in visualizing microvascular changes in the retina and choriocapillaris of diabetic eyes using the ultrahigh speed vertical cavity surface emitting laser (VCSEL) swept source OCT system deployed to the New England Eye Center. 35 normal volunteers and 50 diabetic patients with and without retinopathy were recruited for the study. OCT angiography was performed by scanning 3mm × 3mm and 6mm × 6mm areas centered at the fovea in 69 normal eyes, 9 eyes with proliferative diabetic retinopathy (PDR), 29 eyes with non-proliferative diabetic retinopathy (NPDR), and 53 diabetic eyes without retinopathy. For both field sizes, the scan pattern used was 500 A-scans per B-scan × 500 cross-sections × 5 repeated B-scans per cross-section. Relative erythrocyte motions at a given cross-section were mapped by comparing the sequentially acquired B-scans via intensity cross-correlation. For en face visualization of the retinal vasculature, the Bruch's membrane was segmented semi-automatically and different depth ranges above were averaged to generate mean projection images. The choriocapillaris angiogram was generated by extracting a single en face plane below the Bruch's membrane. Retinal and choriocapillaris vascular abnormalities were observed in all stages of retinal disease. Retinal vascular abnormalities detectable with OCT angiography in PDR and NPDR include clustered capillaries, dilated capillary segments, tortuous capillaries,

capillary dropouts, reduced capillary density, abnormal capillary loops corresponding to microaneurysms, reduced capillary perfusion, vascular remodeling near the FAZ, and FAZ enlargement. In PDR, retinal neovascularization above the inner limiting membrane could be visualized. Diffuse or focal abnormalities in choriocapillaris circulation could also be visualized in PDR and NPDR. Retinal microvascular abnormalities were detected in >30% of the diabetic eyes without retinopathy by inspecting different vascular beds separately utilizing the depth-resolving capability of OCT angiography. Abnormalities in choriocapillaris circulation were also detected in >40% of the diabetic eyes without retinopathy. The abilities of ultrahigh speed OCT angiography strongly suggest that OCT angiography may be a powerful tool for understanding pathogenesis, treatment response monitoring, pharmaceutical development, and earlier detection of vascular abnormalities in diabetic eyes. Dr. Nadia K. Waheed contributed significantly to clinical data analysis and recruitment of the subjects. Eric Moult contributed significantly to OCT image processing, OCT data analysis, and OCT data management. Dr. Mehreen Adhi imaged all the patients and recruited normal volunteers for the study. ByungKun Lee and Chen D. Lu contributed to developing and managing the clinical ultrahigh speed swept source OCT system. Dr. Vijaysekhar Jayaraman developed the VCSEL light source used in the OCT system. Dr. Caroline R. Baumal contributed to patient recruitment and clinical data analysis. Dr. Jay S. Duker, and Prof. James G. Fujimoto provided supervision and guidance.

### 7.2 Introduction

Both retinal and choroidal blood circulation is believed to be altered in diabetic retinopathy (DR), a leading cause of vision loss or impairment in developed countries. There are multiple vascular abnormalities that are potential early markers for DR. Early changes in non-proliferative diabetic retinopathy (NPDR) include capillary pericyte loss, basement membrane thickening, smooth

muscle cell loss and microaneurysms[1-7]. Microaneurysms are important markers for predicting DR progression[8, 9]. A histological study showed microaneurysms cluster upstream from capillary non-perfusion, suggesting they contribute to capillary occlusion[10]. Foveal avascular zone (FAZ) enlargement and capillary dropout have been observed in fluorescein angiography (FA) studies[11-14]. Although DR is generally considered to be a disease of retinal vessels, several post mortem studies suggest that vascular abnormalities occur in the choroid as well. Histological and electron microscopy studies showed choriocapillaris degeneration as well as basal laminar deposit formation associated with diabetes[15-19].

Although diabetic retinopathy is a disease caused by vascular abnormalities, direct visualization of the retinal and choroidal microvasculature in diabetic eyes is not routinely performed, especially for early diagnosis of retinopathy, partially due to the lack of technology that can image the microvasculature noninvasively. Conventional dye-based angiography, such as FA and indocyanine green angiography (ICGA) can visualize the retinal microvasculature by intravenous injection of exogenous dyes. However, these techniques allow short time windows for imaging, and imaging cannot be repeated multiple times during a single patient visit. Furthermore, visualization of the choriocapillaris is challenging with FA because of vessel fenestration[20], which blurs the choriocapillaris due to dye leakage. In addition, the heavily pigmented retinal pigment epithelium (RPE) and choroid heavily attenuates and scatters the signal at the relatively short wavelengths utilized in FA and ICGA.

Optical coherence tomography (OCT) angiography is a relatively new imaging technique that can visualize the retinal and choroidal microvasculature without the injection of exogenous dyes[21-29]. Unlike FA and ICGA, OCT angiography is based on motion contrast imaging. By comparing OCT B-scans repeatedly acquired from a given cross-sectional position, fluctuations

in OCT signal due to erythrocyte movements in retinal vessels and capillaries can be mapped to generate OCT angiograms. Because OCT is a depth-resolved imaging technique, the resulting angiograms are three-dimensional as well, which enables separate visualization of the microvasculature at multiple depths in the retina and choroid, a unique property that conventional dye-based angiography does not possess. Therefore, OCT angiography can separately visualize the choriocapillaris, as demonstrated recently by multiple groups[30-33]. Because OCT angiography is completely non-invasive, imaging can be repeated multiple times if necessary. Unlike FA and ICGA operating at specific wavelengths, OCT angiography can also be performed at longer wavelengths near 1μm, which enables deeper penetration of light into tissue and ocular opacities such as cataract. Since OCT angiography is an extension of standard OCT imaging, comprehensive diagnosis based on tissue and vascular structure becomes possible. In addition to these advantages, OCT is already a clinical standard in ophthalmology clinics, which makes OCT angiography well-positioned to be widely applicable in the near future.

Because OCT angiography requires repeated scan protocols, higher imaging speeds are necessary compared to standard structural imaging. Therefore, application of the technique has only recently been demonstrated in a small number of patients with diabetes. In 2012, Kim et al. demonstrated imaging of the FAZ of 2 healthy subjects and 8 diabetic patients[34]. In 2014, Schwartz et al. reported imaging results from 1 normal subject and 1 NPDR patient[35]. Clearly, there is a need to investigate OCT angiography in a larger number of diabetic patients in order to assess the potential of the technique in diabetes.

In this study, we investigate the potential of ultrahigh speed OCT angiography in visualizing retinal and choroidal microvascular changes in patients with diabetes mellitus. Using an ultrahigh speed swept source OCT prototype with a vertical cavity surface emitting laser

(VCSEL) swept light source recently developed our group[36, 37] ENREF 37, ultrahigh speed OCT angiography imaging at 400kHz A-scan rate was performed in diabetic patients. The ultrahigh imaging speed enabled higher angiography image quality with better retinal coverage. Diabetic patients with proliferative diabetic retinopathy (PDR), nonproliferative diabetic retinopathy (NPDR), and no retinopathy were imaged, and the angiograms at different retinal depths were inspected to investigate vascular abnormalities that can be visualized with ultrahigh speed OCT angiography.

### 7.3 Methods

35 normal volunteers, 7 PDR patients, 16 NPDR patients, and 30 diabetic patients without retinopathy were imaged for this study. The same normal volunteers used in a separate study, Ultrahigh Speed OCT Angiography in Age-Related Macular Degeneration, were used as controls in this study. The study was approved by the Institutional Review Boards at the Massachusetts Institute of Technology (MIT) and the New England Eye Center (NEEC). All participants including healthy normal volunteers and patients were imaged in the ophthalmology clinic at NEEC, and signed written informed consent was obtained from all subjects before OCT angiography imaging. The research adhered to the Declaration of Helsinki and the Health Insurance Portability and Accountability Act. The entry criteria for diabetic patients were based on the Early Treatment Diabetic Retinopathy Study (ETDRS). Patients with Type 1 or Type 2 diabetes without any retinopathy documented on a detailed dilated ophthalmic exam were classified as diabetic patients without retinopathy. In selected patients with DR, FA was performed to correlate the image with the OCT angiogram.

An ultrahigh speed SSOCT system, developed at MIT, was used for OCT angiography. The system was deployed to NEEC in November, 2013. A previous paper[37] from our group provides

a detailed description of a similar system and as such only some of the more pertinent details are outlined here. To achieve a 400kHz A-scan rate our prototype system employs a VCSEL swept light source, which is centered at a 1μm wavelength. The longer wavelength, relative to the commercial standard of ~800nm provides superior light penetration into pigmented tissues, such as the RPE and choroid. The system uses an A-scan rate of 400kHz. Using a Mach-Zehnder interferometer a 1.1 GHz signal was generated and was used to externally clock the analog-to-digital acquisition card (Alazar Technologies, ATS9360). This sampling rate allowed for s ~2.1mm in tissue. A fiber Bragg grating was used to phase stabilize the system resulting in a phase stability of ~1.5mrad at a signal-to-noise ratio of 57dB. The system sensitivity was ~98dB with ~1.8mW incident power and the axial and transverse resolutions in tissue were ~8-9μm and ~10μm full-width at half-maximum (FWHM), respectively.

In this study two different field sizes, 6mm × 6mm and 3mm × 3mm, were used. For both field sizes, 2500 B-scans were acquired from 500 uniformly sampled locations using 5 repeated B-scans per location for motion contrast imaging. Each B-scan consisted of 500 A-scans yielding a total 500×500×5 A-scans per OCT volume; the total acquisition, with a 400kHz A-scan rate and a galvanometer duty cycle of 80-85%, was ~3.9 seconds per volume. The volumetric scan pattern of 500 × 500 × 5 A-scans corresponds to and transverse isotropic sampling of the retina at a 12μm interval for the 6mm × 6mm field size. This sampling rate provides ~2× oversampling compared to the ~24μm Airy disk diameter of the OCT beam on the retina. Smaller field sizes result in transverse sampling rates that are proportionally more oversampled and that provide higher OCT angiogram quality. For all field sizes sequential B-scans are separated by ~1.5ms and the line dwell time is ~7.5ms (~1.5ms × 5) per line.

To generate the OCT angiograms sequential intensity B-scans acquired from the same location, were compared. Our scanning protocol used 5 repeats for each B-scan location, thereby generating four OCT angiograms per B-scan location. These four angiograms were averaged to improve the signal-to-noise. The principle of OCT angiography is that intensity images acquired from stationary tissue will be identical, because there is no change in scattering profiles as a function of time. Tissue that include moving scatterers, such as erythrocytes in blood vessels, will have temporally dependent scattering profiles and will therefore produce temporally dependent intensity B-scans. Quantitating the changes in the intensity B-scans as a function of time allows cross-sectional motion contrast images to be formed. Tracking the temporal dependence over different B-scan locations allows volumetric OCT angiograms to be generated. In all cases a previously described registration algorithm[38] was used to motion-correct B-scans prior to comparison. It should be noted that angiographic shadows are often cast by large retinal and choroidal vessels. This phenomenon is due to blood's high scattering characteristic which causes more rapidly changing speckle pattern below the vessel.

Both the retinal and choroidal vasculature are contained within the three dimensional volumetric angiogram. Choriocapillaris and retinal microvasculature were imaged separately, by automatically segmenting the Bruch's membrane and internal limiting membrane (ILM) using intensity B-scans in the volumetric data set. The segmented Bruch's membrane and ILM locations were then used for partitioning the volumetric OCT angiogram. Using the locations of the Bruch's membrane and the ILM in the intensity volume to partition the angiographic volume is made possible because these two datasets are necessarily co-registered to the cross-sectional OCT angiograms. *En face* retinal OCT angiograms were generated by taking the mean projection of the angiographic data at all depths between the ILM and the Bruch's membrane. A single *en*

*face* plane, immediately below the Bruch's membrane, was used to choriocapillaris OCT angiograms. Retinal vasculatures at different depth ranges were also visualized separately for more sensitive visualization of retinal capillary dropouts. Depth ranges corresponding to retinal nerve fiber layer (RNFL) and ganglion cell layer (GCL), inner plexiform layer (IPL), and outer plexiform layer (OPL) were chosen manually and projected separately in depth using mean projection. For simplicity, fixed depth ranges above the Bruch's membrane were used regardless of the retinal curvature.

## 7.4 Results

### *7.4.1 Healthy Normal Volunteers*

Normal volunteers 39.7 ± 13.8 years old (range 19 to 70 years, 69 eyes from 35 subjects) were recruited for the study. Among the 69 eyes imaged, 33 eyes were from subjects older than 40 years and 7 from older than 60 years. Figure 1 shows representative OCT angiograms of the retinal and choriocapillaris microvasculature of six normal volunteers. Note that the dark patches in the retinal angiogram in Figure 1F does not correspond to retinal capillary non-perfusion but signal attenuation due to focal cataracts, which is the reason why the locations of the dark patches are different for the two field sizes. This was confirmed independently from OCT intensity images as well. In general, the 3mm × 3mm field size provides better details of the microvasculature due to the higher sampling rate compared to the 6mm × 6mm field size. However, the 6mm × 6mm field size enables larger retinal coverage. There was a large variation in the mean FAZ diameter (575 ± 146μm) amongst normal subjects as shown in Figure 7.1. However, there was only a weak correlation between the FAZ size and age ($r = 0.20$).

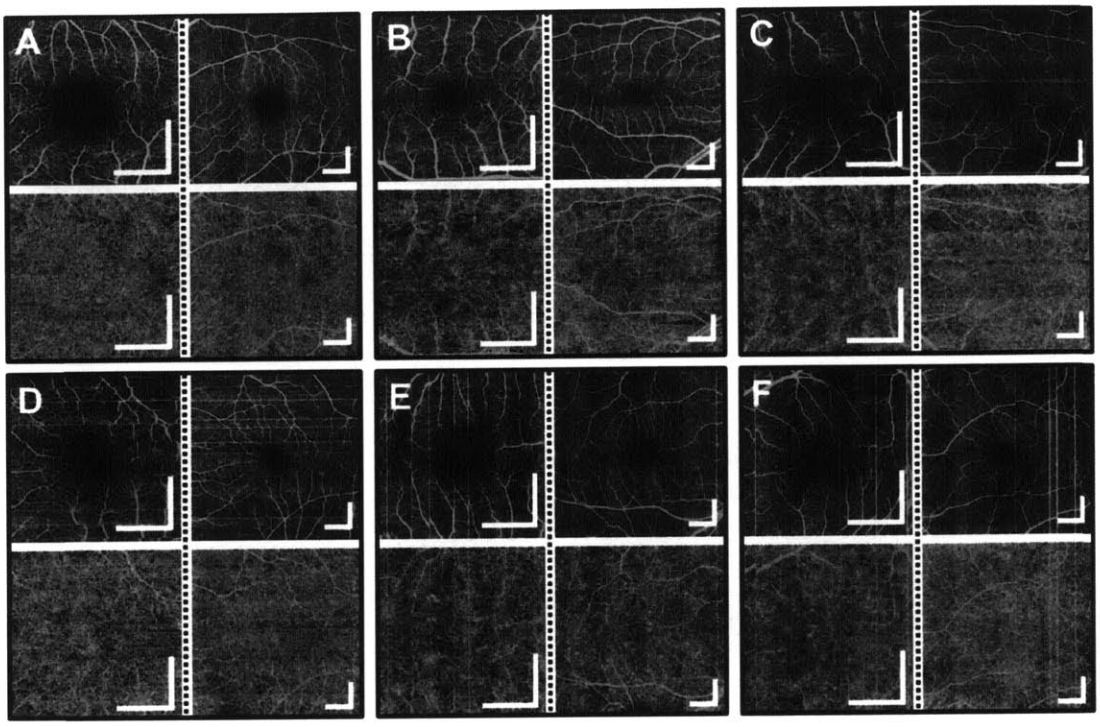


**Figure 7.1.** OCT angiograms of the retinal and choriocapillaris microvasculature from (A) 35, (B) 49, (C) 68, (D) 58, (E) 70, and (F) 65 year old healthy normal volunteers. For each subject, the retinal and choriocapillaris angiograms on the left are from a 3mm × 3mm area, and on the right from a 6mm × 6mm area, both centered at the fovea. A large variation in FAZ size can be observed even in normal subjects. In general, the retinal capillary network is dense and uniformly distributed. The choriocapillaris is tightly packed and homogenous, but small inter-capillary spots of ~100μm are frequently observed. Note that the dark patches in (F) are due to focal cataracts rather than retinal non-perfusion. All scale bars: 1mm.

Although most FAZs were nearly circular in shape as shown in Figure 1, 6 out of the 69 eyes had notably noncircular or asymmetric FAZs as shown in Figure 7.2. For example, 1 eye had a single capillary running across the center of the FAZ (Figure 7.2A). 1 eye had a noncircular FAZ

contour (Figure 7.2B). 4 of the eyes had virtually no FAZ (Figure 7.2C), which may be a historic mark of prematurity[39]. As reported previously, a larger FAZ was usually associated with a larger foveal pit[40, 41]. In addition, the eyes with markedly small FAZs showed non-vanishing retinal nerve fiber layer (RNFL), ganglion cell layer (GCL), inner plexiform layer (IPL), inner nuclear layer (INL), and outer plexiform layer (OPL) thicknesses even at center of the foveal pit (Figure 7.2D), unlike in eyes with larger FAZs.

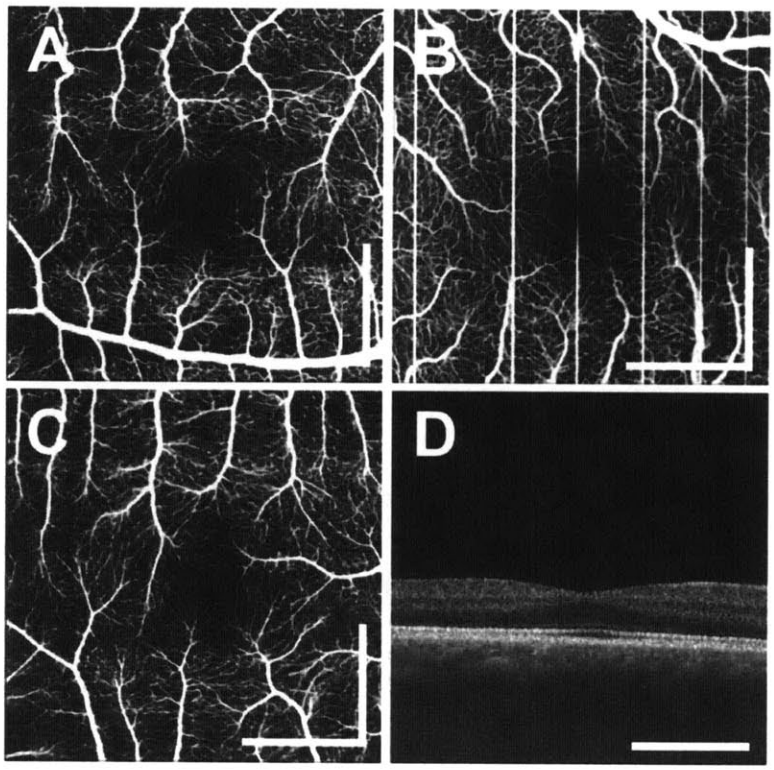


**Figure 7.2.** OCT angiograms of the retinae with noncircular or asymmetric FAZ shapes. (A) A 49 year old normal volunteer with a single capillary branch in the middle of the FAZ. (B) A 53 year old normal volunteer with noncircular FAZ contour. (C) A 19 year old normal volunteer with a very small noncircular FAZ. (D) The intensity cross-sectional image through the fovea of the subject in (C) shows that the inner retinal layers are non-vanishing even at the central fovea. All scale bars: 1mm.

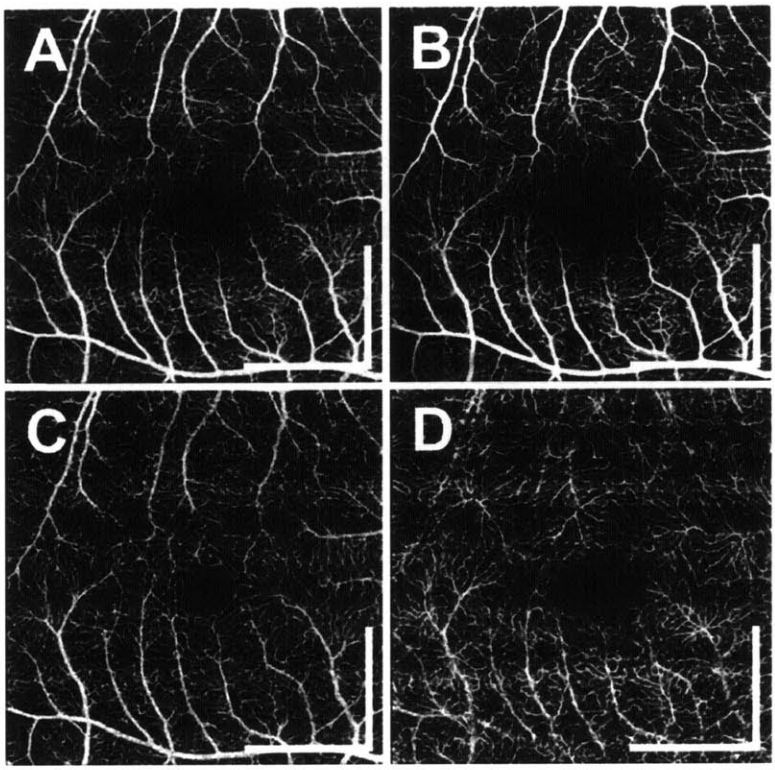


**Figure 7.3.** (A) OCT retinal angiogram of a 33 year old normal volunteer. OCT retinal angiograms projected separately in depths near (B) GCL and RNFL, (C) IPL, and (D) OPL. Retinal microvasculatures at different depths show vascular patterns distinct from one another. At all depths, the retinal capillary network is densely distributed in an orderly manner. All scale bars: 1mm.

In this study, retinal and choriocapillaris capillary microvasculature was not explicitly quantified but inspected qualitatively. For investigation of retinal vascular abnormalities in diabetes, visualizing retinal vasculature at different depths separately was often helpful. An example from a normal subject is shown in Figure 7.3, where the retinal capillary beds located roughly near GCL+RNFL, IPL, and OPL are projected separately. The retinal capillary network was generally dense in all normal subjects. No eyes had as severely tortuous retinal capillary

network as can be observed in some of the diabetic eyes. Although a slight variation in the choriocapillaris density could be observed (Figure 7.1), the choriocapillaris of normal subjects was generally tightly packed and homogeneous in the 3mm × 3mm area centered at the fovea. Isolated inter-capillary spots in the choriocapillaris with well-defined boundaries and diameters smaller than ~100μm were not considered abnormal in this study since they were commonly observed in normal subjects (Figure 7.1). The eye with the sparsest choriocapillaris density is shown in Figure 7.1B. Most other eyes had markedly denser choriocapillaris. Although not explicitly quantified, eyes with thinner choroids tended to have larger numbers of relatively large inter-capillary spots of ~100μm.

*7.4.2 Proliferative Diabetic Retinopathy*

9 eyes from 7 PDR patients (51.4 ± 16.3 years old, range 26 to 67 years) were imaged for the study. Figure 7.4 shows an FA, fundus photograph, and OCT retinal angiogram acquired from a 55 year old PDR patient. The OCT angiogram was acquired from a 3mm × 3mm area indicated by the dotted square in the FA image (Figure 7.4A). The close-up view of the FA is shown in Figure 7.4C for comparison with the corresponding OCT angiogram in Figure 7.4D. The OCT angiogram was manually motion corrected to facilitate the comparison with the FA. In general, OCT angiography has significantly better contrast than FA for visualizing the retinal microvasculature. Note that the retinal capillary density is significantly lower and the capillaries more tortuous when compared to normal eyes. In addition, the FAZ contour is highly asymmetric due to capillary dropouts near the FAZ, which agrees well with the FA. In general, the FAZ diameter in the longest dimension in PDR (1150 ± 165 μm) was significantly larger than that in normal eyes ($p << 0.001$) despite the variation between subjects due to severe capillary dropouts near the FAZ in PDR patients. Many of the microaneurysms in the FA image can also be

identified in the OCT angiogram. For comparison, the microaneurysms are indicated by circles in both the FA and OCT angiogram. In the FA image, microaneurysms appear as hyperfluorescent spots, while in the OCT angiogram they usually appear as capillary loops. Fundamentally, the source of contrast is different for FA and OCT angiography: microaneurysm visibility in FA is due to dye leakage, while it is due to erythrocyte movement in the capillary loops themselves. It should be noted that many of the retinal microvascular abnormalities, such as clustered capillaries and capillary loops, are not necessarily hyperfluorescent in the FA image, which indicates that OCT angiography can provide additional information that FA does not. Retinal microvasculature abnormalities, including clustered capillaries, dilated capillary segments, tortuous capillaries, capillary dropouts, reduced capillary density, capillary loops, and/or enlarged FAZ, were readily visible in all 9 eyes with PDR.

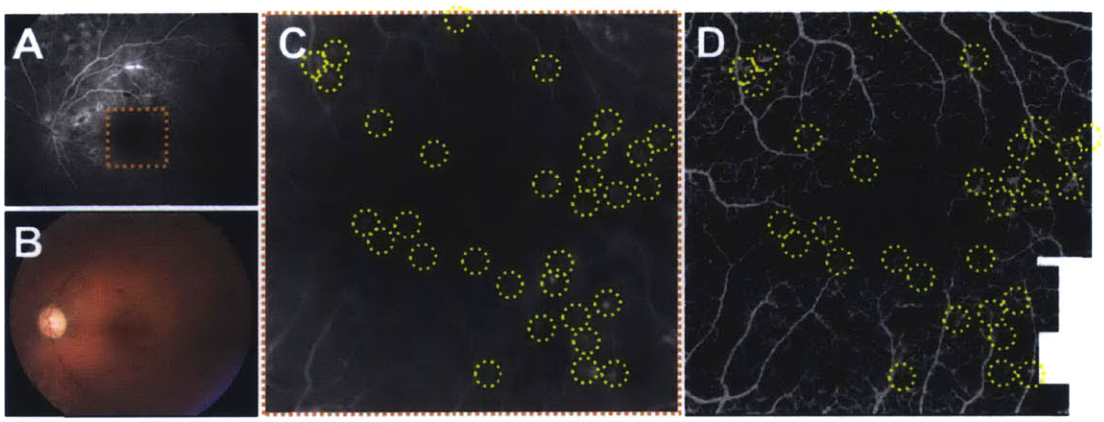


**Figure 7.4.** (A) FA, (B) fundus photograph, (C) close up view of the FA, and (D) OCT angiogram from a 55 year old diabetic patient with PDR. The close up view of the area indicated by the orange square in (A) is shown in (C). The OCT angiogram in (D) show high correspondence to the FA in (C). Many of the microaneurysms indicated by the yellow circles appear as hyperfluorescent spots in the FA while they appear as abnormal

capillary loops in the OCT angiogram. OCT angiogram acquired from a 3mm × 3mm area.

Additional cases of PDR are shown in Figure 7.5. Sometimes retinal neovascularization above the inner limiting membrane could be observed in the field of view as shown in Figures 7.5A-C. Varying degrees of impaired choriocapillaris circulation were also observed in PDR patients. The choriocapillaris angiograms in Figures 7.5E and G show that the choriocapillaris circulation is compromised in these eyes. Although there was some variation in severity, impaired choriocapillaris circulation was a common feature observed in many PDR patients. In some cases, impaired choriocapillaris circulation were more pronounced in localized areas (Figure 7.5E) while in some other cases, they were distributed diffusely throughout the field of view (Figure 7.5G). In two of the eyes, choriocapillaris circulation was almost completely compromised although the choroidal thickness was in the normal range. Focal or diffuse choriocapillaris abnormalities were observed in 7 out of 9 eyes with PDR.

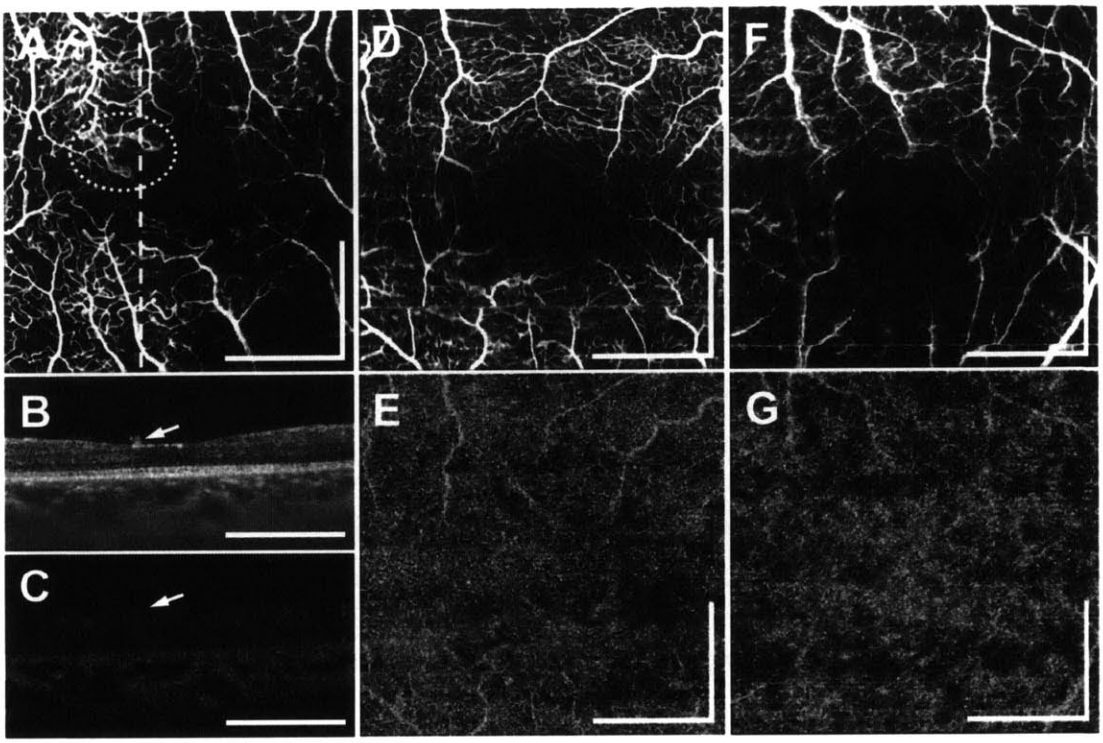


**Figure 7.5.** (A) OCT retinal angiogram showing retinal neovascularization, acquired from a 26 year old PDR patient. The white dotted circle indicates the location of the abnormal vasculature. The intensity cross-section (B) and corresponding angiographic cross-section (C) acquired from the white dashed line in (C) clearly shows that there is an abnormal vessel above the inner limiting membrane indicated by white arrows. (D) OCT retinal angiogram and (E) OCT choriocapillaris angiogram from a 56 year old PDR patient. (F) OCT retinal angiogram and (G) OCT choriocapillaris angiogram from a 60 year old PDR patient. The choriocapillaris angiograms (E) and (G) show varying degrees of impaired choriocapillaris circulation. All images from 3mm × 3mm areas. All scale bars: 1mm.

*7.4.3 Nonproliferative Diabetic Retinopathy*

29 eyes from 16 NPDR patients (60.8±7.4 years old, range 45 to 73 years) were imaged for the study. Figure 7.6 shows a fundus photograph, OCT retinal angiogram, OCT retinal thickness map, and OCT choriocapillaris angiogram from a 51 year old NPDR patient with diabetic macular edema (DME). The OCT retinal thickness map shows the location of edema (Figure 7.6C). In the OCT retinal angiogram, small capillary loops and abnormally tortuous capillary branches are frequently visible in the regions near capillary dropouts. Note that the retinal capillary network near the locations of edema (superotemporal to the fovea) looks slightly different from that away from the edema (Figure 7.6B). Although capillary dropouts are visible at multiple locations, they are more frequently visible near the FAZ and edema. Capillary dropout near the FAZ makes the FAZ appear non-circular and asymmetric. The FAZ diameter in the longest dimension in the NPDR patients was 813 ± 208μm, which was larger than in the normal volunteers and smaller than in the PDR patients ($p << 0.001$ for both). The choriocapillaris angiogram of this patient is generally dense and homogenous. However, a small number of focal impaired choriocapillaris circulation >200μm are visible over the field of view. In two eyes with NPDR (and one PDR eye), inner retinal layer thinning was correlated with patches of retinal capillary non-perfusion. An example from a 57 year old NPDR patient is shown in Figure 7.7. This patient also exhibited capillary dropouts near the FAZ and severely impaired choriocapillaris circulation.

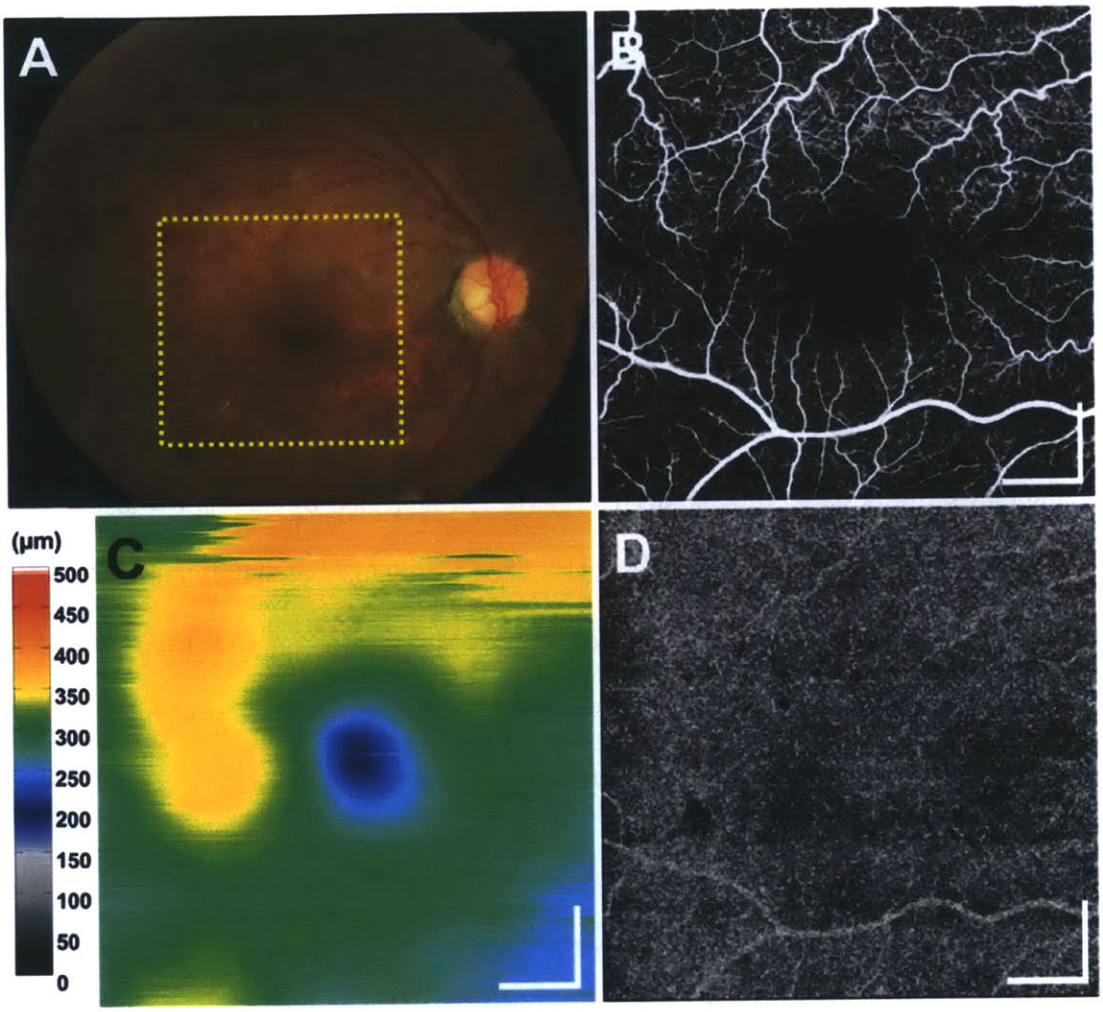


**Figure 7.6.** (A) Fundus photograph and (B-D) OCT data from a 51 year old NPDR patient with DME. (B) OCT retinal angiogram shows vascular remodeling, abnormally tortuous capillary segments at multiple fundus locations, FAZ enlargement, and capillary dropouts at several locations throughout the field of view. (C) Retinal thickness map clearly shows the presence of edema in this eye. (D) OCT choriocapillaris angiogram shows a few focal circulation impairment >200μm, but otherwise dense and homogeneous. OCT data acquired from a 6mm × 6mm area. All scale bars: 1mm.

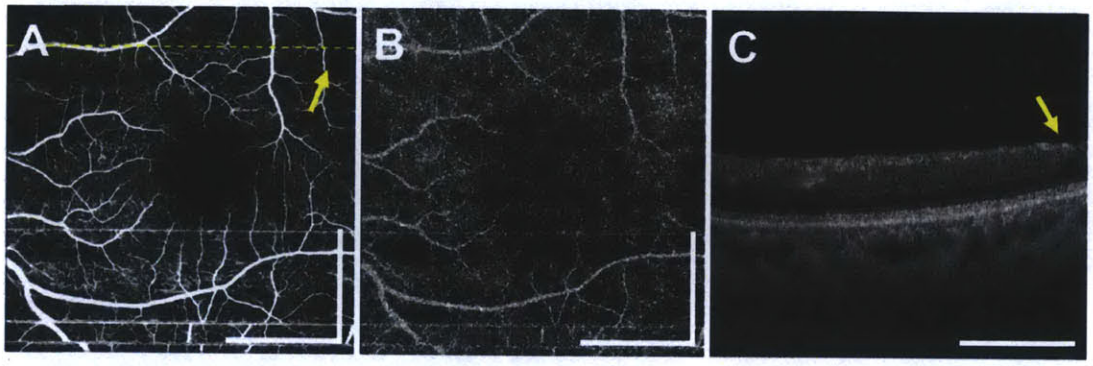


**Figure 7.7.** OCT data acquired from a 57 year old NPDR patient. (A) OCT retinal angiogram shows a patch of capillary non-perfusion indicated by the yellow arrow. (B) OCT choriocapillaris angiogram shows severe choriocapillaris circulation impairment. (C) OCT intensity cross-section extracted from the yellow dashed line in (A). The focal patch of retinal capillary non-perfusion indicated in (A) is correlated with focal inner retinal layer thinning in the intensity image (C) indicated by the yellow arrow.

An additional case is shown in Figure 7.8. The fundus photograph, FA, and OCT data were acquired from a 46 year old NPDR patient with DME. For this patient, imaging was performed longitudinally three times in total. The second imaging was performed ~6 months after the first imaging was performed, and the third imaging was performed ~2 weeks after the second imaging. Note that DME became markedly more severe between the first and second visit as can be seen in the retinal thickness maps in Figures 7.8D-F. On the third visit, FA was performed as well. As was the case in PDR, many, but not all, of the microaneurysms visible in the FA could be identified as retinal capillary abnormalities in the corresponding OCT angiogram in Figure 7.8C. When using mean projection, many microaneurysms in OCT angiograms appear brighter than other normal capillary segments because the microaneurysms are often dilated, which makes the mean signal in depth higher (Figure 7.8J). Note that the microaneurysm indicated by blue arrows

in Figures 7.8G, 7.8H, and 7.8J-L is directly neighboring a cyst, which may be the reason why the early and late phase FA images in Figures 7.8G and 7.8H show that fluorescein leaks from the microaneurysm. Microaneurysms in immediate vicinity of cysts were frequently observed in many NPDR eyes with DME. Another noteworthy finding during the second visit, a patch of capillary non-perfusion in relative to the first visit is visible in the OCT retinal angiograms, as indicated by the yellow arrows in Figures 7.8A-C. Note that on the third visit, the same area became perfused again, which implies that the patch of non-perfusion during the second visit was not due to complete capillary degeneration. Local changes in the retinal capillary network between the two time points can be clearly observed, which demonstrates the potential of OCT angiography for longitudinal studies.

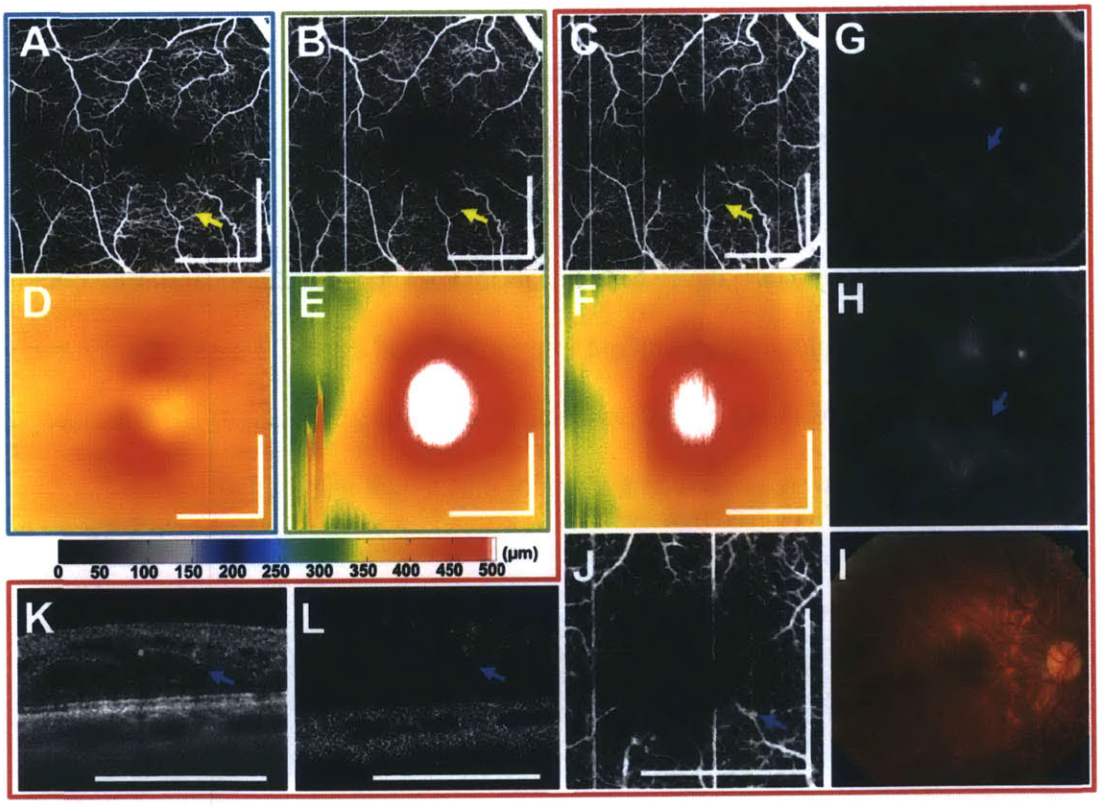


**Figure 7.8.** Fundus photograph, FA, and OCT data from a 46 year old NPDR patient with DME. (A-C) OCT angiograms acquired with 6 month and 2 week time intervals in

between. Note that a patch of capillary non-perfusion appeared in (B) and disappeared back in (C). (D-F) Corresponding OCT retinal thickness maps. Note that DME became more severe. (G) Early and (H) late phase FA images showing leakage at different time points. (J) Close-up view of (C). (K) OCT intensity and (L) angiographic cross-sections extracted from the yellow dotted line in (J) show a microaneurysm in immediate vicinity of a cyst, which may be a cite of leakage, as indicated by blue arrows in (G, H, J-L). (I) Fundus photograph. All OCT data were acquired from a 3mm × 3mm area centered at the fovea. All scale bars: 1mm.

OCT retinal angiograms from three additional NPDR patients are shown in Figure 7.9. Note that capillary dropouts are more easily noticeable when different retinal layers are projected separately. Commonly encountered retinal microvascular abnormalities include patches of reduced capillary perfusion, FAZ enlargement, microaneurysms, capillary dropouts, clustered/tortuous capillaries, significant reduction in retinal capillary density, capillary dilation, and vascular remodeling near the FAZ. Focal and/or diffuse choriocapillaris circulation impairment was also commonly encountered in eyes with NPDR. In 27 out of the 29 eyes with NPDR, at least one of the above retinal vascular abnormalities was observed. Choriocapillaris circulation abnormalities were observed in 15 out of the 29 eyes with NPDR.

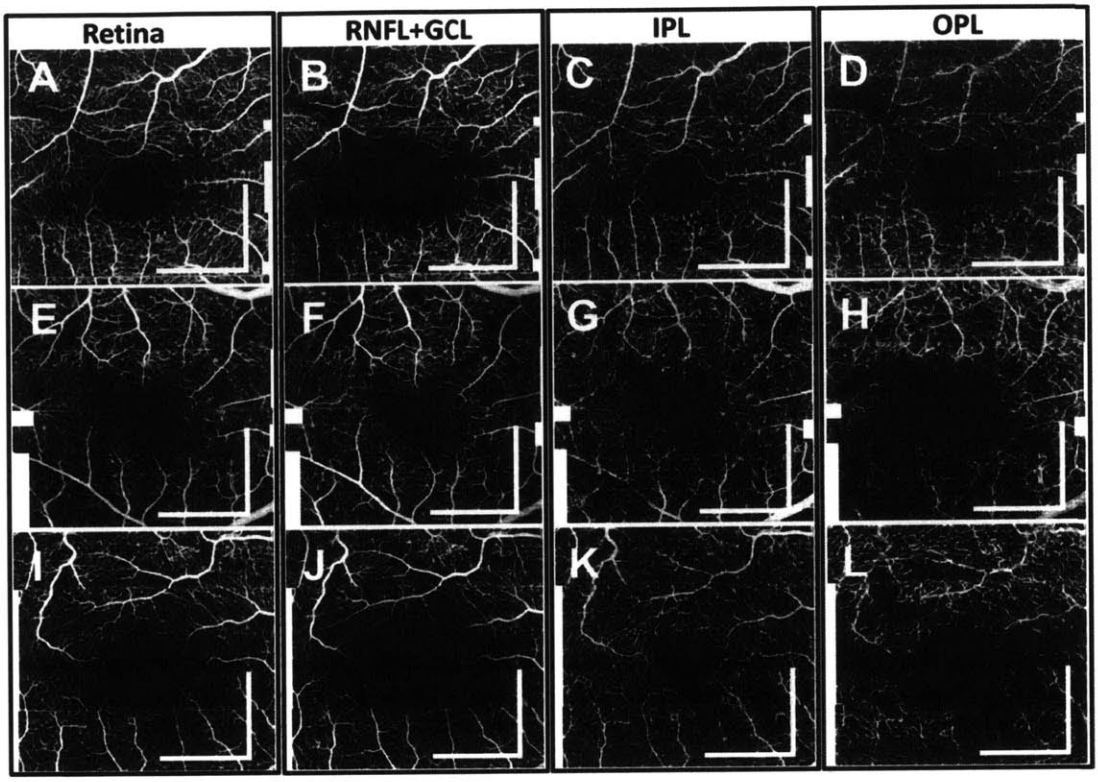


**Figure 7.9.** OCT retinal angiograms from (A-D) 64 year old, (E-H) 63 year old, and (I-L) 51 year old NPDR patients with DME. Projecting retinal vasculatures at different depths separately facilitates visualization of capillary dropouts and patches of reduced retinal capillary perfusion. Angiograms were manually motion corrected. All images acquired from 3mm × 3mm areas. All scale bars: 1mm.

*7.4.4 Diabetes without Retinopathy*

53 eyes from 30 diabetic patients without retinopathy (59.6 ± 12.8 years old, range 26 to 83 years) were imaged for the study. Figure 7.10 shows 4 representative cases of diabetic eyes without retinopathy. Figures 7.10A-D show OCT retinal angiograms projected over the entire retina. In order to visualize retinal capillary dropouts better, retinal angiograms projected over the GCL and RNFL depths are shown in Figures 10E-H, although vascular abnormalities were observed in

other layers as well. Figures 7.10I-L show the choriocapillaris angiograms. The retinal and choriocapillaris abnormalities observed in PDR and NPDR patients were observed in a subset of diabetic patients without retinopathy, albeit with a generally reduced severity. The patient shown in Figures 7.10A, 7.10E, and 7.10I shows abnormally tortuous retinal capillary branches, retinal capillary dropouts, and severe focal impairment of choriocapillaris circulation. As shown in Figures 7.10B, 7.10F, and 7.10J, abnormalities in the retinal capillary network did not always accompany abnormal choriocapillaris circulation. Although the retina shows many capillary dropouts in Figures 7.10B and 7.10F, the choriocapillaris angiogram in Figure 7.10J appears normal. In general, the severity of the choriocapillaris abnormalities was not well correlated with the severity of the retinal capillary network abnormalities. For example, Figures 7.10K and 7.10L show similar degrees of diffusely impaired choriocapillaris circulation while the retinal capillary networks appear markedly more abnormal in Figures 7.10C and 7.10G.

The mean FAZ diameter in the longest dimension in diabetic patients without retinopathy was 696 ± 153μm, which was larger than that in normal volunteers ($p << 0.001$). Noticeable retinal microvascular abnormalities, such as capillary dropouts, dilated capillary loops, tortuous capillary branches, patches of reduced capillary perfusion, irregular FAZ contours, and/or FAZ enlargement, were observed in 18 out of the 53 diabetic eyes without retinopathy. Focal or diffuse choriocapillaris circulation abnormalities were observed in 24 out of the 53 diabetic eyes without retinopathy.

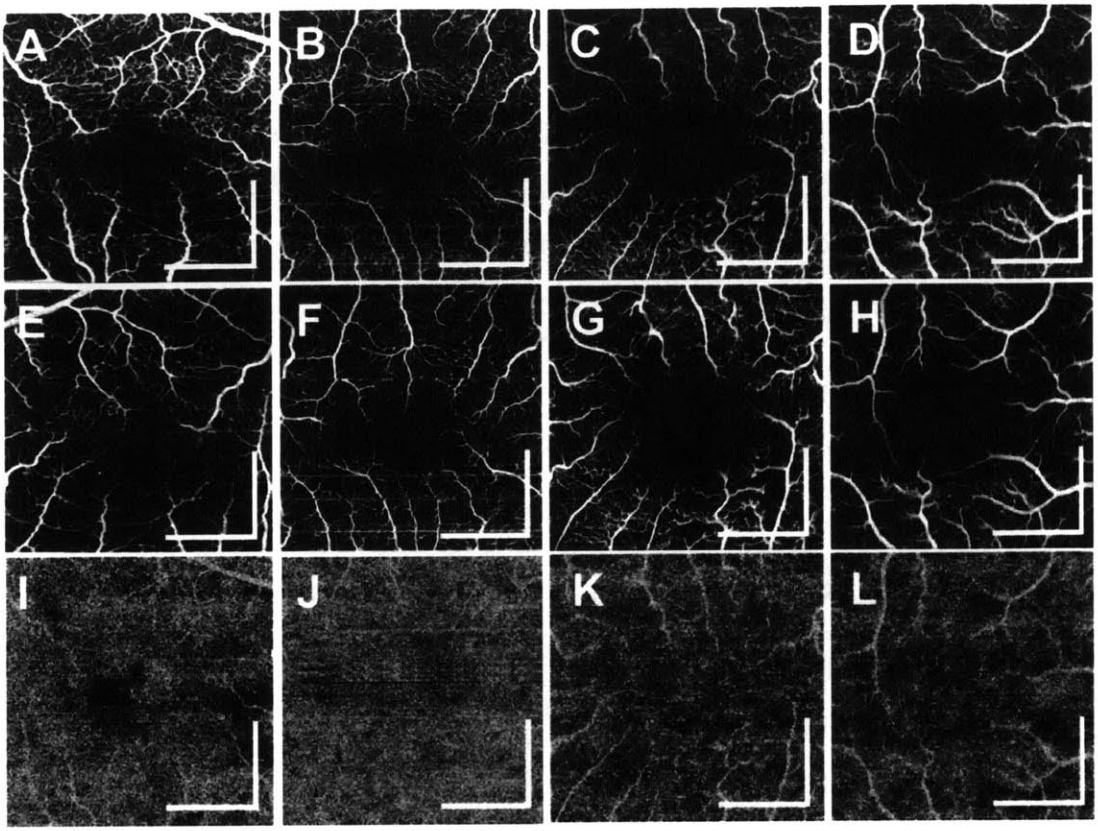


**Figure 7.10.**OCT retinal and choriocapillaris angiograms of 4 representative diabetic eyes without retinopathy. OCT angiograms from (A-D) all retinal depths projected, (E-H) the GCL and RNFL projected, and (I-L) the level of choriocapillaris. (A,E,I) 68 year old diabetic patient. (B,F,J) 68 year old diabetic patient. (C,G,K) 64 year old diabetic patient. (D,H,L) 68 year old diabetic patient. All images acquired from 3mm × 3mm areas and manually motion corrected. All scale bars: 1mm.

### 7.5 Discussion

One of the most interesting features of OCT angiography is that it enables separate visualization of microvasculatures at different depths. OCT angiography can be used to separate vasculatures near RNFL and GCL, IPL, and OPL. In diabetes, this enables more sensitive detection of

capillary dropouts or reduced capillary perfusion as shown in Figures 7.9 and 7.10. In diabetic patients with NPDR and without retinopathy, retinal microvascular abnormalities are often localized to specific depths. Therefore, by projecting all retinal layers together, the microvasculature may still appear too dense to readily identify capillary dropouts. In addition, more subtle abnormalities such as tortuous capillary branches are more easily detectable when different vascular beds are visualized separately. Using this three-dimensional visualization capability, OCT angiography was able to identify preclinical vascular abnormalities in the retina and choriocapillaris in more than a third of diabetic patients without retinopathy. This may play a key role in monitoring diabetic patients for earlier detection of microvascular abnormalities.

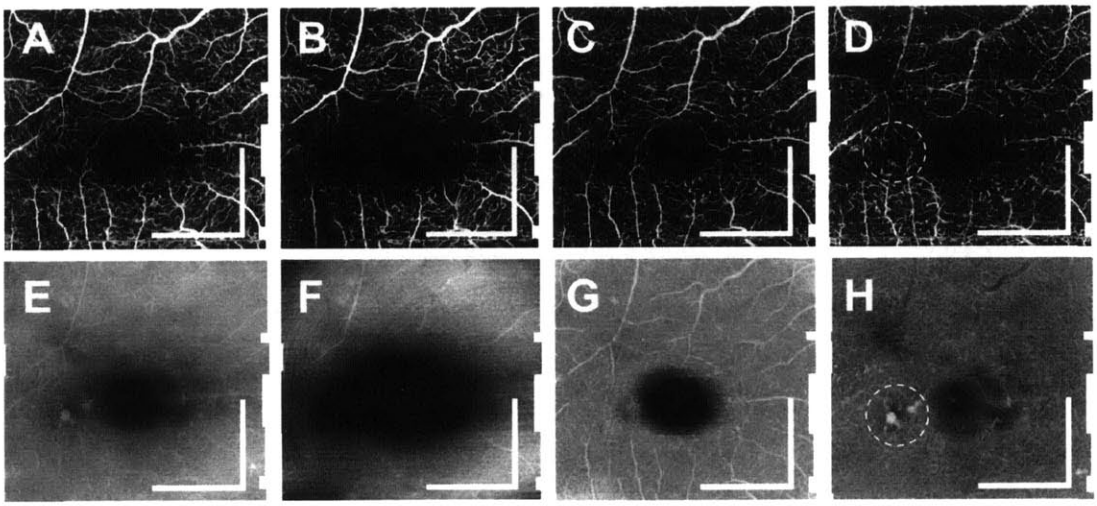


**Figure 7.11.** OCT retinal angiograms and corresponding intensity projection images at different depths from a 64 year old NPDR patient. Images extracted from the same OCT volume used in Figures 9A-D. (A) OCT angiogram projection and (E) OCT intensity projection over the entire retina. (B) OCT angiogram projection and (F) OCT intensity projection near RNFL and GCL. (C) OCT angiogram projection and (G) OCT intensity projection near IPL. (D) OCT angiogram projection and (H) OCT intensity projection near OPL. Note that the abnormal capillary loops in the circled area in (D) are directly

correlated with the hard exudates in (H). Note also that the hard exudates are located exclusively in depths near OPL. All scale bars: 1mm.

Since OCT also provides three-dimensional structural images that are co-registered to the three-dimensional OCT angiograms, it is possible to generate structural en face images corresponding to the en face OCT angiograms. Because OCT angiography is based on motion contrast, abnormalities that are not perfused with erythrocytes do not generate angiography signal. However, lesions such as hard exudates are often hyper-reflective in OCT intensity images, and it is sometimes possible to correlate microvascular abnormalities with hard exudates. For example, Figure 7.11 shows OCT angiograms and corresponding OCT en face projections at different depths, acquired from the same eye as in Figures 7.9A-D. Note that the hard exudates are localized in the depths near the OPL, and seem to have originated from the abnormal capillary loops visible in the OCT retinal angiogram in Figure 7.11D. Since the OCT angiographic volume and the co-registered OCT intensity volume provides complementary contrast for different retinal abnormalities, OCT angiography can be a useful tool for visualizing retinal lesions induced by microvascular abnormalities.

OCT angiography, unlike dye-based angiography techniques, does not provide direct visualization of dye leakage. Although this characteristic can serve as a limitation, particularly in investigations assessing vascular permeability, it can also be an advantage as OCT angiography does not suffer obscuration of leaky vasculature. OCT angiography enables direct visualization of abnormal vasculature and may therefore still serve as a sensitive and direct approach for treatment response monitoring. For example, in DR, dye leakage causes microaneurysms to appear as hyperfluorescent spots in FA. In contrast, OCT angiography provides direct visualization of the microvasculature of the microaneurysms (often as abnormal capillary loops

or dilated and/or diffuse capillary segment). Moreover, OCT angiography can visualize abnormally tortuous capillary segments whereas FA usually does not provide enough contrast to visualize individual capillary segments. Future work enabling automatic detection and quantitative analysis of the microvasculature in OCT angiograms will further increase the power of OCT angiography.

In addition, OCT angiography can also visualize patches of reduced retinal capillary perfusion as shown in Figure 7.9. Because OCT angiography is based on motion contrast, the angiography signal becomes proportional to the flow speed. Therefore, OCT angiography can distinguish fast and slow erythrocyte movements. This is an interesting feature because it implies OCT angiography can detect reduced retinal capillary perfusion before complete vascular dropout occurs, which may be useful for earlier diagnosis of retinal vascular abnormalities. This is interesting for DR because alterations in microvascular structure or perfusion can be monitored longitudinally, as shown in Figure 7.8 where local changes in retinal microvascular perfusion can be clearly visualized. Retinal capillary perfusion in Figure 7.8A, reduced perfusion in Figure 7.8B, and re-perfusion in Figure 7.8C implies that leukocyte adhesion may be involved, which eventually can lead to capillary dropouts[42-44]. Because OCT angiography does not require injection of exogenous dyes, it is completely non-invasive and longitudinal monitoring of patients is greatly facilitated. Noninvasive longitudinal monitoring of patients with retinal diseases may be useful for early diagnosis, disease progression studies, and treatment response monitoring.

OCT angiography has the interesting characteristic that it allows for visualization of the choriocapillaris, which has traditionally been challenging using conventional dye-based techniques. The need for careful interpretation of choriocapillaris OCT angiograms is, however,

underscored by the variation seen amongst normal subjects (Figure 7.1). This variation led us to consider a patient's choriocapillaris as abnormal only if it exhibited a significant reduction in circulation, relative to typical normal subjects, or if it showed significant inhomogeneity in the microvascular density over the field of view. Small inter-capillary spots (<100μm) with no choriocapillaris circulation were not necessarily considered abnormal. There was almost no immediately obvious correlation between abnormally impaired choriocapillaris circulation and RPE/photoreceptor integrity in most diabetic eyes. This is interesting because a parallel study (manuscript in preparation) that we performed on patients with age-related macular degeneration (AMD) suggests that in dry AMD, RPE/photoreceptor integrity is correlated with choriocapillaris circulation. This suggests that impaired choriocapillaris circulation may affect the retina differently in AMD and diabetes. In addition, it was not immediately obvious whether the severity of retinal and choriocapillaris abnormalities were correlated. Very often, one of them was noticeably more abnormal than the other.

One of the more obvious corollaries of using ultrahigh speed OCT angiography is that it enables higher image quality and larger retinal coverage. Because OCT angiography requires repeated B-scan protocol, the field size is more limited compared to conventional structural volumetric imaging with OCT. This can be an important practical limitation of the technique unless ultrahigh imaging speeds are utilized. In this study, 6mm × 6mm field sizes could be achieved with high image quality in patients with retinal diseases by using an SSOCT prototype with an A-scan rate of 400kHz. This volumetric field size is larger than what the standard commercial OCT systems can offer even for conventional structural imaging.

In general, microvascular abnormalities were more severe in PDR than in NPDR and diabetes without retinopathy. However, it was not always the case because the OCT field of view

was limited to a 6mm × 6mm or 3mm × 3mm area near the fovea and retinal lesions can be outside the field of view. For imaging diabetic patients, fields of view even larger than 6mm × 6mm may be helpful, which drives the need for developing OCT systems with higher imaging speeds. Although it is possible to aim for particular lesions during imaging by adjusting the patient's fixation, this is not only time consuming, but also often impossible if the locations of the lesions are not immediately obvious from structural images or fundus photograph. Most of our data were taken centered at the fovea, without specifically aiming for particular retinal lesions, and therefore the investigation was limited to the 6mm × 6mm macular cube. Although current commercial OCT systems cannot provide retinal coverage as large as ours, this problem will eventually be solved in the future as commercial OCT imaging speeds increase.

In this study, retinal and choriocapillaris microvasculature abnormalities were observed in all stages of disease, including some of the diabetic eyes without retinopathy. Ultrahigh speed OCT angiography has several advantages, including the abilities to: (1) visualize the choriocapillaris and retinal microvasculature at different depths separately, (2) provide comprehensive diagnostics using co-registered structural and angiographic information, (3) enable larger retinal coverage and higher image quality compared to slower speed OCT angiography, (4) directly visualize leaky vasculature, which is often obscured in dye-based angiography, rather than leakage, (5) enable frequent and/or repeated imaging noninvasively for longitudinal studies, and (6) assess local perfusion at the capillary level. These abilities of ultrahigh speed OCT angiography strongly suggest that OCT angiography may be a powerful tool for understanding pathogenesis, treatment response monitoring, pharmaceutical development, and earlier detection of vascular abnormalities in diabetic eyes.

## References


1. Cogan DG, Kuwabara T, Toussaint D. Retinal Vascular Pattern. 4. Diabetic Retinopathy. Arch Ophthalmol. 1961;66(3):366-78. PubMed PMID: 13694291.

2. Cogan DG, Kuwabara T. Capillary Shunts in Pathogenesis of Diabetic Retinopathy. Diabetes. 1963;12(4):293-300. PubMed PMID: 14081839.

3. Kuwabara T, Cogan DG. Retinal Vascular Patterns 6. Mural Cells of Retinal Capillaries. Arch Ophthalmol. 1963;69(4):492-502. PubMed PMID: 13927676.

4. Toussaint D, Dustin P. Electron Microscopy of Normal and Diabetic Retinal Capillaries. Arch Ophthalmol. 1963;70(1):96-&. PubMed PMID: 13993857.

5. Speiser P, Gittelso.Am, Patz A. Studies on Diabetic Retinopathy .3. Influence of Diabetes on Intramural Pericytes. Arch Ophthalmol. 1968;80(3):332-7. PubMed PMID: 4174771.

6. Hammes HP, Lin JH, Renner O, Shani M, Lundqvist A, Betsholtz C, Brownlee M, Deutsch U. Pericytes and the pathogenesis of diabetic retinopathy. Diabetes. 2002;51(10):3107-12. doi: DOI 10.2337/diabetes.51.10.3107. PubMed PMID: 12351455.

7. Roy S, Ha J, Trudeau K, Beglova E. Vascular Basement Membrane Thickening in Diabetic Retinopathy. Curr Eye Res. 2010;35(12):1045-56. doi: Doi 10.3109/02713683.2010.514659. PubMed PMID: 20929292.

8. Klein R, Meuer SM, Moss SE, Klein BEK. Retinal Microaneurysm Counts and 10-Year Progression of Diabetic-Retinopathy. Arch Ophthalmol. 1995;113(11):1386-91. PubMed PMID: 7487599.

9. Sjolie AK, Klein R, Porta M, Orchard T, Fuller J, Parving HH, Bilous R, Aldington S, Chaturvedi N. Retinal microaneurysm count predicts progression and regression of diabetic retinopathy. Post-hoc results from the DIRECT Programme. Diabetic Med. 2011;28(3):345-51. doi: DOI 10.1111/j.1464-5491.2010.03210.x. PubMed PMID: 21309844.

10. Stitt AW, Gardiner TA, Archer DB. Histological and ultrastructural investigation of retinal microaneurysm development in diabetic patients. Brit J Ophthalmol. 1995;79(4):362-7. doi: 10.1136/bjo.79.4.362.

11. Bresnick GH, Condit R, Syrjala S, Palta M, Groo A, Korth K. Abnormalities of the Foveal Avascular Zone in Diabetic-Retinopathy. Arch Ophthalmol. 1984;102(9):1286-93. PubMed PMID: 6477244.

12. Arend O, Wolf S, Jung F, Bertram B, Postgens H, Toonen H, Reim M. Retinal Microcirculation in Patients with Diabetes-Mellitus - Dynamic and Morphological Analysis of Perifoveal Capillary Network. Brit J Ophthalmol. 1991;75(9):514-8. doi: Doi 10.1136/Bjo.75.9.514. PubMed PMID: 1911651; PubMed Central PMCID: PMC1042463.

13. Mansour AM, Schachat A, Bodiford G, Haymond R. Foveal Avascular Zone in Diabetes-Mellitus. Retina-J Ret Vit Dis. 1993;13(2):125-8. PubMed PMID: 8337493.

14. Arend O, Wolf S, Remky A, Sponsel WE, Harris A, Bertram B, Reim M. Perifoveal Microcirculation with Non-Insulin-Dependent Diabetes-Mellitus. Graef Arch Clin Exp. 1994;232(4):225-31. doi: Doi 10.1007/Bf00184010. PubMed PMID: 8034211.

15. Fryczkowski AW, Hodes BL, Walker J. Diabetic choroidal and iris vasculature scanning electron microscopy findings. Int Ophthalmol. 1989;13(4):269-79. Epub 1989/07/01. PubMed PMID: 2482264.

16. McLeod DS, Lutty GA. High-resolution histologic analysis of the human choroidal vasculature. Invest Ophthalmol Vis Sci. 1994;35(11):3799-811. Epub 1994/10/01. PubMed PMID: 7928177.

17. Lutty GA, Cao J, McLeod DS. Relationship of polymorphonuclear leukocytes to capillary dropout in the human diabetic choroid. Am J Pathol. 1997;151(3):707-14. Epub 1997/09/01. PubMed PMID: 9284819; PubMed Central PMCID: PMC1857840.

18. Cao J, McLeod S, Merges CA, Lutty GA. Choriocapillaris degeneration and related pathologic changes in human diabetic eyes. Arch Ophthalmol. 1998;116(5):589-97. Epub 1998/05/22. PubMed PMID: 9596494.

19. Gerl VB, Bohl J, Pitz S, Stoffelns B, Pfeiffer N, Bhakdi S. Extensive deposits of complement C3d and C5b-9 in the choriocapillaris of eyes of patients with diabetic retinopathy. Invest Ophthalmol Vis Sci. 2002;43(4):1104-8. Epub 2002/03/30. PubMed PMID: 11923252.

20. von Sallmann L. The structure of the eye. Arch Ophthalmol. 1961;66(6):920-1. doi: 10.1001/archopht.1961.00960010922023.

21. Makita S, Hong Y, Yamanari M, Yatagai T, Yasuno Y. Optical coherence angiography. Optics Express. 2006;14(17):7821-40. doi: Doi 10.1364/Oe.14.007821. PubMed PMID: 19529151.

22. Fingler J, Schwartz D, Yang CH, Fraser SE. Mobility and transverse flow visualization using phase variance contrast with spectral domain optical coherence tomography. Optics Express. 2007;15(20):12636-53. doi: Doi 10.1364/Oe.15.012636. PubMed PMID: 19550532.

23. Tao YK, Davis AM, Izatt JA. Single-pass volumetric bidirectional blood flow imaging spectral domain optical coherence tomography using a modified Hilbert transform. Optics Express. 2008;16(16):12350-61. doi: Doi 10.1364/Oe.16.012350. PubMed PMID: 18679512.

24. An L, Wang RKK. In vivo volumetric imaging of vascular perfusion within human retina and choroids with optical micro-angiography. Optics Express. 2008;16(15):11438-52. PubMed PMID: 18648464.

25. Mariampillai A, Standish BA, Moriyama EH, Khurana M, Munce NR, Leung MKK, Jiang J, Cable A, Wilson BC, Vitkin IA, Yang VXD. Speckle variance detection of microvasculature using swept-

source optical coherence tomography. Opt Lett. 2008;33(13):1530-2. doi: Doi 10.1364/Ol.33.001530. PubMed PMID: 18594688.

26. Vakoc BJ, Lanning RM, Tyrrell JA, Padera TP, Bartlett LA, Stylianopoulos T, Munn LL, Tearney GJ, Fukumura D, Jain RK, Bouma BE. Three-dimensional microscopy of the tumor microenvironment in vivo using optical frequency domain imaging. Nat Med. 2009;15(10):1219-U151. doi: Doi 10.1038/Nm.1971. PubMed PMID: 19749772; PubMed Central PMCID: PMC2759417.

27. Yu LF, Chen ZP. Doppler variance imaging for three-dimensional retina and choroid angiography. J Biomed Opt. 2010;15(1). doi: Artn 016029
Doi 10.1117/1.3302806. PubMed PMID: 20210473; PubMed Central PMCID: PMC2839803.

28. Jonathan E, Enfield J, Leahy MJ. Correlation mapping: rapid method for retrieving microcirculation morphology from optical coherence tomography intensity images. Dynamics and Fluctuations in Biomedical Photonics Viii. 2011;7898. doi: Artn 78980m
Doi 10.1117/12.879812. PubMed PMID: ISI:000292039000013.

29. Blatter C, Klein T, Grajciar B, Schmoll T, Wieser W, Andre R, Huber R, Leitgeb RA. Ultrahigh-speed non-invasive widefield angiography. J Biomed Opt. 2012;17(7). doi: Artn 070505
Doi 10.1117/1.Jbo.17.7.070505. PubMed PMID: 22894461.

30. Kurokawa K, Sasaki K, Makita S, Hong Y-J, Yasuno Y. Three-dimensional retinal and choroidal capillary imaging by power Doppler optical coherence angiography with adaptive optics. Optics Express. 2012;20(20):22796-812. doi: 10.1364/oe.20.022796.

31. Braaf B, Vienola KV, Sheehy CK, Yang Q, Vermeer KA, Tiruveedhula P, Arathorn DW, Roorda A, de Boer JF. Real-time eye motion correction in phase-resolved OCT angiography with tracking SLO. Biomed Opt Express. 2013;4(1):51-65. Epub 2013/01/11. doi: 10.1364/BOE.4.000051
177976 [pii]. PubMed PMID: 23304647; PubMed Central PMCID: PMC3539196.

32. Kim DY, Fingler J, Zawadzki RJ, Park SS, Morse LS, Schwartz DM, Fraser SE, Werner JS. Optical imaging of the chorioretinal vasculature in the living human eye. Proc Natl Acad Sci U S A. 2013;110(35):14354-9. Epub 2013/08/07. doi: 10.1073/pnas.1307315110. PubMed PMID: 23918361; PubMed Central PMCID: PMC3761584.

33. Choi W, Mohler KJ, Potsaid B, Lu CD, Liu JJ, Jayaraman V, Cable AE, Duker JS, Huber R, Fujimoto JG. Choriocapillaris and Choroidal Microvasculature Imaging with Ultrahigh Speed OCT Angiography. Plos One. 2013;8(12):e81499. Epub 2013/12/19. doi: 10.1371/journal.pone.0081499
PONE-D-13-33807 [pii]. PubMed PMID: 24349078; PubMed Central PMCID: PMC3859478.

34. Kim DY, Fingler J, Zawadzki RJ, Park SS, Morse LS, Schwartz DM, Fraser SE, Werner JS. Noninvasive Imaging of the Foveal Avascular Zone with High-Speed, Phase-Variance Optical Coherence

Tomography. Investigative Ophthalmology & Visual Science. 2012;53(1):85-92. doi: Doi 10.1167/Iovs.11-8249. PubMed PMID: ISI:000302694500012.

35. Schwartz DM, Fingler J, Kim DY, Zawadzki RJ, Morse LS, Park SS, Fraser SE, Werner JS. Phase-variance optical coherence tomography: a technique for noninvasive angiography. Ophthalmology. 2014;121(1):180-7. Epub 2013/10/26. doi: 10.1016/j.ophtha.2013.09.002 S0161-6420(13)00807-5 [pii]. PubMed PMID: 24156929.

36. Grulkowski I, Liu JJ, Potsaid B, Jayaraman V, Lu CD, Jiang J, Cable AE, Duker JS, Fujimoto JG. Retinal, anterior segment and full eye imaging using ultrahigh speed swept source OCT with vertical-cavity surface emitting lasers. Biomedical optics express. 2012;3(11):2733-51. PubMed PMID: 23162712; PubMed Central PMCID: PMC3493240.

37. Choi W, Potsaid B, Jayaraman V, Baumann B, Grulkowski I, Liu JJ, Lu CD, Cable AE, Huang D, Duker JS, Fujimoto JG. Phase-sensitive swept-source optical coherence tomography imaging of the human retina with a vertical cavity surface-emitting laser light source. Opt Lett. 2013;38(3):338-40. PubMed PMID: 23381430; PubMed Central PMCID: PMC3721635.

38. Guizar-Sicairos M, Thurman ST, Fienup JR. Efficient subpixel image registration algorithms. Opt Lett. 2008;33(2):156-8. doi: 10.1364/ol.33.000156.

39. Mintz-Hittner HA, Knight-Nanan DM, Satriano DR, Kretzer FL. A small foveal avascular zone may be an historic mark of prematurity. Ophthalmology. 1999;106(7):1409-13. doi: http://dx.doi.org/10.1016/S0161-6420(99)00732-0.

40. Chui TYP, Zhong Z, Song H, Burns SA. Foveal Avascular Zone and Its Relationship to Foveal Pit Shape. Optometry & Vision Science. 2012;89(5):602-10 10.1097/OPX.0b013e3182504227.

41. Dubis AM, Hansen BR, Cooper RF, Beringer J, Dubra A, Carroll J. Relationship between the Foveal Avascular Zone and Foveal Pit Morphology. Investigative Ophthalmology & Visual Science. 2012;53(3):1628-36. doi: 10.1167/iovs.11-8488.

42. Miyamoto K, Hiroshiba N, Tsujikawa A, Ogura Y. In vivo demonstration of increased leukocyte entrapment in retinal microcirculation of diabetic rats. Investigative Ophthalmology & Visual Science. 1998;39(11):2190-4.

43. Kim SY, Johnson MA, McLeod DS, Alexander T, Hansen BC, Lutty GA. Neutrophils Are Associated With Capillary Closure in Spontaneously Diabetic Monkey Retinas. Diabetes. 2005;54(5):1534-42. doi: 10.2337/diabetes.54.5.1534.

44. Lutty GA. Effects of Diabetes on the Eye. Investigative Ophthalmology & Visual Science. 2013;54(14):ORSF81-ORSF7. doi: 10.1167/iovs.13-12979.

# Chapter 8

# Effects of common anesthesia on total retinal blood flow in rats measured with Doppler optical coherence tomography

## 8.1 Overview

In order to perform hemodynamic imaging using Doppler OCT and OCT angiography in small animals, it is crucial to anesthetize the animal. However, the choice of anesthesia greatly affects eye movements and ocular blood flow. Because OCT imaging requires aligning the small animal eye with respect to the imaging interface, severe eye movements under certain anesthetic agents render OCT imaging challenging. Furthermore, variation in ocular blood flow due to anesthesia can dominate the effect of interest, such as the effect of diabetes on ocular blood flow, thereby making the number of animals required extremely large to achieve sufficient statistical power. Therefore, it is important to understand the effect of different anesthetic agents on retinal blood flow and eye movements in the context of OCT imaging. This chapter investigates the effect of multiple anesthetic agents in the rat eye. WooJhon Choi and Eric Moult contributed equally to the study and the manuscript was jointly prepared. Dr. Bernhard Baumann contributed to the initial development of the OCT system and initial investigation of the effect of anesthesia on blood flow. Dr. Allen C. Clermont provided valuable knowledge and assistance in small animal handling and anesthesia. Dr. Edward P. Feener, Dr. David A. Boas, and Dr. James G. Fujimoto provided supervision and guidance.

## 8.2 Introduction

Ocular blood flow measurement is of significant interest to the scientific and clinical communities due to its potential to improve understanding of pathophysiology and serve as an early marker of a variety of ocular diseases, including age-related macular degeneration (AMD), diabetic retinopathy (DR), and glaucoma. The interest in ocular blood flow has driven the development of a variety of measurement technologies including retinal/dynamic vessel analysis[1], microsphere methods[2-4], laser Doppler based velocimetry[5-8] and flowmetry[9-11], laser speckle imaging[11-13], magnetic resonance imaging (MRI) techniques[14-16], color Doppler ultrasound imaging[17-19], dye based techniques[20-22], and optical coherence tomography (OCT) techniques[23-34].

While retinal vessel analysis allows for noninvasive measurement of vessel diameter, and hence vascular tone, it does not, by itself, provide a direct measure of blood flow. Although microsphere techniques provide a direct measurement of ocular blood flow their applicability is limited to terminal studies, making longitudinal studies in the same animal impossible. Laser Doppler velocimetry measures absolute flow at the center of the vessel, which, when combined with vessel diameter measurements, can be used to infer total blood flow. The velocity measure is, however, sensitive to the angle at which the vessel is imaged. Laser Doppler flowmetry and laser speckle imaging both provide indirect measures of average blood flow in tissue. However, neither technique provides a measure absolute blood flow. MRI techniques involve either exogenous dyes or magnetic labelling of endogenous water, the latter of which is referred to as arterial spin labelling (ASL). While MRI techniques can image through optically opaque tissues they have reduced spatial and temporal resolution compared to optical imaging techniques. Color Doppler ultrasound imaging has the disadvantage of limited spatial resolution and dye based techniques have the disadvantage that they require injection of exogenous dyes. Doppler OCT,

the modality used in our study, is a non-invasive technique that combines the principles of LDV and OCT to allow for simultaneous measurement of eye structure and erythrocyte velocity. Since the Doppler and structural OCT signals are acquired from the same data set, the two are intrinsically co-registered. The co-registration property allows blood flow values to be obtained by segmenting the blood vessels and integrating velocity values in the en face plane[31, 35].

Murine models are widely used to study the pathology of, and develop treatments for, a variety of retinal diseases. When using optical methods to measure retinal blood flows of rats and mice, anesthesia must be performed prior to imaging. Within the neuroscience community it has been well established that different anesthetics elicit differing cerebral blood flows[36-38]. There have been, however, relatively few studies examining the influence of anesthetics on ocular blood flow. Muir et al. compared the effects of isoflurane and ketamine-xylazine on ocular blood flow in the mouse eye[14]. Using ASL MRI they found that ketamine-xylazine anesthesia (100 mg/kg ketamine and 10 mg/kg xylazine) had associated blood flow values that were 29% lower ($0.88 \pm 0.22$ mL/g/min versus $1.3 \pm 0.44$ mL/g/min) in the retinal tissue ($p < 0.01$), and 42% lower ($4.3 \pm 1.9$ mL/g/min versus $7.7 \pm 2.1$ mL/g/min) in the choroidal tissues ($p < 0.01$), compared to flows associated with isoflurane anesthesia (1.1%). In a different study using ASL MRI, Li et al. measured total ocular blood flow in rats anesthetized under two different isoflurane dosages[15]. Under 1.0% isoflurane anesthesia the basal blood flow was $6.3 \pm 1.0$ ml/g/min, while under 1.5% isoflurane the basal blood flow of the whole retina was $9.3 \pm 2.7$ ml/g/min. At the resolution used, the reported blood flow measurements were a weighted average of the blood flows in the choroid and the retina.

In the current literature there are a variety of different anesthetic protocols that are used when performing blood flow studies with optical techniques. Correct interpretation and comparison of

reported blood flow values from different studies requires an understanding of the effects elicited by different anesthetic techniques. In this paper, we compare basal retinal blood flow of male Sprague-Dawley rats anesthetized using ketamine-xylazine via intraperitoneal (IP) injection, isoflurane, isoflurane-xylazine where xylazine delivered via IP injection, pentobarbital via IP injection, and ketamine-xylazine in conjunction with vecuronium bromide were all three agents are delivered via intravenous (IV) injection. Blood flow is measured using an ultrahigh speed Doppler OCT system. A brief, non-comprehensive review of the anesthetics used in this study is given below.

Isoflurane, the only inhalation anesthetic used in this study, is widely used due to its ease of use, quick recovery times, and relatively large of safety. Like most halogenated anesthetics, isoflurane depresses cardiovascular function, reducing contractility and inducing bradycardia. Due to cardiovascular depression and decreased systemic vascular resistance isoflurane induces a dose-dependent reduction in systemic arterial blood pressure[39, 40]. Ketamine, a dissociative anesthetic, is a widely used injectable anesthetic. Ketamine has been observed to increase MAP, induce tachycardia, and reduce body temperature[41]. Because ketamine causes catalepsia and does not yield sufficient hypnosis[42] we use ketamine in conjunction with xylazine, an $\alpha_2$-adernergic agonist that acts as a sedative and skeletal muscle relaxant. Xylazine induces bradycardia[43] and is known to produce dose dependent hypothermia in unanesthetized rats[44]. Additionally, in rats xylazine has been associated with reversible cataracts[45], necessitating frequent administration of ocular lubricants. For one anesthesia protocol we administer vecuronium, a nondepolarizing neuromuscular blocking agent. Vecuronium does not cause significant autonomic effects unless given in massive doses[46, 47] and is used to reduce eye movement during imaging. Finally,

pentobarbital is a barbiturate producing a sedated or hypnotic state. Pentobarbital reduces MAP and cardiac output, and induces hypothermina[48-50].

## 8.3 Materials and Methods

### *8.3.1 Animal Preparation*

Male Sprague-Dawley rats (Charles River) weighing between 230-340g were used for this study. Six rats were successfully imaged under ketamine-xylazine IP anesthesia; five rats were successfully imaged under isoflurane anesthesia; six rats were successfully images under isoflurane-xylazine IP anesthesia; five rats were successfully imaged under pentobarbital IV anesthesia; and seven rats were successfully imaged under ketamine-xylazine-vecuronium IV anesthesia. After anesthesia was achieved rats were placed in a custom holder that allowed them to be securely manipulated during imaging. Animals were kept in MIT's Department of Comparative Medicine's veterinary housing unit and were given water and food ad libitum. All procedures were approved by MIT's Committee on Animal Care.

Anesthetic dosages and routes of administration are summarized in Table 8.1. For the ketamine-xylazine-vecuronium regime, rats were anesthetized with 2% isoflurane prior to catheterization; isoflurane was discontinued after the ketamine-xylazine-vecuronium continuous rate infusion (CRI) was initiated. Note also that immediately before the ketamine-xylazine-vecuronium CRI was started a bolus IV injection of vecuronium was administered.

Throughout the procedure the animal's heart rate and blood oxygen saturation were measured with a pulse oximeter. Blood pressure was measured using a tail cuff. Temperature was measured using a rectal probe and was adjusted with an electronically controlled thermal blanket. Intraocular pressure was measured using a rebound tonometer. A mix of medical air and oxygen was provided as needed to keep blood oxygen saturation levels above 95%.

**Table 8.1.** Summary of the dosages and methods of delivery for the anesthetic agents.

| Anesthetic | Dosage | Method of Delivery |
|---|---|---|
| Ketamine-xylazine | 80 mg/kg ketamine and 8 mg/kg xylazine | I.P. bolus injection for both agents |
| Isoflurane | 1.5-2.5% isoflurane | Inhalation |
| Isoflurane-xylazine | 2% isoflurane and 8 mg/kg xylazine | Inhalation for isoflurane and I.P bolus for xylazine |
| Pentobarbital | 50 mg/kg pentobarbital | I.P. bolus injection |
| Ketamine-xylazine-vecuronium | 1.5 mg/kg vecuronium<br>———<br>20 mg/kg/hr ketamine + 2 mg/kg/hr xylazine + 7.8 mg/kg/hr vecuronium | I.V. bolus injection<br>———<br>I.V. continuous rate infusion for all three agents |

*8.3.2 Ultrahigh speed spectral domain OCT system*

The OCT system used for this study is described in detail in Chapter 3. Briefly, an ultrahigh speed spectral domain OCT system with an A-scan rate of 244kHz was used for this study. The axial resolution of the system was 5.7μm with an imaging range of 1.5mm in tissue. The power incident on the cornea was 2.5mW. The phase stability and sensitivity were 1.1mrad and 99dB.

*8.3.3 Doppler OCT imaging protocol*

En face Doppler OCT imaging protocol for the measurement of pulsatile total retinal arterial blood flow was described in detail in Chapter 3. The scan pattern used for this study was 150 × 25 A-scans per volume over a 200μm × 200μm area centered at the central retinal artery. For each acquisition, at least 100 volumes were acquired at a volume acquisition rate of ~55Hz. En face Doppler OCT processing was performed as described in Chapter 3.

**8.4 Results**

Figure 8.1 shows the blood flow values corresponding to the five different anesthetic protocols. The blood flows are plotted as functions of time. For a given anesthetic protocol different colored markers correspond to different animals.

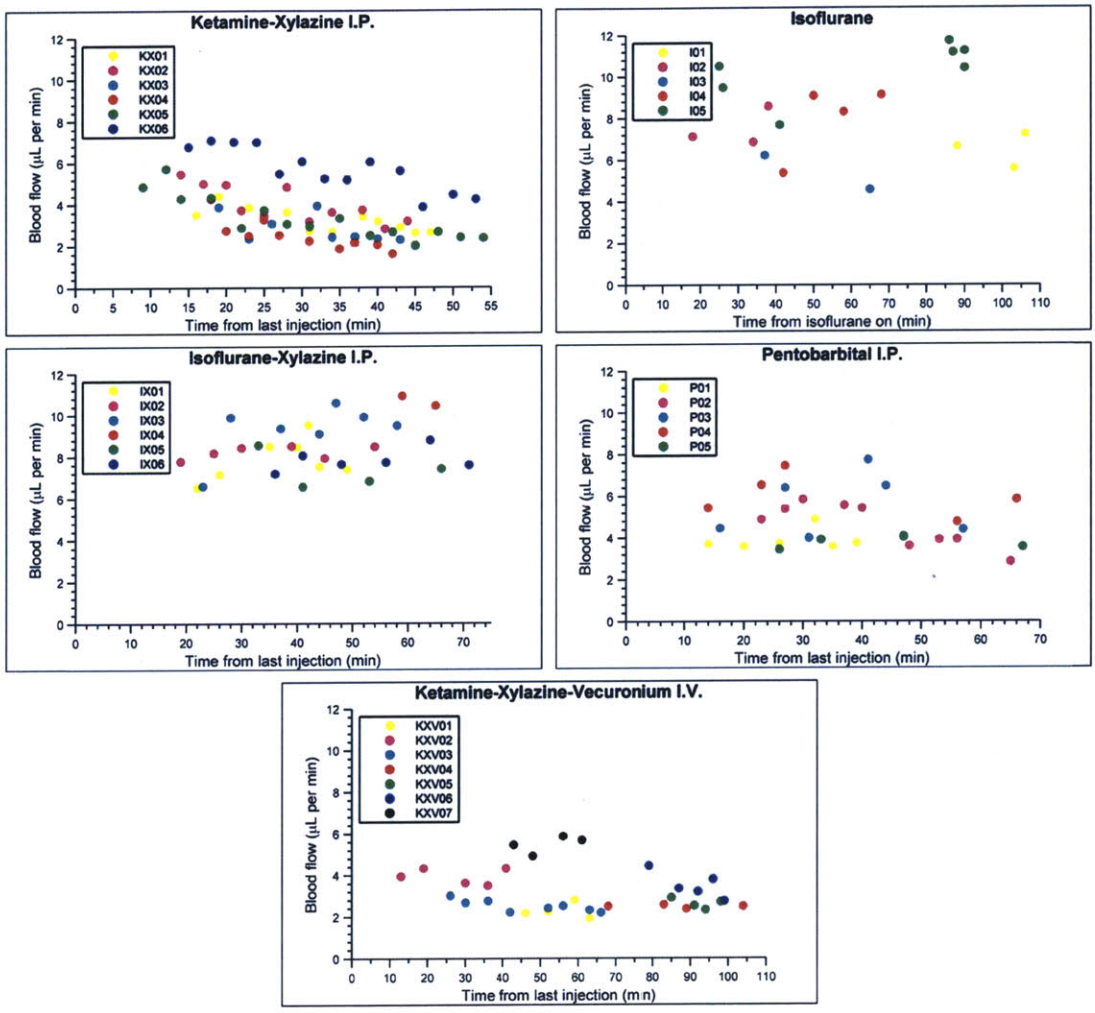


**Figure 8.1.** Blood flow measurements corresponding to the five tested anesthetic protocols. Blood flows are plotted as a function of time. For a given protocol different colored dots correspond to different animals.

## 8.5 Discussion

Before interpreting the results it is useful to define the features that are desirable in an anesthetic protocol, particularly in the context of blood flow imaging using OCT. These features include: (1) minimal time transients so that measurements can be taken at a variety of different times, (2) immobilization of the animal in a manner that facilitates OCT imaging, (3) minimal perturbation

of the animal's unanaesthetized state, and (4) simplicity. In subsequent paragraphs we will evaluate the five different anesthetic protocols in terms of these criteria. Where applicable our measured blood flow values are compared to those in the literature. Such comparison is not always easy, however, as some of the literature reports blood flow qualitatively, not as a total retinal flow, or in units that our not readily convertible to those used in our study (e.g., Doppler OCT measures in units of mL/min whereas MRI measures mL/g/min).

Examining the blood flow plot corresponding to the ketamine-xylazine I.P. protocol, a notable time-dependency is evident. This time-dependency makes it difficult to make repeatable measurements amongst different animals, as it is difficult to measure at the same point the flow-time curve. Although we only imaged up to approximately one hour post-injection, it has been shown that for young rats (8-12 weeks old) voluntary movement occurred approximately 1.5 hours after ketamine-xylazine injection[51]. This suggests that even if the blood flow does stabilize after one hour post-injection there is little time before the anesthetic wears off.

The plots corresponding to isoflurane and isoflurane-xylazine anesthesia show a marked increase in blood flow compared to the other three anesthetic protocols, which is consistent with MRI studies as well as the fact that isoflurane is a known vasodilator[14, 15]. Comparing our measurements to previous literature, a microsphere study using 3% isofluorane anesthesia in Brown-Norway rats (200-300g) reported blood flows of 19 +/- 3.4 uL/min[52]. When imaging rats anesthetized with isoflurane alone we found imaging to be extremely difficult due to eye motion. The relative scarcity and sporadicity of measurements collected under isoflurane anesthesia is a reflection of this difficulty. While we found that IP injection of xylazine significantly reduced eye motion, the vasodilatory effects of isoflurane may make it an unsuitable anesthetic for functional experiments, e.g. flicker stimulus, where vessel dilation is coupled to the stimulus.

Pentobarbital was found to elicit reasonably time-invariant blood flows at rates much lower than those seen when using isoflurane. We found, however, that pentobarbital using anesthesia failed to immobilize the eye, making imaging difficult.

Ketamine-xylazine-vecuronium anesthesia yielded low, relatively stable blood flows. Continuous rate infusion largely removed the time transients that were observed with ketamine-xylazine IP delivery. The addition of vecuronium stabilized the eye, greatly facilitating imaging. The only downside that we found with the ketamine-xylazine-vecuronium protocol is the complexity associated with supplying multiple drugs intravenously and with the need to intubate and ventilate the animal due to paralysis. We feel, however, that the stability and ease-of-imaging justifies the complexity.

### 8.6 Conclusion

Measuring retinal blood flow in the small animal eye provides a model to study the pathology of, and develop treatments for, a variety of retinal diseases. Doppler OCT is powerful technique for measuring ocular blood flow; however, Doppler OCT of small animals must be done under anesthesia. In this study we quantitatively investigated the influence of different anesthetics on total retinal blood flow in the rat retina. We found that a mixture of ketamine, xylazine, and vecuronium provided low, stable blood flows and facilitated imaging by immobilizing the rat eye.

## References


1. Garhofer G, Bek T, Boehm AG, Gherghel D, Grunwald J, Jeppesen P, Kergoat H, Kotliar K, Lanzl I, Lovasik JV, Nagel E, Vilser W, Orgul S, Schmetterer L. Use of the retinal vessel analyzer in ocular blood flow research. Acta Ophthalmologica. 2010;88(7):717-22. doi: 10.1111/j.1755-3768.2009.01587.x.

2. Weiter JJ, Schachar RA, Ernest JT. Control of intraocular blood flow.: I. Intraocular pressure. Investigative Ophthalmology & Visual Science. 1973;12(5):327-31.

3. Wang L, Fortune B, Cull G, McElwain KM, Cioffi GA. Microspheres method for ocular blood flow measurement in rats: size and dose optimization. Exp Eye Res. 2007;84(1):108-17. Epub 2006/10/31. doi: S0014-4835(06)00376-9 [pii]
10.1016/j.exer.2006.09.005. PubMed PMID: 17069799.

4. Orgül S, Cioffi GA, Bacon DR, Bhandari A, Van Buskirk EM. Measurement of optic nerve blood flow with nonradioactive colored microspheres in rabbits. Microvasc Res. 1996;51(2):175-86. doi: http://dx.doi.org/10.1006/mvre.1996.0019.

5. Riva C, Ross B, Benedek GB. Laser Doppler measurements of blood flow in capillary tubes and retinal arteries. Investigative Ophthalmology & Visual Science. 1972;11(11):936-44.

6. Tanaka T, Riva C, Ben-Sira I. Blood velocity measurements in human retinal vessels. Science. 1974;186(4166):830-1. doi: 10.2307/1739855.

7. Pournaras CJ, Riva CE. Retinal blood flow evaluation. Ophthalmologica. 2013;229(2):61-74.

8. Riva CE, Grunwald JE, Sinclair SH, Petrig BL. Blood velocity and volumetric flow rate in human retinal vessels. Investigative Ophthalmology & Visual Science. 1985;26(8):1124-32.

9. Bonner R, Nossal R. Model for Laser Doppler Measurements of Blood-Flow in Tissue. Appl Optics. 1981;20(12):2097-107. doi: Doi 10.1364/Ao.20.002097. PubMed PMID: 20332893.

10. Riva CE, Harino S, Petrig BL, Shonat RD. Laser Doppler flowmetry in the optic nerve. Exp Eye Res. 1992;55(3):499-506. doi: http://dx.doi.org/10.1016/0014-4835(92)90123-A.

11. Briers JD, Fercher AF. Retinal blood-flow visualization by means of laser speckle photography. Investigative Ophthalmology & Visual Science. 1982;22(2):255-9.

12. Fercher AF, Briers JD. Flow visualization by means of single-exposure speckle photography. Opt Commun. 1981;37(5):326-30. doi: http://dx.doi.org/10.1016/0030-4018(81)90428-4.

13. Boas DA, Dunn AK. Laser speckle contrast imaging in biomedical optics. J Biomed Opt. 2010;15(1):011109--12. doi: 10.1117/1.3285504.

14. Muir ER, Duong TQ. MRI of retinal and choroidal blood flow with laminar resolution. Nmr in Biomedicine. 2011;24(2):216-23. doi: Doi 10.1002/Nbm.1576. PubMed PMID: ISI:000288209300013.

15. Li Y, Cheng H, Duong TQ. Blood-flow magnetic resonance imaging of the retina. NeuroImage. 2008;39(4):1744-51. doi: http://dx.doi.org/10.1016/j.neuroimage.2007.10.030.

16. Peng Q, Zhang Y, Nateras OSE, van Osch MJP, Duong TQ. MRI of blood flow of the human retina. Magnetic Resonance in Medicine. 2011;65(6):1768-75. doi: 10.1002/mrm.22763.

17. Lieb WE, Cohen SM, Merton DA, Shields JA, Mitchell DG, Goldberg BB. Color doppler imaging of the eye and orbit: Technique and normal vascular anatomy. Arch Ophthalmol. 1991;109(4):527-31. doi: 10.1001/archopht.1991.01080040095036.

18. Butt Z, O'Brien C, McKillop G, Aspinall P, Allan P. Color Doppler imaging in untreated high- and normal-pressure open-angle glaucoma. Investigative Ophthalmology & Visual Science. 1997;38(3):690-6.

19. Ciulla TA, Harris A, Chung HS, Danis RP, Kagemann L, McNulty L, Pratt LM, Martin BJ. Color Doppler imaging discloses reduced ocular blood flow velocities in nonexudative age-related macular degeneration. Am J Ophthalmol. 1999;128(1):75-80. doi: http://dx.doi.org/10.1016/S0002-9394(99)00061-6.

20. Ben-Sira I, Riva CE, Roberts W. Fluorophotometric recording of fluorescein dilution curves in human retinal vessels. Investigative Ophthalmology & Visual Science. 1973;12(4):310-2.

21. Chung HS, Harrisa A, Ciulla TA, Kagemann L. Progress in measurement of ocular blood flow and relevance to our understanding of glaucoma and age-related macular degeneration. Prog Retin Eye Res. 1999;18(5):669-87. doi: http://dx.doi.org/10.1016/S1350-9462(98)00037-8.

22. Wolf S, Arend O, Reim M. Measurement of retinal hemodynamics with scanning laser ophthalmoscopy: Reference values and variation. Surv Ophthalmol. 1994;38, Supplement(0):S95-S100. doi: http://dx.doi.org/10.1016/0039-6257(94)90052-3.

23. White B, Pierce M, Nassif N, Cense B, Park B, Tearney G, Bouma B, Chen T, de Boer J. In vivo dynamic human retinal blood flow imaging using ultra-high-speed spectral domain optical coherence tomography. Optics Express. 2003;11(25):3490-7. doi: 10.1364/oe.11.003490.

24. Izatt JA, Kulkami MD, Yazdanfar S, Barton JK, Welch AJ. In vivo bidirectional color Doppler flow imaging of picoliter blood volumes using optical coherence tomography. Opt Lett. 1997;22(18):1439-41.

25. Leitgeb RA, Schmetterer L, Hitzenberger CK, Fercher AF, Berisha F, Wojtkowski M, Bajraszewski T. Real-time measurement of in vitro flow by Fourier-domain color Doppler optical coherence tomography. Opt Lett. 2004;29(2):171-3. doi: Doi 10.1364/Ol.29.000171. PubMed PMID: ISI:000187880100011.

26. Wang Y, Bower BA, Izatt JA, Tan O, Huang D. In vivo total retinal blood flow measurement by Fourier domain Doppler optical coherence tomography. J Biomed Opt. 2007;12(4):041215--8. doi: 10.1117/1.2772871.

27. Makita S, Fabritius T, Yasuno Y. Quantitative retinal-blood flow measurement with three-dimensional vessel geometry determination using ultrahigh-resolution Doppler optical coherence angiography. Opt Lett. 2008;33(8):836-8. PubMed PMID: WOS:000255769100026.

28. Wang Y, Lu A, Gil-Flamer J, Tan O, Izatt JA, Huang D. Measurement of total blood flow in the normal human retina using Doppler Fourier-domain optical coherence tomography. Brit J Ophthalmol. 2009;93(5):634-7. doi: 10.1136/bjo.2008.150276. PubMed PMID: WOS:000265530100017.

29. Baumann B, Potsaid B, Kraus MF, Liu JJ, Huang D, Hornegger J, Cable AE, Duker JS, Fujimoto JG. Total retinal blood flow measurement with ultrahigh speed swept source/Fourier domain OCT. Biomed Opt Express. 2011;2(6):1539-52. PubMed PMID: 21698017; PubMed Central PMCID: PMC3114222.

30. Schmoll T, Kolbitsch C, Leitgeb RA. Ultra-high-speed volumetric tomography of human retinal blood flow. Optics Express. 2009;17(5):4166-76. PubMed PMID: 19259253.

31. Choi W, Baumann B, Liu JJ, Clermont AC, Feener EP, Duker JS, Fujimoto JG. Measurement of pulsatile total blood flow in the human and rat retina with ultrahigh speed spectral/Fourier domain OCT. Biomedical Optics Express. 2012;3(5):1047-61. PubMed PMID: 22567595; PubMed Central PMCID: PMC3342181.

32. Wang Y, Fawzi AA, Varma R, Sadun AA, Zhang X, Tan O, Izatt JA, Huang D. Pilot study of optical coherence tomography measurement of retinal blood flow in retinal and optic nerve diseases. Investigative Ophthalmology & Visual Science. 2011;52(2):840-5.

33. Zhi Z, Yin X, Dziennis S, Wietecha T, Hudkins KL, Alpers CE, Wang RK. Optical microangiography of retina and choroid and measurement of total retinal bloodflow in mice. Biomedical Optics Express. 2012;3(11):2976-86. doi: 10.1364/boe.3.002976.

34. Zhi Z, Cepurna W, Johnson E, Shen T, Morrison J, Wang RK. Volumetric and quantitative imaging of retinal blood flow in rats with optical microangiography. Biomedical Optics Express. 2011;2(3):12. PubMed PMID: 21412463; PubMed Central PMCID: PMC3047363.

35. Srinivasan VJ, Sakadzic S, Gorczynska I, Ruvinskaya S, Wu W, Fujimoto JG, Boas DA. Quantitative cerebral blood flow with Optical Coherence Tomography. Optics Express. 2010;18(3):2477-94. doi: 10.1364/oe.18.002477.

36. Hendrich KS, Kochanek PM, Melick JA, Schiding JK, Statler KD, Williams DS, Marion DW, Ho C. Cerebral perfusion during anesthesia with fentanyl, isoflurane, or pentobarbital in normal rats studied

by arterial spin-labeled MRI. Magnetic Resonance in Medicine. 2001;46(1):202-6. doi: 10.1002/mrm.1178.

37. Långsjö JW, Kaisti KK, Aalto S, Hinkka S, Aantaa R, Oikonen V, Sipilä H, Kurki T, Silvanto M, Scheinin H. Effects of Subanesthetic Doses of Ketamine on Regional Cerebral Blood Flow, Oxygen Consumption, and Blood Volume in Humans. Anesthesiology. 2003;99(3):614-23.

38. Sicard K, Shen Q, Brevard ME, Sullivan R, Ferris CF, King JA, Duong TQ. Regional cerebral blood flow and BOLD responses in conscious and anesthetized rats under basal and hypercapnic conditions: Implications for functional MRI studies. J Cereb Blood Flow Metab. 2003;23(4):472-81.

39. Degoute C-S. Controlled hypotension. Drugs. 2007;67(7):1053-76. doi: 10.2165/00003495-200767070-00007.

40. Hayes ES, Barrett TD, Burrill DE, Walker MJA. Effects of halothane and isoflurane on rat ventricular action potentials recorded in situ. Life Sciences. 1996;58(16):1375-85. doi: http://dx.doi.org/10.1016/0024-3205(96)00104-X.

41. Carruba MO, Bondiolotti G, Picotti GB, Catteruccia N, Da Prada M. Effects of diethyl ether, halothane, ketamine and urethane on sympathetic activity in the rat. European Journal of Pharmacology. 1987;134(1):15-24. doi: http://dx.doi.org/10.1016/0014-2999(87)90126-9.

42. Green CJ, Knight J, Precious S, Simpkin S. Ketamine alone and combined with diazepam or xylazine in laboratory animals: a 10 year experience. Laboratory Animals. 1981;15(2):163-70. doi: 10.1258/002367781780959107.

43. Erhardt W, Hebestedt A, Aschenbrenner G, Pichotka B, Blümel G. A comparative study with various anesthetics in mice (pentobarbitone, ketamine-xylazine, carfentanyl-etomidate). Res Exp Med. 1984;184(3):159-69. doi: 10.1007/bf01852390.

44. Livingston A, Low J, Morris B. Effects of clonidine and xylazine on body temperature in the rat. British Journal of Pharmacology. 1984;81(1):189-93. doi: 10.1111/j.1476-5381.1984.tb10760.x.

45. Calderone L, Grimes P, Shalev M. Acute reversible cataract induced by xylazine and by ketamine-xylazine anesthesia in rats and mice. Exp Eye Res. 1986;42(4):331-7. doi: http://dx.doi.org/10.1016/0014-4835(86)90026-6.

46. Dennis F. Kohn SKW, William J. White, G. John Benson. Anesthesia and analgesia in laboratory animals. San Diego, California, U.S.A.: Academic Press; 1997.

47. Marshall IG, Gibb AJ, Durant NN. Neuromuscular and vagal blocking actions of pancuronium bromide, its metabolites, and vecuronium bromide (org nc 45) and its potential metabolites in the anaesthetized cat. British Journal of Anaesthesia. 1983;55(8):703-14. doi: 10.1093/bja/55.8.703.

48. Lomax P. The hypothermic effect of pentobarbital in the rat: Sites and mechanisms of action. Brain Res. 1966;1(3):296-302. doi: http://dx.doi.org/10.1016/0006-8993(66)90094-1.

49. Kawaue Y, Iriuchijima J. Changes in cardiac output and peripheral flows on pentobarbital anesthesia in the rat. The Japanese Journal of Physiology. 1984;34(2):283-94. doi: 10.2170/jjphysiol.34.283.

50. Lee SS, Girod C, Valla D, Geoffroy P, Lebrec D. Effects of pentobarbital sodium anesthesia on splanchnic hemodynamics of normal and portal-hypertensive rats1985 1985-10-01 00:00:00. G528-G32 p.

51. Veilleux-Lemieux D, Castel A, Carrier D, Beaudry F, Vachon P. Pharmacokinetics of ketamine and xylazine in young and old Sprague-Dawley rats. Journal of the American Association for Laboratory Animal Science. 2013;52(5):567-70.

52. Wang YM, Bower BA, Izatt JA, Tan O, Huang D. In vivo total retinal blood flow measurement by Fourier domain Doppler optical coherence tomography. J Biomed Opt. 2007;12(4). doi: Artn 041215 Doi 10.1117/1.2772871. PubMed PMID: 17867804.

# Chapter 9

# Hemodynamic imaging of neurovascular coupling in the small animal retina using ultrahigh speed optical coherence tomography

## 9.1 Overview

This chapter presents hemodynamic imaging of basal blood circulation and neurovascular coupling in the small animal retina using ultrahigh speed spectral domain optical coherence tomography (OCT). Using the same OCT system described in detail in Chapter 3 and an anesthesia protocol similar to one developed in Chapter 8, we performed hemodynamic imaging in the rat eye. It is shown that neurovascular coupling as well as basal retinal blood circulation can be measured both at the macroscopic level using Doppler OCT and microscopic level using OCT angiography. Eric Moult contributed significantly in animal handling and OCT data acquisition. Dr. David A. Boas, Dr. Allen C. Clermont, Dr. Edward P. Feener, and Dr. James G. Fujimoto provided supervision and guidance.

## 9.2 Introduction

Ocular blood circulation plays an important role in retinal diseases such as diabetic retinopathy, glaucoma, and age-related macular degeneration. Since the retina is the only part of the central nervous system that is optically accessible noninvasively, optical imaging of the retina is highly attractive for investigating ocular hemodynamics. Optical coherence tomography (OCT) is a powerful optical imaging technique that enables non-invasive depth-resolved imaging of the retina and choroid[1]. Development of Fourier domain OCT detection technique enabled ultrahigh

OCT imaging speeds[2, 3], which dramatically enhanced the potential of OCT for more comprehensive imaging of the retina. In addition to three-dimensional structural imaging, ultrahigh speed OCT enables hemodynamic imaging of retinal blood circulation both at the total blood flow and capillary levels, using Doppler OCT and OCT angiography imaging techniques.

Retinal and choroidal hemodynamic imaging in small animal models using ultrahigh speed OCT is highly interesting for clinical as well as basic sciences. Developing and validating OCT methods and imaging techniques for small animal imaging is important because studies in small animal models of retinal disease, such as diabetic retinopathy (DR), age-related macular degeneration (AMD) and glaucoma[4-9], enable understanding of disease mechanisms. OCT is noninvasive, enabling repeated imaging in the same animals over time[10]. This reduces the effects of biological variability and promises to improve the efficiency of fundamental studies or pharmaceutical development. In addition, small animal studies are important for validating new OCT technology prior to clinical studies.

There are multiple potential hemodynamic biomarkers that can be imaged using ultrahigh speed OCT. Multiple studies have investigated the effect of diabetes on basal retinal blood flow in streptozotocin (STZ) rat models of diabetes using different techniques, such as video fluorescein angiography and microsphere infusion, but there are contradictory reports on whether basal retinal blood flow increases[11-13] or decreases[14-16] in the STZ rat model. A recent study showed that even in animals with the same duration of diabetes, two different measurement methods, a microsphere infusion technique and mean dye circulation time measurement, showed opposite trends in basal blood flow, suggesting that this disparity might result from capillary network differences[17]. These studies suggest there is a need for a more direct and quantitative way to measure basal blood flow both at the macroscopic and microscopic levels.

Because all major retinal arteries branch out from the central retinal artery located at the optic nerve head region, total retinal blood flow can be directly measured by performing Doppler OCT on the central retinal artery in the small animal eye, as demonstrated previously by our group[18]. Ultrahigh speed Doppler OCT has an advantage that it directly measures pulsatile total retinal blood flow in quantitative units of μL/min, while other commonly used techniques in small animal models measure indirect effects of retinal blood flow, such as dye circulation time or microsphere concentration in tissue. In addition, total retinal blood flow measurement has an advantage that it provides a single quantitative value that can be compared easily between different animals. In general, however, measuring blood flow in small animal models is challenging because most imaging techniques, including OCT, requires anesthesia. It is well known in functional brain imaging that anesthesia affects cerebral blood flow[19, 20] and that a careful anesthesia and monitoring protocol is essential to minimize measurement variability. Although the same is true for ocular blood flow[21], most retinal blood flow studies to date have used simple anesthesia protocols without proper monitoring of animals, which may have attributed significantly to animal to animal variation and time dependency in measured basal blood flow in previously reported studies. Therefore, there is a need to perform a more direct measurements of basal retinal blood flow with a carefully designed anesthesia protocol in order to separate the effect of animal handling and measurement technique limitations from the effects of interest.

Another potential biomarker that ultrahigh speed OCT can measure is functional hyperemia, which is a transient increase in blood flow counterbalancing an acute increase in tissue metabolism induced by external stimuli. In the normal retina, flickering light incident on retinal tissue can increase tissue metabolism, which transiently increase retinal blood flow via

neurovascular coupling[22]. Alterations in functional hyperemic flicker response are thought to be one of the earliest markers in diabetes and glaucoma[23-29]. Multiple studies have investigated neurovascular coupling in the rat eye using various techniques such as laser speckle flowmetry and microsphere infusion[30, 31]. However, direct quantitative measurement of blood flow in units of μL/min was challenging in these studies due to the limitation in the measurement techniques. A more recent OCT study also investigated neurovascular coupling in the rat eye, but measurements were limited to a single retinal vessel due to a limited imaging speed of <50,000 A-scans per second[32]. None of these studies measured the effect of flicker stimulus on total retinal blood flow or retinal and choroidal capillary blood circulation at the microscopic level.

There are several advantages of using ultrahigh speed OCT for measuring retinal neurovascular coupling. Because the increase in total retinal blood flow due to flicker stimulus is transient, measurement techniques need to have good time resolution. Ultrahigh speed Doppler OCT can achieve high volume acquisition rates of tens of volumes per second to enable measurements of pulsatility in retinal blood flow as well as time transients due to functional hyperemia in a single acquisition. Furthermore, the retina has multiple microvascular beds in depths, near the retinal nerve fiber layer (RNFL) and ganglion cell layer (GCL), inner plexiform layer (IPL), outer plexiform layer (OPL), and choriocapillaris, which cannot be visualized separately using conventional techniques. Since OCT is depth-resolved, ultrahigh speed OCT angiography enables depth-resolved three-dimensional visualization of retinal and choriocapillaris microvasculature. Therefore, ultrahigh speed OCT can potentially enable investigation of neurovascular coupling at both the macroscopic and microscopic levels using Doppler OCT and OCT angiography, thereby allowing more rapid and complete characterization of retinal hemodynamics in vivo.

In this study, retinal blood circulation and its response to visual flicker stimulus is investigated in the rat eye using ultrahigh speed spectral domain OCT. Ultrahigh speed Doppler OCT and OCT angiography are used to measure basal total retinal blood flow and to visualize retinal and choriocapillaris microvasculature, respectively. The same techniques are also used to investigate neurovascular coupling. In order to see how sensitive the measurement techniques are in detecting alterations in basal blood circulation and functional hyperemic response between different groups of animals, NG-nitro-L-arginine methyl ester (L-NAME), a nitric oxide synthase (NOS) inhibitor, was used at two different dosage levels to modulate ocular hemodynamics. Since nitric oxide (NO) is a vasodilator known to be involved in retinal hemodynamics[33, 34], the injection of L-NAME is expected to reduce basal retinal blood flow and functional hyperemic response in the rat eye. It is shown that ultrahigh speed OCT is capable of quantitatively measuring the effect of L-NAME on basal blood flow and functional hyperemia both at the macroscopic and microscopic levels.

## 9.3 Material and methods

### *9.3.1 Animal preparation*

Experiments were performed on normal male Sprague-Dawley rats (250-350g, n=22). Unlike structural imaging, functional hemodynamic imaging is highly sensitive to the physiological state of the animal. Therefore, the animal was anesthetized and monitored carefully to minimize measurement variability due to anesthesia. Initially, anesthesia was induced with 2.5% isoflurane in a mixture of medical air and oxygen. Blood oxygen saturation was continuously monitored using a pulse oximeter (Kent Scientific, PhysioSuite MouseSTAT) and maintained within normal physiological ranges (94-99%) by adjusting the oxygen flow rate. Body temperature was continuously monitored using a rectal probe and maintained at 37-38°C (Harvard Apparatus,

Homeothermic Monitor). Under isoflurane anesthesia, the lateral saphenous vein was catheterized and continuous intravenous infusion of Ketamine (30mg/kg/hr) and xylazine (15 mg/kg/hr) was started using a syringe pump (Manufacturer). The heart rate was continuously monitored using the pulse oximeter, and isoflurane was discontinued once the heart rate fell by ~20% of the initial value and stabilized. The rat was then intubated and mechanically ventilated (Harvard Apparatus, Inspira ASV). Once the animal was mechanically ventilated, a bolus of rocuronium (6 mg/kg) was delivered through the intravenous catheter to paralyze the animal, and the Ketamine and xylazine infusion rates were reduced to 20mg/kg/hr and 10mg/kg/hr, respectively, in order to minimize the depth of anesthesia. Immediately after this, continuous intravenous infusion of rocuronium (37.5 mg/kg/hr) was followed using another syringe pump (Harvard Apparatus, PumpII Elite). End tidal $CO_2$ was monitored continuously using a capnometer (Kent Scientific, PhysioSuite CapnoScan). The end tidal $CO_2$ and blood oxygen saturation were maintained within normal physiological ranges (35-45mmHg and 94-99%) by adjusting the oxygen concentration in inhaled gas, tidal volume, and breathing rate. Blood pressure and intraocular pressure was continuously monitored using a non-invasive pressure cuff system (Kent Scientific, CODA Monitor) and a tonometer (TonoLab). Instead of actively modulating intraocular pressure (IOP), animals with abnormal readings were excluded from the analysis (IOP of 8-10mmHg was considered normal). Imaging was performed ~45 minutes after the onset of rocuronium continuous infusion to avoid anesthestic transients. Prior to OCT imaging, animal eyes were dilated with 1% tropicamide, and topical anesthetic agent hydrochloride proparacaine was applied. Hypromellose 2.5% ophthalmic demulcent solution (Goniovisc) and artificial tears were periodically applied to prevent corneal dehydration.

*9.3.2 Injection of L-NAME*

In this study, L-NAME (Sigma-Aldrich) was used to modulate basal retinal blood flow and flicker stimulus response. L-NAME was prepared in saline vehicle at three different concentrations (0, 20, and 40mg/ml). The three solutions were intravenously injected via the lateral saphenous vein catheter ~15 minutes prior to OCT imaging in three different groups of rats (0mg/ml: n = 7, 20mg/ml: n = 7, and 40mg/ml: n = 8) at a dose volume of 1ml/kg.

*9.3.3 Ultrahigh speed spectral domain OCT*

The ultrahigh speed spectral domain OCT prototype used in this study was previously described in detail by our group[18]. Therefore, only the key characteristics and changes to the system are described in this section. An updated schematic of the system is shown in Figure 9.1. The prototype used a superluminescent diode (Superlum) with a bandwidth of ~55nm centered at 840nm, providing an axial resolution of ~5.7μm in tissue. The spectrometer used a 1200lpmm holographic diffraction grating (Wasatch Photonics) and a Basler Sprint line scan camera, utilizing only the center 832 pixels to achieve an A-scan rate of 244kHz. With an optical power of ~2.5mW incident on the cornea, the sensitivity was 99dB. A non-contact pivoted scanning configuration was used in the small animal imaging interface to avoid altering the intraocular pressure. The spot size on the retina was simulated to be ~15μm in Zemax using a standard rat eye model. The total imaging range in tissue was ~1.5mm, sufficient for small animal retinal and choroidal imaging. A custom electroretinograph was built using a differential amplifier (Tektronix ADA400A) to verify that visual flicker stimulates the inner retina. A custom-made silver chloride electrode loop with an inner diameter of ~5mm was gently placed on the cornea to record electroretinogram without blocking the flicker stimulus or OCT beam. The reference and ground electrodes were placed on the ears with the reference attached to the ear closer to the eye.

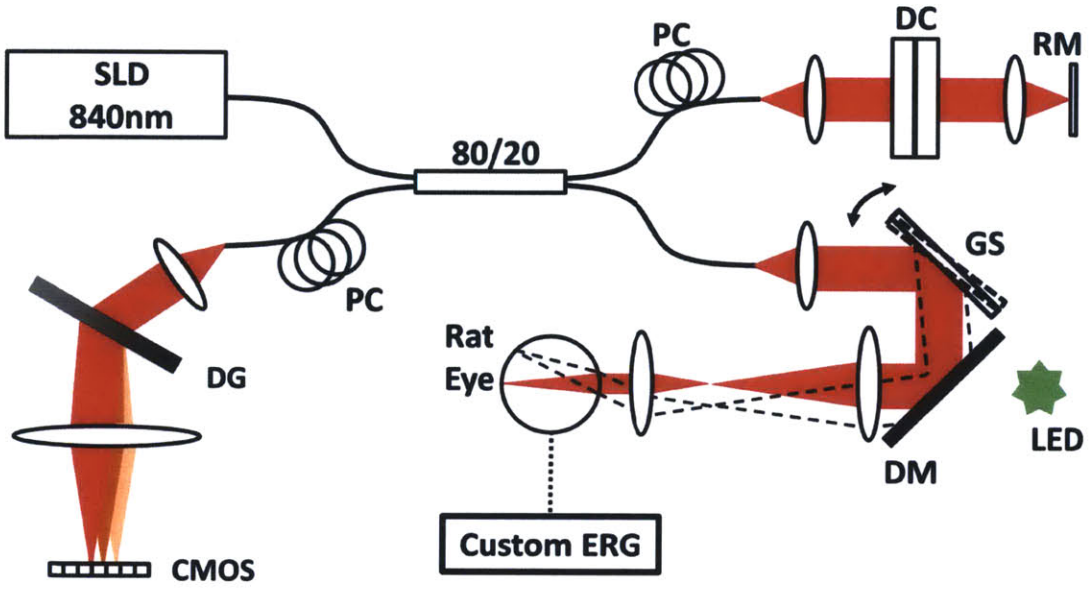


**Figure 9.1.** A schematic of the ultrahigh speed spectral domain OCT prototype. A fiber-based modified Michelson interferometer is used with an SLD light source centered at 840nm and an ultrahigh speed spectrometer to perform OCT imaging. SLD: superluminescent diode, PC: polarization controller, DC: dispersion compensation glass, RM: reference mirror, DG: diffraction grating, CMOS: line scane camera, DM: dichroic mirror, GS: galvanometer scanner, LED: light emitting diode, ERG: electroretinogram.

*9.3.4 Delivery of flicker stimulus*

Using a dichroic mirror, the OCT beam at centered at ~840nm was folded to simultaneously deliver green light emitted by a light emitting diode (LED) at ~525nm (Figure 9.1). Because the LED was located at one focal length away from the scan lens in the small animal imaging interface, the optical configuration generated a uniform Maxwellian illumination of green light over a circular area of ~2mm in diameter on the retina, limited by the lens tube. This in-line delivery of visible stimulus light guarantees that the center of the OCT imaging field of view is the center where visual flicker stimulus is delivered. The total power of the green light incident

on the cornea was 1.5mW at a 100% duty cycle, which was evenly distributed over a circular region with a diameter of 2mm. Green visual flicker stimulus was generated by modulating the LED driving current (Thorlabs, LDC205B) with a 12.5Hz square wave of 50% duty cycle. Visual flicker stimuli used in this study had durations of 15 seconds for all OCT scan patterns in order to avoid potential bias induced by the order of scan patterns used in a given rat. Because the typical OCT image acquisition time was less than 8 seconds, flicker stimulus continued for a few seconds even after an OCT data set was acquired.

*9.3.5 Ultrahigh speed Doppler OCT*

The ultrahigh speed Doppler OCT protocol for measuring pulsatile total retinal arterial blood flow in the rat eye was described previously in detail by our group[18]. In this study, a slightly modified protocol was used to measure the effect of visual flicker stimulus on total retinal blood flow. To summarize, en face Doppler OCT, which does not require measuring the angle between the OCT beam and blood vessel, was used over a 200μm×200μm area centered at the central retinal artery. By rapidly scanning the area with 150×25 A-scans per volume at a 85% galvanometer scanner duty cycle, a volume acquisition rate of ~55Hz was achieved, which was fast enough for resolving pulsatility in arterial blood flow. 400 volumes in total were acquired in a single continuous acquisition of ~7.3 second duration. Continuous visual flicker stimulus with duration of 15 seconds was started 2 seconds after the onset of Doppler OCT data set acquisition. Therefore, a single Doppler OCT data set contained basal retinal blood flow data for the first 2 seconds as well as hemodynamic visual flicker response. This avoided a potential bias from realigning the animal before and during a visual flicker stimulus.

Doppler OCT data was processed by comparing the phases of neighboring A-scans in the oversampled scan direction, which generated a three-dimensional axial velocity profile. The

axial velocity components in the central retinal artery cross-section in an en face plane intercepting the vessel were summed to calculate total retinal arterial blood flow through the central retinal artery. The algorithm for measuring total retinal arterial blood flow was completely automated as described previously[18]. Ultrahigh speed en face Doppler OCT enabled quantitative measurements of instantaneous total retinal blood flow in units of μL/min.

*9.3.6 Ultrahigh speed OCT angiography*

Ultrahigh speed OCT angiography was performed by calculating speckle decorrelation between sequential B-scans using the following equation, which maps the degree of speckle decorrelation between 0 and 1:

$$\overline{D}(x,y,z)=\frac{1}{N-1}\sum_{n=1}^{N-1}D_n(x,y,z)=\frac{1}{N-1}\sum_{n=1}^{N-1}\frac{\{I_n(x,y,z)-I_{n+1}(x,y,z)\}^2}{I_n^2(x,y,z)+I_{n+1}^2(x,y,z)} \tag{9.1}$$

where $x$ is the coordinate in the B-scan direction, $y$ the coordinate in the slow scan direction, $z$ the coordinate in depth, $I_n(x,y,z)$ OCT intensity (magnitude squared of the electric field) in the $n^{th}$ frame at $(x,y,z)$, and $N$ the total number of B-scans from a cross-section. Because the speckle pattern is stationary for stationary tissue, $\overline{D}(x,y,z)$ yields non-zero value only when there is an erythrocyte moving in a blood vessel, which results in local changes in OCT intensity at that location. Note that performing this operation at different cross-sectional locations in the slow scan direction generates a three-dimensional OCT angiogram. Because noise is uncorrelated, an intensity threshold is applied to suppress spurious decorrelation signals. A schematic of this operation is shown in Figure 9.2.

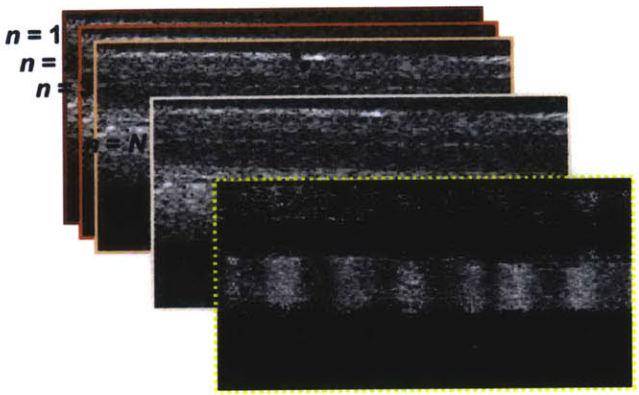


**Figure 9.2.** Ultrahigh speed speckle decorrelation OCT angiography. By comparing sequentially acquired B-scans from a given cross-sectional location, a cross-sectional OCT angiogram can be generated. Because noise is uncorrelated, an intensity threshold is applied to suppress spurious decorrelation signals. The OCT angiogram appears black when the decorrelation signal after intensity thresholding is zero, with higher values appearing progressively brighter. A three-dimensional volumetric OCT angiogram can be generated by performing this operation at multiple cross-sections.

Note that Equation (9.1) can be used to partially extract the velocity information of a red blood cell if certain conditions are met. If the B-scan time interval is sufficiently short, the change in OCT intensity due to erythrocyte movement can be considered relatively small, and it is possible to make the following approximation:

$$D_n(x,y,z) \simeq \frac{\{\Delta I_n(x,y,z)\}^2}{2I_n^2(x,y,z)} \tag{9.2}$$

where $\Delta I_n \equiv I_n - I_{n+1}$, which is assumed to be much smaller than $I_n$. If the point spread function of the OCT system is Gaussian in both the axial and transverse directions, the intensity of the speckle from a red blood cell can be expressed as:

$$I_n(x,y,z) = I_0 \exp[-(x_d^2 + y_d^2)/\sigma_{x,y}^2 - z_d^2/\sigma_z^2] \tag{9.3}$$

where $x_d^2$, $y_d^2$ , and $z_d^2$ are the deviations of the red blood cell location with respect to $(x, y, z)$ and $\sigma_{x,y}^2$ and $\sigma_z^2$ are the transverse and axial resolutions of the OCT system. By taking the differential, Equation (9.3) can be used to derive the following approximation:

$$\frac{\Delta I_n(x,y,z)}{I_n(x,y,z)} \simeq -\frac{2x_d\Delta x_d}{\sigma_{x,y}^2} - \frac{2y_d\Delta y_d}{\sigma_{x,y}^2} - \frac{2z_d\Delta z_d}{\sigma_z^2} \tag{9.4}$$

Assuming that the expectation values of $x_d$, $y_d$, and $z_d$ are all zero, the expectation value of Equation (9.2) can be expressed as:

$$\begin{aligned}\left\langle D_n(x,y,z)\right\rangle &\simeq \frac{2\left\langle x_d^2(\Delta x_d)^2\right\rangle}{\sigma_{x,y}^2} + \frac{2\left\langle y_d^2(\Delta y_d)^2\right\rangle}{\sigma_{x,y}^2} + \frac{2\left\langle z_d^2(\Delta z_d)^2\right\rangle}{\sigma_z^2} \\ &= \frac{2\left\langle x_d^2\right\rangle(\Delta x_d)^2}{\sigma_{x,y}^2} + \frac{2\left\langle y_d^2\right\rangle(\Delta y_d)^2}{\sigma_{x,y}^2} + \frac{2\left\langle z_d^2\right\rangle(\Delta z_d)^2}{\sigma_z^2}\end{aligned} \tag{9.5}$$

The last equality in Equation (9.5) is valid when steady flow, or equivalently, a constant erythrocyte velocity is assumed over the time it takes to acquire all $N$ B-scans from a given cross-section. Note that $\left\langle x_d^2\right\rangle$, $\left\langle y_d^2\right\rangle$, and $\left\langle z_d^2\right\rangle$ are constants assuming that $x_d$, $y_d$, and $z_d$ are random variables, and Equations (9.1) and (9.5) imply that the speckle decorrelation value is proportional to the sum of the magnitude squared of the transverse erythrocyte velocity and axial erythrocyte velocity, weighted by the transverse and axial resolutions of the OCT system.

In reality, $x_d$, $y_d$, and $z_d$ are not generally random variables, and certain conditions need to be imposed on the OCT scan pattern to ensure that the assumptions made in this section are not too invalid. Firstly, the B-scan interval needs to be short enough that $\Delta I_n << I_n$ is valid. Since the erythrocyte speeds in the retinal capillaries are typically ~1mm/s or less and the transverse resolution of the system is ~15μm, the minimum B-scan time interval required to ensure that the erythrocyte moves by less than a tenth of a transverse spot is ~1.5ms, which is ~670Hz in terms of the B-scan rate. In this study, the number of A-scans per B-scan was chosen to be 200 with a

galvanometer scanner duty cycle of 73%, which resulted in a B-scan rate of ~890Hz. At this B-scan rate, the erythrocyte travelling at ~1mm/s moves by ~1.1μm between sequential B-scans. Secondly, the dwell time at a given cross-section should be long enough that the expectation values of $x_d$, $y_d$, and $z_d$ are all zero. This condition can be roughly met by waiting longer than the time it takes for the erythrocyte to move more than a transverse spot size. In this study, 32 B-scans were acquired per cross-section, thereby allowing the erythrocyte travelling at ~1mm/s to move by ~35μm, which was larger than the transverse spot size of ~15μm. In summary, the scan pattern for ultrahigh speed OCT angiography used in this study was 200 A-scans × 200 cross-sections × 32 B-scans per cross-section with a duty cycle of 73%, which took ~7.2 seconds to acquire. Note that in retinal and choroidal OCT angiography, the microvasculature is predominantly in the transverse direction and the axial component of the erythrocyte movement was neglected in the study.

Three-dimensional OCT angiograms were segmented at the retinal pigment epithelium (RPE) using the co-registered OCT intensity volume. OCT angiograms at different depth ranges were projected separately in order to investigate the effect of flicker stimulus on retinal hemodynamics at the capillary level. After taking a basal volumetric OCT angiogram, a second volumetric OCT angiogram was acquired ~2 seconds after the onset of visual flicker stimulus without realigning the animal in order to measure the flicker response. OCT angiogram projections at different depths before and during flicker stimulus were compared during post-processing. Note that although the degree of speckle decorrelation does not provide absolute velocity by itself, the percent change in speckle decorrelation values do provide the percent change in the magnitude squared of velocity according to Equation (9.5), which enables the assessment of functional hyperemia at the capillary level.

*9.3.7 Data analysis*

For basal total retinal arterial blood flow and flicker response, the student t-test was performed to assess the effect of L-NAME at different concentrations. Performing a similar statistical analysis on OCT angiography data was challenging due to the three-dimensional nature of the resulting volumetric images. Instead, representative OCT angiography data with known amounts of flicker response, inferred from the percent increase in total retinal arterial blood flow measured with ultrahigh speed Doppler OCT, were analyzed to see the effect of functional hyperemia in the retina on OCT angiograms at the capillary level.

## 9.4 Results and Discussion

*9.4.1 Total retinal blood flow*

Figure 9.3 shows a representative functional hyperemic response to a continuous flicker stimulus started at t = 2s along with a simultaneously acquired electroretinogram acquired from a normal rat. By repeatedly scanning 150 × 25 A-scans per volume over a transverse area of 200μm × 200μm centered at the central retinal artery, a volume acquisition rate of 55Hz can be achieved, which is fast enough for dynamic total retinal blood flow imaging. A diffuse flicker stimulus was applied to the rat retina during OCT imaging using a dichroic mirror as shown in Figure 9.1, and therefore, potential error from realigning the animal between measurements could be avoided. An acute transient increase in pulsatile total retinal arterial blood flow in response to flicker stimulus can be clearly observed. In this particular case, basal flow was measured to be 2.50μl/min, and flicker response for t > 4s 3.47μl/min, resulting in a mean increase in blood flow by 38.9%. Note that the simultaneously acquired ERG shows that there is an oscillating potential at 12.5Hz after the onset of the flicker stimulus at 12.5Hz, which confirms that the retina is stimulated.

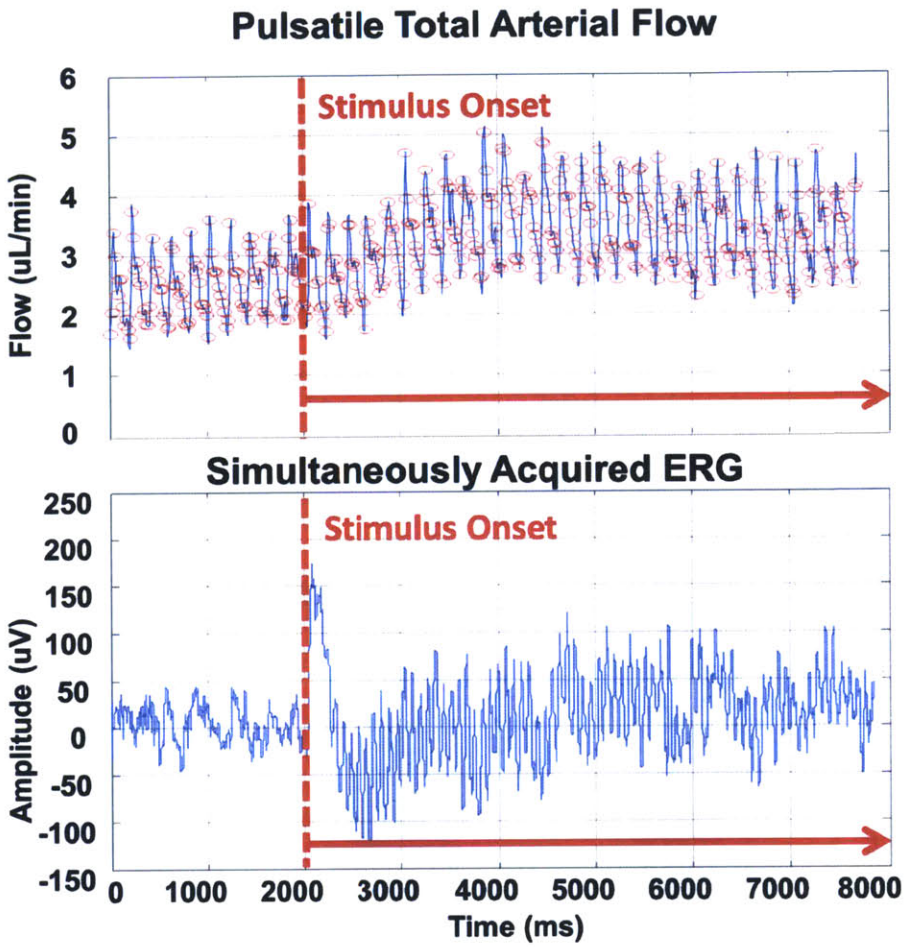


**Figure 9.3.** Pulsatile total retinal arterial blood flow measured in the rat retina with ultrahigh speed Doppler OCT and simultaneously acquired electroretinogram (ERG). Flicker stimulus at 12.5Hz was applied starting from t = 2s and lasted for 15 seconds. An acute transient increase in pulsatile total arterial retinal blood flow in response to continuous flicker stimulus can be observed. The simultaneously acquired ERG shows that there is an oscillating potential at 12.5Hz after the onset of the stimulus, which confirms that the retina is stimulated.

Note that the Doppler OCT measurement shown in Figure 9.3 provides basal total retinal blood flow and flicker response. In order to investigate the effect of L-NAME on retinal

hemodynamics in the rat retina and to assess how sensitive the measurement technique is in detecting changes in blood flow and flicker response, ultrahigh speed Doppler OCT imaging was performed on three different groups of rats. Each of the groups received a different amount of L-NAME: (1) Saline: n = 7, (2) 20mg L-NAME/kg-body weight: n = 7, and (3) 40mg L-NAME/kg-body weight: n = 8. Note that a statistical significance was reached for the L-NAME dose of 40mg/kg-body weight, which reduced basal blood flow by 28.3% on average.

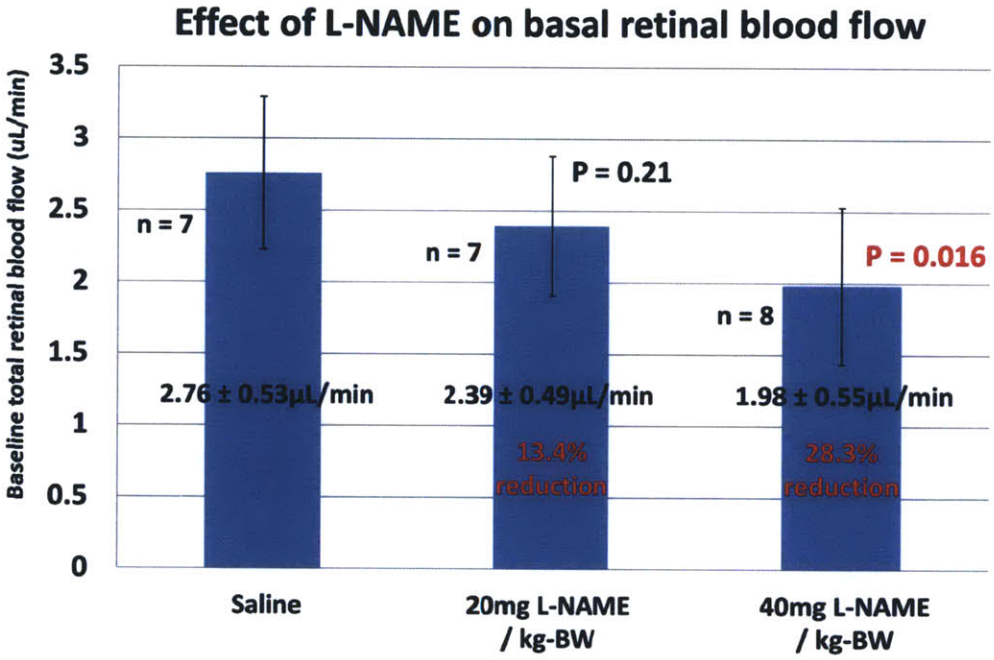


**Figure 9.4.** Effect of L-NAME on basal total retinal arterial blood flow. Basal retinal blood flow decreases in a dose-dependent manner. Note that a statistical significance is reached for the L-NAME dose of 40mg/kg-body weight, which reduces basal blood flow by 28.3% on average.

In general, the coefficient of variation for each of the three groups was relatively high (~20% or higher). However, it should be emphasized that the purpose of small animal imaging in general is not to make a diagnosis on individual animals. Therefore, as long as the coefficient of

variation is not excessively high, a moderate individual to individual variation is not an issue. In general, the coefficient of variation can depend heavily on anesthesia. Here, we demonstrate that when total retinal blood flow decreases by ~28.3%, $p = 0.016$ can be reached with $n = 7$ or 8 for the control and experimental group, under ketamine-xylazine anesthesia with paralysis using rocuronium. Although L-NAME was used in this experiment to modulate basal retinal blood flow, the reduction in blood flow may occur due to retinal diseases, such as diabetes in the streptozotocin rat model.

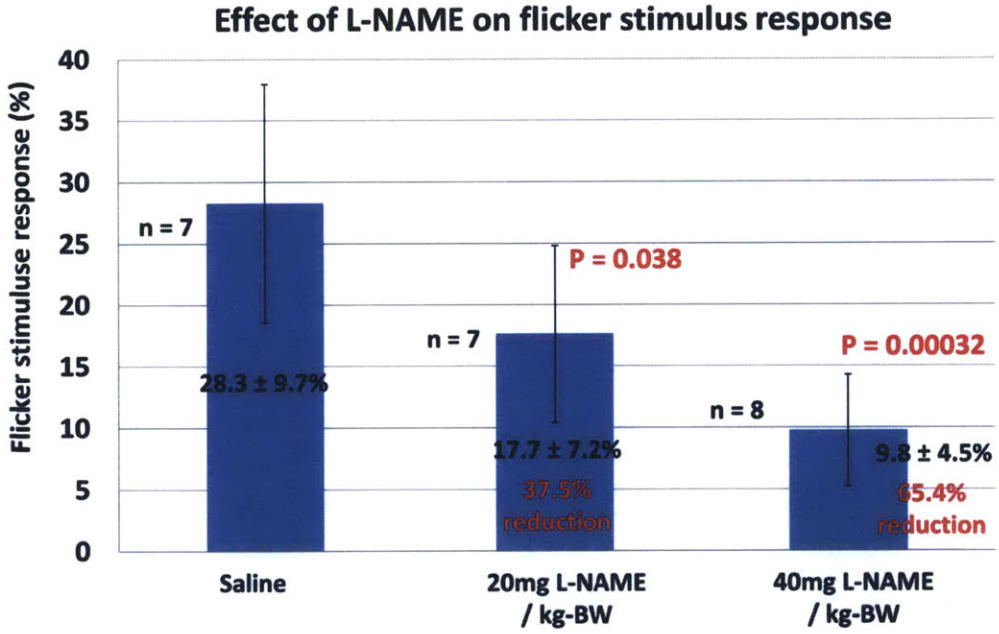


**Figure 9.5.** Effect of L-NAME on flicker stimulus response. Flicker response decreases in a dose-dependent manner. Note that a statistical significance is reached for the L-NAME doses of both 20mg/kg-body weight and 40mg/kg-body weight, which reduces basal blood flow by 37.5% and 65.4% on average, respectively.

As expected, L-NAME also reduced retinal functional hyperemic response to flicker stimulus in a dose-dependent manner. Note that a statistical significance was reached for both 20mg L-

NAME/kg-body weight and 40mg L-NAME/kg-body weight. Considering that basal total retinal blood flow was lower for higher L-NAME doses, the reduction in percent increase in blood flow is not due to an artifact from dividing with basal flow values.

*9.4.2 Capillary blood circulation*

Ultrahigh speed OCT angiography could visualize the capillary network in the small animal retina. Figure 9.6 shows the effect of flicker stimulus on ultrahigh speed OCT retinal angiograms from a normal rat retina with saline vehicle injected intravenously (0mg/ml L-NAME concentration). The increase in blood flow in the capillaries due to flicker stimulus can be clearly visualized. Note that the major retinal arterioles and venules also increased in diameter.

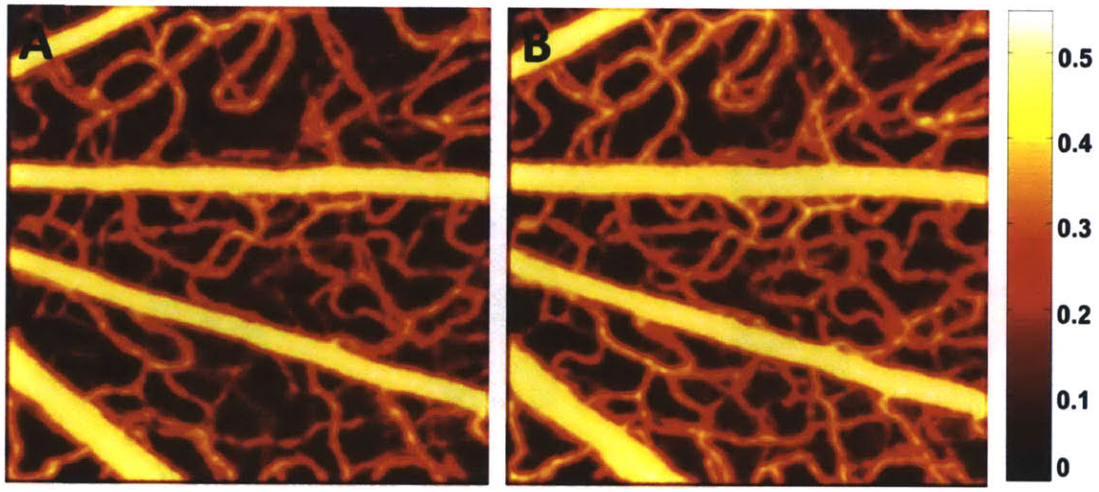


**Figure 9.6.** Ultrahigh speed OCT retinal angiograms (A) before and (B) during flicker stimulus in the normal rat retina with saline vehicle injected intravenously (0mg/ml L-NAME concentration). The increase in blood flow in the capillaries due to flicker stimulus can be clearly visualized. Note that the major retinal arterioles and venules also increased in diameter. 500μm × 500μm field of view. The colorbar shows the degree of speckle decorrelation.

For this particular data set, the increase in retinal blood flow at the capillary level was 12.3%, using the method described in Section 9.3.6. It should be noted that in Section 9.3.6, the degree of speckle decorrelation provides information on velocity only. However, in the retinal capillary network, most capillary branches follow single-profile flow, where only a single red blood cell travels through a capillary cross-section at a time. Therefore, the velocity information extracted from the speckle decorrelation value approximately provides the information on retinal tissue blood circulation. More detailed quantitation of dynamic responses of the capillary network to flicker stimulus is currently under investigation.

## 9.5 CONCLUSION

These results demonstrate the potential of ultrahigh-speed OCT for investigation of dynamic functional imaging of neurovascular coupling in the retina in response to flicker stimulus as well as conventional three-dimensional structural imaging. This method should be useful for investigation of small animal models of ocular diseases.

## References


1. Huang D, Swanson EA, Lin CP, Schuman JS, Stinson WG, Chang W, Hee MR, Flotte T, Gregory K, Puliafito CA, Fujimoto JG. Optical Coherence Tomography. Science. 1991;254(5035):1178-81. PubMed PMID: 1957169.

2. Choma MA, Sarunic MV, Yang CH, Izatt JA. Sensitivity advantage of swept source and Fourier domain optical coherence tomography. Optics Express. 2003;11(18):2183-9. PubMed PMID: 19466106.

3. Leitgeb R, Hitzenberger CK, Fercher AF. Performance of Fourier domain vs. time domain optical coherence tomography. Optics Express. 2003;11(8):889-94. PubMed PMID: 19461802.

4. Junod A, Lambert AE, Stauffac.W, Renold AE. Diabetogenic Action of Streptozotocin - Relationship of Dose to Metabolic Response. J Clin Invest. 1969;48(11):2129-39. doi: Doi 10.1172/Jci106180. PubMed PMID: 4241908; PubMed Central PMCID: PMC297467.

5. Nakhooda AF, Like AA, Chappel CI, Murray FT, Marliss EB. Spontaneously Diabetic Wistar Rat Metabolic and Morphologic Studies. Diabetes. 1977;26(2):100-12. doi: DOI 10.2337/diabetes.26.2.100. PubMed PMID: 320072.

6. Heriot WJ, Henkind P, Bellhorn RW, Burns MS. Choroidal Neovascularization Can Digest Bruch Membrane - a Prior Break Is Not Essential. Ophthalmology. 1984;91(12):1603-8. PubMed PMID: 6084226.

7. Dobi ET, Puliafito CA, Destro M. A New Model of Experimental Choroidal Neovascularization in the Rat. Arch Ophthalmol. 1989;107(2):264-9. PubMed PMID: 2464985.

8. Frank RN, Das A, Weber ML. A Model of Subretinal Neovascularization in the Pigmented Rat. Curr Eye Res. 1989;8(3):239-47. PubMed PMID: 2468453

9. Morrison JC, Moore CG, Deppmeier LMH, Gold BG, Meshul CK, Johnson EC. A rat model of chronic pressure-induced optic nerve damage. Exp Eye Res. 1997;64(1):85-96. doi: 10.1006/exer.1996.0184. PubMed PMID: 9093024.

10. Ruggeri M, Webbe H, Jiao SL, Gregori G, Jockovich ME, Hackam A, Duan YL, Puliafito CA. In vivo three-dimensional high-resolution imaging of rodent retina with spectral-domain optical coherence tomography. Investigative Ophthalmology & Visual Science. 2007;48(4):1808-14. PubMed PMID: 17389515

11. Tilton RG, Chang K, Pugliese G, Eades DM, Province MA, Sherman WR, Kilo C, Williamson JR. Prevention of Hemodynamic and Vascular Albumin Filtration Changes in Diabetic Rats by Aldose Reductase Inhibitors. Diabetes. 1989;38(10):1258-70. doi: DOI 10.2337/diabetes.38.10.1258. PubMed PMID: 2507378

12. Pugliese G, Tilton RG, Speedy A, Santarelli E, Eades DM, Province MA, Kilo C, Sherman WR, Williamson JR. Modulation of Hemodynamic and Vascular Filtration Changes in Diabetic Rats by Dietary Myoinositol. Diabetes. 1990;39(3):312-22. doi: DOI 10.2337/diabetes.39.3.312. PubMed PMID: 2307293

13. Cringle SJ, Yu DY, Alder VA, Su EN. Retinal Blood-Flow by Hydrogen Clearance Polarography in the Streptozotocin-Induced Diabetic Rat. Investigative Ophthalmology & Visual Science. 1993;34(5):1716-21. PubMed PMID: 8473111.

14. Bursell SE, Clermont AC, Shiba T, King GL. Evaluating Retinal Circulation Using Video Fluorescein Angiography in Control and Diabetic Rats. Curr Eye Res. 1992;11(4):287-95. doi: Doi 10.3109/02713689209001782. PubMed PMID: 1388117.

15. Higashi S, Clermont AC, Dhir V, Bursell SE. Reversibility of retinal flow abnormalities is disease-duration dependent in diabetic rats. Diabetes. 1998;47(4):653-9. doi: 10.2337/diabetes.47.4.653. PubMed PMID: 9568700.

16. Lee S, Morgan GA, Harris NR. Ozagrel reverses streptozotocin-induced constriction of arterioles in rat retina. Microvasc Res. 2008;76(3):217-23. doi: 10.1016/j.mvr.2008.07.005. PubMed PMID: 18718478; PubMed Central PMCID: PMC2601578.

17. Leskova W, Watts MN, Carter PR, Eshaq RS, Harris NR. Measurement of retinal blood flow rate in diabetic rats: disparity between techniques due to redistribution of flow. Invest Ophthalmol Vis Sci. 2013;54(4):2992-9. Epub 2013/04/11. doi: 10.1167/iovs.13-11915. PubMed PMID: 23572104; PubMed Central PMCID: PMC3638664.

18. Choi W, Baumann B, Liu JJ, Clermont AC, Feener EP, Duker JS, Fujimoto JG. Measurement of pulsatile total blood flow in the human and rat retina with ultrahigh speed spectral/Fourier domain OCT. Biomedical Optics Express. 2012;3(5):1047-61. PubMed PMID: 22567595; PubMed Central PMCID: PMC3342181.

19. Franceschini MA, Radhakrishnan H, Thakur K, Wu W, Ruvinskaya S, Carp S, Boas DA. The effect of different anesthetics on neurovascular coupling. NeuroImage. 2010;51(4):1367-77. doi: http://dx.doi.org/10.1016/j.neuroimage.2010.03.060.

20. Masamoto K, Kanno I. Anesthesia and the quantitative evaluation of neurovascular coupling. J Cereb Blood Flow Metab. 2012;32(7):1233-47.

21. Muir ER, Duong TQ. MRI of retinal and choroidal blood flow with laminar resolution. Nmr in Biomedicine. 2011;24(2):216-23. doi: Doi 10.1002/Nbm.1576. PubMed PMID: ISI:000288209300013.

22. Riva CE, Logean E, Falsini B. Visually evoked hemodynamical response and assessment of neurovascular coupling in the optic nerve and retina. Prog Retin Eye Res. 2005;24(2):183-215. doi: DOI 10.1016/j.preteyeres.2004.07.002. PubMed PMID: 15610973.

23. Riva CE, Salgarello T, Logean E, Colotto A, Galan EM, Falsini B. Flicker-evoked response measured at the optic disc rim is reduced in ocular hypertension and early glaucoma. Investigative Ophthalmology & Visual Science. 2004;45(10):3662-8. doi: 10.1167/iovs.04-0100. PubMed PMID: 15452074.

24. Garhofer G, Zawinka C, Resch H, Huemer KH, Schmetterer L, Dorner GT. Response of retinal vessel diameters to flicker stimulation in patients with early open angle glaucoma. J Glaucoma. 2004;13(4):340-4. doi: 10.1097/00061198-200408000-00013. PubMed PMID: 15226664.

25. Garhofer G, Zawinka C, Resch H, Kothy P, Schmetterer L, Dorner GT. Reduced response of retinal vessel diameters to flicker stimulation in patients with diabetes. Brit J Ophthalmol. 2004;88(7):887-90. doi: DOI 10.1136/bjo.2003.033548. PubMed PMID: 15205231; PubMed Central PMCID: PMC1772243.

26. Pemp B, Garhofer G, Weigert G, Karl K, Resch H, Wolzt M, Schmetterer L. Reduced Retinal Vessel Response to Flicker Stimulation but Not to Exogenous Nitric Oxide in Type 1 Diabetes. Investigative Ophthalmology & Visual Science. 2009;50(9):4029-32. doi: Doi 10.1167/Iovs.08-3260. PubMed PMID: 19369238.

27. Mandecka A, Dawczynski J, Blum M, Muller N, Kloos C, Wolf G, Vilser W, Hoyer H, Muller UA. Influence of flickering light on the retinal vessels in diabetic patients. Diabetes Care. 2007;30(12):3048-52. doi: Doi 10.2337/Dc070927. PubMed PMID: 17728481.

28. Nguyen TT, Shaw J, Kawasaki R, Vilser W, Wang JJ, Wong TY, Kreis AJ. Flicker Light-Induced Retinal Vasodilation in Diabetes and Diabetic Retinopathy. Diabetes Care. 2009;32(11):2075-80. doi: Doi 10.2337/Dc09-0075. PubMed PMID: 19641162; PubMed Central PMCID: PMC2768208.

29. Lecleire-Collet A, Audo I, Aout M, Girmens J, Sofroni R, Erginay A, Le Gargasson J, Mohand-Said S, Meas T, Guillausseau P, Vicaut E, Paques M, Massin P. Evaluation of Retinal Function and Flicker Light-Induced Retinal Vascular Response in Normotensive Patients with Diabetes without Retinopathy. Investigative Ophthalmology & Visual Science. 2011;52(6):2861-7. doi: Doi 10.1167/Iovs.10-5960. PubMed PMID: 21282578.

30. Srienc AI, Kurth-Nelson ZL, Newman EA. Imaging retinal blood flow with laser speckle flowmetry. Frontiers in neuroenergetics. 2010;2. Epub 2010/10/14. doi: 10.3389/fnene.2010.00128. PubMed PMID: 20941368; PubMed Central PMCID: PMC2950742.

31. Shih YY, Wang L, De La Garza BH, Li G, Cull G, Kiel JW, Duong TQ. Quantitative retinal and choroidal blood flow during light, dark adaptation and flicker light stimulation in rats using fluorescent microspheres. Curr Eye Res. 2013;38(2):292-8. Epub 2013/01/16. doi: 10.3109/02713683.2012.756526. PubMed PMID: 23317112; PubMed Central PMCID: PMC3752417.

32. Radhakrishnan H, Srinivasan VJ. Multiparametric optical coherence tomography imaging of the inner retinal hemodynamic response to visual stimulation. J Biomed Opt. 2013;18(8):086010-. doi: 10.1117/1.jbo.18.8.086010.

33. Buerk DG, Riva CE, Cranstoun SD. Nitric Oxide Has a Vasodilatory Role in Cat Optic Nerve Head during Flicker Stimuli. Microvasc Res. 1996;52(1):13-26. doi: http://dx.doi.org/10.1006/mvre.1996.0040.

34. Kondo M, Wang L, Bill A. The role of nitric oxide in hyperaemic response to flicker in the retina and optic nerve in cats. Acta Ophthalmol Scan. 1997;75(3):232-5. doi: 10.1111/j.1600-0420.1997.tb00762.x.